Astron Astrophys Rev (2008) 16:1–153
DOI 10.1007/s00159-008-0013-x

REVIEW ARTICLE

# Sixty-five years of solar radioastronomy: flares, coronal mass ejections and Sun–Earth connection

**Monique Pick · Nicole Vilmer**

Received: 15 February 2008 / Published online: 15 October 2008


**Abstract** This paper will review the input of 65 years of radio observations to our understanding of solar and solar–terrestrial physics. It is focussed on the radio observations of phenomena linked to solar activity in the period going from the first discovery of the radio emissions to present days. We shall present first an overview of solar radio physics focussed on the active Sun and on the premices of solar–terrestrial relationships from the discovery to the 1980s. We shall then discuss the input of radioastronomy both at metric/decimetric wavelengths and at centimetric/millimetric and submillimetric wavelengths to our understanding of flares. We shall also review some of the radio, X-ray and white-light signatures bringing new evidence for reconnection and current sheets in eruptive events. The input of radio images (obtained with a high temporal cadence) to the understanding of the initiation and fast development in the low corona of coronal mass ejections (CMEs) as well as the radio observations of shocks in the corona and in the interplanetary medium will be reviewed. The input of radio observations to our knowledge of the interplanetary magnetic structures (ICMEs) will be summarized; we shall show how radio observations linked to the propagation of electron beams allow to identify small scale structures in the heliosphere and to trace the connection between the Sun and interplanetary structures as far as 4AU. We shall also describe how the radio observations bring useful information on the relationship and connections between the energetic electrons in the corona and the electrons measured in-situ. The input of radio observations on the forecasting of the arrival time of shocks at the Earth as well as on Space Weather studies will be described. In the last section, we shall summarize the key results that have contributed to transform our knowledge of solar activity and its link with the interplanetary medium. In conclusion, we shall indicate the instrumental radio developments at Earth and in space, which are from our point of view, necessary for the future of solar and interplanetary physics.

M. Pick (✉) · N. Vilmer
LESIA, UMR CNRS 8109, Observatoire de Paris, Meudon 92195, France
e-mail: monique.pick@obspm.fr

**Keywords** Solar activity · Solar coronal mass ejections · Solar flares · Solar radio radiation · Solar terrestrial relations · Interplanetary medium

## Contents

## 1 Introduction

**L' essentiel est invisible pour les yeux** (A. de Saint Exupéry, *Le Petit Prince*)

Until the 1940s (start of radioastronomy), astronomers and among them solar physicists had a still limited knowledge of the universe and of the Sun, since the information that they were using to unveil the mysteries of the celestial objects were limited to wavelengths in the optical domain. Therefore, they had very few information on the hot and tenuous matter (plasma) which is essentially invisible at optical wavelengths (apart from natural or artificial eclipses made with coronographs or from its detection in optical lines from highly ionized atoms); this is very important to understand the connections between phenomena observed at the solar surface (such as sunspots) and in the terrestrial atmosphere (such as aurorae). Since the middle of the last century, the whole electromagnetic spectrum has been opened step by step: radio observations and then, after the launch of the first artificial satellites, access to UV and X-ray observations and also (quite important for solar–terrestrial physics) to in-situ measurements of the interplanetary medium and of the close environment of the Earth.

This paper will review the input of radio observations to our understanding of solar and solar–terrestrial physics. It will not cover however the whole field of solar radioastronomy, in particular the observations of the quiet Sun and the variability of solar radio emission with the solar cycle, nor the aspects linked to radio scintillations in the interplanetary medium. This review is focussed on the active Sun and on the radio observations of phenomena linked to solar activity.

This paper will cover the period going from the first discovery of the radio emissions of the Sun to present days (and the celebration of International Heliophysical Year, IHY); it will summarize our knowledge of the radio observations associated to flares, eruptive events and coronal mass ejections (CMEs) before the launch of the Hinode and STEREO missions. We shall show how radio observations provided since their first measurements a lot of information on solar activity and on the production of energetic electrons in the corona and how these radio observations, when combined with observations at other wavelengths, led to pioneering discoveries in the field of solar–terrestrial physics and prediction of geomagnetic activity even before the discovery of CMEs in 1973. Good and more complete reviews of solar radio physics from the early period to now can be found in the books of Kundu (1965), Krueger (1979), Melrose (1986), McLean and Labrum (1985), Gary and Keller (2004). This paper is not aimed either at reviewing the plasma processes at the origin of radio emissions (the reader will find a good overview of these processes in the books of Melrose (1986), Benz (1993) and the Chap. 10 of Gary and Keller (2004)); this paper is thus not aimed at discussing processes observed with excellent spectral resolution (such as zebra patterns, fibers, spikes) and of their input to emitting processes (see, e.g. a recent review by Benz in Chap. 10 of Gary and Keller 2004). The short appendix at the end will only give some basic information on the general context for the propagation and emission of radio waves in a plasma.

This review which is aimed at solar activity (flares and CMEs) is focussed on the input of spatially resolved observations at radio wavelengths and will follow the progress of radio imaging starting from the first interferometers in the 1960s to the more complex solar dedicated radioheliographs operating today in the microwave and the metre/decimetre wavelength range. We shall also point out that after the International Geophysical Year (1957–1958) and the beginning of the space era, most of the results were obtained through a multi-wavelength/multi-instrument approach, for example radio, X-rays and in-situ particles for the study of particle acceleration, UV, X-ray and coronographs for the study of CMEs. We shall also describe what could be learnt with observations from future solar dedicated radioheliographs.

The paper is organized as follows:

- Section 2 provides an overview of solar radio physics from the discovery of the emission to the 1980s after the first detection of CMEs and prior to the launch of Solar Maximum Mission aimed at the study of solar flares and CMEs. This historical overview will be focussed on the active Sun and on the premices of solar–terrestrial physics, in particular on the first discoveries on flares and CMEs.
- Section 3 will provide a brief overview of the radio diagnostics allowing to measure the coronal magnetic field. The magnetic topology is indeed a major and fundamental parameter to understand all the aspects of solar activity described in the following sections.
- Section 4 will be devoted to the input of radio astronomy to our understanding of solar flares on: first, characterization of the acceleration sites of energetic electrons and of their evolution in the course of flares as deduced from spatially resolved metric and decimetric radio observations and comparison with X-ray observations of energetic electrons; secondly, quantitative diagnostics of energetic electrons and constraints on acceleration mechanisms obtained from combined X-ray and radio observations at microwave wavelengths. This section will also discuss the observations obtained in the new radio window recently opened at submillimetre wavelengths which provides in particular the information on the extremes of particle acceleration in solar flares. The questions raised on the interpretation of a new radio component observed in this frequency range will be briefly discussed.
- Section 5 will focus on the input of combined radio and X-ray observations for our understanding of flares and eruptive phenomena. In particular, we shall describe the new evidence for reconnection and current sheets in eruptive events as observed at radio and X-ray wavelengths and for the associated electron acceleration.
- Section 6 will be devoted to CMEs. We shall demonstrate how radio observations, in particular radio images of the corona obtained with a high temporal cadence provide crucial information on the initiation, the development and the propagation of CMEs in the low corona (both on the disk and on the limb) and on the importance of the interplay between different spatial scales for the development of CMEs. We shall also describe how radio observations may underline the coronal structures which will be linked to the ejected material.
- Section 7 will describe the radio observations of shocks in the corona and in the interplanetary medium and their relationship with flares and CMEs.
- Section 8 will be devoted to the input of radio observations to our knowledge of the interplanetary magnetic structures (ICMEs). We shall indeed show how radio observations linked to the propagation of electron beams allow to identify small scale structures in the heliosphere and to trace the connection between the Sun and structures measured in-situ in the interplanetary medium. Interactions of fast and

slow CMEs and associated electron acceleration are also revealed by the combination of radio observations at long wavelengths and of white light observations.

– Section 9 will describe how the radio observations allow to understand the relationship and connections between the energetic electrons in the corona and the electrons measured in-situ, as well as to improve our knowledge on the origin and propagation of energetic particles, in particular events with an enriched composition of $^3$He.
– The last two sections will be aimed at the input of radio observations on the forecasting of the arrival time of shocks at the Earth as well as on Space Weather studies: radio bursts and impact on wireless communication systems, prediction of solar energetic particle events and of geomagnetic storms.
– Finally we shall summarize in the last section, how the results presented in this review has significantly contributed to transform our knowledge of the processes occurring on the Sun and in the interplanetary medium. We shall also briefly discuss the progress expected in this field with the new solar dedicated radioheliographs under development and with the space missions starting to operate, in particular the STEREO mission dedicated to the study of CMEs. We shall finally emphasize the need for a network of radio spectral measurements.

## 2 Historical context

### 2.1 The 1940–1965 period

On February 27 and 28, 1942, a chain of British radar stations observed in the metric wavelength range a strong radio noise originating from the direction of the Sun, that Hey associated with a big solar flare (Hey 1942). The connection between intense radio bursts and flares was recognized soon after (Hey 1946; Appleton and Hey 1946a,b). The first published report of radio waves from the Sun was made by Reber (1944). During the same period, Southworth (1945) discovered the solar thermal microwave radio emission. Since these initial discoveries in the forties, solar radio astronomy has developed very promptly in different directions covering technical research and development, physics of the solar atmosphere and of the solar–terrestrial system, and plasma physics related to emission mechanisms and propagation of electro-magnetic waves.

Historically, radio emission was divided into three categories: the quiet Sun emission, the slowly varying component (SVC) associated with the transit on the solar disk of structures such as active regions or streamers, and sporadic activity which includes a large variety of bursts. With the progresses accomplished nowadays in the observations and in the knowledge of the physical processes responsible for radio emission, this classification appears somewhat arbitrary now.

#### *2.1.1 The slowly varying component*

Covington (1948) found that there was a relationship between the intensity of the 10.7 cm emission and the presence of sunspots on the disk. Denisse (1948) and Pawsey and Yabsley (1949) showed independently that, in addition to the quiet Sun component, which remains constant over long periods, there is another component called the SVC, which varies from day to day and which is correlated with the sunspot areas. The SVC is most prominent in the wavelength range from 3 to 60 cm. Positions of bright regions were obtained with multi-element interferometers, first introduced by Christiansen and Warburton (1953). Figure 1 displays a succession of daily records obtained at 21 cm which shows the one-dimensional brightness distribution over the solar disk. A typical source of the SVC observed at 3 cm (Kundu 1959b) and 8 mm (Salomonovich 1962) is usually composed of two regions: (a) a polarized region of small diameter ($<1.5'$) called the *core*, which overlays sunspots and (b) a less intense weakly polarized region of larger diameter ($4$–$5'$), which corresponds to active regions. The contrast between core and halo is much less at 8 mm than at 3 cm. At wavelengths longer than 3 cm, the relative contribution of the core decreases with increasing wavelength. At 21 cm, the emission is dominated by the large component corresponding to the plage in the active region. Two dimensional measurements of angular sizes (Christiansen and Mathewson 1959) indicated brightness temperatures ranging up to a cut-off of about $1.5 \times 10^6$ K. Swarup et al. (1963) found core temperatures between 1.6 and $3.8 \times 10^6$ K near 10 cm. However, the resolving power of the instruments was not sufficient to determine accurately the temperature range of the core itself. The core emission at 8 mm was attributed to thermal bremsstrahlung (free–free emission) resulting from Coulomb interaction of thermal electrons with ions, and at cm wave-

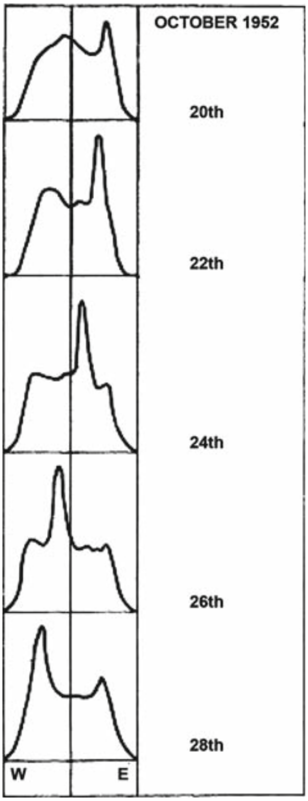


**Fig. 1** A succession of daily records showing the one-dimensional brightness distribution over the solar disk (from Christiansen and Warburton 1953)

lengths to gyro resonance radiation at the harmonics $2w_h$ and $3w_h$ of the gyrofrequency of the electrons spiralling along magnetic field lines (Zheleznyakov 1962; Kakinuma and Swarup 1962). It was concluded that the process of resonance absorption at the harmonics of the gyrofrequency could explain the small size of the sources at centimetre wavelengths, the observed spectrum and polarization (see also Lantos 1968). No observation was available at that time to detect the predicted structure.

### *2.1.2 Identification of radio bursts and emitting mechanisms*

Until 1950, all observations of radio bursts were made at single-frequencies. The flare-associated bursts were referred to as outbursts by Allen (1947). Some of these outbursts, when observed simultaneously at several single frequencies, showed onset times varying with frequencies (high frequencies appearing first) and a delay of the radio emission with respect to the optical flare. This is illustrated in Fig. 2. These observations led Payne-Scott et al. (1947) to link the outbursts to the passage in the corona of disturbances that propagate outwards with a velocity of several hundred $\mathrm{km\,s^{-1}}$ and trigger radio emission into regions of decreasing electronic density. It was also found that only a fraction of the bursts at metre wavelengths were associated with optical flares. In particular, long duration emissions, such as the one shown in Fig. 3,

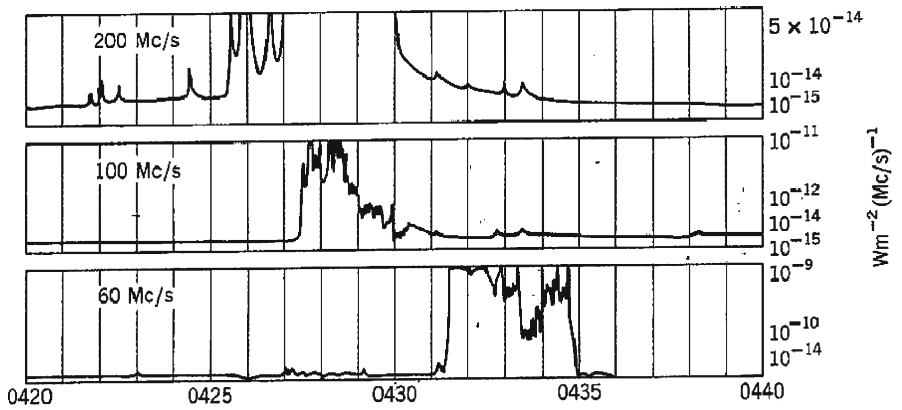


**Fig. 2** Records of the outburst of March 8, 1947 on 60, 100 and 200 $\mathrm{Mc\,s^{-1}}$. Note the progressive time delay in the onset of the outburst on different frequencies (from Payne-Scott et al. 1947)

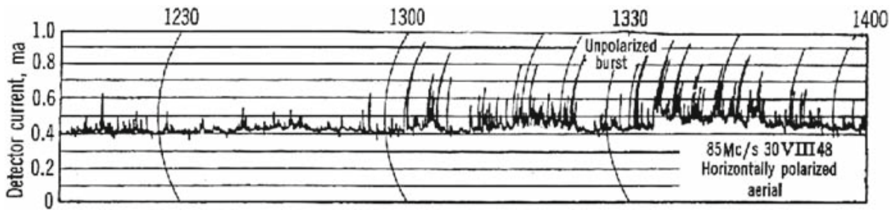


**Fig. 3** Typical recording of enhanced radiation at 85 $\mathrm{Mcs^{-1}}$ (adapted from Payne-Scott 1949)

frequently called type I noise storms and composed of short-lived (a few seconds) and narrow band (a few MHz) bursts superposed on a continuum were also characterized in the early 1950s (e.g. Payne-Scott et al. 1947; Dodson et al. 1953). Noise storms lasting for hours and days represent the most common form of solar activity from non-thermal origin at metric and decametric wavelengths.

The next important step was the development of radiospectrographs which allowed to continuously record the intensity of the solar emission as a function of frequency and time. The first observations were made in the frequency range 40–70 MHz (Wild and McCready 1950). The dynamic spectra of the bursts showed a great complexity and very different sporadic features that could last from a fraction of a second to several hours as shown in Fig. 4. The analysis revealed a large variety of bursts drifting toward lower frequencies. Two sub-classes of drifting bursts were identified: the type II and the type III bursts which are respectively characterized by a frequency drift of $\sim$0.25 and $\sim$20 $\mathrm{MHz\,s^{-1}}$. Harmonic features with a 2:1 frequency separation were also observed in the spectra of type II and type III bursts (Wild et al. 1954). An example is shown in Fig. 5. The discovery of harmonics was taken as evidence that these emissions originate from a common source producing oscillations at a fundamental frequency w and at its second harmonic 2w. Furthermore the observed narrow bandwidth (2–3% of the central frequency) led to the conclusion that a natural frequency is controlling the oscillations (either electron gyro-frequency or plasma frequency). The

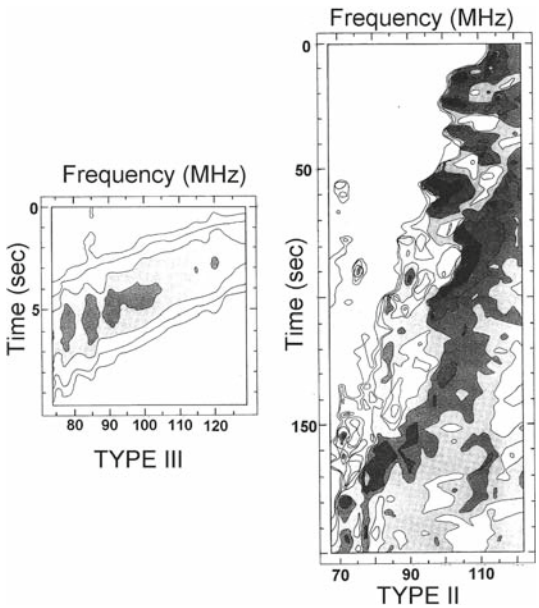


**Fig. 4** Observations of the spectrum of high intensity solar radiation at metre and decametre wavelengths (adapted from Wild and McCready 1950)

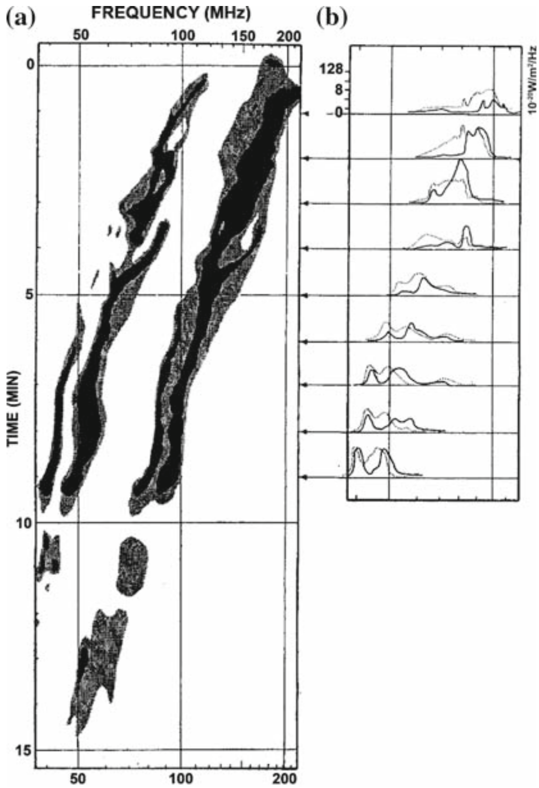


**Fig. 5** The outburst of November 21, 1952, 23 h 50 min UT. **a** The dynamic spectrum. The intensity contours correspond to levels of approximately 5 and 20 W$m^{-2}$ $Hz^{-1}$. **b** Profiles at 1-min intervals. The second harmonic is shown *dotted* and displaced in frequency by a factor of 2 (from Wild et al. 1954)

combination of the observations of a 2:1 ratio in the harmonic bands and of the already known difficulties of escape of emission at the fundamental gyrofrequency from the solar atmosphere (Roberts 1952) allowed to conclude that the drifting emissions were at the local plasma frequency $f_p$ and its second harmonics. Because the density (thus the plasma frequency) decreases outward from the Sun, the emission drifts rapidly from high to lower frequencies.

With the construction of a two element swept frequency interferometer allowing to estimate the positions of sources as different frequencies, the conclusion was reached that type II bursts are excited by a disturbance travelling through the corona at speeds of $\sim 10^3\ \mathrm{km\,s^{-1}}$, whereas type III bursts are generated by electron beams with typical speed of $10^5\ \mathrm{km\,s^{-1}}$ (Wild et al. 1959a,b). The disturbance associated with the type II burst was later identified as a MHD shock by Uchida (1960) who also associated type II bursts with H$\alpha$ Moreton waves that were discovered by Moreton and Ramsey (1960). Moreton waves travel from the flare region with speeds ranging from a few hundreds to a few thousands $\mathrm{km\,s^{-1}}$. They were interpreted as the chromospheric trace of MHD coronal waves.

Two element interferometers were shortly followed by multi-element (grating) interferometers that provided scans of the solar brightness in one or two directions. They were realized on many wavelengths from metre to centimetre wavelengths (e.g. Christiansen and Warburton 1953; Tanaka and Kakinuma 1955; Blum et al. 1957; Firor 1959; Pick-Gutmann and Steinberg 1959). In 1957, Boischot identified, with the Nançay 32-element interferometer operating at 169 MHz, a new class of emission, the type IV burst (Boischot 1957, 1958). Type IV bursts occur after a solar flare, usually follow a type II burst and last for tens of minutes. Type IV burst sources are generally of large diameter (typically $8'$–$12'$) with no spatial structure (smooth appearance) and move outwards with speeds of several hundred $\mathrm{km\,s^{-1}}$, or even more. One example is shown in Fig. 6. Boischot and Denisse (1957) interpreted the type IV emission as being due to synchrotron radiation of relativistic electrons spiralling in the coronal magnetic field. It was, however, rapidly recognized that type IV bursts were much more complex events with an extended spectral range covering a large domain of frequencies in which several components of distinct physical origins could be distinguished. Intense centimetre-wave outbursts were associated with metric type IV emissions (Kundu 1959b). Two phases were schematically distinguished (Pick-Gutmann 1961) as illustrated in Fig. 7. The first phase (called *flare-continuum* in 1970 by Wild) corresponds to a broad band emission, from centimetre to metre wavelengths, which starts near the flash phase of the optical flare; the intensity variations are roughly similar at all frequencies and the radiation has little directivity. The second phase, called *continuum storm* (*stationary type IV burst* in the 1963 Wild et al. terminology) is characterized by a smooth continuum detected in the dm-dam wavelengths which can last many hours and becomes progressively an ordinary type I storm. The emitting source is stationary, has a small angular diameter, is strongly polarized in the ordinary mode and is directive. Taking in consideration all these properties, the continuum storm was interpreted as due to a plasma emitting mechanism. In addition to these two phases, subsequent radioheliographic observations revealed, 10 years later, that the moving type IV bursts, identified by Boischot (1957), originates from the same solar position as the first phase, i.e. from the position of the flare continuum (Robinson and Smerd 1975).

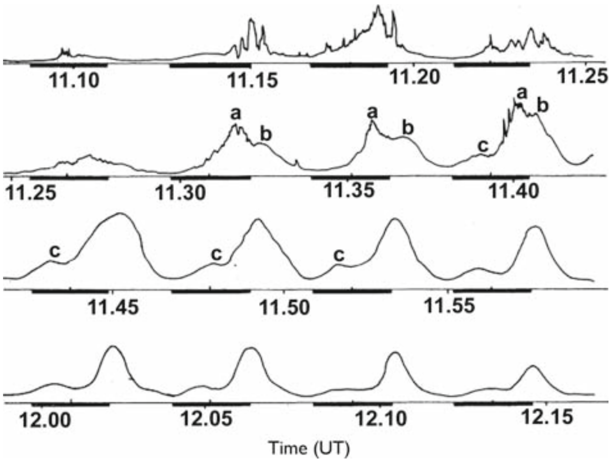


**Fig. 6** November 7, 1956 event recorded at 169 MHz by the East-West Nançay grating interferometer. The variable source a is probably the source of a type II burst followed by the smooth source b of type IV burst; the peaks c are generated in the side lobes of the interferometer; the *black bars* indicate the position of the photospheric disk through the successive main lobes of the interferometer; the recording time of each main lobe is indicated below (adapted from Boischot 1958)

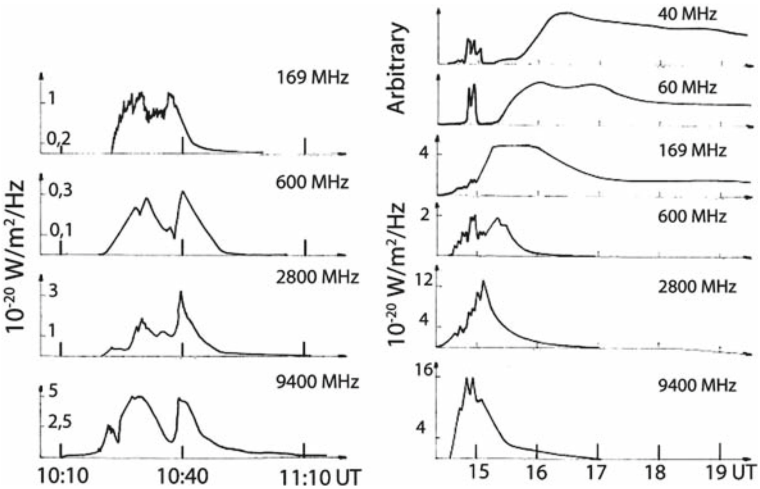


**Fig. 7** *Left panel* First phase of the type IV burst on August 28, 1958: Flux evolution measured at discrete frequencies. *Right panel* Flux evolution of the type IV burst observed on August 22, 1958; The first phase seen from high frequencies to 169 MHz at least is followed by a continuum storm of long duration well developed below 600 MHz (adapted from Pick-Gutmann 1961)

While observations of radio bursts at metric wavelengths led to a classification into physically significant spectral types, the burst spectra in the microwave domain have been less explored. The general features of the microwave bursts have been known since about 1947, but systematic studies of their source characteristics have been initiated mainly during the International Geophysical Year—IGY (July 1957–December

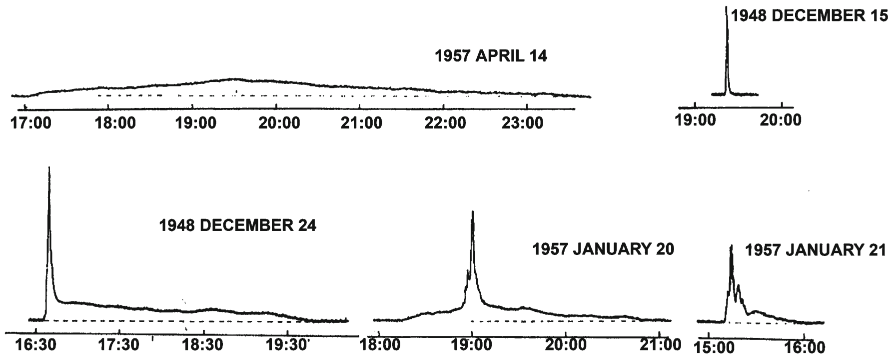


**Fig. 8** Single-frequency flux recording of microwave bursts made at 10.7 cm made by Covington and his collaborators (adapted by Wild et al. 1963)

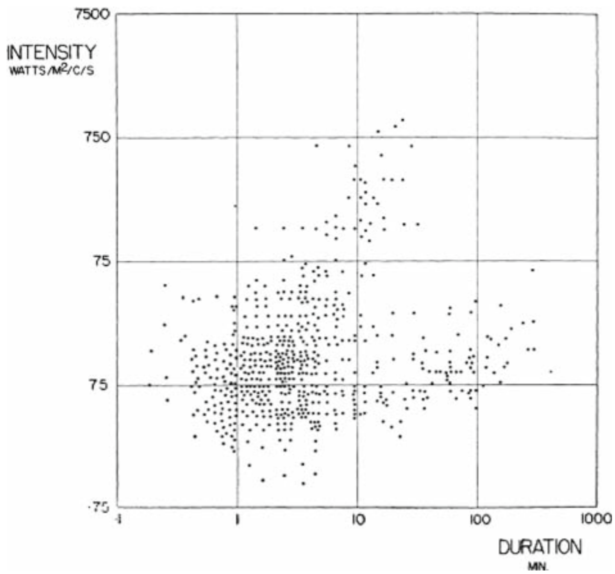


**Fig. 9** Scatter diagram of simple bursts for 1956. Log of intensity versus log of duration (from Covington and Harvey 1958)

1958). Because of their relatively simple structures, microwave bursts were classified according to their appearance on single-frequency flux records, i.e. by their intensity, total duration and duration of the rise and fall phases (Dodson et al. 1954). Figure 9, which displays a scatter diagram of 10 cm intensity versus duration, shows a well developed two branch distribution that indicates the existence of two types of simple bursts: the first one corresponds to impulsive bursts of relatively high intensity and short duration and the second one to long-lasting bursts of relatively low intensities (Covington and Harvey 1958). This long-lasting type includes in fact two types of events, the Gradual Rise and Fall (GRF, see Figs. 8, 9) and the post burst increase identified later on by Kundu (1959a). The bursts may appear in various types of com-

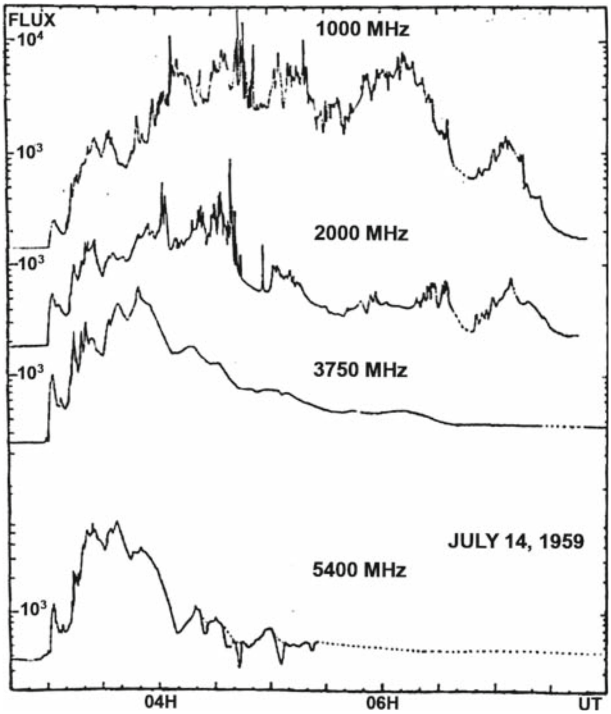


**Fig. 10** Single frequency observations of microwave type IV bursts (from Kakinuma and Tanaka 1961)

binations. Kundu (1959b) determined from interferometric observations the different types of centimetre wave bursts: a nonthermal origin was proposed for the impulsive bursts (see also the appendix). In addition to the impulsive and the gradual events, Kundu (1959b) and Kakinuma and Tanaka (1961) identified another type of complex broad-band microwave outbursts (see Fig. 10), characterized by a relative high intensity and long duration. Takakura (1959) showed that these outbursts could be caused by synchrotron emission of medium energy electrons and were the high frequency counterparts of the type IV phenomenon (see for a review Kundu 1965, Chap. 11).

During this period, the most detailed spectral analysis, of microwave bursts was made by Hachenberg and Volland (1961). The spectra were measured for 10 events at 6 frequencies in the range 500–25,000 MHz. The burst intensity first increases with frequency up to a few GHz (usually with $f^2$). Above a few GHz, the intensity remains in some cases independent of frequency. The transition between the rising part and the flat part of the spectrum occurs sometimes through a broad maximum. An additional component is sometimes observed in the region of constant flux (see left panel in Fig. 11). The spectrum resembles the spectrum produced by thermal free–free radiation with an optically thick part at low frequencies and an optically thin one at high frequencies. Hachenberg and Wallis (1961b) also proposed that the additional component sometimes observed is produced by synchrotron radiation of electrons in magnetic fields between 100 and 1,000 G.

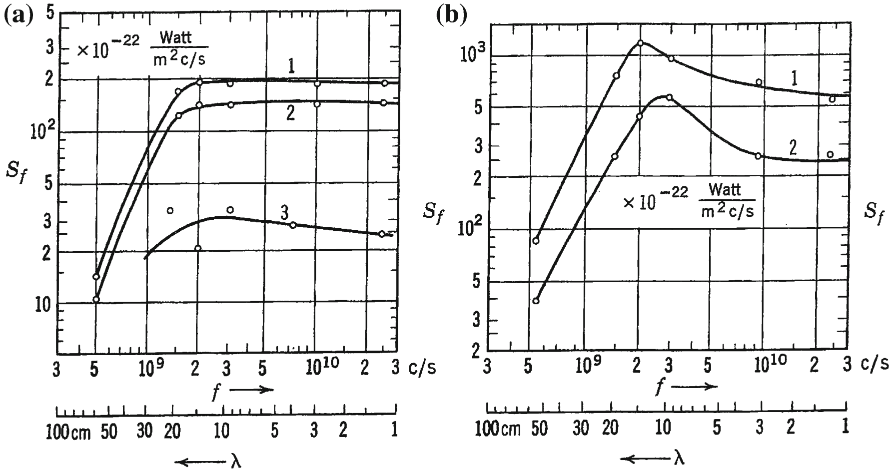


**Fig. 11** Spectra of microwave bursts (adapted from Hachenberg and Volland 1961)

After 20 years of exploration of the processes, the different radio emissions produced by electrons at widely different energies can be summarized as follows:

- The thermal emission is produced by thermal bremsstrahlung and by gyroresonance emission of thermal electrons in the presence of a magnetic field above active regions.
- The supra thermal electrons in the energy range 10–100 keV (electron beams or shock accelerated electrons) generate plasma oscillations which produce electromagnetic emissions at the plasma frequency, *fp* and at its second harmonic *2fp* (primarily type III and type II bursts).
- The relativistic electrons in the MeV energy range produce gyro-synchrotron emission (type IV burst and microwave outbursts). The discovery of the moving type IV bursts stimulated, later, many theoretical studies of the synchrotron radiation from electrons embedded in a plasma (e.g. Lacombe and Mangeney 1969; Ramaty 1969).

### *2.1.3 Association between radio emissions and energetic particles detected at the Sun or at the vicinity of Earth*

The fact that type IV emissions reveal the presence in the corona of MeV electrons stimulated many investigations on the association of these solar outstanding events with energetic particles detected in the Earth environment (e.g. Avignon and Pick 1959; Hakura and Goh 1959; Thompson and Maxwell 1960; Denisse et al. 1960; Sakurai and Maeda 1961). The relativistic protons associated with solar flares produced large increases in the counting rates of several ground level cosmic ray monitors (see for example Meyer et al. 1956). Proton events of lower maximum energy were detected later during the International Geophysical Year (IGY) (1957–1959) by direct measurements using balloons and rockets and by indirect measurements using their ionospheric effects (polar cap absorptions due to 10–100 MeV protons).

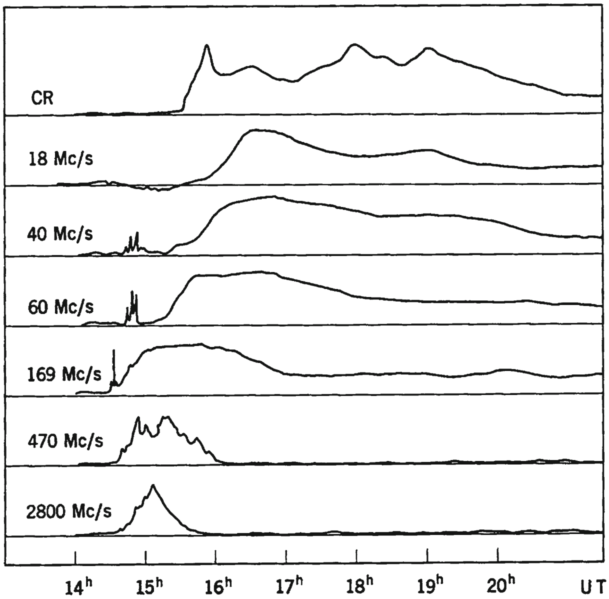


**Fig. 12** August 22, 1958: Flux of cosmic rays and of radio emission measured at various frequencies. The intensity scales are different and arbitrary from graph to graph (from Boischot and Warwick 1959)

Boischot and Warwick (1959) discovered, for the August 22, 1958 event, a striking relationship between the variations of the cosmic rays intensity and the continuum-storm intensity at decametric wavelength as illustrated in Fig. 12. The cosmic rays which are, in the present case, protons of about 170 MeV, were measured in a balloon flight (Anderson 1958). Numerous studies investigated the association between 10 and 100 MeV protons detected by their PCA effects and type IV bursts. A quasi systematic association was found for type IV bursts radiating in the microwave domain with a flux density greater than $10^{-17}$ J/m$^2$/Hz and with a second long duration phase at metric wavelengths. The radio importance of a flare was defined as the energy radiated at 10 cm ($\approx$ the flux density measured at the maximum multiplied by the duration). These proton events are associated with a flare located in the western solar hemisphere (Pick-Gutmann 1961). This association also led to the idea that cosmic ray particles are accelerated by the same process as the fast electrons responsible for the type IV radiation.

The organization of the International Geophysical Year stimulated many national and international cooperations and projects, in particular in the radio exploration of the Sun and its comparison with emissions at other wavelengths. Frequent flights of X-ray, gamma ray and particle detecting instruments were achieved on balloon, rocket and satellite platforms. The first observations of energetic photons from a solar flare were made by Peterson and Winckler (1958, 1959) (see Fig. 13). They detected a burst which coincided exactly with a microwave burst. The time profiles were similar (see also Kundu 1961 for other events). Terrestrial effects, including SID (Solar Ionospheric Disturbances) and Earth-current disturbances were associated with this event. The

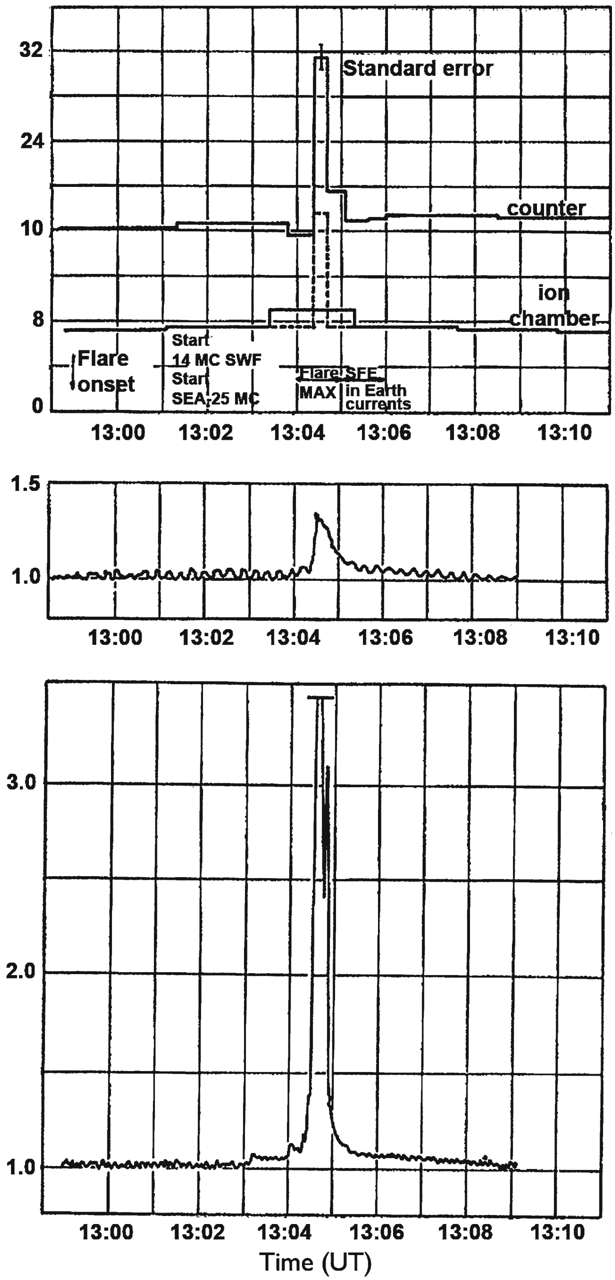


**Fig. 13** March 20, 1958: *Top panel* response of ionization chamber and counter during flare. *Centre and lower panel* solar radio emission recorded (courtesy of J.F. Denisse) at 21 cm (*middle*) and at 3 cm with the Nançay interferometer (from Peterson and Winckler 1958)

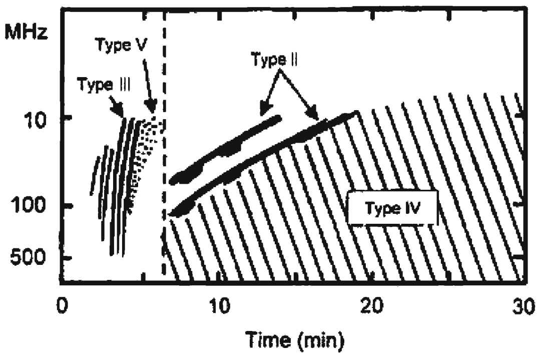


**Fig. 14** Idealized sketch of a complete radio event (from Wild et al. 1963)

burst emission was attributed to electrons in the ~0.5 to 1 MeV energy range producing X-ray bremsstrahlung emission and betatron radiation in the radio domain. As the same population of energetic electrons could be responsible for the Hard X-Ray (HXR) and microwave emissions, it opened a new field of investigation on the origin of particle acceleration and emitting mechanisms based on joint HXR and radio observations in a broad frequency range (see Sect. 4).

The classification of radio bursts introduced in 1963 by P. Wild et al. linked the development of the radio flare emissions to the observations of protons and geomagnetic effects in the interplanetary medium. The association between radio bursts, solar flares observed at different wavelengths and observations of protons led to the long-lasting belief that well developed flares present two successive phases: one *impulsive* phase with typical duration of a few minutes, characterized by impulsive HXR and microwave bursts and by dm-m activity including type III bursts; a subsequent *gradual* phase, occurring only in large flares and initiated directly by the first phase, with typical duration of tens of minutes. This second phase is characterized by intense radio continua (type IV). In this model, schematized in Fig. 14, the shock wave revealed by the type II burst initiated during the impulsive phase, creates conditions suitable for the acceleration of particles to very high energies; they will be either partly trapped in coronal loops or will escape in the interplanetary medium. A few years later, when HXR data became available thanks to the instrumentation on OSO5, a long duration HXR burst evolving in time through two non thermal phases was observed. This burst was considered to be due to bremsstrahlung of electrons accelerated in two stages in the solar atmosphere (see Fig. 1 in Frost and Dennis 1971). The authors concluded that the X-ray observations support particle acceleration in two stages or phases, as described by Wild et al. (1963) and proposed the second phase to be due to shock acceleration. This picture today has been greatly modified as it will be discussed in Sect. 8.

## 2.2 The 1965–1980 period

This period was marked by two major instrumental radio developments which opened possibilities for more sophisticated data analysis and transformed our knowledge of the physics of the corona and of the interplanetary medium. One was the access to spatially resolved observations of the corona with radio imaging instruments (in particular the

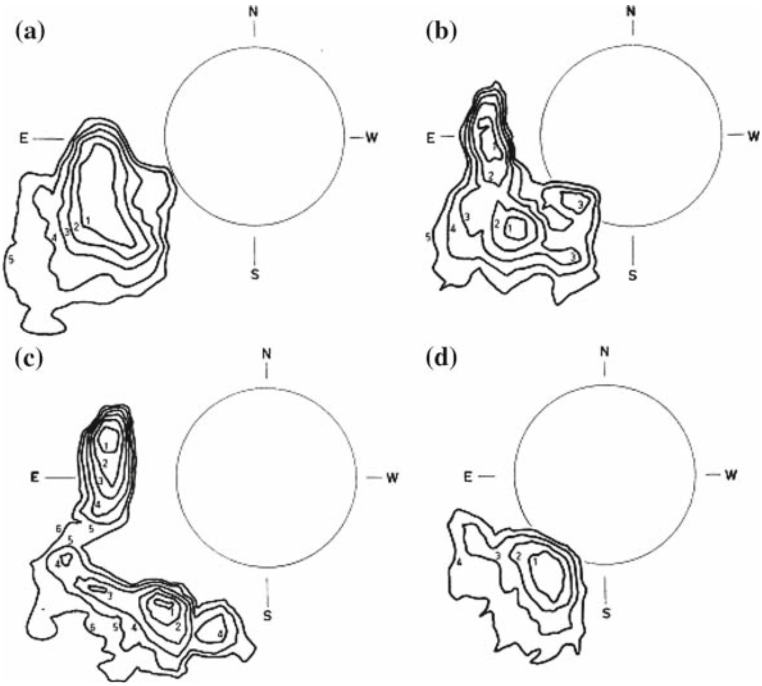


**Fig. 15** Contour plots of the brightness distribution, at four successive times, recorded by the Culgoora radioheliograph at 80 MHz during the expansion of an arch. The contours $n = 1, 2, 3 \ldots$ represent $2^{-n/2}$ power levels of the maximum brightness (adapted from Kai 1970)

two first important ones: the Culgoora radioheliograph, Wild 1967; the Teepee Tee Array of the Clark Lake Radio Observatory, Erickson and Fisher 1974). The second was the possibility of measuring radio emission in the interplanetary medium with space experiments: observations below 10 MHz became available, while they are not with ground-based instruments because of the ionospheric cut-off (except today the BIRS radiospectrograph, see Sect. 7). Significant progress on our knowledge of solar activity was achieved from joint observations covering a large frequency range.

### *2.2.1 Radio imaging observations*

Imaging observations gave access to a visualization of the coronal structures illuminated by accelerated electrons either trapped in coronal arches (Kai 1970; Daigne 1971) as illustrated in Fig. 15, or escaping along open field lines. These observations also revealed the complexity and the variety of spatial scales of the magnetic structures in which eruptive phenomena and electron acceleration took place. They showed that these complex magnetic structures are not restricted to the flaring active region but also involve magnetic structures at larger scales. The three following examples illustrate this statement, which is of fundamental importance for our present knowledge of the link between flaring activity and CMEs:

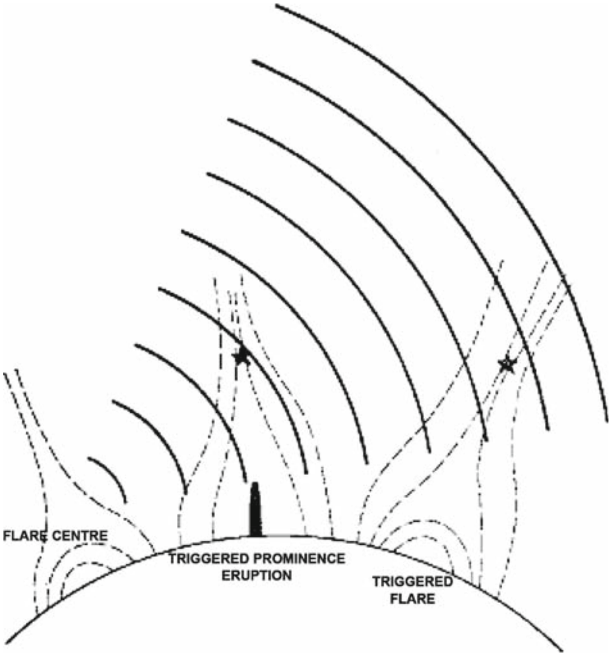


**Fig. 16** Diagram showing the possible way in which the shock wave from a flare may trigger prominence eruptions and other flares by causing instabilities at neutral sheets high above them in the corona at regions indicated by the *asterisk* (adapted from Wild 1969)

Wild (1969) reported radio evidence of interactions of shock waves with preexisting coronal structures; he showed the possible way in which a shock wave from a flare can trigger prominence eruptions and other flares, at far distances from the flaring region, by causing instabilities in coronal neutral sheets (see Fig. 16).

Correlated bursts from two distant emitting sources appearing with short time delays (sometimes less than 1 s) were observed. These observations dismissed the hypothesis of causal disturbance travelling from one source to the other, since the speed would have to exceed the velocity of light. This led to suggest that the initiating instability occurred high in the corona (see schema in Fig. 17) and was caused by rearrangement of magnetic field lines linked to the different sources (Wild 1968).

The sources of moving type IV bursts showed a large variety of complex configurations (e.g. Wild and Smerd 1972). One variety has the shape of a wide irregular arc, *the advancing shock front*, which appears a few minutes after a type II source has occurred. It was suggested that these moving type IV bursts were caused by shock waves. A second variety was attributed to radiation from electrons trapped in a magnetic arch structure that expands with time, *the expanding magnetic arch*. Sheridan (1970) and Riddle (1970) reported for the first time observations at 80 MHz of a *plasmoid* ejected in association with an eruptive solar prominence. In both cases, the moving radio source created by energetic electrons, appeared soon after the prominence eruption and travelled in the same direction with a constant speed of the order of 300 km s$^{-1}$ (see Fig. 18). Moreover, in the case studied by Sheridan (1970), an underlying sta-

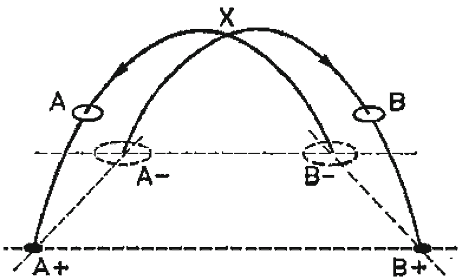


**Fig. 17** Interpretation of correlated and strongly polarized bursts of the same sense in which time delays of $\leq 1$s: occur between distant sources A and B. The energy is supposed to be conveyed by electrons guided by magnetic field configurations (indicated by *full lines*) and the point X marks the region of instability near which the electrons are accelerated (adapted from Wild 1968)

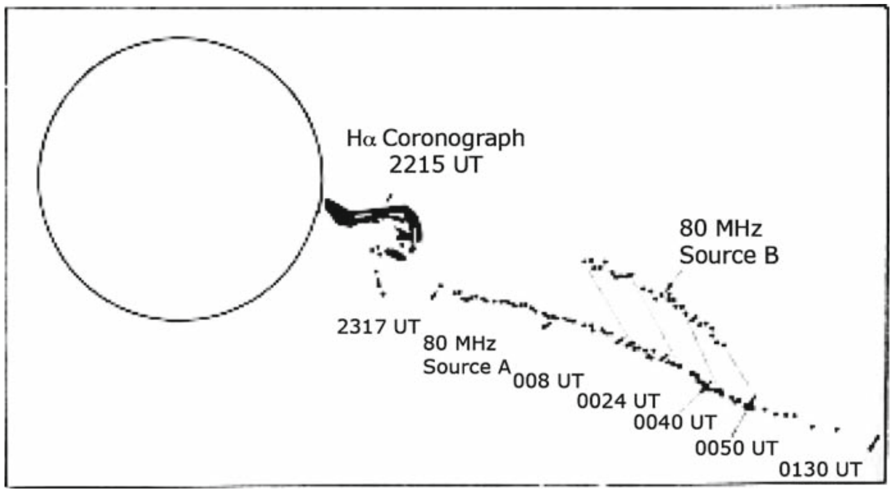


**Fig. 18** Temporal and spatial relationship between a rising H$\alpha$ prominence and a moving type IV burst at 80 MHz observed by the Culgoora heliograph (adapted from Riddle 1970)

tionary source (that could be plausibly interpreted today as radio emission from flare loops) developed later on. These observations could be interpreted today as signatures of coronal magnetic field interactions resulting in ejecta and in the build-up of post-erupting loops.

As already briefly mentioned in Sect. 2.1.2, imaging observations of type IV bursts led to a much better understanding on the development and emission processes involved in these emissions. These observations revealed for some continua brightness temperatures too high to be explained by incoherent gyro-synchrotron emissions (Stewart et al. 1978; Duncan 1981). It was proposed that a plasma emission from trapped electrons at either the fundamental plasma frequency or its second harmonic is the most likely process. A similar conclusion was drawn by Trottet and Kerdraon (1980) to explain the short-term modulations during a moving type IV burst.

Generally speaking, the relative contribution between incoherent gyro-synchrotron and coherent plasma emissions depends upon the observing frequency. Gyrosynchrotron emission, which is in the optically thin regime proportional to the number of radiating electrons, usually dominates at frequencies above about 3 GHz (see Sect. 4.3). These emissions provide diagnostics on the ambient plasma, on the energetic radiating electrons and on their evolution with time. Coherent plasma emission (electrons radiating in phase) most often dominates at frequencies below 3 GHz and is caused by plasma instabilities that ultimately produce observable electromagnetic radiations.

### *2.2.2 Radio astronomy at low frequencies*

Radio bursts in the Interplanetary Medium (IP) were first detected by experiments on Alouette in the frequency range 1.5–10 MHz (Hartz 1964). The results of detailed studies of the early satellite observations at low frequencies have been reported by Hartz (1969); Alexander et al. (1969); Haddock and Graedel (1970). These observations provided estimates of the velocity of the type III burst sources in the 0.1–0.15 c velocity range, c being the speed of light. As the source locations of the radio emission were not known, the results were very strongly model dependant. The observations made in the frequency range 0.2–5.4 MHz with the radio astronomy explorer (RAE-1), launched in July 1968, yielded an emission level that scales with a power-law dependence on the distance R to the Sun of the observing frequency $f_{\rm obs} = 66.8\ \mathrm{R}^{-1.315}$, where R is in solar radii and $f_{\rm obs}$ is the type III burst frequency in MHz, valid for $\mathrm{R} > 10\ R_\odot$ (e.g. Fainberg and Stone 1974). This power law dependence holds over many decades (Alvarez and Haddock 1973). In order to derive the electron density versus distance from the Sun, it is necessary to know if the burst radiation is at the first or second harmonic of the plasma frequency. The density scale in Fig. 19 is based on the assumption that the type III radiation was observed at the fundamental of the local plasma frequency. The derived densities are an order of magnitude higher than estimates for the corona at the solar minimum. If, however, the radiation occurs at twice the plasma frequency, the derived densities are a factor of 4 lower. The IMP-6 satellite, launched in 1971 utilized spin modulation to obtain direction finding measurements of type III radio sources in a frequency range going from 10 MHz to below 10 kHz; the trajectories of the energetic electron streams which generate the radio emission were obtained (Fainberg et al. 1972). Observation of a burst is illustrated in Fig. 20 which shows the envelopes of the burst and an example of the spin modulated data recorded at 250 kHz (see inset figure). In order to determine the trajectory of the electrons, one needs a relationship between electron density and distance from the Sun. Two models were used for locating the emission region. In the first one, the density-distance scale was obtained from radio observations of RAE-1 satellite in the 10–40 solar radii range and was extrapolated to 1 AU. In the second one, the emission region was placed, for each frequency, at the minimal coronal distance from the Sun compatible with the measured directions of arrival. The two sets of point obtained are reported in Fig. 21 (black dots and open circles); they represent bounds on the particle trajectories and determine a spiral magnetic field configuration as expected under average conditions.

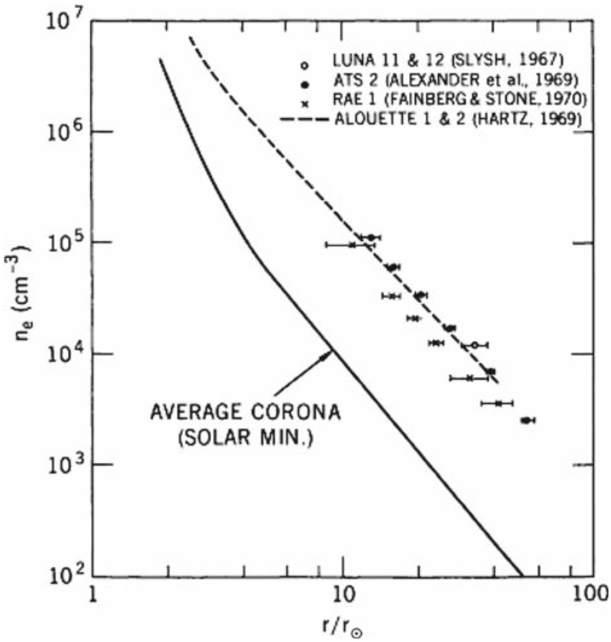


**Fig. 19** Electron density versus distance from the Sun in the outer corona. The *solid curve* represents the values given by Newkirk (1967) as best estimates during solar minimum. The values given by the radio measurements are from single bursts and are placed assuming the type III radiation was observed at the fundamental of the local plasma frequency. They should be displaced downward a factor of 4 if the radiation was observed at twice the plasma frequency (from Fainberg and Stone 1974)

Later on, solar bursts were tracked simultaneously with two satellites spinning in the ecliptic plane and in a plane perpendicular to it (Baumback et al. 1975). Fitzenreiter et al. (1977) reported electron trajectories travelling along magnetic field lines originating from the active region and, later on, crossing the ecliptic plane. This allowed to detect a strong, large scale, north–south component of the interplanetary magnetic field.

The combination of radio observations at the lower frequencies with in-situ measurements of non-relativistic electrons at 1 AU provided strong evidence that these electrons are responsible, through wave-particle interactions, for the radio type III emission (Frank and Gurnett 1972; Lin and Anderson 1973).

Type II bursts in the interplanetary medium were first detected by Malitson et al. (1973) using IMP6 data.

### *2.2.3 First inputs of radio observations to solar–terrestrial physics: energetic particles and escape in the interplanetary medium*

Very early, it was recognized that the flare-initiated radio bursts originate from the sources of the SVC and that the microwave flux of an active region was probably a more determining parameter than its optical importance for predicting the radio burst

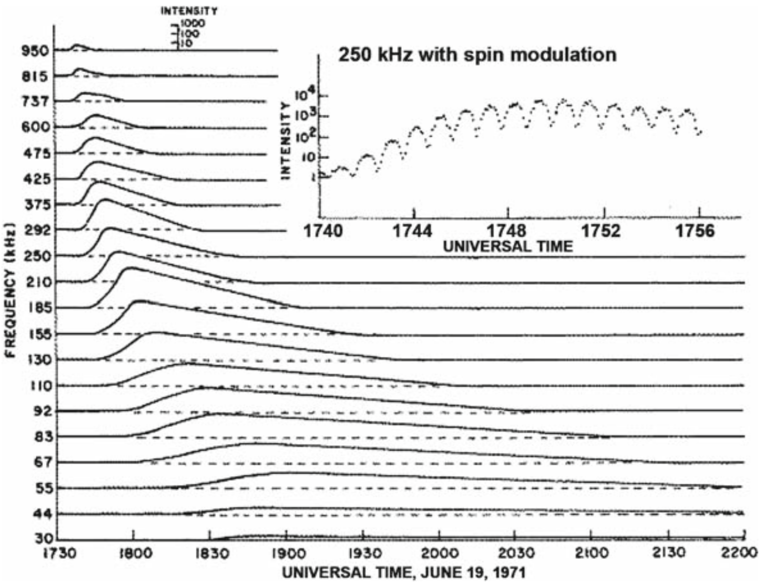


**Fig. 20** A type III burst observed between 1 MHz and 30 kHz by the IMP-6 radio experiment. The inset figure illustrates the observed spin modulation at a frequency of 250 kHz, while for the main figure, only the burst envelopes are shown for clarity (from Fainberg et al. 1972)

**Fig. 21** Direction of arrival (in the ecliptic plane) determined from the spin modulation; the trajectory shown by the *black dots* is fixed by using the RAE-1 emission level scale (see text); the trajectory shown by the *open circles* is determined by the distance of closest approach permitted by the arrival direction (from Fainberg et al. 1972)

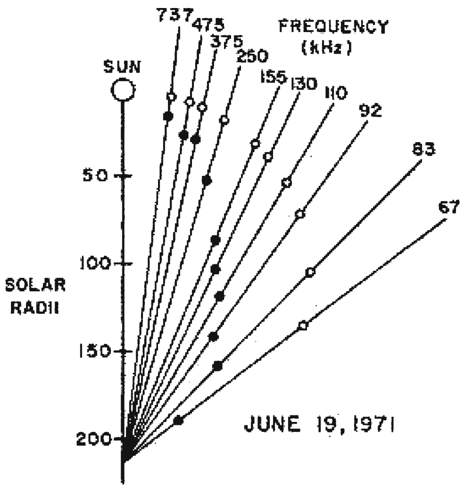


occurrences (Kundu 1959b). Pick-Gutmann (1961) showed that the probability of occurrence of centimetre-wavelength type IV bursts is about 80 times larger for active region sources with a flux density greater than $60 \times 10^{-22}\,\mathrm{Wm^{-2}\,Hz^{-1}}$ measured at 3.2 cm than for those with a flux density less than $30 \times 10^{-22}\,\mathrm{Wm^{-2}\,Hz^{-1}}$. This clearly established a relationship between the frequency of occurrence of centimetre wavelength type IV bursts and the intensity of pre-existing sources at 3.2 cm. The brightest compact sources measured at 3 cm were found to be located over regions with strong magnetic field gradients (two very close regions with opposite polarities) (Avignon et al. 1966; Felli et al. 1974). Moreover, the presence of opposite polarities was recognized as a favourable situation for the creation of current sheets so that particle acceleration originating in these regions could be expected (see for a review Pick 1977).

These early results pointed out that, besides the strength of the magnetic field, an even more important parameter for the flare prediction is the magnetic topology. In this early period, radio observations played a major role in initiating various studies concerning the evolution of the magnetic structure of active regions. These observations showed in particular how the appearance of a parasitic polarity (satellite polarity) in a sunspot group can lead to major radio bursts implying efficient particle acceleration.

*Characteristics of flares at optical wavelengths associated with solar cosmic rays and strong radio emissions*

In a study of flares connected with ground level cosmic ray increases (protons with energies above $10^3$ MeV) and PCA events (linked to protons in the 10–100 MeV energy range), Ellison et al. (1961, 1962) discovered that these flares were systematically associated with peculiar magnetic features: two sunspot rows of very close opposite magnetic polarities in the active region with the H$\alpha$ flare lying between these rows and evolving towards two chains of bright points overlapping the spots (this kind of flares is known today as two ribbon flares). A relationship was established between PCA events and type IV bursts (e.g. Hakura and Goh 1959; Thompson and Maxwell 1960), in particular for the broadband centimetre-wave outbursts typical of the first phase of type IV radiation (Kundu and Haddock 1960). These results led Martres and Pick (1962) and Avignon et al. (1964) to propose a new classification of the *importance of a flare* linked to its capacity of producing energetic particles. They first found that the radio events associated with PCA were systematically associated with flares with a configuration similar to the two ribbon flares (Ellison et al. 1961). They also considered the general case of H$\alpha$ flares associated with long duration radio events (type IV burst or noise storm emission) at metric wavelengths; for the events not associated with a PCA, the existence of a plage filament, most often disappearing during the flare, seemed to determine the location of the H$\alpha$ flare and the occurrence of the metric event. As for the largest scale filaments, the plage filament occurs at boundaries between opposite polarity magnetic fields. The main conclusions of these studies were the following: (a) the magnetic structures involved in the flare development leading to strong radio emissions include not only the sunspot but also plage filaments; (b) the occurrence of strong radio emissions is enhanced by the presence of a strong magnetic field gradient due to the proximity of spots of opposite polarities and to the presence of a relatively strong or twisted horizontal field revealed by the filament. These results are illustrated in Fig. 22. The complex magnetic structure and the presence of a filament appeared to be a key point to explain how the effects of the flaring activity are not restricted to the low layers of the solar atmosphere and how the accelerated particles can escape in the high corona and the interplanetary medium. Later on, Sheeley et al. (1975) identified events, characterized by the disappearance of a filament and accompanied by long duration soft X-rays and microwave emissions.


**Fig. 22** Flare (*grey hashed line surfaces*) and sunspot (*black*) configurations associated with radio and corpuscular emissions. **Configuration A**: Type IV bursts and ground level cosmic ray increases or polar cap absorptions (PCA); two ribbon flare overlapping two rows of sunspots of opposite magnetic polarities. **Configurations A′ and B**: Type IV bursts of less importance or noise storm enhancements; two ribbon flare overlapping partly sunspots of opposite polarities; the flare extends along a filament either pointing toward these two sunspots or surrounding a sunspot (from Avignon et al. 1965)

*Magnetic configuration of flares associated with electron acceleration and coronal injection into the interplanetary medium*

Several authors had already pointed out the high variability of the type III burst production by flares from one active region to the other (Loughead et al. 1957; Simon 1962). Axisa (1974) investigated the role of the magnetic configuration of the optical flare for the production of type III solar radio bursts and of centimetre and HXR events. He found that, when the optical flare occurs outside the general bipolar pattern of the active region, there is a higher rate of association with type III bursts (>50%) than for those taking place inside the bipolar pattern (<20%). On the other hand, centimetric and HXR events are more likely to be produced in connection with optical flares located inside strong magnetic fields arising from well developed sunspots. Such results point out the concept of "*Flare Production Sites*", FPS. The location of the type III related flares indicates that FPS connected to open field lines are encountered at the border of active regions in well localized photospheric sites. FPS which are located inside strong magnetic fields are more efficient than the others in producing energetic electrons. When the magnetic configuration is entirely closed, only microwave and HXR events will be expected. Though these earlier results were rather crude, they may, however, be considered today as precursors in solar–terrestrial research on the origin and propagation of solar particles.

### *2.2.4 First inputs of radio observations to solar–terrestrial physics: solar radio bursts and geomagnetic storms*

In the forties, geomagnetic storms were already known to be closely related to particularly intense flares (e.g. Newton 1943; Allen 1944). Sinno (1959) showed that major outbursts which have at 200 MHz a strong, long duration emission after the flare maximum cause geomagnetic storms. Kundu (1962) showed that only if a type II burst is associated with a type IV burst, it can produce a geomagnetic storm. Hakura (1958) and Simon (1960) showed that only flares associated with intense microwave outbursts are significantly correlated with geomagnetic activity. In addition, Hakura found that the power spectrum of bursts associated with geomagnetic storms either increases with decreasing frequencies or is rather flat (see Fig. 23). These two outburst properties,

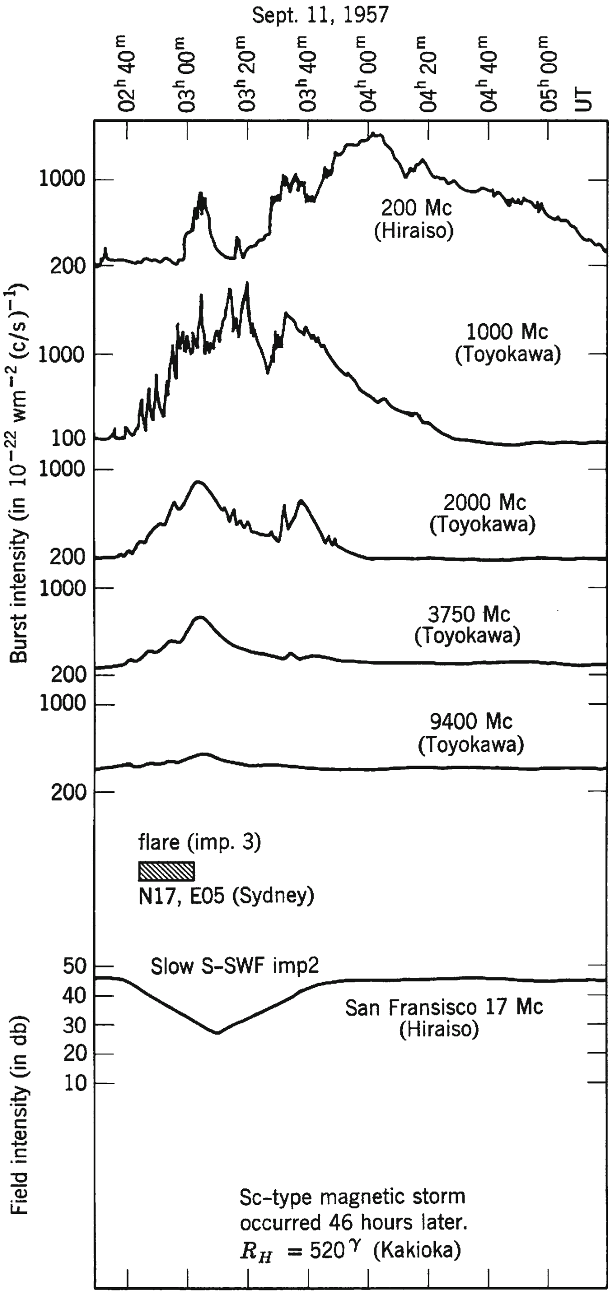


**Fig. 23** Illustrating the power spectra of outbursts associated with geomagnetic activity (adapted from Hakura 1958)

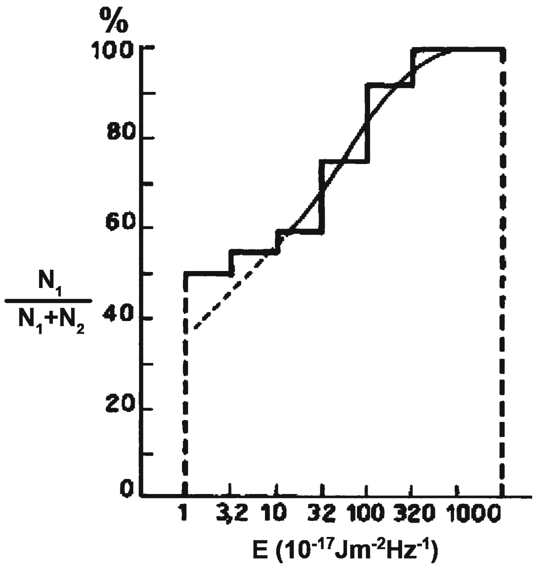


**Fig. 24** Probability of a flare to be associated with a SSC versus its radio importance, i.e. the energy radiated at 2.8 GHz (adapted from Caroubalos 1964)

strong microwave emission and spectral shape, are characteristic of type IV bursts. In 1964, Caroubalos investigated in detail the association between type IV bursts and sudden storm commencements (SSCs). Each type IV burst was characterized by two parameters: its radio importance (the energy radiated at 10 cm, see Sect. 2.1.3) and its spectral character defined as the ratio p of the duration of the metric emission measured at 169 MHz to the duration of the microwave emission measured at 10 cm; the value of this parameter provides an information on the existence of a second phase. The main results of this study are summarized as follows:

– The probability of type IV bursts to be followed by a SSC is a function of their radio importance. Figure 24 shows that this probability increases rapidly for events with energies roughly greater than $30 \times 10^{-17}$ Jm$^{-2}$ Hz$^{-1}$.
– There is a statistical relationship between the Sun–Earth transit time of the disturbances responsible for SSCs and the radio energy emitted by the associated type IV bursts (see Fig. 25, left panel).
– Two important effects, related to the influence of the interplanetary medium on the transit time, were brought to light: A disturbance which follows, within a few days a first disturbance propagates faster than the initial disturbance; also, the conditions encountered by the second disturbance (labelled second SSC in Fig. 25, see right panel) in the interplanetary medium are much more regular than those encountered by the first one.
– The existence of a second phase, of relatively long duration, appears as an essential condition for a type IV burst to be followed by a SSC; 76% of cases with $p \neq 0$ are followed by a SSC, whereas the percentage is only 37% for cases with $p = 0$. These percentages become 84 and 12%, respectively, when only the central solar zone only is considered (±45°). Thus, it must be underlined that the cases for

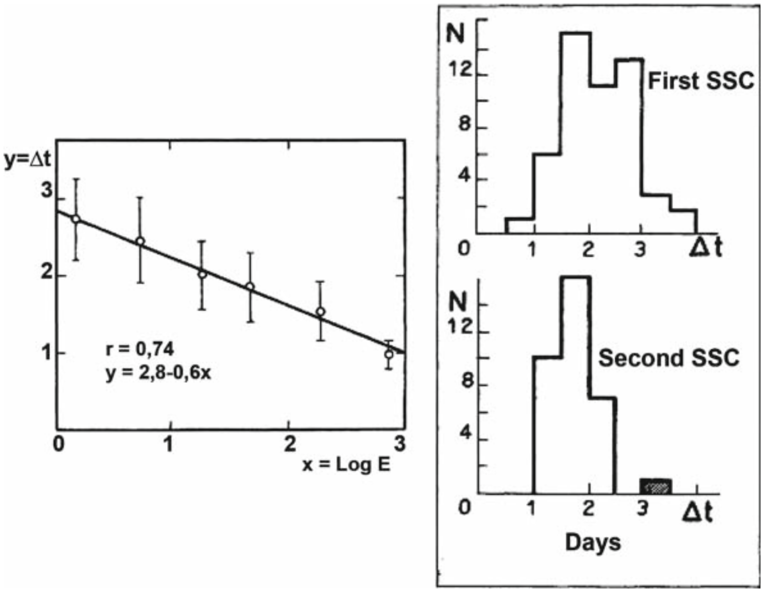


**Fig. 25** *Left panel* Transit time of disturbances followed by a SSC versus the radio importance of the associated flare. *Right panel* Histogram of the transit times of disturbances after reduction to a reference energy by using the relationship Δt, LogE displayed in the *left panel*; *top Histograms* for the first SSCs; *bottom* for the second SSCs (see text) (adapted from Caroubalos 1964)

which no second phase was detected are probably due to a directivity effect of this emission (see Pick-Gutmann 1961).

Interpretation of these results were not easy at that time, as the CMEs and, a fortiori their relationship with radio emission were not yet discovered. We shall come back in Sect. 10, on the meaning of these early results.

## 2.3 Concluding remarks

The above sections demonstrate that, very early in the history of solar radio astronomy, many important results, related for example to electron acceleration and radiation processes, and to eruptive phenomena were already known, even if researchers at that time did not have the instruments which allowed to put together the different pieces of the puzzle. It was for example, firmly established that:

– Non-thermal radio emissions exhibit significant evolution over 1 s time scales
– The magnetic energy release that leads to an eruptive event results from the coupling of different magnetic scales from the very small ones, not directly observable, to very large ones. This energy release is not necessarily limited to the active regions in which the H$\alpha$ flares are produced.
– Different layers of the solar atmosphere, from the photosphere to the high corona, are involved in the triggering and subsequent development of eruptive phenomena, as well as in the particle acceleration processes.

The first Coronal Mass Ejection (CME), was discovered on December 14, 1971 by Tousey (1973). This event was detected in white light by the OSO-7 orbiting coronagraph which measured the Thomson scattering of the photospheric light by the coronal electrons in the ejected mass. CMEs are large scale magnetically structured plasmas which are expelled from the Sun and propagate to large distances in the heliosphere, often beyond 1 AU. This important discovery represented a turning point in the history of solar activity. If it was recognized that flares and CMEs are the dominant sources of energy release in the solar corona, their association and link were not understood and gave rise during three decades to a hot and controversial debate. Only in recent years, it was accepted that, even if flares and CMEs can be produced in a same event, there is, however, no causal relationship between these two phenomena; they are two different aspects of a common magnetic instability and energy release.

## 3 Radio diagnostics of coronal magnetic fields

One of the key measurements to analyse and understand solar activity (flares, CMEs, energetic particles...) is the one of the magnetic field, in particular the coronal magnetic field. The radio domain is one of the few wavelength domains which can contribute to these difficult measurements. This is not the scope of this review to describe in details the different radio techniques which allow to measure magnetic fields since a good and detailed overview of all the radio measurements can be found in the Chaps. 4–7 of the book "Solar and Space Weather Radiophysics" (Gary and Keller 2004). However, given that magnetic fields are of fundamental importance for all the topics discussed in the next sections, we shall briefly review here the existing input of radio observations to coronal magnetic field measurements.

Since the pioneer studies in the early 1960s (see Sect. 2) which predicted that the strong microwave emissions above active regions are associated with gyroresonance opacity, several observations have confirmed the early findings that the gyroresonance emission is usually the dominant mechanism above the sunspots. Observations were made with, e.g. the Westerbork Synthesis Radio Telescope at 6 cm (Alissandrakis and Kundu 1984), with the Ratan600 instrument at 2–4 cm (Akhmedov et al. 1982) and with the VLA at several wavelengths (see, e.g. Fig. 26). A detailed discussion can be found in Chap. 5 of Gary and Keller (2004).

Owens Valley Solar Array observations at 1.2–7 GHz further demonstrated the interest of combining spatial and high spectral resolution (Gary and Hurford 1994). Solar maps were obtained at 22 frequencies covering both the domain of thermal free–free and gyroresonance emissions and allowing to determine the main emission mechanism at each frequency. This allows to map not only the magnetic fields in the active region but also the temperature and electron emission measure (see Fig. 27).

Another method to derive magnetic field maps from radio observations consists in combining the radio imaging observations at a few discrete frequencies with X-EUV images and spectra. Both radiations depend on temperature and density but only the radio emission depends on the magnetic field. EUV and X-ray images at different wavelengths provide information on the temperature and emission measure maps in the active region which allows to compute the free–free brightness temperature as a function of frequency and to compare maps of free–free radiations to the observed radio images. The comparison of the radio maps computed with the extrapolated photospheric fields shows a good consistency with the observed brightness temperatures above the sunspots if gyroresonance emission is assumed (e.g. Alissandrakis et al. 1996). The combination of radio and X-ray or EUV observations also allows to derive the three dimensional coronal magnetic field above the sunspot and in its close surroundings (Brosius et al. 2002) (see for more details Brosius, Chap. 13, in Gary and Keller 2004).

Radio observations also provide ways to measure the longitudinal component of weak magnetic fields in both active and quiet regions of the Sun. The method consists in the measurement of the level of circular polarization of the free–free component which will depend on the magnitude of the longitudinal magnetic field component. Further details are given by Glefreikh, Chap. 6 in Gary and Keller (2004).

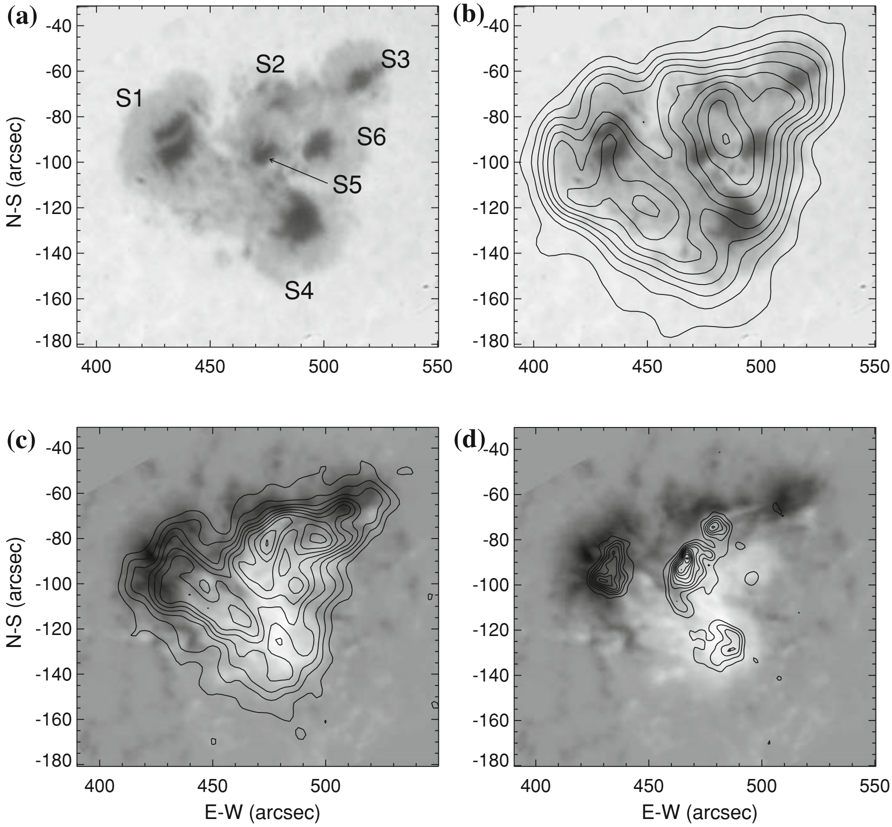


**Fig. 26** **a** A white-light picture of AR 6615 obtained by Big Bear Solar Observatory. **b** Total intensity contours at 4.9 GHz overlaid on the while light picture. Total intensity contours at **c** 8.4 GHz and **d** 15 GHz overlaid on the longitudinal magnetogram. The maximum intensities are $4.4 \times 10^6$ K at 4.9 GHz, $4.6 \times 10^6$ K at 8.4 GHz and $1.8 \times 10^6$ K at 15 GHz. Contours begin at 10% of the maximum intensity and then are 10% apart (Lee et al. 1997).

The last technique to measure magnetic fields is the observation of an inversion of the circular polarization of the radio emission due to the propagation of the extraordinary and ordinary modes in the corona. In the case of weak coupling between the two electromagnetic wave modes, this inversion occurs when the wave crosses a transverse field region (QT). Observations of polarization inversion provide a unique diagnostic on the magnetic field in coronal layers at 0.05–0.4 Rs, well above the height of formation of the microwave emission. However, the determination of the value of this magnetic field depends on the electron density at the QT level (e.g. Alissandrakis et al. 1996; Ryabov et al. 1999). This method is independent of the emission mechanism. Further details are given by Ryabov, Chap. 7 in Gary and Keller (2004).

In the following sections, it will be shown on several examples how extrapolations of magnetic field measurements from the lower atmosphere into the corona provide important diagnostic tools to understand flare/CME models. Radio observations also

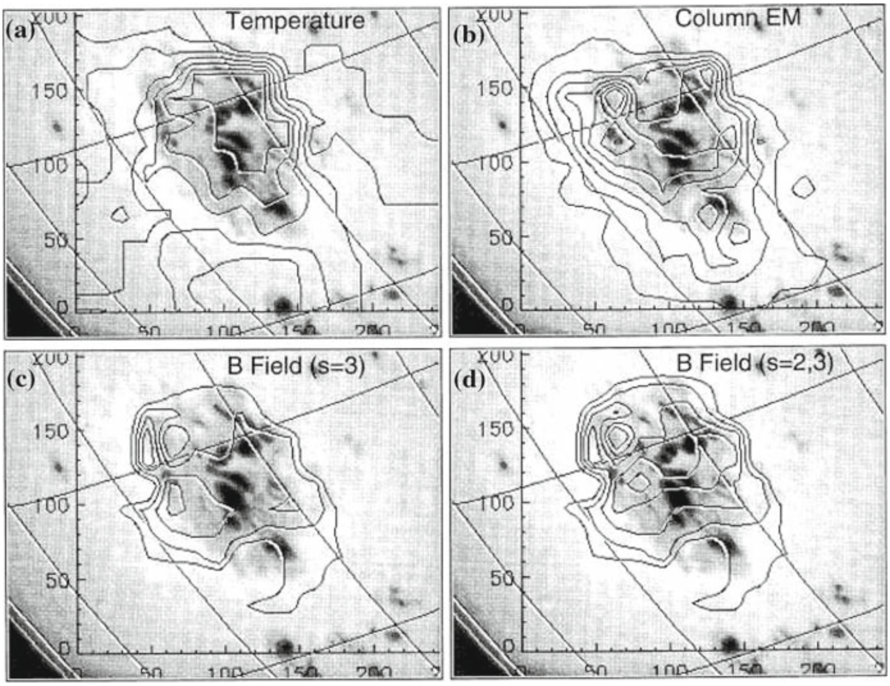


**Fig. 27** Physical maps obtained by interpretation of brightness temperature spectra. **a** Electron temperature with contour levels 0.9, 1.15, 1.4, 1.9, and $2.09 \times 10^6$ K. **b** Electron column emission measured from free-free spectra or an upper limit deduced from gyroresonance spectra. The contour levels are 20, 30, 40, 50, 60, 70 and $90 \times 10^{27}\,\mathrm{cm}^{-3}$. **c** Total magnetic strength at the base of the corona assuming harmonic $s = 3$ everywhere. The values are as measured from gyroresonance spectra. The contour levels are 200, 400, 600, 800 and $10^3$ G. **d** The same as in c except $s = 2$ has been assumed in upper right part of the active region. The highest contour is in this case $1.2 \times 10^3$ G (Gary and Hurford 1994)

provide the possibility to check the validity of a given extrapolation. The measured coronal magnetic fields sometimes exceed the fields extrapolated with a simple potential model (current free models) suggesting the presence of coronal electric currents. A reversal of the field direction is expected to be observed across the current layer (see, e.g. Alissandrakis and Chiuderi Drago 1995). Other tests of the topology of magnetic field lines derived from extrapolations can be in principle provided by observations made at different frequencies: indeed, each radio frequency corresponds to a different value of the magnetic field strength (e.g. Lee et al. 1999).

In this domain, major spectacular advances are expected in the future from broadband imaging spectroscopy such as provided by the solar dedicated FASR project (Gary and Keller 2004).

## 4 Input of combined radio and X-ray observations to the understanding of solar flares

As recalled in Sect. 2, it has been known for more than 20 years that coherent plasma radiations in the metric (and also decimetric) domains provide sensitive diagnostics of supra-thermal electrons (around a few tens of keV) accelerated in the low and middle corona in connection with solar flares and that gyrosynchrotron emissions of flare accelerated electrons provide quantitative constraints on the energetic electrons. Ground-based spectral observations are nowadays obtained in a wide frequency domain (from a few GHz to 10–15 MHz depending on the ionospheric cut-off) with many spectrographs (see, e.g. ARTEMIS IV Multichannel solar radiospectrograph of the University of Athens, Bruny Island Radio Spectrometer, Culgoora Solar Radio spectrograph, ETH Zurich Radio Astronomy Group, Green Bank Solar Radio Burst Spectrometer, Hiraiso Solar Radio Observations, IZMIRAN Solar Radio Observatory, Nançay Decametre Array, Ondrejov Observatory, Tremsdorf Solar Radio Observatory). A few solar-dedicated imaging instruments are now available: the Gauribidanour Radioheliograph (Ramesh et al. 1998, 40–150 MHz), the Owens Valley Radio Observatory (OVRO Gary and Hurford 1990, 1–18 GHz), the Siberian Solar Radio Telescope (SSRT Zandanov et al. 1999, 5.7 GHz), the Ratan-600 radio telescope (Bogod et al. 1998, 610–30 GHz). In addition, two solar-dedicated radioheliographs produce daily images of the solar corona, accessible on line to the solar community. At metric/decimetric wavelengths, the Nançay Radioheliograph which started to provide in 1980 (for the launch of the Solar Maximum Mission) 2D images of the solar corona at 169 MHz (Bonmartin et al. 1983) was implemented and produced, after 1986, in addition to this 2D image, two one-dimensional images at several frequencies in the 450–150 MHz domain (The Radioheliograph Group 1989). After 1996 the Nançay Radioheliograph (NRH) produced 2D images of the radio sources observed in the middle corona between 450 and 150 MHz (Kerdraon and Delouis 1997) with a spatial resolution of $0.3 - 6'$ depending on the frequency and direction. Sections 4.1 and 4.2 will describe how the combination of spectrally and spatially resolved observations provides crucial information on the location of electron acceleration sites associated with flares of all sizes and on the link between the characteristics of flare accelerated particles and of the magnetic structures in which electrons are injected. Apart from a few papers, most of the studies combining radio and HXR observations have been performed until recently with data with no spatial resolution in the HXR domain. In the microwave domain, the Nobeyama Radioheliograph (NoRH) provides since 1992 systematic images of the Sun at 17 GHz (Nakajima et al. 1991) and has been more recently upgraded to provide observations at 34 GHz (Takano et al. 1997). The spatial resolution is, respectively, $10''$ at 17 GHz and $5''$ at 34 GHz. The Very Large Array (VLA) and the solar dedicated Owens Valley Radio Observatory Solar Array (OVRO) and Siberian Solar Radio Telescope also provide spatially resolved observations of flare emissions with spatial resolution of 10 arc sec or better at frequencies in the GHz range. Section 4.3 will show how the combination of microwave and X-ray observations provide quantitative information on the flare accelerated electrons as well as information on the electron acceleration/interaction sites. Section 4.4 will be devoted to the observations in the submillimetre domain

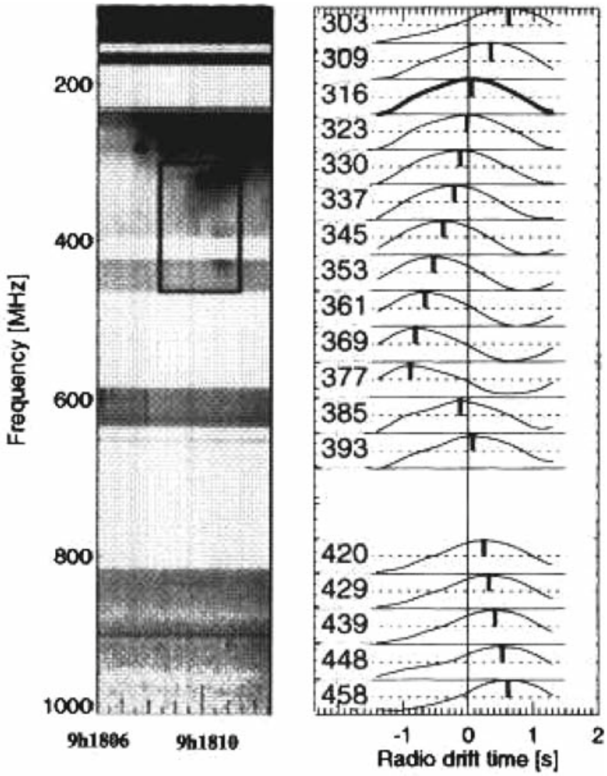


**Fig. 28** *Left panel* Radio dynamic spectrum from Ikarus; grey scale of logarithmic radio flux. *Right panel* Cross correlation of the radio time profile at different frequencies with the time profile at the peak frequency 316 MHz marked with a thick time profile. The frequency window is indicated by a *box* in the left figure (adapted from Aschwanden et al. 1995)

which is the most recently opened domain in the field of radio observations of solar flares.

## 4.1 Location of the electron sites in flares as diagnosed from decimetric/metric and X-ray observations

### *4.1.1 Electron acceleration sites deduced from type III and X-ray observations*

Indirect evidence of electron acceleration sites in the corona first came from broad band radio spectral observations. Electron beams propagating along magnetic field lines in the corona produce coherent emissions at the local plasma frequency or at its harmonic. The emitted radio bursts (type III, respectively, reverse type III bursts) will exhibit characteristic frequency drifts either towards lower, respectively, higher frequencies if the beam propagates in the direction opposite to the ambient electron density gradient (upwards), respectively, in the direction of the gradient (downwards). Pairs of type III and reverse type III bursts are sometimes observed (Fig. 28) and

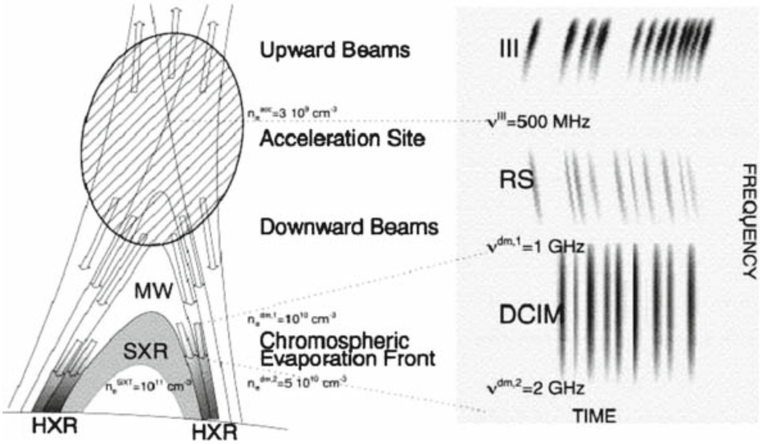


**Fig. 29** *Left panel* Diagram of a flare model envisioning magnetic reconnection and based on the radio observations of electron beams. *Right panel* Dynamic radio spectrum showing the radio bursts in a frequency–time plot. The acceleration region is located in a low density region (in the cusp) with a density around $10^9\,\mathrm{cm}^{-3}$ from where electron beams are accelerated in upward (type III) and downward (RS bursts) directions (from Aschwanden and Benz 1997)

their starting frequencies have been used to deduce a mean density in the electron acceleration site (e.g. Aschwanden et al. 1995; Aschwanden and Benz 1997). The starting frequencies of pairs of decimetric type III bursts are found to be between 220 and 910 MHz which implies a range of electron densities in the acceleration region between $6 \times 10^8$ and $10^{10}\,\mathrm{cm}^{-3}$ for fundamental emission or $1.5 \times 10^8$–$3 \times 10^9\,\mathrm{cm}^{-3}$ for harmonic emission. This implies a much lower density in the acceleration region than the one observed in the bright soft X-ray loops ($10^{10}$–$10^{11}\,\mathrm{cm}^{-3}$) and suggests that the acceleration region lies above them, being located, e.g. in a cusp reconnection site (Fig. 29 from Aschwanden and Benz 1997). X-ray observations of flares suggest also that energy release appears either near the top of $10^4$ km magnetic loops (loop top sources) possibly in the cusp region (e.g. Takakura et al. 1993) or close to the interaction region between loops or loop systems of different sizes ($10^4$–$10^5$ km) (e.g. Hanaoka 1999a).

Typical heights where electrons of tens to a few hundreds of keV are accelerated can be estimated from time of flight analysis of HXR emissions leading to estimates of the acceleration heights also ranging between $2 \times 10^4$ and $5 \times 10^4$ km (Aschwanden et al. 1998). New evidence of X-ray loop top sources has been found recently with RHESSI observations (Sui and Holman 2003; Sui et al. 2004) (see Fig. 30 from Sui and Holman 2003). These observations show that in addition to the loop top sources previously observed by YOHKOH, coronal sources at higher altitudes are observed with RHESSI at energies up to 20 keV. While the temperature of the loop-top sources derived from the positions of thermal HXR sources at different energies increases towards higher altitudes, the temperature of the coronal sources increases towards lower altitudes. The hotter sources lie towards the region located between the loop-top and the coronal sources and may indicate the formation of a current sheet between the

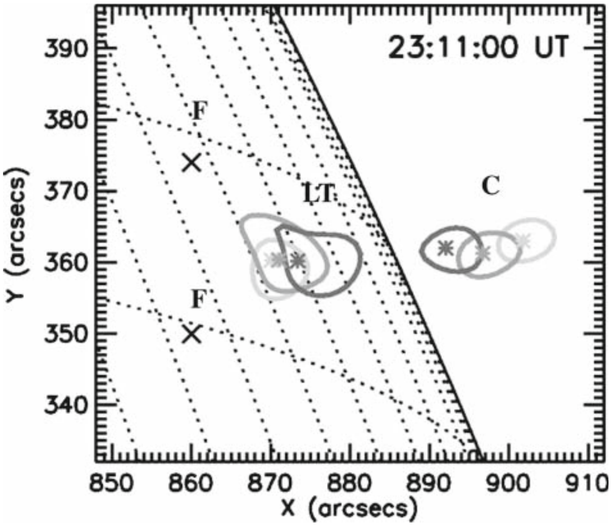


**Fig. 30** RHESSI X-ray images in different energy bands. The three contours (80% of the peak flux in each image) on the solar disk indicate the top of loops in the energy bands 6–8, 10–12 and 16–20 keV (from light to dark contours). The contours (80% of the peak flux of the coronal source in each image) above the limb are for the 10–12, 12–14 and 14–16 keV bands (from light to dark contours). The *crosses* mark the two footpoints of the X-ray loop (adapted from Sui and Holman 2003)

top of the flare loops and the coronal source. This brings new observational evidence for magnetic reconnection and cusp geometry in flares (see also Sect. 5).

Finally even if the bulk of the non-thermal electrons is produced at heights close to $10^4$ km, some observations show that significant acceleration of energetic electrons (a few tens of keV) may occur at heights as high as $2 \times 10^5$ km. This is in particular deduced from observations of occulted X-ray flares (see, e.g. the X-ray stereoscopic observations from Kane et al. 1992; Trottet et al. 2003; Kane et al. 2005).

### *4.1.2 Electron acceleration sites deduced from spike and X-ray observations*

Besides the classical burst types defined in the metric band in the 1960s, a second type of coherent radio emissions has been observed at metric and decimetric wavelengths. These are the narrowband (few per cent of the centre frequency) and short (few tens of ms) spikes which were first discovered in the early 1960s around 300 MHz (see Bastian et al. 1998 for a review) and which were later on more extensively observed above 1 GHz (Droege 1977; Slottje 1978) during the rise phase of flare-associated gyrosynchrotron emission. These narrowband spikes have been more recently used to advocate fragmentation of energy release in flares (e.g. Benz 1985). Although probably originating from the same emission process, spikes have been classified in two types (e.g. Bastian et al. 1998) called *decimetric* and *metric* spikes (see definitions below).

Metric spikes are confined to a narrow frequency range from about 200 to 400 MHz and are observed near the starting frequency of metric type III bursts (Fig. 31). Even if they are less frequently observed than decimetric spikes, metric spikes are thus

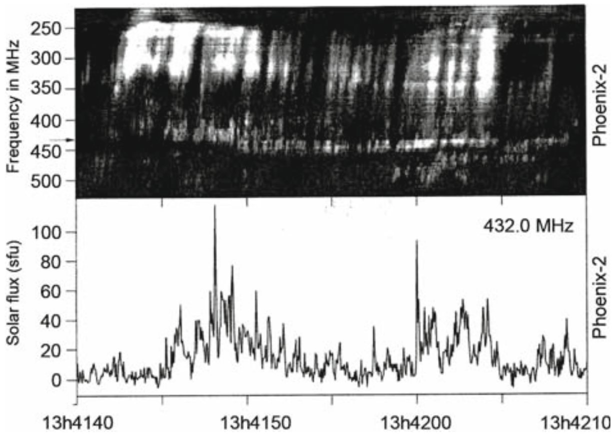


**Fig. 31** *Top panel* Spectrogram observed by Phoenix-2. *White* regions correspond to enhanced flux; the frequency axis is from top to bottom. *Bottom panel* Light curve of metric spikes recorded by the Phoenix-2 spectrometer at a single frequency (432.0 MHz). The *arrow* in the top panel indicates the position of 432.0 MHz (adapted from Paesold et al. 2001)

particularly interesting with respect to the observations of electron acceleration sites. Electron acceleration in the corona can be traced by imaging and spectral observations of these spikes. The first imaging investigation of metric spikes was performed with VLA at 333 MHz (Krucker et al. 1997). Spike sources were found at high altitudes suggesting that the spike source could be closely connected to the acceleration region of electrons. Later on, by combining spectral and multi-wavelength imaging observations with the Nançay Radioheliograph, Paesold et al. (2001) have shown that the extrapolation to lower altitudes of the observed type III trajectories is in close coincidence to the position of the metric spike source. This strongly supports the hypothesis that spikes reflect electron acceleration sites in the corona. In some cases, different type III bursts from the same group may follow divergent paths from the same spike region located close to the interaction region of different loop systems. This supports again the idea that acceleration sites are located near interaction regions of several loops.

The so-called *decimetric* spikes are more commonly observed at decimetric wavelengths. Contrary to the metric spikes they do not appear near the starting frequency of metric type III bursts. They occur however, during the impulsive phase of flares and are often associated with HXR emissions (e.g. Benz and Kane 1986). The association rate with HXR flares is high (95%, Guedel et al. 1991). The correlation of the frequency integrated spike flux with HXR is often very close, but the spike activity is often delayed with respect to impulsive HXRs at 25 keV by 2–5 s (e.g. Aschwanden and Guedel 1992). Several scenarios have been proposed to explain these observations but no conclusion was reached because of the lack of spatial resolution. Decimetric spikes have indeed been rarely mapped and their location with respect to HXR and microwave signatures of energetic electrons is not well explored. Benz et al. (2002), Saint-Hilaire and Benz (2003) and Khan and Aurass (2006) studied a few events (less than 10) where the low frequency part of spike clusters could be located by the Nançay Radioheliograph. It was found by Benz et al. (2002) and Saint-Hilaire and Benz (2003)

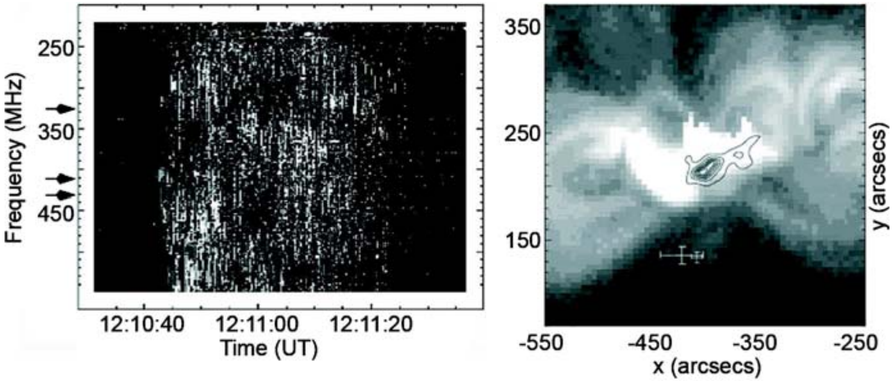


**Fig. 32** *Left panel* Spectrogram of a rich cluster of spikes observed by Phoenix-2. The *arrows* indicate the frequencies observed by the NRH. *Right panel* Spike and HXR positions superposed on a SXT/Yohkoh image for another group of similar spikes. The centroid positions of the spike sources at 432 MHz as observed by the NRH are drawn with *white error bars* representing their scatter in time. The hard X-ray intensity as observed by HXT/Yohkoh (M1 channel) is displayed by isophotes (from Benz et al. 2002)

that the spike sources are far (20″–400″) from the HXR sources (see, e.g. Fig. 32) and from the thermal flare plasma seen in soft X-rays and EUV lines. In most cases no bright footpoint is found nearby and in some cases spikes are near loop tops. Thus these observations do not confirm the view that the spike emission is produced by some loss-cone instability near the footpoints of flare loops (e.g. Benz 1986). The fact that the spike sources are found far away from the major flare site may, however, be related to the fact that the spikes which can be imaged are low frequency ones. Their occurrence after the main flare phase suggests that they are not related to the main sites of flare electron acceleration. They seem to indicate secondary acceleration sites related to the rearrangement of the coronal magnetic field after the main flare and are indicative of post-flare high-corona acceleration sites. This is also what is suggested by the observations of Khan and Aurass (2006). These spatially resolved observations could thus support the interpretation that the radio emission from spikes arises from electrons accelerated in MHD cascading waves, probably generated in the plasma outflows from the magnetic field reconnection (Karlický et al. 1996; Bárta and Karlický 2001).

As a conclusion, imaging spikes at radio wavelengths together with imaging the X-ray counterparts is very promising. However, only few spikes have been imaged so far, given the limited frequency range of decimetric/metric radio images. Clearly, observations of spikes at higher frequencies (around and above 500 MHz) combined with type III observations at lower frequencies and X-ray observations would be crucial to get further information on electron acceleration sites in the corona.

## 4.2 Evolution of electron interaction sites in the course of flares as diagnosed from imaging studies at X-rays and metric/decimetric wavelengths

### *4.2.1 Temporal evolution of radio and X-ray emissions from flares*

As already stated, complementary observations of the radio emitting electrons are provided by the HXR emissions produced by the energetic electrons when impinging

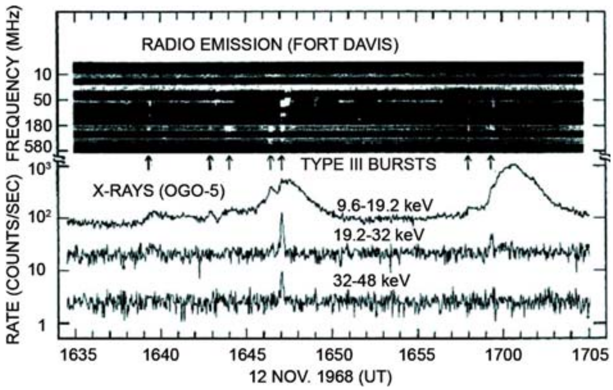


**Fig. 33** One example of time-correlation between impulsive solar X-rays observed above 10 keV by OGO5 and type III radio bursts in the 10–580 MHz frequency range (from Kane 1972)

the dense regions of the solar atmosphere. The first studies of the relationship between type III bursts and HXR emissions were performed by Kane (1972) and Kane (1981) using HXR observations from OGO 5 (Fig. 33). The association between type III bursts and HXR emissions was preferentially found for intense type III bursts and/or type III bursts observed with a starting frequency higher than 200 MHz, i.e. for type III producing electron beams accelerated low enough in the corona. When the association is found, there is a good similarity between both emissions, suggesting that the two emissions are linked to electrons produced at a common acceleration site (see also the cartoon of Fig. 29a).

These studies which first concerned the relationship between HXR and metric/decimetric radio emitting electrons, during the impulsive phase of flares were extended on longer timescales to the gradual emissions by, e.g. Hudson (1978) and Klein et al. (1983) (Fig. 34, left panel). It was found that when the gradual emission at metric wavelengths consists of a flare continuum with or without a moving type IV burst (see Sect. 2.1.2 for definitions), HXR and radio emissions start and end within a few minutes and have similar global time evolutions despite the large distance in heights of emitting sources. Electrons are thus found to be continuously produced and injected in magnetic structures of different scales. It was also found that when a stationary type IV burst is observed, it is often no longer associated with the production of HXR emissions (within the sensitivity of the X-ray experiments) but with softer X-ray emissions. This indicates that this long duration emission is associated to a less efficient production of energetic electrons (Fig. 34, right panel). Some reactivation of the post flare loops formed after major flares are, however, sometimes observed to produce small bursts in the HXR range in association with modulations of the stationary type IV burst (e.g. Svestka et al. 1982).

### *4.2.2 Temporal evolution of spatially resolved metric/decimetric sources in flares*

The combined spectrally and spatially resolved observations at radio wavelengths obtained provide crucial information on the location of the electron acceleration sites

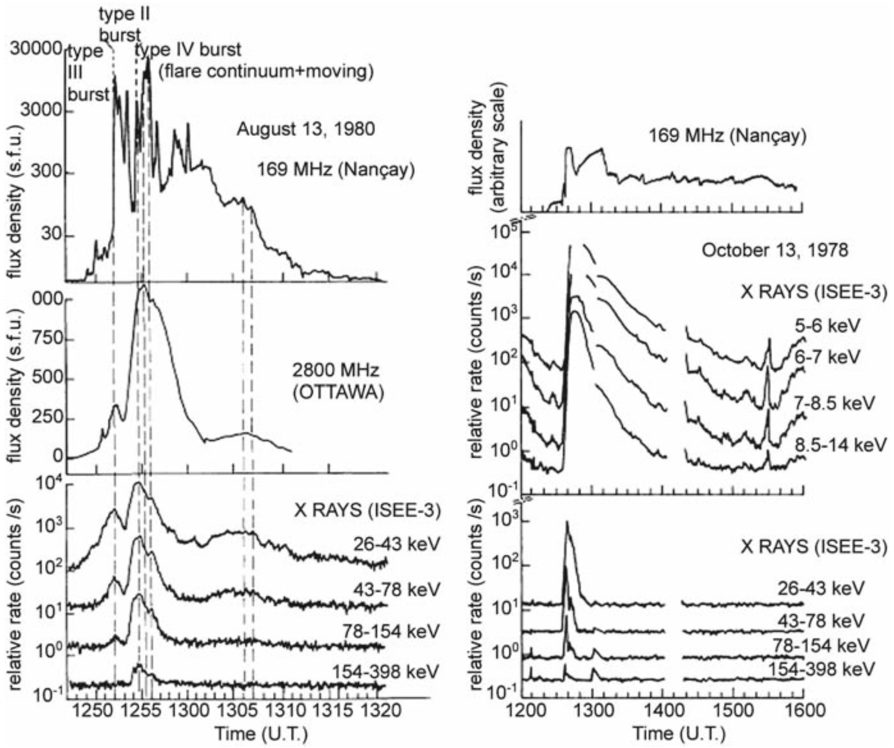


**Fig. 34** *Left panel* Time evolutions of the radio flux densities at 169, 2.8 GHz compared with the time evolution of the hard X-ray flux observed by ISEE3 in several energy bands. *Right panel* Time evolution of the radio flux density at 169 MHz compared with the time evolutions of the soft X-ray and hard X-ray fluxes observed in several energy bands by ISEE3 (from Klein et al. 1983)

associated with flares of all sizes (see, e.g. Trottet 1994; Vilmer and Trottet 1997 for reviews). The first comparisons were performed with the Nançay Radioheliograph at one frequency (169 MHz) (see, e.g. Kane et al. 1980; Kane and Raoult 1981; Benz et al. 1983; Raoult et al. 1985; Chupp et al. 1993; Trottet et al. 1994). The best prospect for understanding the development of the acceleration process emerged from observations made with a cadence $\leq 1$ s. They showed that HXR and radio emissions arise from electrons produced in a common acceleration site and injected, respectively, in low height magnetic structures where they produce X-rays and in larger scale, higher magnetic features where they emit decimetric and metric radiations.

Many of these observations have also shown that in the course of the flare, various diverging large scale coronal structures are successively and simultaneously the sites of non-thermal electron radiation. This is consistent with what was also observed combining high resolution microwave observations with VLA and type III radio observations. It was found that in the course of one event, a small change by about $10''$ in the centimetric burst location could correspond to a change of 0.5 solar radius for the type III location at 169 MHz (Lantos et al. 1984).

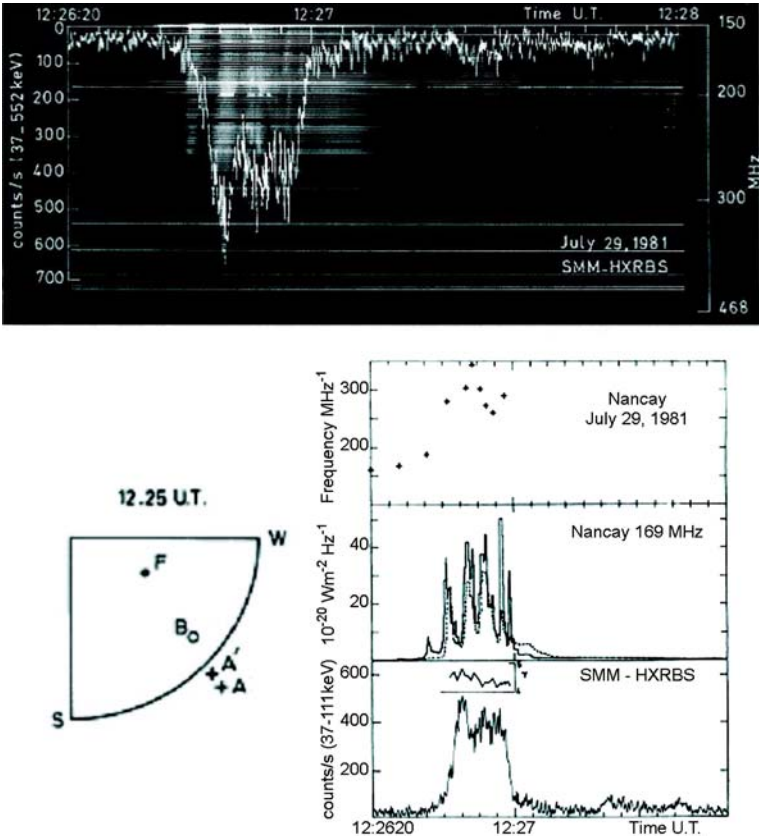


**Fig. 35** *Top* Spectrogram of the radio bursts observed with the Nançay radiospectrograph and associated hard X-ray burst observed with HXRBS/SMM. Note the inverted vertical scale for X-ray data. *Bottom Left panel* Locations of radio sources A, A′, B (see text for details) observed during the development of the flare. The point labelled F shows the location of the Hα flare. *Right panel* from top to bottom: Evolution of the starting frequency of radio bursts as observed with spectrograph, of the radio flux from sources A′ (*solid line*) and B (*broken line*) as observed with the Nançay Radioheliograph and of the HXR emission and of the power law spectral index observed with HXRBS/SMM (adapted from Raoult et al. 1985)

Raoult et al. (1985) showed that the spectral characteristics of the flare energetic electrons (as deduced from HXR observations) evolve with time in close temporal association with the "activation" of new large scale magnetic structures in which radio emission is produced. Sources of type III burst may consist of several components which radiate quasi simultaneously. This is illustrated in the example shown in Fig. 35. Two radio emission sites A and A′ are detected in the rise phase of the event. A new source B appears at the time of the largest increase of the X-ray flux and of the brightening of source A′. The two sources A′ and B fluctuate together and the simplest interpretation which was proposed is that the accelerated electrons are injected simultaneously into two magnetic structures which interact at the electron acceleration site, possibly by reconnection (see also Fig. 38). The appearance of the new site also coincides to a sudden increase of the starting frequency of type

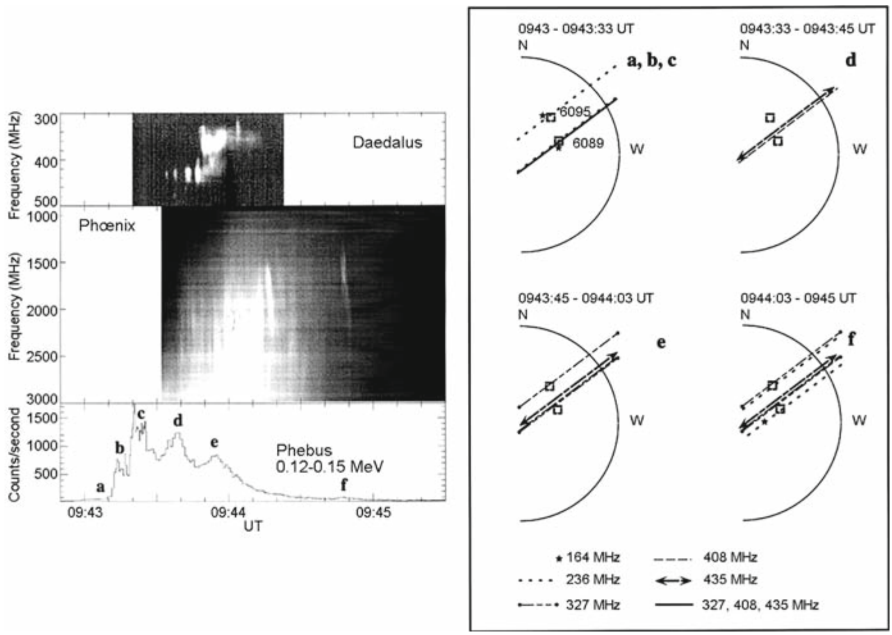


**Fig. 36** *Left panel* from top to bottom: Radio dynamic spectra recorded by Daedalus and Phoenix in the 300–500 MHz and 1–3 GHz bands and time history of the 120–150 keV count rate measured by PHEBUS. *Right panel* Location of the 164, 236, 327, 408 and 435 MHz radio emitting sources obtained with the NRH during the different time intervals. The *squares* give the locations of NOAA regions 6089 (where the flare occurred) and 6095 (adapted from Trottet et al. 1998)

III bursts. Such a relationship between the time variation of the starting frequency of type III bursts and the HXR flux was found for three events and was interpreted as an increase of the acceleration efficiency process linked to the downward shift of the electron/acceleration region (Kane and Raoult 1981; Raoult et al. 1985). On a study based on three other flares, Benz et al. (1983) also showed that the starting frequencies of the type III bursts appear to correlate with the electron temperature. This temperature was derived from isothermal fits to the HXR spectra with the most intense HXR emission appearing at the time of the higher starting frequency. This is another way of saying that the spectral characteristics of the HXR radiating energetic electrons are linked to the evolution of the starting frequency.

The previous results were based on events for which radio images were recorded at the single 169 MHz frequency since the Nançay Radioheliograph was operating at this single frequency until 1985. One solar cycle later, similar studies were done using the capability of the Nançay Radioheliograph to provide in addition to this 2D image, two one-dimensional images at four other frequencies (see, e.g. Trottet et al. 1998; Raulin et al. 2000). Some of the analysed events show variations of HXR emitting electron spectra simultaneous with stepwise changes of metric/decimetric spectra and appearance of new radio sources (see Fig. 36 adapted from Trottet et al. 1998). Peak d (the hardest peak of the event observed above 10 MeV) corresponds to the appearance of radio emission in the 550–375 MHz range while peak e corresponds

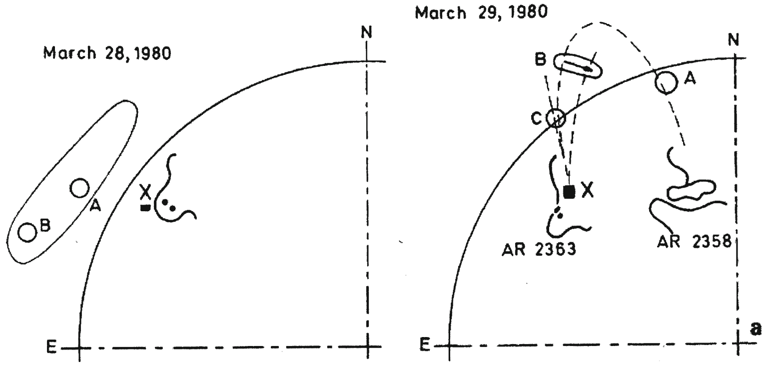


**Fig. 37** Positions of soft X-ray (marked with a X) and radio emission sources (A, B, C) at 169 MHz for two flares. The sunspots are indicated by *black dots* and magnetic neutral lines are indicated. The large area around radio positions shows the position of the continuum emission at 169 MHz (from Benz et al. 1983)

to emissions in the 450–300 MHz with a new source appearing at 327 MHz and peak f to emissions below 260 MHz. It should furthermore be noted that compared to the previous studies, the radio spectrograph used here is limited to frequencies above 260 MHz, while the evolution of starting frequencies of type III bursts with the rise of HXR emission mentioned in the previous paragraph was mostly observed in the 150–400 MHz range. Both sets of results are then not inconsistent, showing several aspects of the relationship between the production of energetic particles and the evolution of the site of production of energetic electrons.

Correlations between changes in the particle spectra and the appearance of new radio sources has also been found for X-ray/$\gamma$-ray events (e.g. Trottet 1994; Chupp et al. 1993; Trottet et al. 1998). A new radio source was indeed found at the time of the initiation of the major increase in HXR/$\gamma$-ray radiation when the photon spectrum hardens significantly and photon emission $>10$ Mev is produced (Chupp et al. 1993). It thus suggests that the electron spectral variability and also the electron to proton ratio is linked to the magnetic configurations in which particles are produced.

### *4.2.3 Temporal evolution of spatially resolved metric/decimetric and HXR sources in flares*

Figure 37 shows two flares for which the positions of X-ray sources observed for energies between 3.5 and 30 keV with HXIS/SMM were compared with the positions of the radio sources at 169 MHz determined at different times in the event (Benz et al. 1983). This comparison shows that the radio emission at 169 MHz is produced in large scale loops potentially interconnecting the flaring active region to another one. The indication that interaction sites between small flaring loops and larger scale ones could be preferential sites for energy release and acceleration also came from the comparison between the spatially resolved observations of HXIS/SMM with the spatially resolved observations at metric/decimetric wavelengths (Fig. 38 from Hernandez et al. 1986). Such a picture is consistent with the previous results from Machado et al. (1983) based

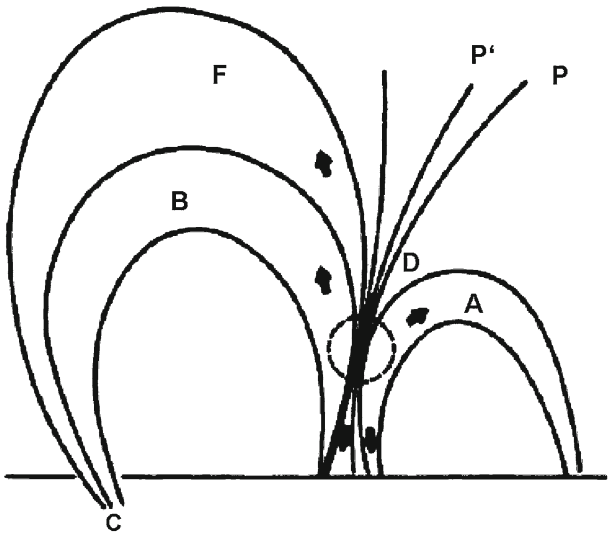


**Fig. 38** Model deduced from radio and X-ray images: The *dashed circle* is the site of energy release and acceleration. The *arrows* show the paths of accelerated particles. Labels A, B, C and D refer to the locations of X-ray emissions. P and P′ refer to the positions of radio sources at metre wavelengths (from Hernandez et al. 1986)

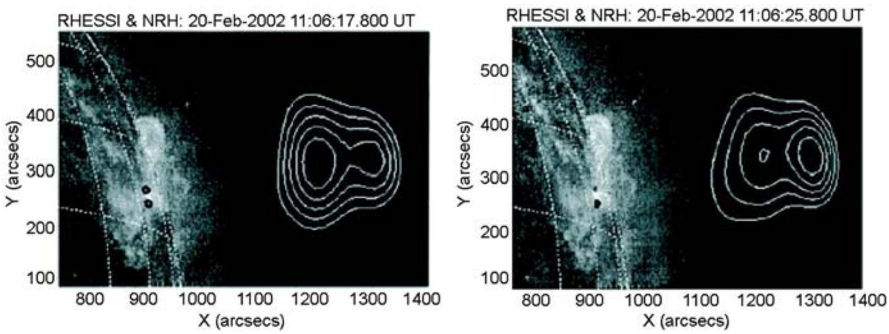


**Fig. 39** RHESSI isocontours (*black*) (40, 60, 80% of the maximum) at 25–40 keV and NRH contours at 410 MHz (white) (50, 60, 70, 80, 90%) observed at a time when similar X-ray fluxes are emitted by the X-ray sources (*left*) and at a time when the southernmost X-ray source is predominant (*right*). The RHESSI and NRH contours are superposed on an EIT image (adapted from Vilmer et al. 2002)

on HXIS/SMM observations and is reminiscent of that involved in the emerging flux models of solar flares (Heyvaerts et al. 1977).

More recently, similar studies could be performed for flares for which HXR images and radio images at several frequencies in the decimetric/metric domains were obtained using YOHKOH/HXT or RHESSI and NRH data (e.g. Vilmer et al. 2002, 2003; Dauphin et al. 2005, 2006; Pick et al. 2005a; Trottet et al. 2006). For one event, a very close correspondence is observed between the change on the time scale of a few seconds of the pattern of the HXR source in the 25–40 keV range and the pattern of the radio source at the highest frequency (410 MHz) which can be imaged (Fig. 39

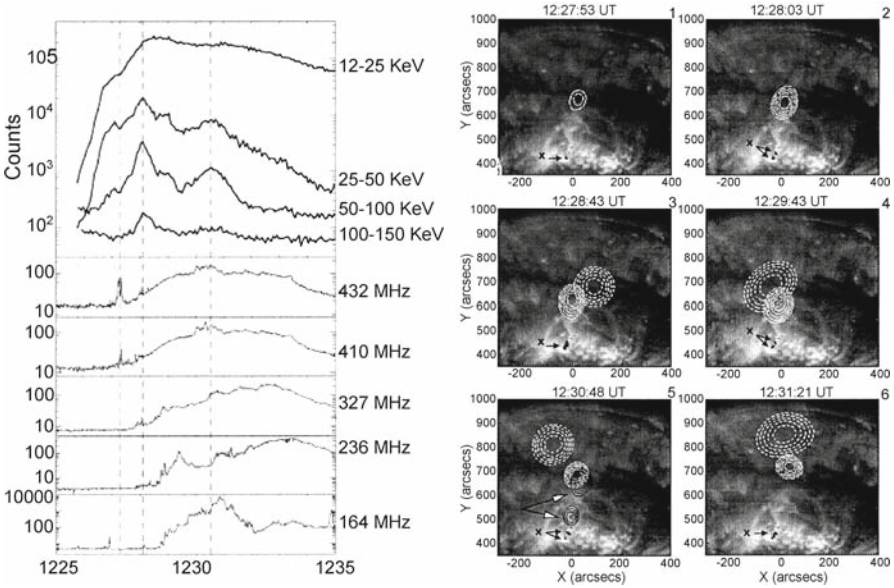


**Fig. 40** *Left panel* from top to bottom: Time evolution of the X-ray RHESSI count-rates in four energy bands and time evolution of the radio flux density observed in the flare region by the Nançay Radioheliograph. The *dashed vertical lines* indicate the first radio 432 MHz burst at 12:27:20 UT and the two main HXR peaks above 50 keV around 12:28 UT and after 12:30 UT. *Right panel* RHESSI isocontours (*thick black*) (75, 80, 85, 90, 95% of the maximum) and NRH contours at 327 MHz (*dashed-dotted white*) (75, 80, 85, 90, 95% of the maximum) and 164 MHz (*dotted white*) (75, 80, 85, 90, 95% of the maximum) observed at different times. Note that the 164 MHz emission appears later in the flare (from image 3). The two components at 432 MHz (indicated by *arrows*) are overlaid for comparison (*black contours*) in image 5. The RHESSI and NRH contours are overlaid on the EIT image. The RHESSI contours are obtained in the 40–65 keV range and are indicated by *black arrows* (from Vilmer et al. 2003)

from Vilmer et al. 2002). This strongly supports the previous suggestion of common acceleration/injection sites for HXR and decimetric radio emitting electrons. Direct comparisons between the evolution with time of HXR and radio sources at different heights have been obtained using images made by the NRH at several frequencies. The association between radio and HXR emission discussed in the previous paragraph can be better understood when combining radio spectral data with spatially resolved observations at several frequencies. Figure 40 shows indeed that while the first strong HXR peak at energies above 50 keV is not associated with strong radio emission, the second one is associated to intense decimetric/metric (and dekametric emissions). This implies that, during the first peak, energetic electrons are confined in low lying loops (heights of several $10^4$ km) with no access to the higher ($>10^5$ km) corona. It is found that the second HXR peak comes from a slightly different position in the active region and is associated with the appearance of new radio components at all frequencies with positions further away from the active region. This second peak thus results from energy release in different magnetic structures and large scales ($>10^5$ km) are now involved in the process. These new radio components appear at the time of the extension of strong radio emission below 14 MHz and may trace electron beam injection towards the high corona and the interplanetary medium. The fact that the first peak is associated with very weak radio emission at decimetric/metric wavelengths is furthermore consistent with the fact that 10–17% of HXR producing electrons have no detectable emission at decimetre and longer wavelengths (e.g. Simnett and Benz 1986; Benz et al. 2005).

In summary, combining HXR images with NRH images at different frequencies demonstrates the potentiality of understanding the link between the energetic electrons interacting at the Sun and the injection of the escaping electrons which produce the radio emissions at the lowest frequencies. Radio images have been obtained so far only in the 450–150 MHz range. It is clear that to further probe electron acceleration sites both in the high and low corona, radio images in a complete frequency range and in particular in the 500 MHz–1 GHz never imaged so far are clearly needed.

## 4.3 Quantitative diagnostics of flare energetic electrons as provided by their gyrosynchrotron emissions

As recalled in Sect. 2.2.1, gyrosynchrotron emission in solar flares usually dominates at frequencies above 3 GHz, i.e. in the microwave domain. Gyrosynchrotron emission is a well understood process (see, e.g. the review by Dulk 1985) and can be used to determine the energy spectra of flare-accelerated electrons at energies $>100$ keV. We shall not present here a comprehensive review of microwave emission but focus on a few points related to the complementary aspects of microwave and HXR emissions. Other reviews on this topic can be found in, e.g. Marsh and Hurford (1982), Bastian et al. (1998) and Klein (2005).

### *4.3.1 Microwave and HXR radiating emitting electrons: determination of the number of electrons*

Figure 41 from Nita et al. (2004) illustrates a typical flare spectrum observed above 1 GHz by the Owens Valley Solar Array (OVSA). At frequencies above 3 GHz the flare emission is dominated by gyrosynchrotron emission and exhibits first a spectrum increasing to a peak frequency (between 5 and 6 GHz in the present case) which is the optically thick part and a decay towards higher frequencies (optically thin part of the spectrum). The emission below 3 GHz is of different origin, most probably coherent emissions dominant at decimetric and longer wavelengths (see previous sections). The optically thick part of the gyrosynchrotron spectrum is governed by self absorption by the non-thermal electrons, absorption by thermal electrons from the ambient medium or by suppression and absorption of the gyrosynchrotron emission in a dense plasma at frequencies close to the electron plasma frequency (Razin effect) (Ramaty 1969; Klein 1987; Belkora 1997). The spectral slope at high frequencies (optically thin part of the spectrum) reflects the slope of the radiating energetic electrons. The spectral index $\alpha$ of the microwave flux (flux density $\sim\nu^{\alpha}$) in the optically thin part can be predicted in the case of simple models, e.g. radiation in a homogeneous source from an isotropic power-law electron distribution with spectral index $\delta (N(E) \sim E^{-\delta})$. The relationship is $\alpha = 1.22–0.9\delta$ for mildly relativistic electrons and $0.5(1 - \delta)$ for

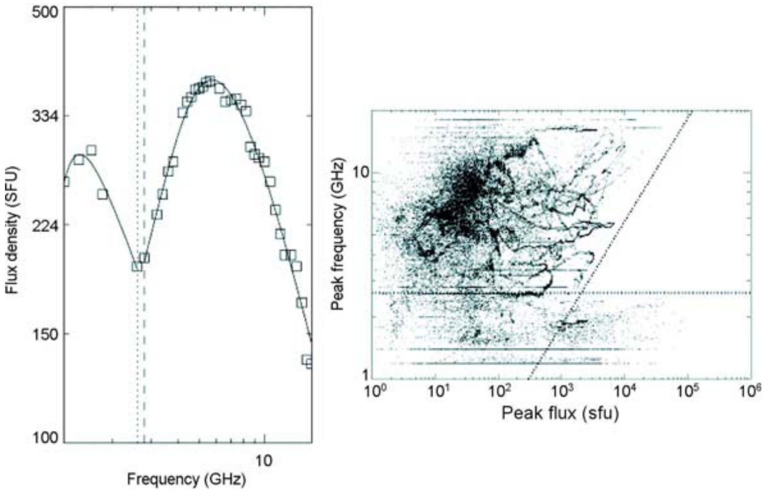


**Fig. 41** *Left panel* Example of a radio spectrum observed by the Owens Valley Solar Array (OVSA) above 1 GHz. *Right panel* Distribution based on the analysis of 412 events of the peak frequency as a function of the peak flux at this frequency. The *horizontal stripes* are due to data artefacts. The *horizontal line* around 2.6 GHz represents an empirical dividing line between dm plasma emissions and cm gyrosynchrotron emissions (from Nita et al. 2004)

relativistic electrons (Dulk and Marsh 1982). An important feature resulting from such a model for gyrosynchrotron emission is the correlation which is expected between the peak frequency and the radiated flux at this frequency. This tendency is observed on a sample of more than 400 events observed with OVSA (Fig. 41, right panel) which shows the peak frequency as a function of the emitted flux at this peak frequency. The tendency is better observed for the events located above the horizontal line (which delineates the rough limit between plasma and gyrosynchrotron dominated emissions). For strong events, the frequency domain for which the emission is not optically thin can extend to frequencies above 10 GHz. Correia et al. (1994) have in particular shown, on a sample of more than 100 events observed with the whole Sun patrol observations of the University of Bern, that nearly half of the bursts are not optically thin in the range 20–35 GHz.

The relationship between microwave and HXR bremsstrahlung emitting electrons was first studied by Peterson and Winckler (1959) and Kundu (1961) (see also Sect. 2.1.3). The fact that the same population of energetic electrons could be at the origin of both HXR and microwave observations has been since then extensively studied and has been a topic with a long and sometimes controversial history.

As summarized in, e.g. Kai (1986) the comparison of X-ray and microwave emitting electrons led to several discrepancies. The number of electrons necessary to produce the HXR emission was usually found to be $10^3$–$10^5$ times larger than the number required to radiate microwave emission. In 1985, Gary (1985) showed, however, that this apparent discrepancy was due to the fact that the quantities which were deduced independently from radio and HXR observations were instantaneous numbers of electrons and also that a too strong value of magnetic field was assumed in the microwave emitting region (thus reducing the number of electrons required to produce the emission).

As was shown by Kai (1986) the strong disagreement disappears if X-rays and microwave emitting electrons are linked as in a trap plus precipitation model. In such a model, the same population of electrons produces gyrosynchrotron microwave radiation in regions with moderate magnetic field and efficiently produce HXR emission in a thick target approximation after precipitating in the dense layers of the chromosphere (see, e.g. the geometry of Fig. 29). This first study used single frequency radio measurements as well as flare-integrated X-ray emission. No effect of magnetic field convergence on precipitating electrons was furthermore taken into account. The introduction of trap plus precipitation models led to more complete studies of electron evolution in the trap region in which microwave emission is produced (e.g. Klein et al. 1986) and showed that both microwave and X-ray spectral evolution with time could be reproduced by the same injected (accelerated) electrons. Further developments of this model included betatron energy losses of relativistic electrons in an expanding arch. Applied to a large gradual flare, this model showed again that the temporal and spectral evolution of X-rays and microwave emissions can be explained by a common source of electrons injected in trap regions (Bruggmann et al. 1994).

As a conclusion, these studies based on trap plus precipitation models confirmed the hypothesis made in the 1960s that energetic electron populations giving rise to HXR and microwave radiations were closely linked.

### *4.3.2 Spatial configurations of microwave sources*

In this section, we shall describe the spatial configurations expected in the case of gyrosynchrotron emission from isotropic energetic electron distributions injected in a magnetic loop and compare these expectations with spatially resolved observations.

Figure 42 shows a schematic configuration of gyrosynchrotron emitting sources at different frequencies as expected if the emission from an isotropic distribution of non-thermal electrons comes from a magnetic loop configuration with ambient density $3\times10^{10}$ cm$^{-3}$; the two footpoints are separated by $20''$ with magnetic field values below the photosphere of, respectively, 1,000 and 500 G (A and B) and sizes of, respectively, $5''$ and $7.1''$ (from Bastian et al. 1998). The results are summarized in Fig. 42 where contour maps at 8 frequencies are shown as well as spectra from different parts of the emitting source (see also similar results in Preka-Papadema and Alissandrakis (1992)). This model shows that in the optically thick part of the spectrum, i.e. in the present case up to 5 GHz, the emission comes mostly from the loop top and overlays the total size of the loop. When the emission progressively comes from the optically thin part of the spectrum (in the present case above 5 GHz), the emission is more and more concentrated in the loop footpoints with the highest frequencies coming from the footpoint with the stronger magnetic field. As recalled in the previous section, the peak frequency varies from one flare to the other and even in the course of a flare; these source configurations can be used however, to predict what should be observed in, respectively, optically thin and thick parts of the spectra.

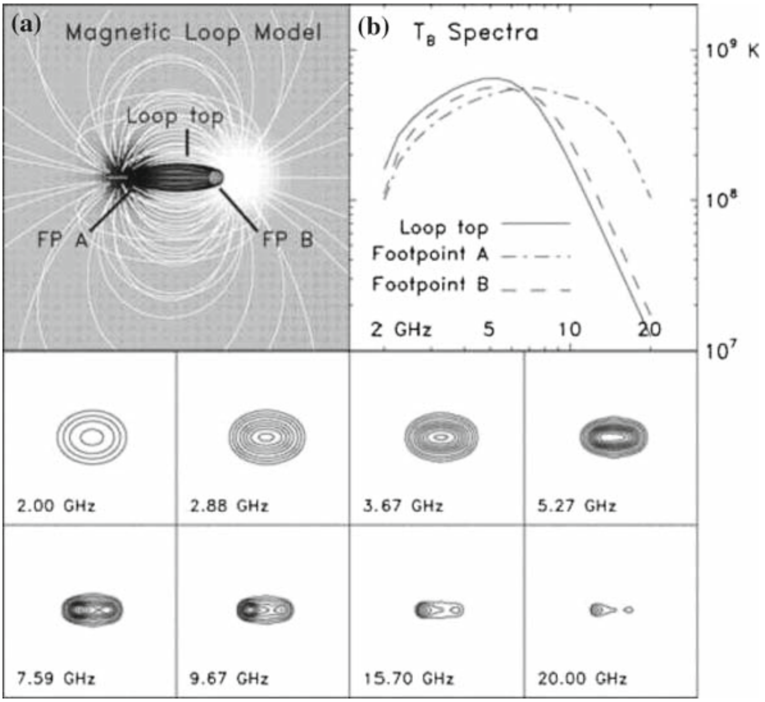


**Fig. 42** Gyrosynchrotron emission from a model coronal magnetic loop. *Top left* Representation of the magnetic field lines. *Top right* Brightness temperature spectra of the gyrosynchrotron emissions at magnetic footpoints A and B and at the loop top. *Bottom rows* brightness distributions of the radio intensity at eight frequencies (contours are at 2, 5, 10, 20, 30, 40, 50, 60, 80 and 90% of $6.8 \times 10^8$ K) (from Bastian et al. 1998)

Tests of these configurations can be obtained by comparing with the microwave source morphologies which have been observed with spatial resolution around 10″ or better by the Very Large Array (VLA) at, e.g. 5 and 15 GHz, around 20″ by the Siberian Solar Radio Telescope (SSRT) at 5.7 GHz and more systematically with the Nobeyama Radioheliograph (NoRH) which provides images at 17 GHz with a spatial resolution of 10″ (Nakajima et al. 1991). Early VLA observations at 5, 15 and 22 GHz (Marsh et al. 1980; Marsh and Hurford 1980) provided the first observational evidence that the emissions were coming at the flare peak time from compact singles source overlying the magnetic neutral line. Compact emitting sources were also observed with the early VLA observations at 1.4 and 5 GHz by Lang et al. (1981) and Kundu et al. (1981). Simultaneous VLA images of a flare at two frequencies combined with spectra obtained at OVSA between 2 and 15 GHz have shown that the observed magnetic source configurations are consistent with the configurations expected from the emission in a magnetic loop configuration (see, e.g. Figure 43 from Nindos et al. 2000 and Fig. 42 for the computed configuration). This shows that the radio emission from flares observed in the microwave domain is reasonably well interpreted in the framework of simple models of gyrosynchrotron radiation from energetic electrons.

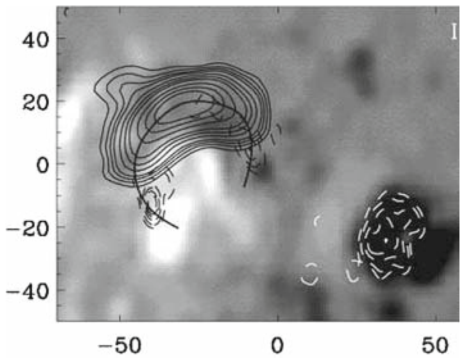


**Fig. 43** Contour plots of a flare observed with VLA overlaid on a Kitt Peak photospheric magnetogram. The *solid contours* show the 5 GHz emission and the dashed contours the 15 GHz emission (from Nindos et al. 2000)

### *4.3.3 Production sites of energetic electrons as deduced from spatially resolved microwave and HXR sources*

Combined spatially resolved observations of HXR and microwave emissions have been obtained for many flares using the SXT and HXT experiments aboard YOHKOH as well as the Nobeyama Radioheliograph (NoRH) and Owens Valley Radio Observatory Solar Array (OVSA) (e.g. Hanaoka 1997; Nishio et al. 1997; Lee and Gary 2000). Nishio et al. (1997) compared the radio sources morphologies observed by the NoRH at 17 GHz with the HXR morphologies for 14 events (Fig. 44). For most flares, two loops are involved: a compact one ($<20''$) coinciding with a double HXR source and brighter in soft X-rays. The second loop (often identified by comparing with soft X-ray images) has a larger spatial scale (30–80$''$) and the radio emission is usually observed close to the footpoint remote from the primary HXR emitting loop. These observations reveal a more complex magnetic loop configuration than the simple scheme discussed in the previous subsection. This more complex configuration was interpreted as a signature of reconnection between a small emerging loop (HXR sources and primary microwave emitting source) and an overlying large scale loop (Fig. 44 and Hanaoka 1999b). Electrons would be accelerated at the interface between the small and the large loops and injected into both loops. This is consistent with what was obtained a solar cycle earlier when HXIS/SMM observations were combined with spatially resolved observations at metre/decimetre wavelengths (see Sect. 4.2.3).

The first comparison of HXR images above 100 keV (i.e. in an energy range closer to the energy of the radiating microwave electrons) with radio images at 17 and 34 GHz from the Nobeyama Radioheliograph was done for one event observed by RHESSI on July 23, 2002 (White et al. 2003). As expected in the case of an optically thick radiation (which is the case at 17 GHz at the peak time in this event), the peak of the radio emission appears to lie at the top of the arcade of loops seen with TRACE, close to the peak in the 12–20 keV radio image and between the loop footpoints observed above 100 keV (Fig. 45e). Later on, when the emission at 17 GHz has become optically thin, the two 17 GHz sources lie above or close to the footpoints observed above 100 keV (Fig. 45g). The combination of radio images at 17 and 34 GHz and of the images at 12–25 keV in the preflare phase of this event (Fig. 45a) allows to confirm the existence in the onset

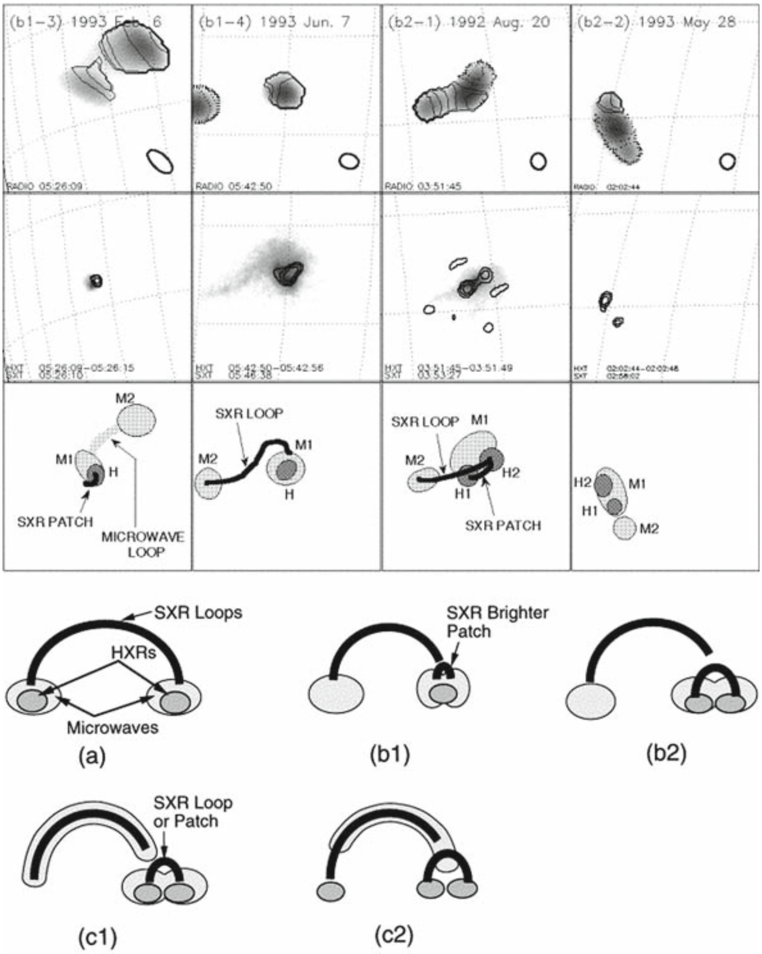


**Fig. 44** *Top panel* Coaligned 17 GHz images (*upper panel*), HXT/YOHKOH 23–33 keV images (contours in middle panels) and SXT images (grey scale in middle panels) for four events. The 17 GHz images are shown in brightness temperature with grey scales and in degree of circular polarization with contour levels (5, 10, 20, 40, 60 and 80%). The *circle* with the thick outline shown at the bottom right of each image represents the FWHM beamwidth of the Nobeyama Radioheliograph. HXR contours are drawn at 50, 25 and 12.5%. *Lower panels* are cartoons representing the spatial relationship between the microwave, HXR and SXR sources. Microwave sources are shown by *light grey* patches (M1, M2,...) while HXR sources are shown by *dark grey* patches (H1, H2,...). SXR sources are marked by thin black lines. *Bottom* schematic drawing of the spatial relationship between microwave, hard-X-ray and soft X-ray sources derived from the analysis of 14 events (adapted from Nishio et al. 1997)

phase of a coronal non-thermal source inferred from HXR observations and which contains a large amount of energy (Lin et al. 2003; Holman et al. 2003; White et al. 2003).

### 4.3.4 Angular distributions of radiating electrons

Additional information on the acceleration/interaction sites and the angular distributions of emitting electrons can be obtained by combining radio and X-ray images to

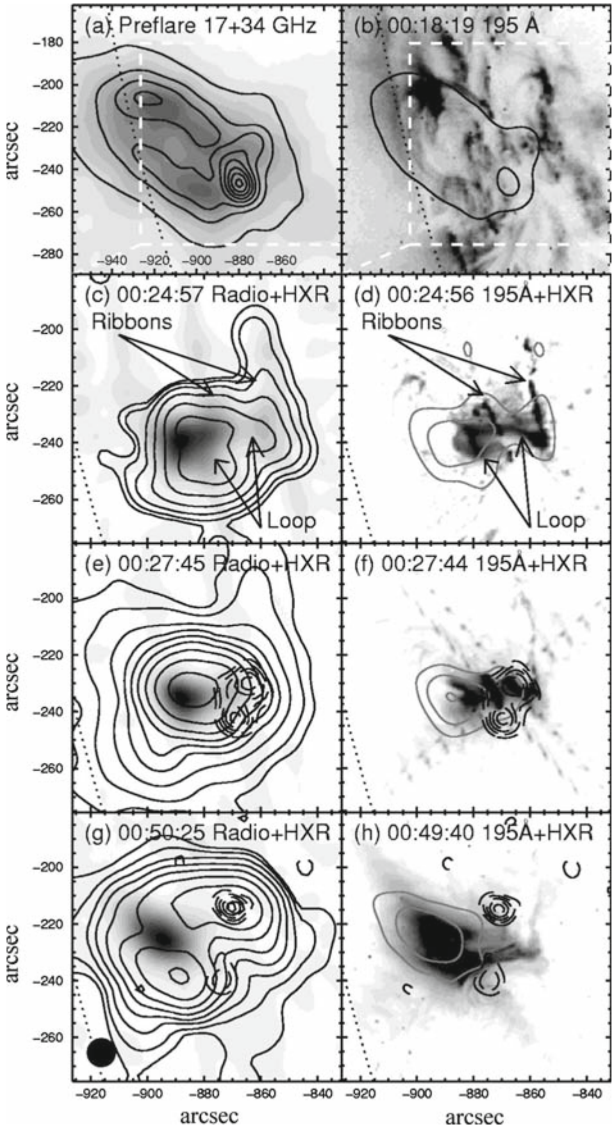


**Fig. 45** Images of a flare at X-ray, EUV and radio wavelength. The *top row* of panels shows radio and EUV images in the preflare phase. On the *left*, 17 GHz contours overlaid on a grey scale 34 GHz image. On the *right* the EUV image with two contours at 17 GHz. The other panels show the region outlined by *white dots* in the upper panels. The *left panels* show the grey-scale image at 12–20 keV overlaid with the 17 GHz total intensity contours (*solid curves*) and RHESSI 100–150 keV contours (*dashed curves*). The *right panels* show the EUV image of the same region overlaid with the *solid grey contours* for RHESSI 12–20 keV images and *dashed black contours* for RHESSI 100–150 keV hard X-rays (from White et al. 2003)

magnetic field extrapolations. The magnetic field geometry is found to be an important additional ingredient to understand the characteristics of the gyrosynchrotron emission as further illustrated in Figs. 46 and 47 from Lee et al. (2000b). The first example

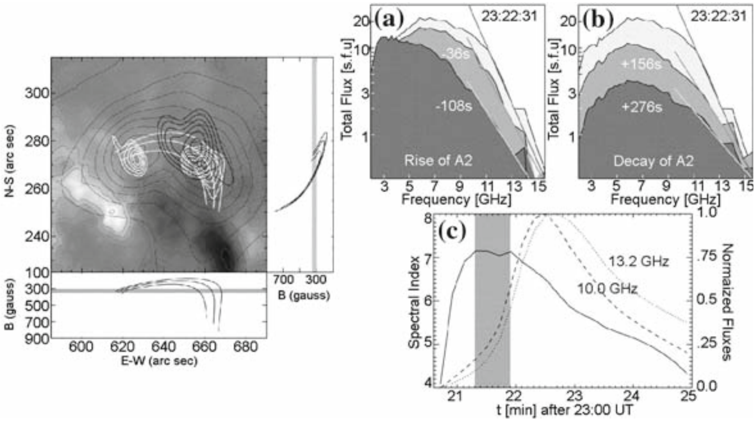


**Fig. 46** *Left panel* Magnetic field morphology and radio emitting sources for an impulsive event. The image shows 5 GHz (*thick black contours*), 10.6 GHz (*white contours*) and 17 GHz (*thin black contours*) on top of the longitudinal magnetogram. The *thick white curves* are selected field lines from the field extrapolation to represent the loop involved in the flare. The two *boxes* at the right and bottom give the field strength of the three field lines as function of distance along east-west and north-south, respectively. The *grey strip* in the boxes locates the magnetic trap. *Right panel* Evolution of the radio spectra in the rise and decay of the event and time evolution of the radio spectral index and of the radio flux in two optically thin frequencies (10.0 and 13.2 GHz). The *shaded section* indicates the rise period of injection (from Lee et al. 2000b)

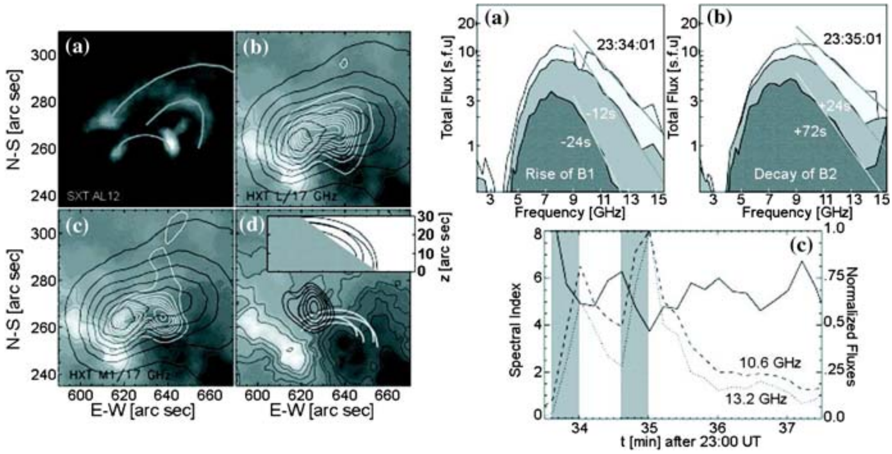


**Fig. 47** *Left panel* radio and X-ray morphologies for another impulsive event: **a** SXT images with hypothetical loops (*grey scale*), **b** 17 GHz (*black contours*) and YOHKOH/HXT in the 14–23 keV band (*white contours*), **c** 17 GHz (*black contours*) and YOHKOH/HXT in the 23–33 keV band (*white contours*), **d** 7 GHz map and the magnetic lines selected to represent the loop. The inset in (*d*) is the trajectory of the field lines on the $x$–$z$ plane. *Right panel* Evolution of the radio spectra in the rise and decay of the event and time evolution of the radio spectral index and of the radio flux in two optically thin frequencies (10.6 and 13.2 GHz). The *shaded sections* indicate the rise period of injections (from Lee et al. 2000b)

shows a single source at 5 GHz observed close to the top of magnetic loops and double sources at 10.6 and 17 GHz on both sides of the magnetic loops as expected from the schematic representation of Fig. 42. However, one of the sources at 10.6 and 17 GHz (the more western ones) does not seem to coincide with the western footpoint inferred from magnetic field extrapolation but is located somewhere intermediate between the loop top and the footpoint. As the western leg has a higher magnetic ratio ($B_{\rm foot}/B_{\rm top}$) than the eastern branch, one interpretation is that the radiation is produced by trapped electrons in the loop: as the mirror ratio is higher for the west leg, the height where the electrons are mirrored is higher in the loop than for the eastern leg (see the grey lines in Fig. 46. The efficient electron trapping which exists in this magnetic loop system then explains the smooth time profiles observed at different frequencies, the time delays between peak times at different frequencies and the flattening of the optically thin part of the microwave spectrum in the decay of the event. The second example (Fig. 47) shows images of a flare observed at 7 GHz with OVSA, 17 GHz with NoRH as well as in HXR with YOHKOH. While some diffuse component extending along the HXR source is observed at 17 GHz, a single bright compact source at 7 and 17 GHz is found at only one of the HXR footpoint. This somewhat surprising observation, given the expectations from Fig. 42, can, however, be explained in terms of the intrinsic directionality of gyrosynchrotron radiation and of the magnetic field geometry. The coronal magnetic field extrapolation shows indeed that the magnetic field inclination angle with respect to the observer is close to 90° at the east footpoint where emission can thus be observed and close to 0° for the western footpoint where no emission is observed (see the inset in Fig. 47d in which $z$ is directed towards the observer). The extrapolation also shows that the field strength does not strongly vary over the loop leading to a uniform HXR loop structure with a small magnetic mirror ratio. In a trap plus precipitation model, this leads to a high electron precipitation rate. This also explains the spectral evolution (steepening) of the microwave spectrum in the flare decay phase.

Combining radio, HXR images with magnetic field extrapolations thus allows a better understanding of the spatial distribution of the sources and of the temporal evolutions of the emissions. Further modelling of the transport of microwave emitting electrons in loop systems with magnetic mirroring (e.g. Lee and Gary 2000), can be used to deduce information on the angular distribution of energetic electrons from the temporal evolution of microwave fluxes at different frequencies. Magnetic mirroring in a coronal trap increases the microwave flux as compared to the HXR flux and indeed induces a different behaviour for the temporal evolution of the HXR and microwave spectral indices.

A previous and more "extreme" example of the effect of magnetic trapping on the relative time profiles of HXR and radio emissions was given by Bruggmann et al. (1994)) which showed a good correspondence between the observed time profiles and spectra of HXR and microwaves under the assumption that both are produced by electrons injected during several minutes in a coronal trap. Such a trapping was also suggested by the observations of large delays (several tens of seconds) between the peaks at microwaves, high energy and low energy HXRs. Electron trapping effects can also be demonstrated directly using microwave radioheliograph data by looking at the time profiles of loop-top and foot-point sources at 17 and 34 GHz (Melnikov et al. 2002).

### 4.3.5 *Electron energy spectra as deduced from microwave and HXR/GR emitting electrons*

Information on the energy spectra of bremsstrahlung and gyrosynchrotron emitting electrons in flares can be obtained from the combined observations of HXR/GR spectra over a wide energy band and of centimetre/millimetre radiation over a wide frequency range. This topic has been the subject of extensive discussions in the literature (e.g. Kundu et al. 1981; Nitta and Kosugi 1986; Lu and Petrosian 1989; Lee and Gary 1994; Bastian et al. 1998; White 1999; Silva et al. 1999; Melnikov and Silva 1999) and there is still controversy on the issue of how to relate these spectra. Indeed, while HXR emitting electrons sample the energy range of a few tens of keV in the case of thick target radiation (see Brown 1971 as a reference), microwave emitting electrons will sample, depending on the frequency, either trapped electrons of a few tens of keV or mildly relativistic electrons. For a given value of the magnetic field, the peak frequency of the gyrosynchrotron emission from mono energetic electrons is indeed proportional to the square of the Lorentz factor of the electrons so that higher frequency emissions are produced by higher energy electrons.

Discrepancies between the energetic electron spectral indices deduced from the optically thin part of the gyrosynchrotron spectrum and from the HXR spectrum have been reported in several cases (see, e.g. Marsh et al. 1981). However, with the advent of imaging spectroscopy in the 1–12 GHz range with OVSA, this issue was reexamined for a few flares of GOES class C to M using spatially resolved microwave spectra (Wang et al. 1994, 1995, 1996). It was found that when spatially resolved spectra are obtained, the microwave spectral index predicted by the electron spectrum deduced from X-ray spectroscopy is consistent with the measured microwave spectral index at the footpoint (see, e.g. Wang et al. 1994) but not with the one measured at the top of the loop. The location of the emission peak at each frequency usually shifts $60 - 100''$ from 1 to 14 GHz in good consistency with the schematic configuration derived from Fig. 42. The radio peak frequency as well as the slope of the optically thin part of the spectrum also varies from the loop top to the footpoint. While at the footpoint, the microwave emission is likely emitted by gyrosynchrotron emission of the same electrons which produce X-rays, at the looptop the emission is more consistent with a thermal gyrosynchrotron emission from a superhot component also detected at low energies in X-rays. Figures 48 and 49 illustrate one of these examples. Spatially resolved X-ray and microwave emissions show that at frequencies around 10 GHz, the primary microwave source is located in one of the footpoint of the soft X-ray emitting loop while the HXR source is located in the other leg. In good consistency with the model presented in Fig. 42 and with the discussion of the previous section, the microwave footpoint is the one with the higher magnetic field. As expected, the centroid of the microwave emission shifts towards the strong magnetic field footpoint as frequency increases. The HXR spectrum consist of two components: a superhot component with a temperature of $8.4 \times 10^7$ K. and a power law component with a spectral index of 4.2 (Wang et al. 1995). The microwave spectra (Fig. 49) show the same two components: a thermal component near the looptop with a brightness temperature similar to the one deduced from the superhot component in X-rays and a non-thermal component at the foot point of the loop produced by an electron spec-

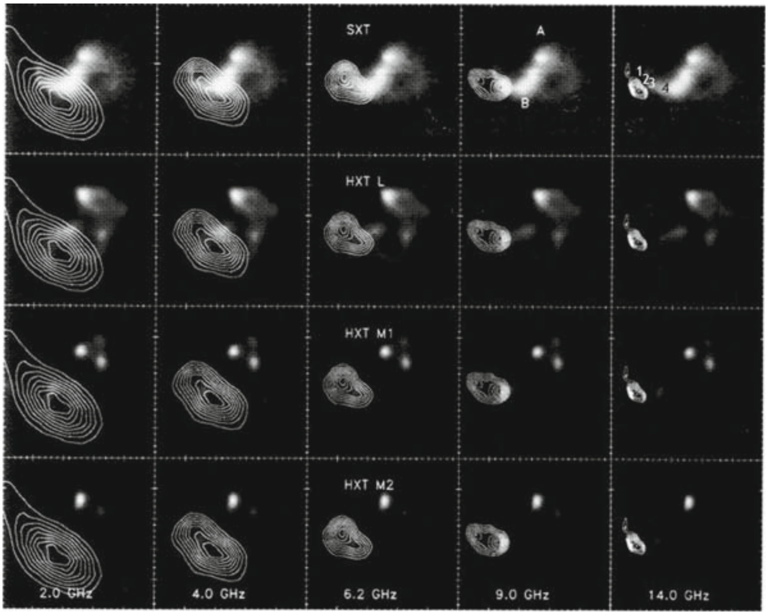


**Fig. 48** Comparisons between X-ray and microwave emissions. The *contours* show the OVRO microwave sources at five frequencies: 2.0, 4.0, 6.2, 9.0 and 14.0 GHz. These contour maps are repeated four times from top to bottom with underlying grey scale images showing YOHKOH X-ray images in four energy channels: SXT and HXR in the L0 (13.9–22.7 keV); M1 (22.7–32.7 keV); M2 (32.7–52.7 keV). The numbers 1, 2, 3, 4 (*top, image on the right*) indicate the location in the SXR loop which corresponds to the location in the microwave source of the spatially resolved spectra shown in Fig. 49 (adapted from Wang et al. 1995)

trum consistent with the one deduced from X-rays. These measurements thus show that microwaves and HXRs are due to the same group of electrons even if the emission sites are separated by $3.5 \times 10^3$ km. Even if the same electrons travel to both footpoints, the stronger magnetic field at one footpoint prevents the electrons to penetrate deep (thus reducing the X-ray emitting efficiency and increasing the radio emitting efficiency). The reverse situation occurs at the other footpoint. This example clearly shows the strength of imaging spectroscopy to better understand electron acceleration and transport in flares. This is one of the direction which should be aimed at in the next future.

At higher frequencies (in the millimetre range),the first observations at 86 GHz obtained with BIMA (Berkeley-Illinois- Millimetre Array) (White and Kundu 1992; Kundu et al. 1994) showed other examples of discrepancies between X-ray and radio emitting electrons. It was indeed found that: (1) the millimetre wave emission which is produced by high energy electrons (above or around 1 MeV) is characterized by an electron spectrum much flatter than the one deduced from HXR observations above a few tens of keV to 100 keV and (2) the high energy population detected at centimetre/millimetre wavelengths is produced in the very beginning of the flare, even if the number of high energy electrons is too small to generate a detectable high energy HXR/GR signature.

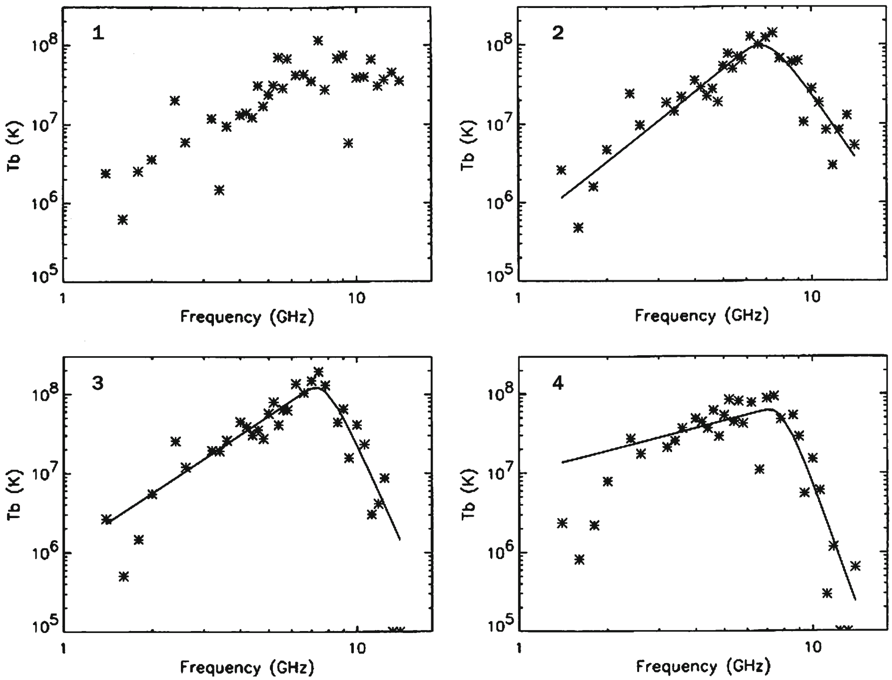


**Fig. 49** Microwave brightness temperature spectra ranging from footpoint (1) to a point well up the loop leg (4) for the same time period as Fig. 48. The *solid lines* show the least-square fits of the spectra. In particular the high frequency slopes for locations 2–4 are, respectively: 5.4, 8.2, and 10.3 (adapted from Wang et al. 1995)

The observations of HXR/GR spectra above a few hundreds keV lead to an improved understanding of the relationship between the spectral information deduced from HXR bremsstrahlung and from gyrosynchrotron emitting electrons. A significant hardening of the HXR photon spectra (and thus of the emitting electron spectra) above a few hundreds keV has indeed been reported in many HXR/GR events observed by SMM, Hinotori (Dennis 1988; Marschhäuser et al. 1994; Yoshimori 1989). A few events observed by PHEBUS/GRANAT with a photon spectrum extending up to 10 or even 100 MeV show a clear hardening of the spectrum at high energies, much greater than what would be expected from the hardening due to changes at high energies in the bremsstrahlung cross sections and electron energy loss rates (Barat et al. 1994; Trottet et al. 1998; Vilmer et al. 1999; Trottet et al. 2000) (Fig. 50). The flattening in photon spectra observed in several flares may thus easily explain why electron spectra deduced from >1 MeV gyrosynchrotron emitting electrons are flatter than the spectra deduced at tens of keV from X-rays. Simple attempts to relate the spectral slopes of bremsstrahlung and synchrotron emitting electrons have shown that the centimetre/millimetre emitting electrons are related to the flat, high energy region of the HXR/gamma-ray spectrum (Trottet et al. 1998, Trottet et al. 2000). This is illustrated here for one event for which significant emission above several hundreds of keV (above 10 MeV for peak d) was observed for several peaks (c to e). The photon

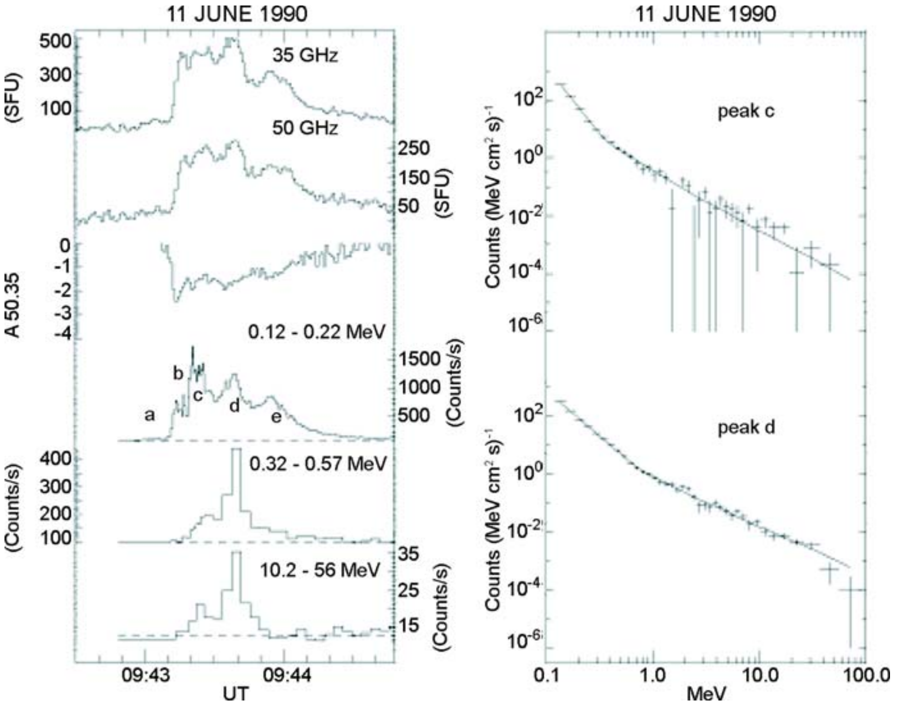


**Fig. 50** *Left panel* from top to bottom Time evolution of the centimetric-millimetric flux density observed by the Bern polarimeters at 35 and 50 GHz, of the power law index derived from the relative fluxes at 35 and 50 GHz and of the HXR/GR flux detected by PHEBUS/GRANAT in three energy bands: 0.12–0.22, 0.32–0.57 and 10.2–56 MeV. *Right panel* Background-subtracted HXR/GR count spectra observed by PHEBUS during peaks c and d. For each spectrum, the solid curve represents the best fit model (adapted from Trottet et al. 1998)

spectra are well represented by a double power law with a clear spectral hardening above a break energy in a range going from 400 to 700 keV. A clear difference of HXR spectral indices deduced below and above the break energy (i.e. in the 100 keV and 1 MeV range, respectively) is observed (between 1.2 and 2.2 depending on peak). The photon spectral index in the MeV range is always around or slightly below -2. The spectral index in the optically thin part of the microwave spectrum a1 (derived from the relative fluxes at 35 and 50 GHz is around -1.5 during peaks b,c,d,e and can be related (see Sect. 4.3.1) to the HXR/GR emitting ones above the energy break, i.e. to the flat part of the spectrum observed at 1 MeV (see Trottet et al. 1998) and not to the HXR spectrum at low energies which is much too steep. During the rise part of the flare (peak a), the values of the microwave indices furthermore show that the high energy component is already produced even if it is too faint to produce a detectable HXR/GR emission. All these results are in good consistency with what was suggested previously by Kundu et al. (1994) from observations with BIMA (see the previous paragraph).

More recent observations combining HXR/GR and microwave spectra have been obtained for the flare of July 23, 2002 observed with RHESSI and NoRH (White et al. 2003). The spectral index of the energetic electrons derived from the optically thin

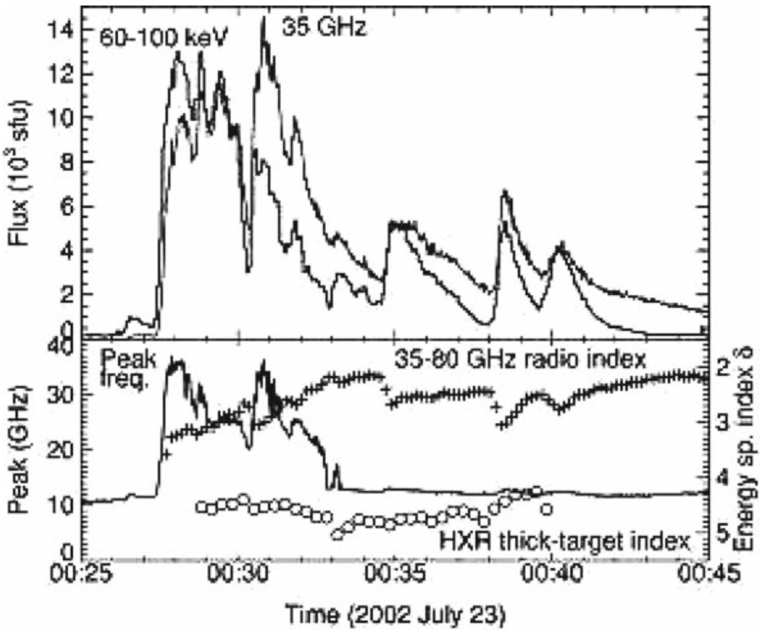


**Fig. 51** *Top panel* Comparison of the RHESSI 60–100 keV HXR light curve and the Nobeyama radio polarimeter 35 GHz light curve. *Bottom panel* Time evolution of the radio spectral peak frequency, of the radio spectral index from 35 to 80 GHz converted to an electron spectral index assuming optically thin gyrosynchrotron emission and of the thick target electron energy index obtained from the RHESSI 100 to 400 keV spectrum (see text for details) (from White et al. 2003)

part of the microwave spectrum (35 to 80 GHz) lies in the range [2,3] and as expected from the previous discussion does not agree with the value derived from the HXR spectrum in the 100–400 keV range plotted as the HXR thick target index (Fig. 51). The HXR/$\gamma$-ray continuum of the event exhibits however, a flattening of the spectrum above 600 keV (see Smith et al. 2003; Share et al. 2003) with a photon slope of 2.2 at high energies. Assuming a thick target model for HXR/GR emissions, this spectrum implies an electron instantaneous number spectrum with a slope $-3.2$ in the case when microwave emitting electrons are partially trapped in the radiating loop (see Ramaty et al. 1994; Trottet et al. 1998). Under these circumstances, the value derived from the high energy photons is roughly consistent with the values inferred from the 35 to 80 GHz index and these observations agree with the conclusion that electron spectra inferred from high-frequency microwave and gamma-ray continuum at high energies are compatible, while the HXR emitting electrons with energies up to a few hundreds keV have steeper spectra.

### 4.4 A new observing window for flares: millimetre to submillimetre observations

Prior to this millennium, few millimetre observations (i.e. frequencies above 100 GHz) of radio bursts had been reported (e.g. Croom 1970) and no submm observations had been performed. However, as shown in the previous section, submillimetre observa-

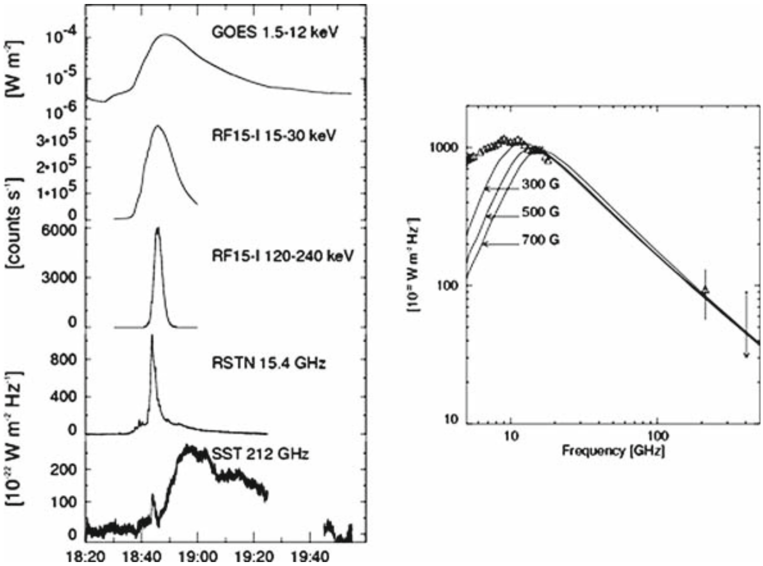


**Fig. 52** *Left panel* from top to bottom, time evolution of the 1.5–12 keV soft X-ray flux observed by GOES, the 15–30 keV and 120–240 keV HXR emission observed by RF15-I on Interball, the 15.4 GHz radio flux density measured by RSTN and the 212 GHz flux density detected by SST. *Right panel* The radio spectrum measured over a 10 s time interval at the impulsive peak maximum (*triangles*). The *solid lines* are theoretical spectra computed for magnetic fields of 300, 500 and 700 G (from Trottet et al. 2002)

tions of solar flares provide diagnostics for analysing the highest energy electrons produced in solar flares. Indeed, if emitted by gyrosynchrotron mechanism, emissions at submillimetre wavelengths must be produced by ultra relativistic electrons ( few MeVs). The first detection of impulsive radio emission at 212 GHz (Trottet et al. 2002) was reported quite recently (Fig. 52). When coupled with the observation of the radio spectrum between a few GHz and 20 GHz, it could be shown that the very high frequency emission results from a population of ultra relativistic electrons with a relatively hard energy spectrum ($\delta = 2.7$) and numbers consistent with what would be observed for a middle size X-ray event above 100 keV (Trottet et al. 2002). A similar conclusion was drawn by Raulin et al. (2004) when analysing another middle-size X-ray event for which observations at 200 and 400 GHz were obtained together with HXR and gamma-ray observations above 6 MeV (Fig. 53). It was found that around $5 \times 10^{36}$ accelerated ($\geq$20 keV) electrons per second with a spectral index $\delta \sim 3$ radiating in a region with a magnetic field of $10^3$ G could easily explain the millimetre to submillimetre-wave emissions at least during the main phase of the flare showing that synchrotron emission is the dominant radiation mechanism. However, in the early phase of the event, the submillimetre emission does not look as a simple extension of the microwave spectrum, since the flux seems to rise slowly from 200 to 400 GHz (Fig. 53, right panel).

The existence of a new radio component at high frequencies was in fact highlighted by the almost simultaneous observations of large flares by two teams: the X28 and X17 flares on November 4, 2003 and October 28, 2003 were indeed measured, respectively,

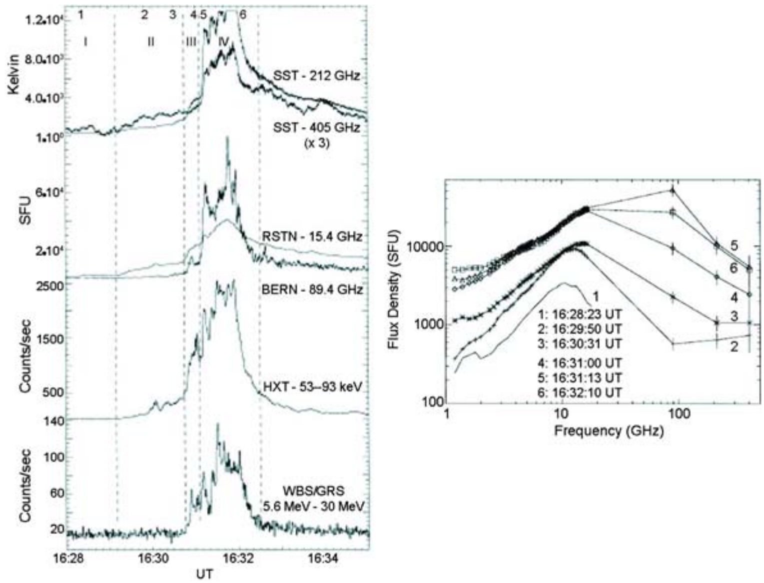


**Fig. 53** *Left panel* Multifrequency time profiles. *From top to bottom* 405, 212 GHz antenna temperatures (K); 89.4, 15.4 GHz total flux densities (sfu); hard X-ray count rates in the 53–93 keV channel and $\gamma$-ray count rate above 5.6 MeV. *Numbers 1–6* on top indicate times of the spectra plotted on the right figure. *Right panel* Radio spectra at different times as observed with OVSO, RSTN, Bern and SST (from Raulin et al. 2004)

by the SST (Solar Submillimetre Telescope) at El Leoncito in Argentina (Kaufmann et al. 2004) and the Koln Observatory for Submillimetre and Millimetre Astronomy (KOSMA) at Gornergrat in Switzerland (Lüthi et al. 2004a,b). For these two large flares, the new spectral component is clearly observed at high frequencies and is characterized by a strong increase of the radio flux from 200 to 400 GHz (Fig. 54). Very similar solar burst components have now been identified for other large flares observed by SST (Silva et al. 2007; Kaufmann et al. 2007). The spectral up-turn seen at high frequencies is found to be inconsistent with an optically thin thermal source which would imply an unbelievably huge soft X-ray event (Kaufmann and Raulin 2006), as well as with the high frequency extension of the optically thin gyrosynchrotron emission of energetic electrons observed below 100 GHz. The origin of this radiation is still under discussion. If of thermal origin, the emission is likely to be produced in deep atmospheric layers (Ohki and Hudson 1975). In the case of non-thermal emissions, the 200 GHz emission may arise from optically-thick synchrotron emission from relativistic electrons in a source different from the one emitting at low frequencies, free–free emission from the chromosphere due to energy deposited by electrons or protons or by synchrotron emission from pion-decay positrons. This last process described a long time ago by Lingenfelter and Ramaty (1967) could be reconsidered for the high frequency observations given the possible observations of $\pi_0$ decay high energy $\gamma$-rays from some of the flares showing a spectral increase above 200 GHz (Myagkova et al. 2004; Silva et al. 2007). As proposed by Kaufmann and Raulin (2006), the processes producing bright broadband coherent synchrotron radiation bursts in laboratory accel-

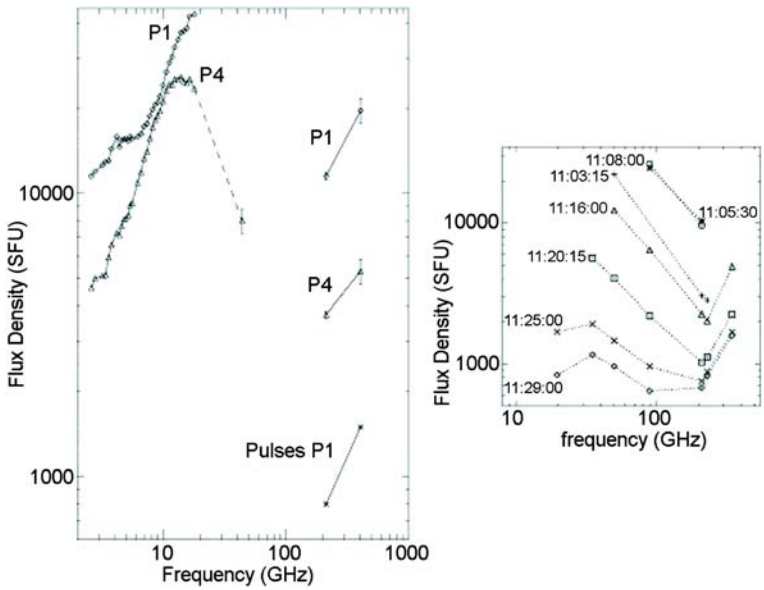


**Fig. 54** *Left panel* Spectra of radio pulses from 1.2 to 405 GHz showing two distinct components: the gyrosynchrotron source at microwaves observed by OVSA between 1.2 and 18 GHz and the new component observed at 212 and 405 GHz with SST (from Kaufmann et al. 2004). *Right panel* Temporal evolution of the radio spectrum between 19.6 and 345 GHz observed with the Bumishus patrol instruments and KOSMA for another flare (from Lüthi et al. 2004b)

erators could also happen in flares and provide a plausible explanation to the simultaneous observations of the microwave and submillimetre components. In such a context, the submillimetre component (200 GHz) is produced by incoherent synchrotron radiation and is the optically thick-part of a component with a peak frequency in the THz range. Beam density perturbations of the same electron population set microbunch instabilities and produce intense coherent synchrotron radiation at lower frequencies (see Kaufmann and Raulin 2006). Other possibilities linked to coherent emission mechanisms is that the submillimetre emission be produced coherently by beams of relativistic electrons accelerated downwards in dense regions (Sakai et al. 2006).

The major limitation for the understanding of this new component is in fact the poor knowledge of the flare spectrum for three frequency decades: i.e. from 400 GHz (the highest frequency observed so far) to the near IR (300 THz or 1 μ). This is the reason why the Solar Submillimetre Telescope (SST) is now being upgraded to perform observations at 850 GHz and in the mid- infrared region (43–21.5 THz or 7–14 μ). To complement the results obtained at submillimetre wavelengths, a new set-up has also been developed to observe solar activity in the mid-IR region (30 THz or 10 μ). Mid-IR small flares were detected with a surprisingly high intensity (80,000 sfu) in correspondence with relatively weak soft-X-ray bursts (Melo et al. 2006). A new concept for space observations (DESIR on the SMESE project) has also been proposed to carry submm/far IR observations (2 and 8.6 THz) to make complementary observations of the new component in the THz domain and in order to further investigate its origin (Molodij and Trottet 2005; Trottet et al. 2006).

## 5 Evidence for reconnection and current sheets during eruptive events

In this section, the term "eruptive event" corresponds to all kinds of transient events involving mass motion, whether or not associated with a flare.

### 5.1 Observational input of the radio and X-ray data

Many signatures of eruptive phenomena observed nowadays are consistent with the concept of magnetic reconnection. However, the role played by magnetic reconnection in the onset of these events and/or in the magnetic restructuring occurring during their development is far from being properly understood. As recalled in Sect. 2.2.1, the early imaging observations made at 80 MHz with the Culgoora Radioheliograph contained already some of the ingredients supporting the present reconnection models for eruptive events. Several evidences for reconnection and current sheets deduced from flare events were presented in Sect. 4. We recall here some of these observations. While in Sect. 4, emphasis was put on the origin and on the production of non-thermal electrons, we focus here on the input of these observations to the understanding of mass motions at all scales (ejecta, CMEs...).

Observations of pairs of type III and reverse type III bursts (see Fig. 29 in Sect. 4.1.1) provide strong support to the production of non-thermal electron beams in cusp reconnection sites. Electron beams are also found to follow various coronal magnetic field lines which diverge from interaction sites located between magnetic structures at different scales (see Figs. 38, 44 derived from metric/decimetric and microwave radio observations). X-ray observations of solar eruptive phenomena provide many results that bring additional support to flare models involving magnetic reconnection. For instance, Masuda et al. (1994) and Masuda et al. (1995) discovered in some impulsive events observed at the limb compact HXR sources above the soft X-ray flare loop. This also suggests that energy release occurs in a reconnection cusp region. Reconnection models in flares were also supported by observations of soft X-ray ejecta (see references in Ohyama and Shibata 1998). Finally, observations of soft X-ray arcades (usually called post-flare loops) which form and grow in the aftermath of eruptions, were interpreted as signatures of magnetic reconnection occurring progressively at higher and higher altitudes.

All these observations fit well within "standard" eruptive and flare models such as the ones schematically described in Fig. 55 from (Schwenn et al. 2006a) and derived from the model of Lin and Forbes (2000). In this classical reconnection model, an initial, close and stressed magnetic configuration becomes unstable and erupts. Magnetic field lines are then stretched by the eruption and a current sheet is formed above the photospheric magnetic inversion line, behind the eruption of the flux rope. Then, magnetic reconnection occurs along this current sheet, first at low altitude then at progressively higher ones (see Forbes 1996). It should be noted that the diagram of a flare model derived from radio observations and presented in Sect. 4.1.1 (Fig. 29) can be easily related to this "standard" model, the acceleration site of Fig. 29 being located in the region of the current sheet (see also Fig. 63).

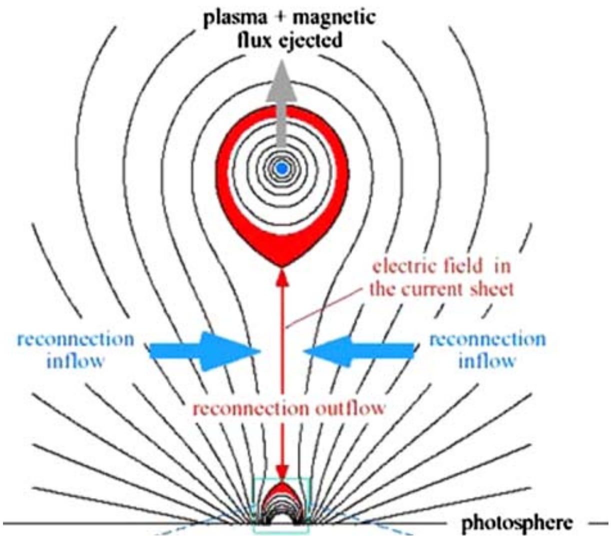


**Fig. 55** Sketch of the flux rope/CME model of Lin and Forbes (2000) showing the eruption of the flux rope, the current sheet formed behind it, and the postflare/CME loops below as well as the inflows and outflows associated with the reconnection (from Schwenn et al. 2006a)

More recently, RHESSI observations have given new evidences of magnetic reconnection in flares attributed to the formation of current sheets (see in Sect. 4.1.1, Fig. 30, and Sui and Holman 2003; Sui et al. 2004). Furthermore, Sui et al. (2005) reported the observations at 34 GHz with the NoRH of a cusp structure seen approximatively at the same time as the peak flare emission, further supporting this model. Figure 56 shows height versus time plots of the loop-top and of the coronal source described in Sect. 4.1.1 (Fig. 30). While the coronal source (interpreted as the upper anchor of the current sheet) initially remains stationary, the loop-top source initially moves downward (see another example in Veronig et al. 2006). This first downward motion seems to contradict the reconnection models (see. e.g. Forbes 2000) which directly associate the energy release with a plasmoid eruption. Conversely, this observation could be consistent with the need to extract energy from the coronal magnetic field (see Hudson 2000). After the main flare phase, it is interesting to note that both coronal and loop-top X-ray sources move upwards with speeds around 300 km s$^{-1}$. This can be related to the kinetic evolution of CMEs (see Sect. 6.2)

## 5.2 Magnetic reconnection, electron acceleration in connection with jets and plasmoids

As recalled in the previous section, soft X-ray ejecta supporting reconnection models in flares have been observed. It was shown, e.g. by Kundu et al. 1995 that these ejections of hot plasma (jets) are also associated with the production of electron beams which generate type III bursts. The radio locations at different frequencies, e.g. 236.6 and 164 MHz, are observed to be aligned along the length of the jet. These observations

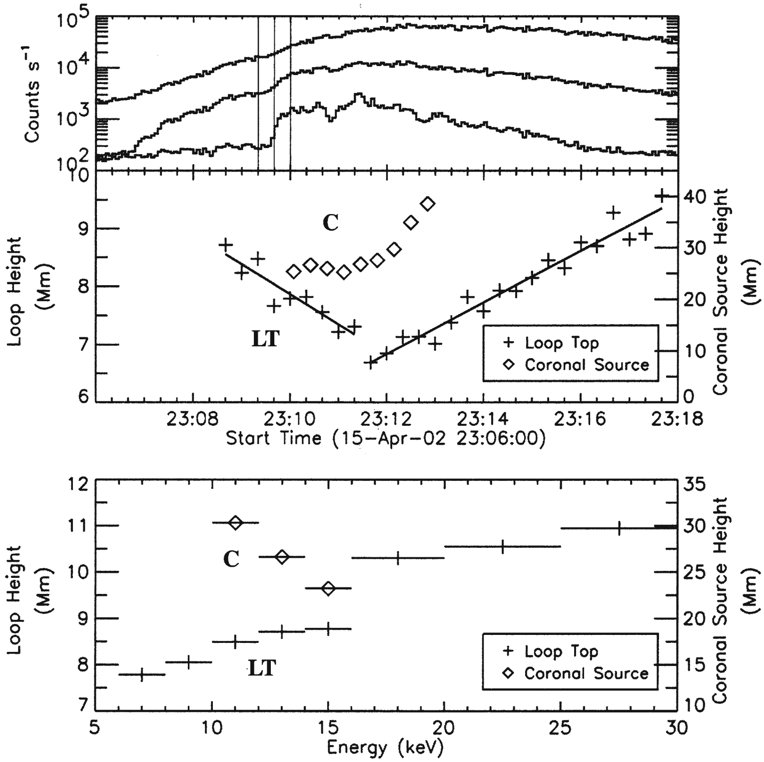


**Fig. 56** *Top panel* RHESSI light curves in three energy bands *(from top to bottom)*: 3–12, 12–25, and 25–50 keV. To avoid overlap, the *light curves* are scaled by 2.0, 0.5, and 1.0, respectively. *Middle panel* Time history of the loop height (obtained from the 10 to 12 keV images) and of the coronal source height (obtained from the 10 to 25 keV images) (see Fig. 30 for the definition of coronal and loop-top sources). The *solid lines* are linear fits. *Bottom panel* Height of the loop and of the coronal source at different energies at 23:11:00 UT. The *horizontal bars* represent the energy bandwidths of the RHESSI images (from Sui and Holman 2003)

imply that jets are associated with the acceleration of electrons up to several tens of keV together with the heating responsible to the soft X-ray emission.

SXR plasmoids with speeds in the range 100–200 km s$^{-1}$ may also drive radio emissions in the decimetric/metric domain. These are the slowly drifting radio features which have been mainly observed in the 2–0.6 GHz range (see, e.g. Karlický and Odstrcil 1994; Hori 1999; Kliem et al. 2000; Karlický et al. 2002; Karlický 2004) and sometimes below 0.6 GHz (Khan et al. 2002). As discussed below, they can be interpreted as radio emissions originating from electron beams accelerated in the magnetic reconnection volume and injected into magnetic islands (plasmoids) (see Karlický and Bárta 2005). As an example, Fig. 57 shows observations at decimetric wavelengths (e.g. 2–0.6 GHz) of long series of quasi-periodic pulsations which deeply modulate non-thermal radio continua slowly drifting towards lower frequencies. The narrow frequency band of these pulsations and the observed small frequency drift at a rate of 3 MHz s$^{-1}$ suggest that the burst emission originates either from the plasmoid

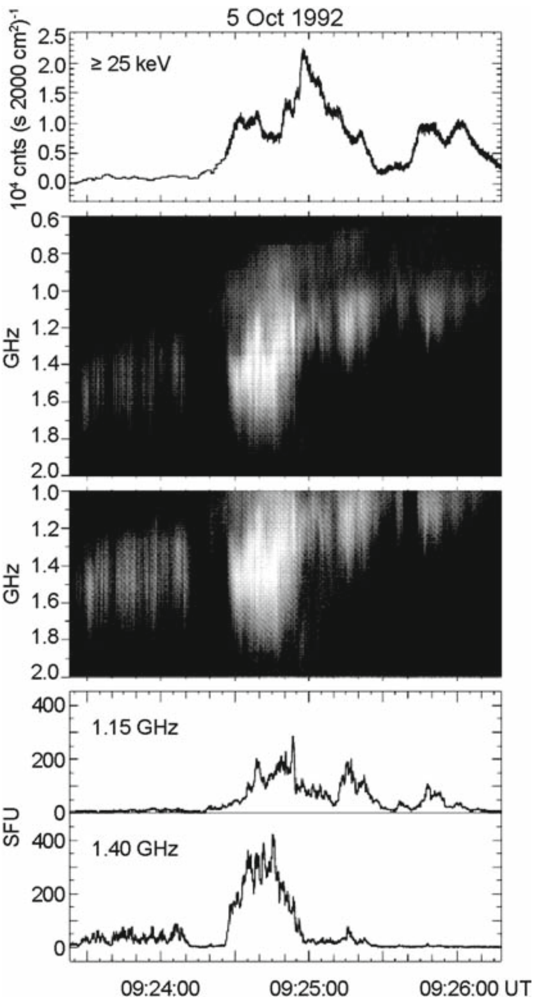


**Fig. 57** *Top panel* The hard X-ray light curve of the October 5, 1992 flare (BATSE data). *2nd and 3rd panels*, respectively, the dynamic radio spectrum (Zurich and Ondrejov radiospectrographs, respectively). *Bottom panel* Two single-frequency cuts of the dynamic spectrum. The Ondrejov spectrum contains a gap of ≈6 s at 09:25:38 UT (from Kliem et al. 2000)

itself or from dense plasmoid-like structures in the current sheet. The frequency drift is then interpreted as being due to the ejection and to the further expansion of the plasmoid at a higher altitude (leading to a decreasing density in the plasmoid). Kliem et al. (2000) proposed that the pulsations of the radio flux are caused by a quasi-periodic particle acceleration resulting from a dynamic phase of magnetic reconnection in the current sheet lying above the soft X-ray loop. This process involves the repeated formation of magnetic islands, their subsequent coalescence occurring on small scales in the current sheet, while the formation and the growth of a large scale plasmoid is fed by the repeated coalescence of islands. Bursts of accelerated electrons are produced with the formation of new magnetic islands. This unified explanation of plasmoid formation and electron acceleration agrees with the ideas of Ohyama and Shibata (1998). These authors concluded from the observations of soft X-ray ejecta that the current sheet

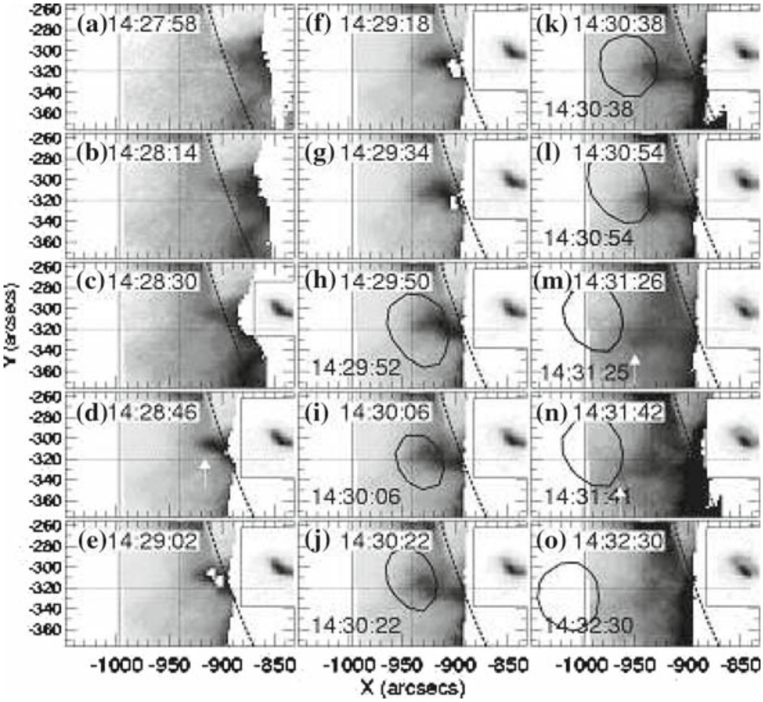


**Fig. 58** August 25, 2000 event: A sequence of SXT (composite) images showing the simultaneous evolution of the soft X-ray ejecta and of the NRH 327.0 MHz sources (indicated by the 90% contour level in each radio image) before and during the drifting pulsation structure. The solar limb is indicated by the *thick dashed black line* in each image. The SXT images inside the *box/inset* show the flare kernel region (from Khan et al. 2002)

was not formed by the ejection of the plasmoid. They rather proposed that the current sheet could be due to either the formation (or acceleration) of the plasmoid within a pre-existing current sheet or to the simultaneous formation of both structures by a global MHD instability.

A comparison between the locations of the source of the radio pulsating and drifting structures and of the SXR plasmoid has been performed by Khan et al. (2002) for a case where the drifting pulsating structure was seen below 500 MHz and could thus be imaged by the NRH. Figure 58 shows that the radio sources of the drifting pulsation structure move outward in close connection with the soft X-ray ejecta. This strongly suggests that the electron acceleration is linked to the ejection of the plasmoid and that the radio emission originates from inside the plasmoid or in its close vicinity. These results are another support of the unified explanation proposed by Kliem et al. (2000).

Propagation of X-ray plasmoids to high altitudes can also produce electron acceleration in the corona on longer time scales. These accelerated electrons can be detected as wide band decimetric-metric radio continua occurring after the main phase of the flare observed in HXRs (e.g. Kundu et al. 2001). This is exemplified in Fig. 59: the timing of the continuum emission, as well as the location of the 410 MHz source (close to the altitude at which the plasmoid was last identified in the SXT images), suggest a strong

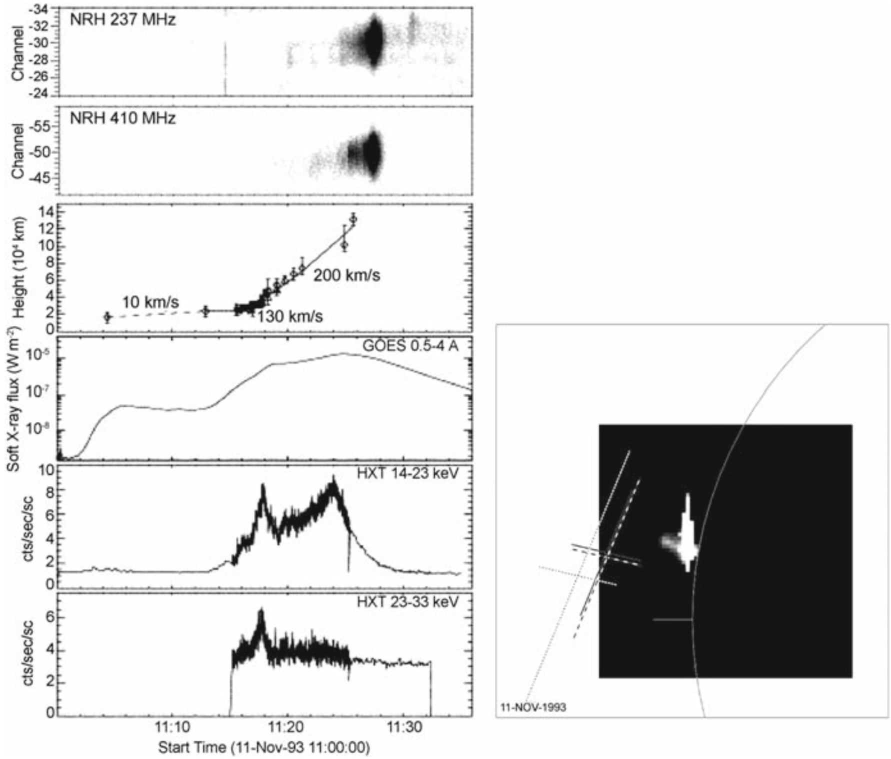


**Fig. 59** *Left panel* Time evolution of the November 11, 1993 event. *(Top panel)*: Grey-scale representation of the one-dimensional brightness distribution as a function of time and of position observed at 237 MHz near the eastern solar limb by the NRH. The *vertical axis* denotes distance from the disk centre (located in channel 0) along the terrestrial east-west direction (*east is up*). Integration time is 10 s. *(Second panel)*: Same as top panel at 410 MHz. *(Third panel)*: Height of the plasmoid ejecta as a function of time (data taken from SXT). *Fourth to sixth panels* The soft X-ray time profile from GOES and the hard X-ray time profiles from YOHKOH/HXT in the 14-23 and 23-33 keV energy ranges, from Ohyama and Shibata 1998). *Right panel* SXT partial frame image observed at 11:18:19 UT; centroid positions and half-widths of the radio sources as measured at 11:27:24 UT at 410 MHz *(solid line)* and 327 MHz are superposed in the image (from Kundu et al. 2001)

relationship between the propagation of the plasmoid and the late acceleration of radio emitting electrons. As the plasmoid moves to higher and higher altitudes, its interaction with more and more extended magnetic field lines may create new coronal sites for the production of non-thermal electrons. It must finally be recalled that much faster SXR ejecta or rising loops (700–900 $\mathrm{km\,s^{-1}}$) may drive large-scale coronal shocks seen as radio type II bursts (Gopalswamy et al. 1997; Klein et al. 1999) and starting sometimes at unusually high frequencies (Dauphin et al. 2006) (see also Sect. 7).

## 5.3 X-ray and radio signatures of magnetic reconnection behind eruptive flux ropes

Joint spectral and radio imaging observations at multiple frequencies may provide direct evidence and also constraints on the formation of reconnecting current sheets

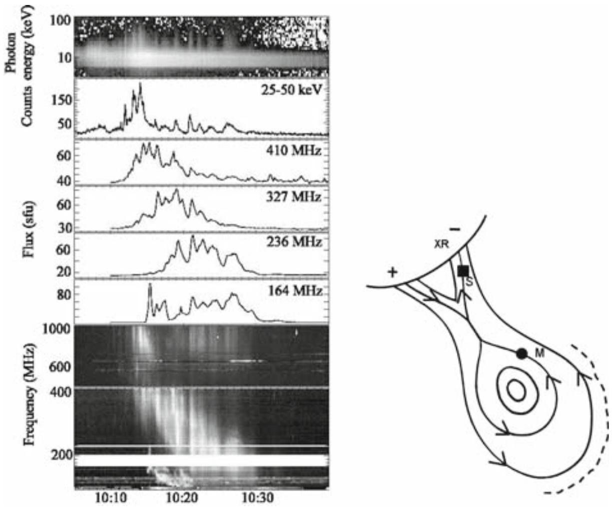


**Fig. 60** June 02, 2002 event: *Left panel* Comparison between the photon histories measured by RHESSI (*two top panels*), the flux evolution measured at four frequencies by the NRH (*middle four panels*), and the spectral evolution measured by OSRA and by WAVES (bottom panels). *Right panel* Two-dimensional sketch of the magnetic configuration involved in the eruption. A twisted flux rope erupts, driving magnetic reconnection behind it. The particles accelerated in the reconnection region propagate along the reconnected field lines, giving the observed hard X-rays (XR) and the main radio sources (S and M), which correspond to the quasi-stationary sources and moving sources (see text). A shock is propagating at the front edge of the flux rope (*dashed line*) (from Pick et al. 2005a)

behind ejected flux ropes. As an example, Fig. 60 Left, shows a long duration broad band continuum (type IV burst) drifting towards lower frequencies. This continuum is modulated by successive packets of fast sporadic bursts in close temporal coincidences with HXR peaks (Claßen et al. 2003, Pick et al. 2005a). The continuum emission originates from two sources: a fast-moving one with a mean projected speed around 400 km s$^{-1}$ and a quasi-stationary one (drift of 170 km s$^{-1}$ at 410 MHz). Both stationary and moving sources are located along the northern edge of an ascending EIT arch overlying the flare (speed of 540 km s$^{-1}$). The time coincidence found between the peak flux of the moving source and of the underlying stationary and HXR sources detected by RHESSI implies a causal link: the source of the accelerated electrons producing radio and X-ray emissions is the same. Such observations are consistent with an erupting twisted flux rope with the formation of a current sheet behind. The accelerated electrons form beams along the newly reconnected field lines and propagate both upward and downward. The moving and the stationary radio sources are located on each side of the current sheet (Pick et al. 2005a). A schematic two-dimensional view of this evolution is outlined in Fig. 60, right panel. A similar conclusion was reached by Dauphin et al. (2005), Dauphin et al. (2006) for the November 3, 2003 flare: broad-band modulations were simultaneously observed in X-rays and at radio wavelengths, from 300 MHz to several tens of GHz, during the late phase of this event. Particle acceleration giving rise to HXR and radio modulations occurs at the reconnection sites triggered in the current sheets behind the eruptive flux rope.

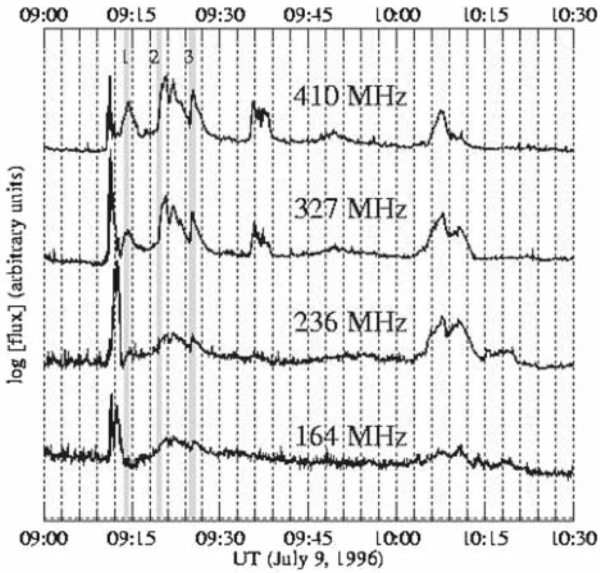


**Fig. 61** July 9, 1996 event: Time evolution of the radio flux at distinct frequencies. The *grey bars* correspond to selected periods for which the spatial maps of the successive emitting radio sources are displayed in Fig. 62 (Pick et al. 1998)

Multiwavelength radio imaging observations have thus the capability of following the evolution of a reconnecting current sheet behind an ejected flux rope over an altitude range not accessible by X-ray observations.

## 5.4 Reconnection sites and interacting coronal loops

Signatures of coronal loop interactions leading to repetitive electron acceleration processes are found during long lasting continua. As an example, Fig. 61 displays the time evolution of a radio event which occurred on July 9, 1996. Two sequences may be distinguished: after a first outburst which ends at about 09:13 UT, a long duration continuum is observed in the whole spectral range of the NRH (432–150 MHz). This continuum exhibits two major series of sudden flux enhancements at all frequencies. Figure 62 displays the temporal evolution of the location of the emitting regions, with an integration time of 5 s, during selected periods indicated by thick grey bars and numbers in the left panel. Two emitting sources are first detected and remain detectable until the end of the flare. In coincidence with each sudden flux enhancement, a strong modification of the radio sources is observed at all frequencies. It is characterized by the appearance of a new component between the two pre-existing components with an east west orientation almost perpendicular to the former structure. During the first enhancement, this component appears first at 410 MHz then at 327 MHz. and is immediately followed by a strong change of the emitting region at these two frequencies. The same scenario repeats at each enhancement. The topology and the evolution of the emitting sources strongly suggest successive interactions between rising arches and

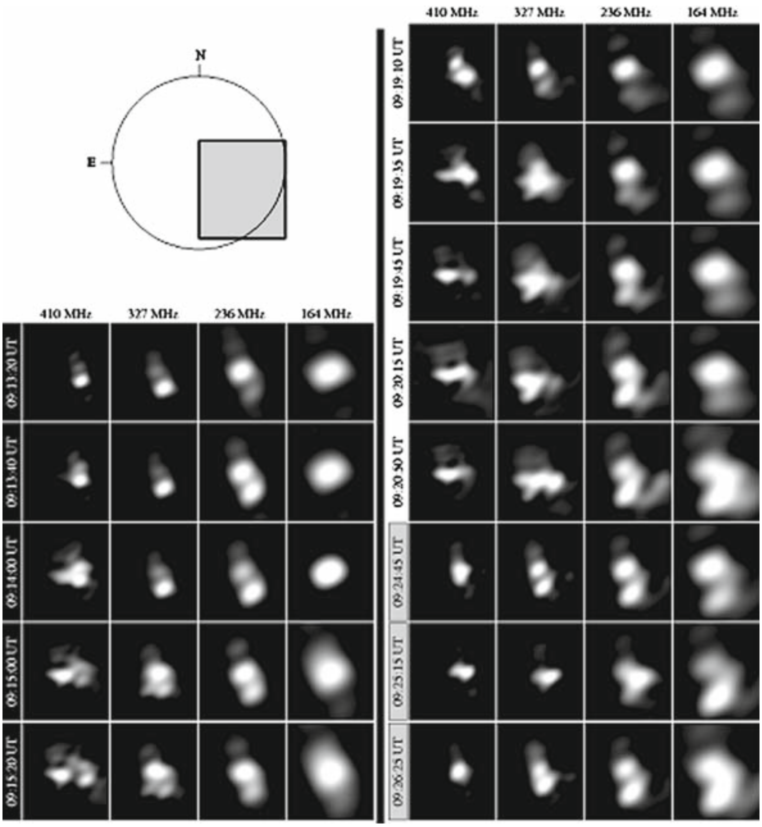


**Fig. 62** July 9, 1996 event: Spatial evolution of the successive radio-emitting sources observed at all frequencies during the development of the radio continuum after 09:12 UT. The selected periods are indicated in Fig. 61 by *grey bars* (from Pick et al. 1998)

other loops. The electrons responsible for the flux enhancements could be the result of these magnetic interactions (Pick et al. 1998).

## 6 Coronal mass ejections

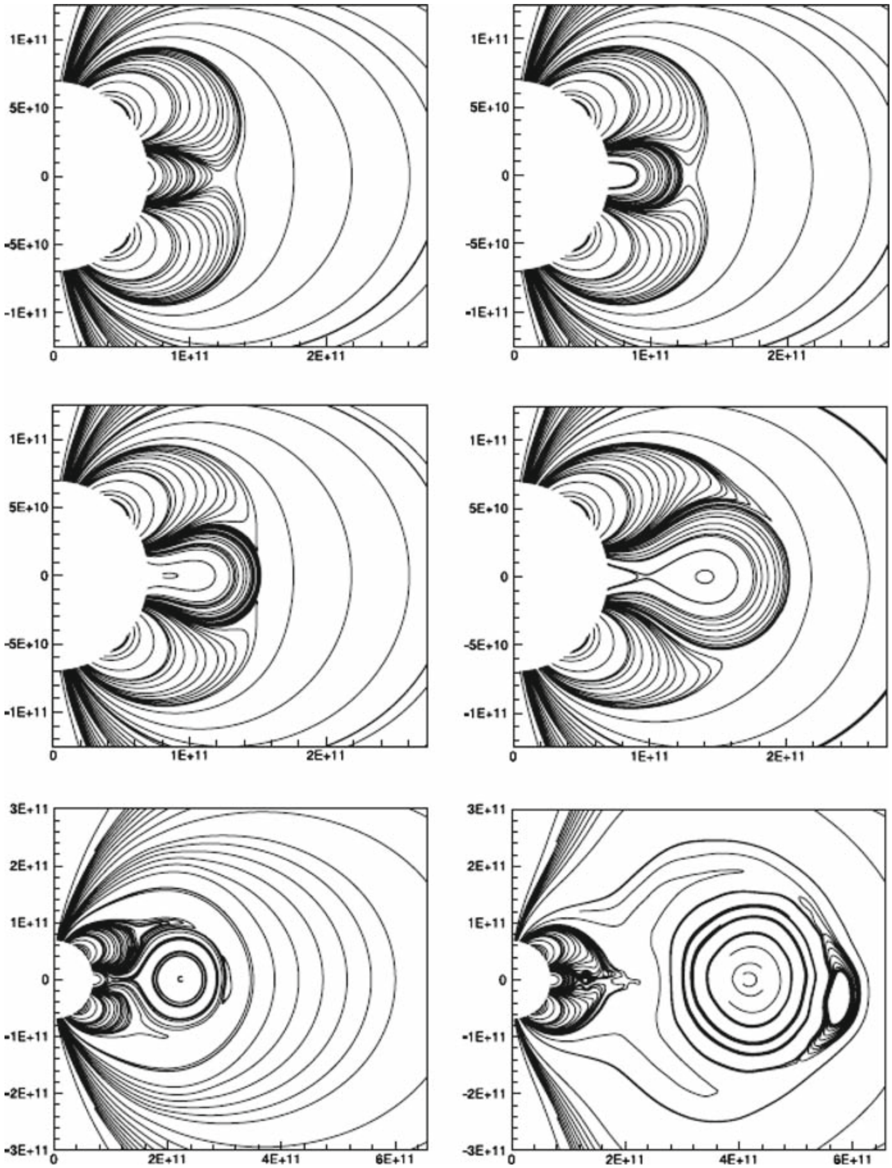


**Fig. 63** Snapshots of selected field lines in the inner region of the numerical simulation of the break-out model for Coronal Mass Ejections. Snapshot times are, from left to right and top to bottom 0, 50251, 70680, 79008, 85185, and 95020 s, respectively. The spatial scale in the last two frames is expanded in the last two frames to best show the expanding flux rope (from MacNeice et al. 2004)

## 6.1 Introduction

Since their discovery (Tousey 1973), CMEs have been observed by many ground-based and space-borne white light coronagraphs that have enabled to analyse their basic properties. Several large CMEs, called halo CMEs because they surround the occulting disk like a halo, have also been observed by the white-light coronagraph, Solwind on the satellite P78-1 (Howard et al. 1982). Since 1996, CME observations have been made with the very sensitive SOHO/LASCO instrument (Large Angular Spectrometric Coronagraph) which consists of several coronographs. These observations also combined with the ones from other instruments have, for the first time, made possible to continuously follow the detailed progression of CMEs and related phenomena from the low corona to the interplanetary medium (see for reviews Kunow et al. 2006). Joint multi-wavelength observations have led to a better understanding of how the interplay between different spatial scales contributes to the CME initiation, development and propagation. However, this investigation is difficult when using only imaging space-borne instruments because of their limited time-cadence. This is one of the area where the mission STEREO will bring new observational input, given the higher cadence of its observations and where previously only radio observations could contribute significantly. Indeed, radio telescopes can observe, with a high cadence ($<1$ s), emissions from both the solar disk and above the solar limb out to a few solar radii. Radio observations are sensitive to different aspects of CMEs depending on the selected wavelength domain (Pick et al. 2006b).

The CME speeds range from a few tens up to $2 \times 10^3\,\mathrm{km\,s^{-1}}$. It is well known that CMEs are often associated with eruptive prominences (EP) or with the disappearance of filaments on the solar disk. In that case, CMEs contain three distinct regions: a bright core, surrounded by a dark cavity, surrounded itself by a bright compression front. The bright core is formed by the material ejected from the cool ($8 \times 10^3$ K) and dense ($\sim 10^{10}$ to $10^{11}\,\mathrm{cm^{-3}}$) prominence. CMEs have frequently a much more complex structure than the one just described; they may indeed involve multiple magnetic flux systems and neutral lines. Fast CMEs are also often associated with flares.

## 6.2 Kinetic evolution of CMEs

### *6.2.1 Input of UV, X-ray and microwave radio observations*

It has been speculated that CMEs may be classified into two distinct classes: gradual CMEs and impulsive CMEs. The acceleration in the inner corona can vary by three orders of magnitude (from a few $\mathrm{m\,s^{-2}}$ to several thousand $\mathrm{m\,s^{-2}}$). The gradual CMEs have a weak ($<20\,\mathrm{m\,s^{-2}}$) acceleration which can persist during several hours. Their velocity is usually slower than $100\,\mathrm{km\,s^{-1}}$ in the inner corona, i. e. below 2 $R_\odot$ (e.g. Sheeley et al. 1999; Srivastava et al. 1999a). CMEs associated with EP are, in the absence of flares, mostly gradual events. On the contrary, impulsive CMEs, which are associated with flares, have a short duration but are subjected to a strong acceleration in the low corona; after the acceleration phase, they propagate with constant speeds that are frequently faster than the ones for EP/CMEs.

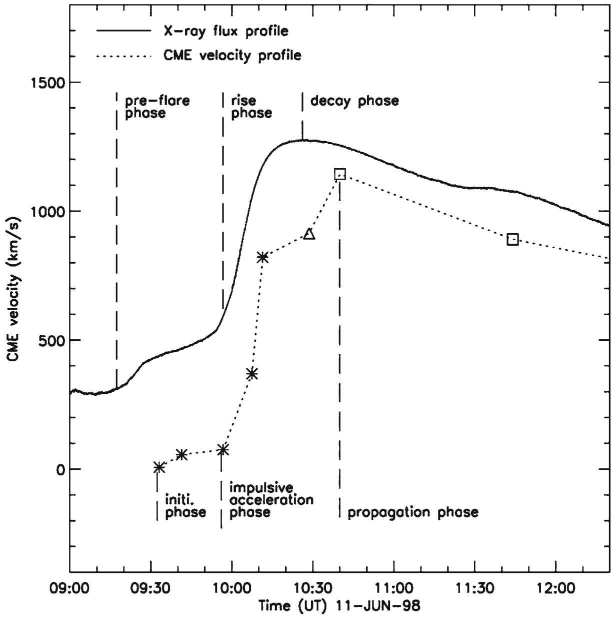


**Fig. 64** June 11, 1998 event. Illustration of three phases of the CME velocity-time profile (*dotted line*) and the flare soft X-ray flux temporal profile (*solid line*) for the event on June 11, 1998. Note that the CME impulsive acceleration phase coincides well with the flare rise phase (from Zhang et al. 2001)

The development in the corona of some large flare/CME events suggests that at the origin of the CME, there is a large-scale coronal structure which undergoes a quasi-static evolution and reaches a critical point at which a violent magnetic energy release occurs, possibly triggered by magnetic reconnection (see Forbes and Priest 1995, and the discussion in Sect. 5.1). Alternatively, as in the break-out model (Antiochos et al. 1999), the eruption can be triggered by reconnection, occurring above the stressed magnetic configuration, between a sheared arcade and the neighbouring larger scale flux system. This last model requires a more complex magnetic configuration (at least topologically equivalent to a 2D quadrupole) as well as an increasing magnetic stress. The region with growing magnetic stress expands, then builds a current sheet with the overlying, oppositely directed, stabilising field. When reconnection starts at a significant rate, the eruption of the underlying stressed field is triggered (see Fig. 63). Results of numerical studies of the breakout model show that the plasmoid ejection occurs at the speed of the coronal Alfven speed and that the breakout model can produce fast CMEs (MacNeice et al. 2004). The evolution of posteruptive flare loops can also be explained in this model (Lynch et al. 2004).

Soft X-rays and microwave imaging observations are useful for investigating the pre-eruptive and eruptive scenarios of a CME. The bright core and the prominence materials are in particular optically thick at microwave frequencies.

Based on the velocity profiles of CMEs, Zhang et al. (2001) described the kinematic evolution of flare-associated CMEs by a three-phase scenario: initiation, acceleration and propagation (see also Neupert et al. 2001). One example is shown in Fig. 64. The

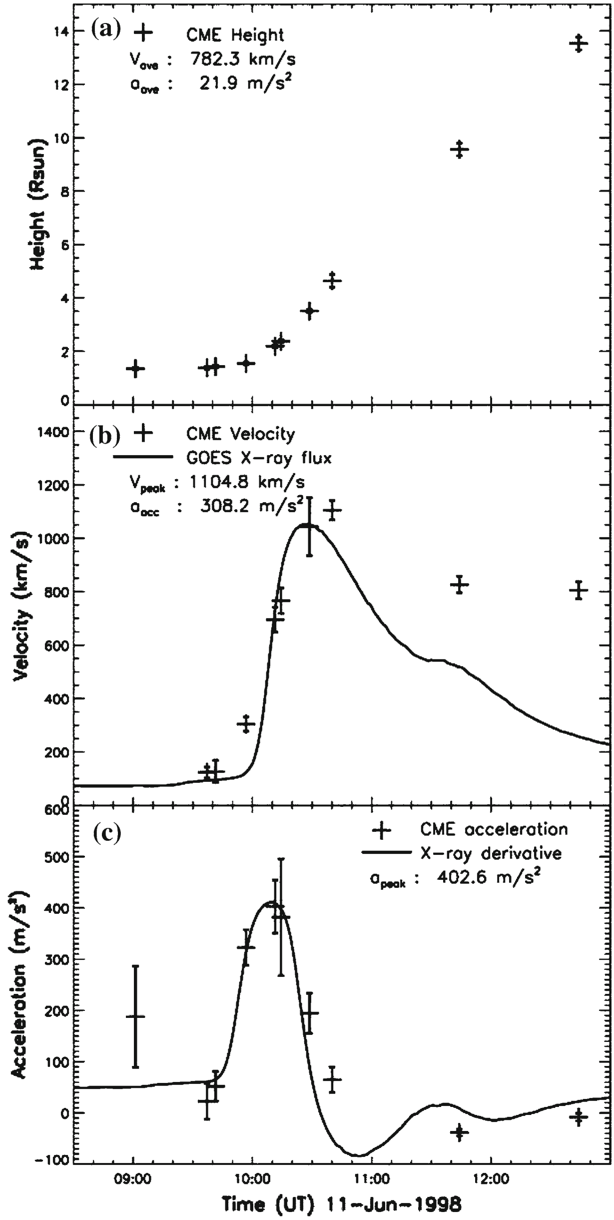


**Fig. 65** Kinematic plots for the June 11, 1998 CME: **a** height versus time, **b** velocity versus time, and **c** acceleration versus time. The CME parameters are indicated by *plus signs* with error bars. The *solid curves* in **b** and **c** are the GOES X-ray profile and the derivative of the X-ray profile, respectively (from Zhang et al. 2004)

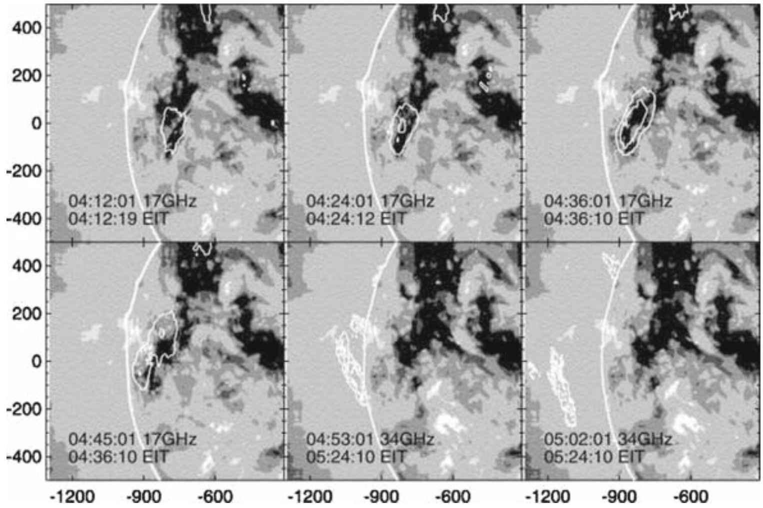


**Fig. 66** November 17, 2001: Overlays of contours of the NoRH radio images on the EIT 195 Å images demonstrating the motion of the filament against the disk and its continuation in the radio images above the limb. The erupting filament is seen as a dark feature in the EIT images until the last EIT image, at 05:24, before the data gap. The first four radio images, in which the filament is seen as a depression of radio emission in projection against the bright disk, are 17 GHz images, while the last two radio images are at 34 GHz, where the material above the limb emits with a brightness temperature of order $9 \times 10^3 - 12 \times 10^3$ K above the dark background (from Kundu et al. 2004)

initiation phase occurs before the rapid and large onset of the associated flare observed in soft X-rays, lasts for some tens of minutes and is characterized by a slow ascension of the CME in the low corona ($\sim$1–3 $R_\odot$). The rapid acceleration of CMEs ceases before the peak time of soft X-ray flares. The propagation phase is characterized by a constant or slowly decreasing speed. During the acceleration phase, there is a close temporal association between the CME velocity and the soft X-ray flux of the flare, and thus between the CME acceleration and the derivative of the soft X-ray flux (which is often used as a proxy of the HXR flux: the "Neupert effect", (Neupert 1968)). This is illustrated in Figs. 64 and 65, respectively. Zhang et al. (2004) concluded from this last association that the CME acceleration and the flare particle acceleration phases are strongly coupled.

The detection of rising UV and soft X-ray loops in the low corona and at the onset of CMEs by Gallagher et al. (2003) and Dauphin et al. (2006) provides further arguments in favour of an association between the CME acceleration and the particle acceleration phases. Figure 68 from Gallagher et al. (2003) shows the height, velocity and acceleration time profiles of the rising UV loops and of the CME. The time development of the UV structure is consistent with the three component kinematic evolution of flare-CME events. Dauphin et al. (2006) also found a good temporal association between the acceleration phase of a soft X-ray rising loop and the HXR emission observed by RHESSI above 150 keV (see also Fig. 87 in Sect. 7).

Microwave observations provide other tools to confirm that the CME acceleration and flare particle acceleration phases are strongly coupled (Kundu et al. 2004). Using

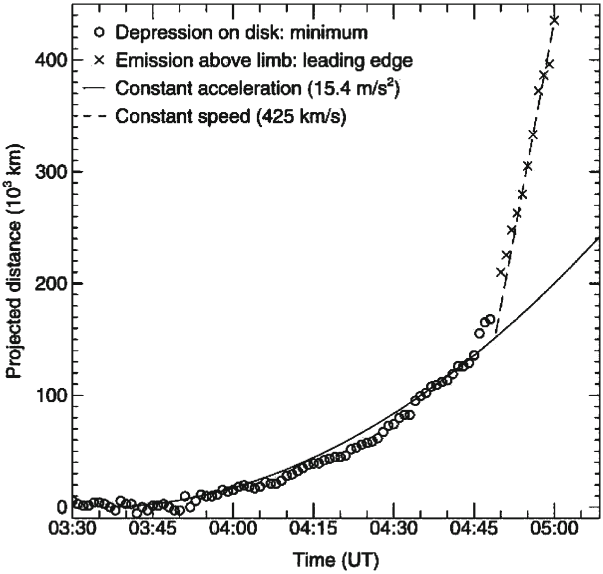


**Fig. 67** November 17, 2001: Motion of the erupting filament from NoRH 34 GHz data. The *circles* show the position of the depression minimum when the filament was seen against the solar disk, averaged over 100 arcsec, vertically after rotating the images of 22° anticlockwise to bring the filament motion to the horizontal direction. The filament was typically 4,000 K below the disk brightness temperature. The *crosses* show the location of the leading edge once the filament became visible as an emission feature above the limb. A (*solid*) line of constant acceleration, $15\,\mathrm{m\,s^{-2}}$, loosely fits the circles; a (*dashed*) line of constant velocity ($425\,\mathrm{km\,s^{-1}}$) fits the measured heights above the limb: the outer edge of the filament appears to accelerate rapidly between 04:45 and 04:55 UT. The distances shown are those measured in projection on the sky: if the filament is moving radially outward from E45° on the solar disk, the true distances are larger by a factor ∼1.4 (from Kundu et al. 2004)

microwave data obtained at a high cadence, Kundu et al. (2004) analysed an EP/CME event also associated with a GOES (M2.8) X-ray flare (see Figs. 66, 67). They showed that the filament activation (EP), detected on the disk at 17 GHz and above the solar disk at 34 GHz, exhibits first a gradual onset, then an abrupt acceleration phase coincident with the impulsive phase of the flare and the launch of a fast CME. These results suggest that, as already argued by Zhang et al. (2001), the disruption of a large scale coronal magnetic field simultaneously generates the acceleration of the filament (EP) and the flare energy release. As for previous events, the rapid phase of filament acceleration stops approximately at the end of the first, and main impulsive microwave burst of non-thermal origin, but much before the soft X-ray peak.

Not all CMEs display a full three phase scenario. Gradual events can show a weak acceleration which persists during several hours (e.g. Srivastava et al. 2000). A typical example of a very slowly evolving CME event associated with an eruptive prominence is shown in Fig. 69. Figure 70 displays time-lapse images of the radio prominence at 17 GHz observed by the Nobeyama radioheliograph. These images exhibit the slow eruption of the prominence. Figure 71 shows that this CME is seen to rise for many hours with low speeds lower than $50\,\mathrm{km\,s^{-1}}$ in the low corona (below $2R_\odot$). The acceleration in the outer corona is also quite gradual and decreases beyond

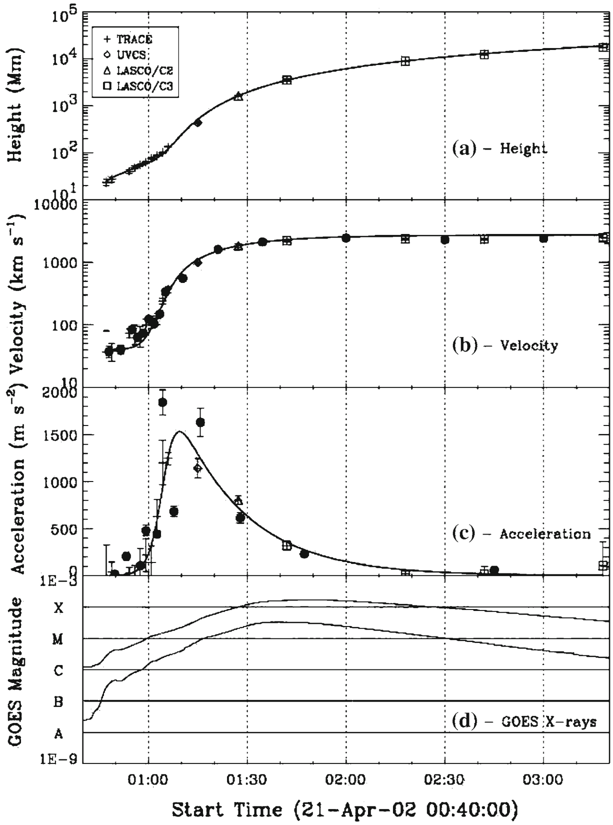


**Fig. 68** April 21, 2002 event: **a** The height-time profile. **b** and **c** give the velocity and acceleration profiles, obtained by taking the first and second numerical derivatives, respectively. The first-difference values are given as *filled circles*, while the three-point difference values are given using the same symbol as **a**. The *solid line* gives the best fit to the data. **d** The GOES-10 soft X-ray flux for the corresponding time period (from Gallagher et al. 2003)

20 R$\odot$. There is no observational evidence of magnetic reconnection or impulsive energy release for this kind of event. The differential rotation and the subsequent shearing of coronal magnetic fields have been suggested as a possible mechanism to explain in such a case the CME initiation mechanism (e.g. Linker and Mikic 1995).

### *6.2.2 Input of the decimetric and metric observations*

In the decimetric and metric wavelength domain, the coronal structures, detected by their free–free thermal emission, should be in principle similar to those seen by the white light coronagraphs. Indeed, they both depend on the emission measure of the electrons, $\sim \int n_e^2 dl$ for the free–free radio emission, and on $\sim \int n_e dl$ for Thomson scattering. However, as CMEs have coronal temperatures and a low density, their

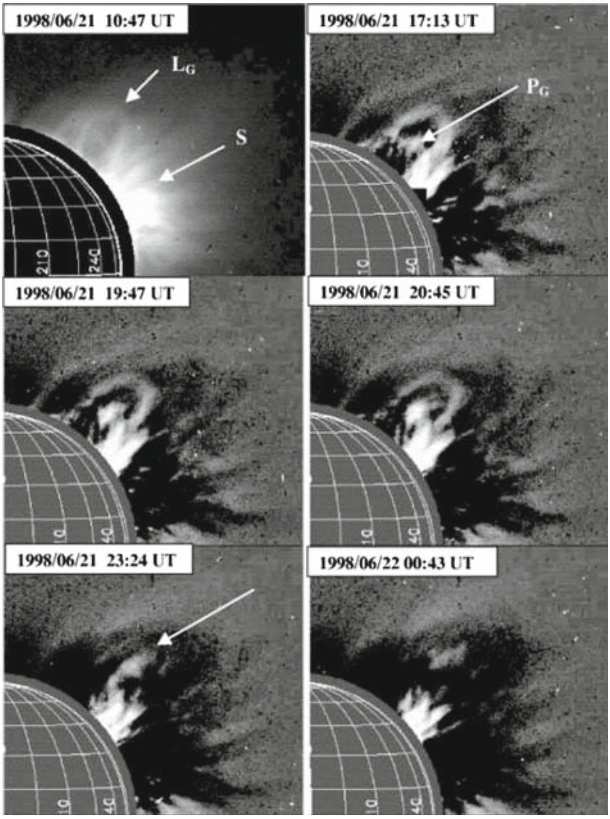


**Fig. 69** June 21–22, 1998 CME event: Time-lapse images taken by LASCO-C1 coronagraph in Fe XIV emission line. The field of view is 1.13 $R_{\odot}$. All the images shown here have been subtracted from a reference image taken before the occurrence of the CME, except the one at 10:47 UT. The 10:47 UT frame is an on-line image with a nearby continuum subtracted from it in order to show the bright streamer adjacent to the CME (from Srivastava et al. 2000)

free–free emission is expected to be optically thin and therefore difficult to detect. Moreover, radio sources from non-thermal origin have often brightness temperatures consistent with thermal sources, which makes even more difficult the detection of thermal emission from CMEs.

When the corona is quiet enough, radio images show cavities surrounding quiescent filaments. The observed local decrease of brightness corresponds to a density drop of 25–50% from its mean value (Marqué et al. 2002). There is a clear continuity between the radio depression observed in the low corona and the corresponding CME, when observed together. Figure 72 presents an event associated with a dark sigmoid filament which erupted on February 18, 2001 (Marqué et al. 2002). A few hours before the eruption, a small parasitic polarity, detected as a bright point in H$\alpha$ appeared on one edge of the filament and was followed, later on, by the production of weak type III-like bursts indicating the destabilization of the overlying magnetic structure and the beginning of the eruptive event. The radio depression expands to the south-west,

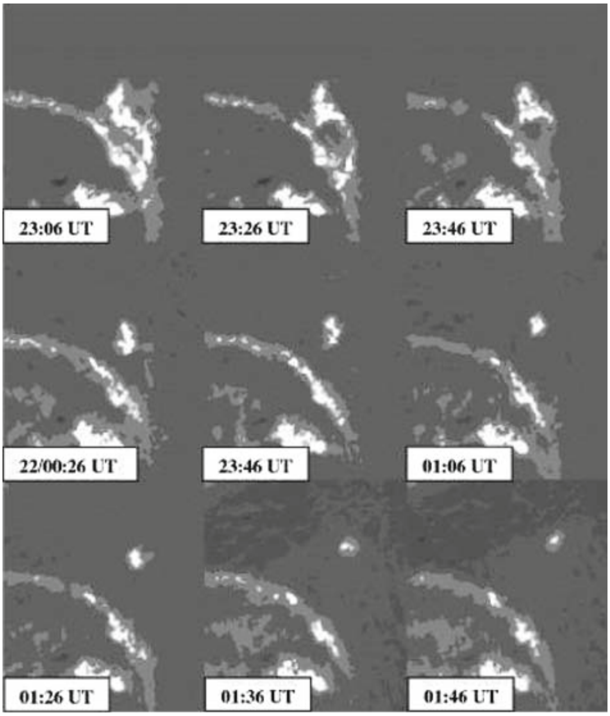


**Fig. 70** June 21–22, 1998 CME event: Eruptive prominence as seen in the time-lapse images of the Sun (17 GHz) by the Nobeyama radioheliograph over the limb between 23:00 UT on June 21 and 02:45 UT on June 22 (from Srivastava et al. 2000)

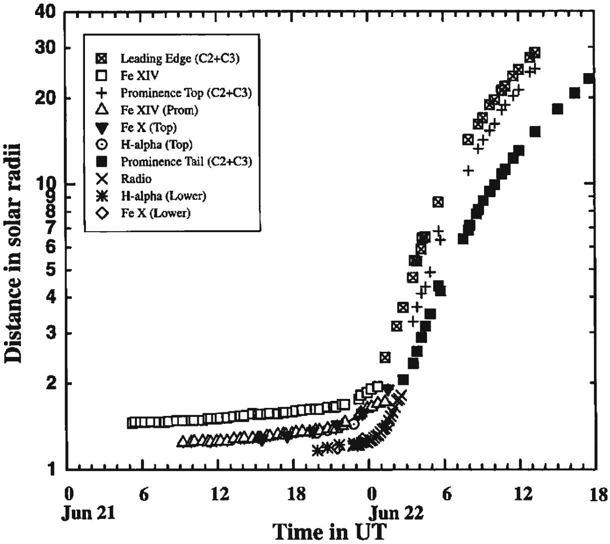


**Fig. 71** June 21–22, 1998 CME event: Plot of height (on log scale) versus time for different features of the CME, viz., the leading edge, the prominence top, and the tail, as measured from the images obtained in different wavelengths by various instruments (from Srivastava et al. 2000)

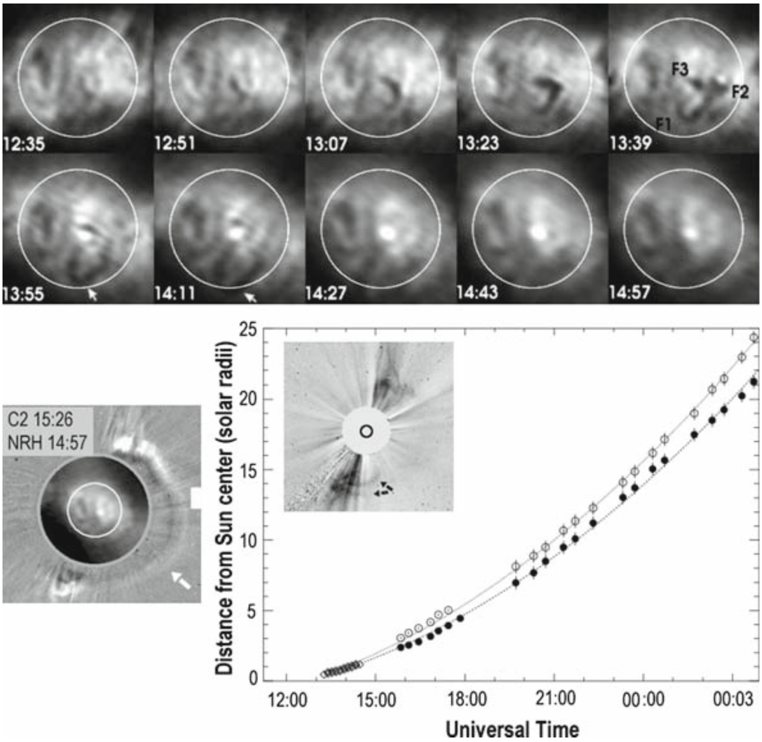


**Fig. 72** February 28, 2001 event: *Top*: Nancay Radioheliograph observations at 327 MHz showing the expansion of the radio depression associated with the filament, up to the limb (pointed out by *white arrows* on two lower images). *Bottom*: *Left panel* the image shows the expansion of the halo CME seen in LASCO-C2 coronagraph, as indicated by the *white arrow*. The CME is mainly expanding westward as expected by the orientation of the filament. *Right panel* height versus time plot of the structure indicated in the inner C3 image by *black arrows*, compared to the evolution of the radio depression associated with the filament (from Marqué et al. 2002)

up to the solar limb. A halo CME was later observed as shown in the left panel of Fig. 72. The comparison of the time evolutions of the radio depression and of the cavity seen by LASCO is shown as a one dimensional plot in the right panel of Fig. 72.

## 6.3 Noise storm radio emissions and dynamical evolution of the corona

Noise storms are generated by supra thermal electrons accelerated continuously over time scales of hours or days in the presence of solar active regions. These storm emissions are related to emerging magnetic loops interacting with overlying loops and leading to magnetic coronal reconfiguration (Habbal et al. 1996; Bentley et al. 2000). A close spatial and temporal relationship was established between noise storm onsets or enhancements and white light transient activity (Lantos et al. 1981; Kerdraon et al. 1983). They were found to be associated with CMEs or with the appearance of additional material in the corona at the vicinity of the radio emitting source. They were also found to be associated with filament disappearance (Lantos et al. 1981; Marqué et al. 2001). Noise storm enhancements are also sometimes observed in association with a flare-like sudden energy release in the active region, either as a fully developed flare or, more often as a microwave (Raulin et al. 1991) or soft X-ray brightening without H$\alpha$ signature (Raulin and Klein 1994). A few cases have also been reported in which 10–30 keV emission from a superhot plasma or non-thermal electrons have been observed at the onset of noise storms (Crosby et al. 1996) confirming that a flare-like energy release in the lower corona could be a necessary condition for noise storms to start. The longer duration of noise storms with respect to these flare-like signatures argue however, for a continuous, time extended acceleration taking place in the vicinity of the noise storm source and linked to a more gradual reorganization of the coronal magnetic field. Sources of radio noise storms are also very sensitive to the onset of CMEs in their vicinity. Their sudden disappearance is often a reliable indicator of a large-scale magnetic reconfiguration of the corona, consecutive to the occurrence of a CME (Habbal et al. 1996). One example is provided by Willson (2005) who combined VLA observations at 91 cm with SOHO EIT, MDI and LASCO data. For one event a transient increase of the brightness of a radio source at 91 cm was simultaneously observed with a gradual and transverse displacement of the radio source during the initial onset of a CME and of its associated EUV ejection located $\sim 35°$ north of the region (see Fig. 73). Willson proposed that the projected motion of the 91-cm source (speed $\sim 28\,\mathrm{km\,s^{-1}}$) represents the initial sideways expansion speed of the CME loop. The passing CME may produce, through compression of the surrounding corona (or possibly through the injection of non-thermal electrons) an increase of the electron density in the slowly-varying 91-cm loop, leading to a change in the brightness of the emitting source. This shows how radio observations can be used to determine the lateral expansion of the CME motion (see also Sect. 5.4).

## 6.4 Large and fast flare/CME events

When CMEs are associated with flares, strong non-thermal radio emissions are observed over a broad frequency range. Whereas it is well established that flares do not drive CMEs, it is now well accepted that both CMEs and flares reflect the coronal response to the same magnetic energy release.

### *6.4.1 Initial phase*

The development, in the low corona, of large flare/CME events is often extremely fast and is accompanied by the opening of the magnetic field over a large region, which has been observed in EUV as a large scale dimming or in soft X-rays in the form of dimmings or disappearing transequatorial loops (e.g. Sterling and Hudson 1997; Zarro et al. 1999; Thompson et al. 1998a, 2000; Khan and Hudson 2000; Pohjolainen et al. 2001, 2005). During the few minutes preceding the impulsive phase of the associated flare, radio bursts start to be detected and are the signature of electron beams accelerated during the early magnetic field interactions. The first radio emissions which are either reverse slope type III bursts, U or J bursts (incomplete U-bursts), reveal the

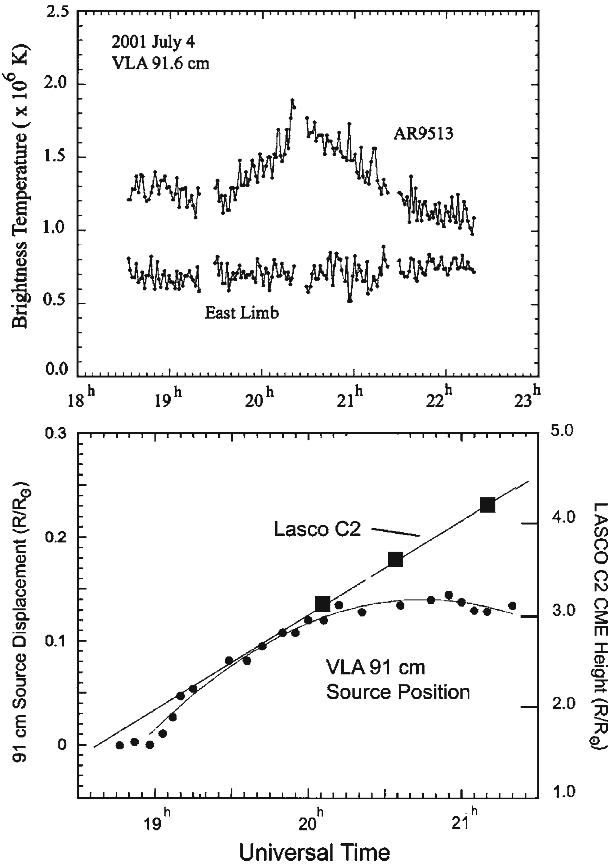


**Fig. 73** July 04, 2001 event: *Top panel* Plot of the peak brightness temperature measured at 91.6 cm from the source associated with AR9513 on the west limb and from a source on the east limb (chosen as reference). *Bottom panel* Plots of the temporal displacement of the source (*full circles*) and of the leading edge of the CME (*full square*) (adapted from Willson 2005)

presence of two distant and nearly simultaneous emitting regions. These bursts may be used as the first tracers of the large-scale magnetic field lines (transequatorial interconnecting loop) which start to be destabilized, before their ejection as part of the CME (Pohjolainen et al. 2001, 2005). These observations are consistent with the occurrence of magnetic reconnection in a multipolar complex magnetic field and also provide some support to the break-out model proposed by Antiochos et al. (1999).

### 6.4.2 *Lift-off and angular spread of CMEs in the corona*

Fast flare/CMEs have usually a complex development; they are observed to start with a relatively small angular projected dimension and reach their full extent in the low corona (below 2R⊙) in a few minutes. Radio images from the Nançay Radioheliograph show that the radio emission sites are first localized in a coronal region in the vicinity

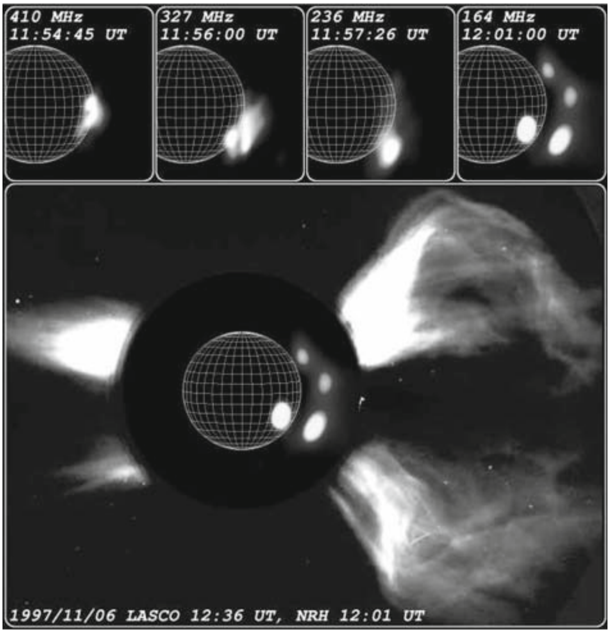


**Fig. 74** November 6, 1997 event: *Upper panel* Radio images at distinct frequencies which show the complexity of the emitting region: the emission expands toward the Northern hemisphere. *Lower panel* Composite image of a LASCO/C2 CME image with a radio NRH image at 164 MHz showing that there is a close correspondence between the extent in latitude of the CME seen by LASCO-C2 and the sites of radio emission (adapted from Maia et al. 1999)

of the flare site and then expand by successive magnetic interactions at progressively larger distances from the flare site. Signatures of these interactions are detected by bursts in the dm-m wavelength domain (Maia et al. 2001). For the large and fast CME that occurred on the west limb on November 6, 1997, Maia et al. (1999) compared the radio observations to the optical observations. The CME expanded laterally and reached its full size in the low corona within 5 min. Figure 74 shows a good similarity between the final extent of the radio emitting sites and the extent of the legs of the white light CME structure. The large scale destabilization of the magnetic field can be interpreted as the result of the interaction of a coronal disturbance propagating from the flare site (typical speed of $\sim 10^3\,\mathrm{km\,s^{-1}}$) with magnetic loop systems at further locations. To understand the nature of this disturbance, it is interesting to compare the limb observations with those of on-disk events because the two perspectives give a more complete picture.

For the on-disk halo event of May 02, 1998 Pick et al. (1999b) and Pohjolainen et al. (2001) observed the spatial and temporal link between a propagating EIT disturbance associated with an H$\alpha$ Moreton wave (see, e.g. Uchida 1960) and the successive components of coronal type II-like bursts. This is illustrated in Figs. 75 and 76. For this event, the front of the H$\alpha$ wave coincides with the EUV disturbance also called EIT wave (Thompson et al. 1998a; Moses et al. 1997).

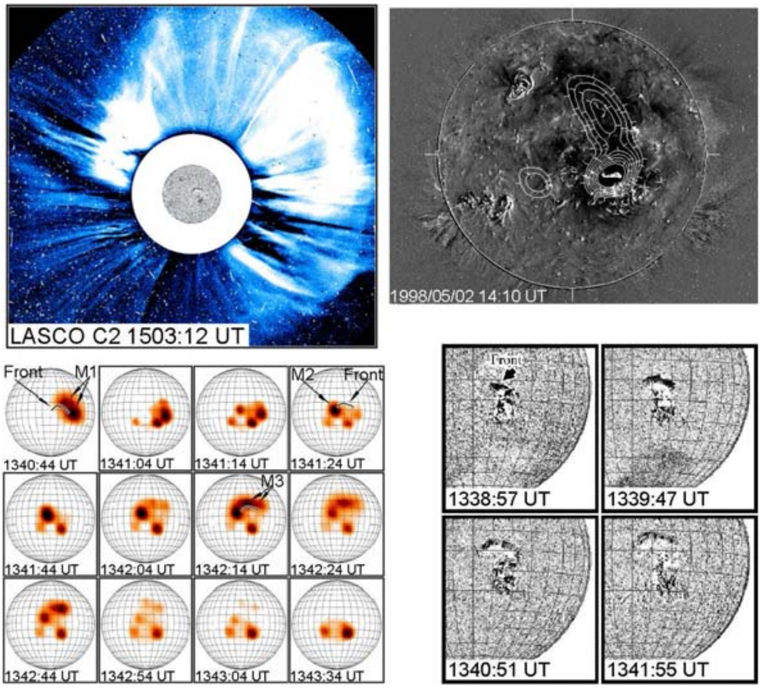


**Fig. 75** May 02, 1998 event: *Upper panel, Left* SOHO LASCO C2 image showing the halo CME. *Right* 195 Ådifference image showing the SOHO EIT dimming region at 14:10 UT; the NRH 236 MHz image at 13:48:21 UT is overplotted in contours. At the time of the EIT image, this radio source had already disappeared. *Lower panel*, *Left* NRH images at 164 MHz and 236 MHz showing the location of the sources labelled, M1 (164 MHz), M2 (236 MHz), M3 (164 MHz) marked by an arrow at selected times (see Fig. 76). *Right* Running difference of Kanzelhohe H$\alpha$ images showing the moving H$\alpha$ wave front (marked by an *arrow* in the first difference image) (adapted from Pohjolainen et al. 2001)

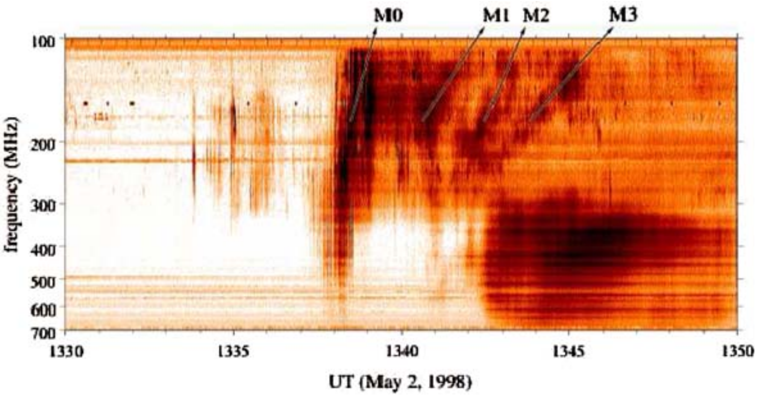


**Fig. 76** May 02, 1998: Artemis IV radio spectra: the spectral drifting sources are labelled Mo for the one in the flash phase and M1, M2, M3 for the type II-like emissions (adapted from Pohjolainen et al. 2001)

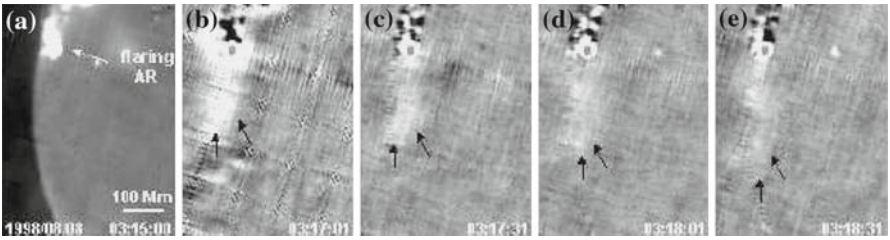


**Fig. 77** The flare wave on August 8, 1998 as shown by 17 GHz difference images (**b**–**e**). Image **a** is a pre-event direct radioheliogram showing the flaring active region and the undisturbed chromosphere (from Warmuth et al. 2004)

The EIT waves have been found to have a strong association with CMEs (Biesecker et al. 2002) and often with EUV dimmings which are usually restricted to the region traced by the transit of the Moreton waves (see upper panel, right in Fig. 75). Moreton waves are usually interpreted as the chromospheric trace of a super-Alfvenic disturbance (coronal shock wave). Since the discovery of the EIT waves and in addition to the Moreton waves, many other waves have been identified in different spectral ranges: soft X-rays (Hudson et al. 2003), HeI (Vršnak et al. 2002; Gilbert and Holzer 2004) and radio wavelengths (Warmuth et al. 2004; Vršnak et al. 2005). Figure 77 shows an example of wave fronts observed at 17 GHz by the Nobeyama radioheliograph; these wave fronts appear as an increase in microwave emission and roughly resemble the accompanying Moreton wave both in shape and in angular extent. While Warmuth et al. (2004) suggested that the wave signature could be due to the compression and/or heating of the chromosphere and transition region, White and Thompson (2005) concluded from a detailed study of one event, that the bright wave front was more consistent with optically thin thermal emission from the corona than with an optically thick chromospheric emission. It was suggested by Warmuth (2007) that the waves observed in the different spectral ranges are closely related: sharp EIT waves, SXT waves, HeI waves and waves seen at 17 GHz are all closely spatially related to H$\alpha$ Moreton waves. This supports the interpretation of these disturbances in terms of propagating waves. The origin of EIT waves, which seem to consist of two classes of events, sharp and diffuse, is still not fully understood; their association with type II bursts will be further discussed in Sect. 7.1. It is worthwhile recalling here that another interpretation of the EIT waves (Delannée and Aulanier 1999) links the location of the EIT brightening to the result of the compression of the plasma near the footpoints of opening field lines and not to the propagation of a wave. This bright feature can propagate as the field opens, further and further away from the original site (see also Delannée et al. 2007). This last scenario may also account for the rapid development of the extent of the radio-emitting sources on the disk (see Fig. 75) and to the formation of type II-like bursts as the field opening proceeds farther and encounters preexisting magnetic features (see Figs. 75, 76). In all cases, the propagation of the wave or of the compression region produces additional magnetic destabilization as well as magnetic interactions along their travelling path. The induced reconnection process leads to the opening of other magnetic field lines, thus allowing other magnetic structures to merge and to give rise to the white light transients. The radio sources and the EIT and SXT dimming

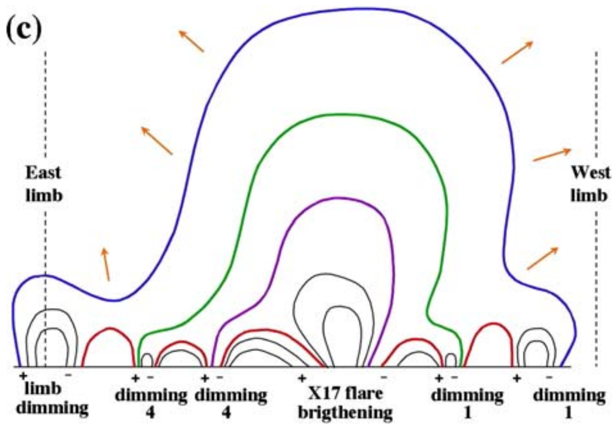


**Fig. 78** Reconnection of the CME field configuration with the surrounding dipoles; By successive reconnections, the outer shell of the CME expanding magnetic field is progressively anchored in more distant regions; the just reconnected field lines are thicker and set to *red* for the short loops (from Mandrini et al. 2007)

regions finally trace the on-the-disk locations of the CME source regions. Chen et al. (2002) proposed a theory which also implies that all the field lines covering the flux rope are open successively to form the apparent propagation of EIT wave fronts.

For some CMEs, the presence of a coronal null point and the observations of two distinct and nearly simultaneous radio sources give strong arguments in favour of the generalized break-out process for the triggering of the eruption. The magnetic reconnection occurs at the null point before the start of the eruption. The subsequent development of the event suggests that large interconnecting loops are ejected together with the CME, while secondary reconnections at lower altitudes occur further away from the active region. The triggering and evolution of the complex CME involve multiple magnetic flux systems over a large coronal volume surrounding the flare site and results from the coupling of magnetic structures at different scales (Maia et al. 2003).

As a general conclusion, for the fast flare associated CMEs, reconnection processes lead first to the opening of the magnetic field which then allows magnetic arches to be expelled. Reconnection processes and interactions with other adjacent magnetic structures contribute by progressive steps to the CMEs development. This conclusion agrees with recent results from Mandrini et al. (2007) who studied the flare, and CME that occurred on October 28, 2003. The CME on this day is associated with large-scale dimmings, located on either side of the main flaring region. The authors propose, as shown in Fig. 78, that, by successive reconnections the outer shell of the CME expanding field is progressively rooted in more distant regions (see also for discussion Démoulin (2007). Moreover, radio observations show that the full development of this class of events takes place in the low corona in 5–15 min. The observations are in favour of the generalized breakout model (Antiochos et al. 1999; Aulanier et al. 2000). It must be noted that there is also a link between the fast CME development and the development of shocks in the low corona. This association needs to be understood

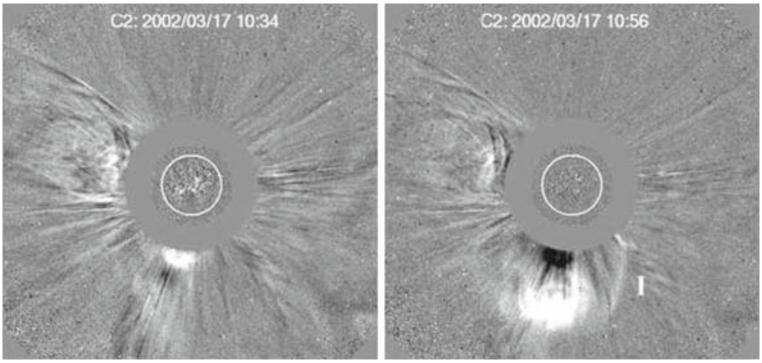


**Fig. 79** March 17, 2002 event: Two LASCO C2 images showing the development of the CME. The structure labelled I is interpreted as the signature of a coronal shock (from Yan et al. 2006)

within the more general problem of the relationship between CMEs and coronal shocks (see Sect. 7 where the relationship between EUV coronal waves, Moreton waves, and shocks is further discussed).

## 6.5 Build up of compression regions during CME's expansion

Many CMEs accompanied by a flare originate above a complex multipolar configuration of the magnetic field in which the active region responsible for the flare is located. When the CME starts expanding, the neighbouring open field line region can become progressively more and more compressed.

Figure 79 shows two successive LASCO images of a CME observed on March 17, 2002. The CME has the appearance of a bright loop in expansion that propagates in the southward direction. In addition, a narrow structure, labelled I, becomes visible in the image at 10:56 UT. This sharp feature, which propagates transversally to that of the CME has been interpreted as the signature of a coronal shock (or coronal compression wave) driven by the CME lateral expansion of its western edge (Yan et al. 2006). Another evidence of the build up of this compression region is provided by radio and HXR observations. The key points of these observations and of their interpretation may be summarized as follows: during the development of this CME, the RHESSI imager observed an HXR emission closely associated in space and time with a group of type III bursts. These two kinds of emission were likely produced by the same population of accelerated electrons. The region which is the site of the X-ray emission, is composed of two small loops that emerge inside, or close to, an open unipolar region. The X-ray and type III burst sources are found to be distributed, respectively, at the root and along the downward extrapolation of the CME edge. Figure 80 shows the location of these sources which are reported on a MDI magnetogram. Magnetic field lines calculated from a potential field configuration are superposed on the figure. The sources of the type III bursts, measured at two given frequencies, move progressively toward the south-west direction. This progressive shift versus time is interpreted as an increase of the local plasma frequency, thus of the electron density during the build-up of the

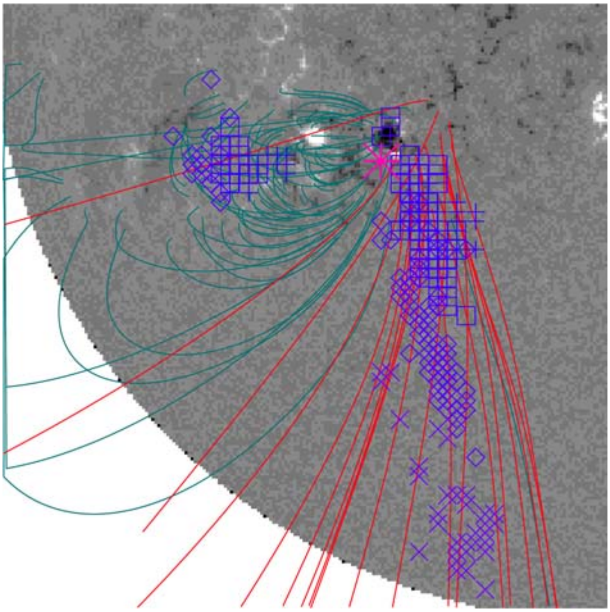

**Fig. 80** March 17, 2002 event: The sources of type III bursts are reported in a MDI magnetogram with the reconstructed magnetic field structure (see the text) represented by open (*red*) and close (*green*) field lines. The *pink "star"* symbol indicates the RHESSI HXR location; The symbols, *cross, diamond, square*, and *plus* represent the sources of 164, 236, 327 and 410 MHz, respectively (from Yan et al. 2006)

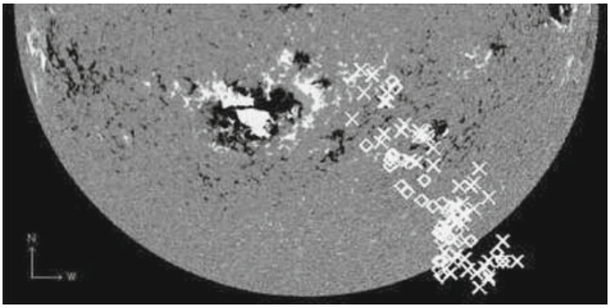


**Fig. 81** October 28, 2003 event: Positions of type III bursts at 236 MHz (*diamonds*) and 164 MHz (*crosses*) reported in a MDI magnetogram (from Pick et al. 2005b)

compression region. The increase is roughly by a factor of 10 at frequencies higher than 164 MHz. Similar signatures were observed during other events (see for example Pick et al. 2005b; Fig. 81). Moreover, it was observed that, for several CMEs, streamers are seen to bend as the CME flank impinges on them. Vourlidas et al. (2003) established for an event, which occurred on April 02, 1999, that the speed and density of the CME front and flanks are consistent with the existence of a shock.

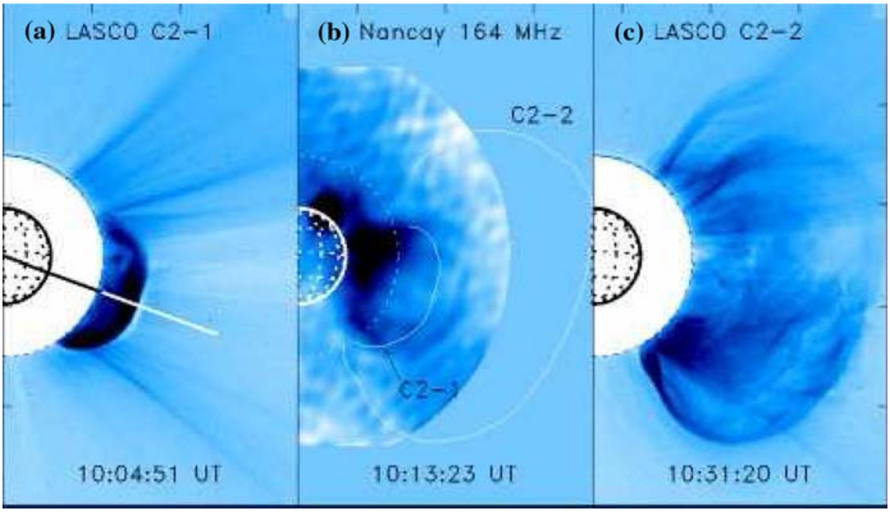


**Fig. 82** April 20, 1998 radio CME: **a** LASCO C2 coronagram obtained at 10:04:51 UT, just before the radio CME was first detected. **b** Radio CME seen at the time of maximum flux at 164 MHz. The *white lines* indicate the position of the leading edge of the CME at the time shown in **a** and **c**. LASCO C2 coronagram shortly after the radio CME was no longer detectable (from Bastian et al. 2001)

## 6.6 Direct imaging of radio CMEs

Bastian and Gary (1997) discussed the possibility of detecting, at radio wavelengths, thermal bremsstrahlung and/or synchrotron radiation from CMEs and concluded that the metre/decimetre wavelength range is the most convenient one for such detections. Thermal emissions of CMEs were reported at frequencies around 80 MHz (Sheridan et al. 1978; Gopalswamy and Kundu 1992) with the Culgoora and Clark Lake interferometers, and at 109 MHz with the Gauribidanur radioheliograph (Kathiravan and Ramesh 2005). However, several inconclusive attempts to detect the thermal emission from CMEs were made at 74 MHz with the VLA (Gary 1998). A few faint sources were observed by the NRH, in the 410–150 MHz range, in association with the leading edge of CMEs. Their emission was, however, consistent with a non-thermal one. To date, no recent observation convincingly confirms the earlier claims of CMEs thermal detection at frequencies lower than 80 MHz (see also Gary and Keller 2004, Chap. 11).

For the first time, Bastian et al. (2001) reported CME loops which were directly imaged at radio wavelengths by the NRH. This radio CME was associated with a flare just over the southwest limb. Figure 82 shows that this event is seen as an expanding ensemble of loops, detected up to $3R_\odot$ behind the CME front, and it closely looks like the white light CME. This faint radio emission was attributed to incoherent synchrotron radiation due to 0.5–5 MeV electrons interacting with magnetic fields ranging from 0.1 to a few gauss (see Fig. 83). While the white light coronagraphic observations are sensitive to the thermal plasma contained in the CME loops, the radio emission from the CMEs originates from those magnetic loops containing relativistic electrons. The

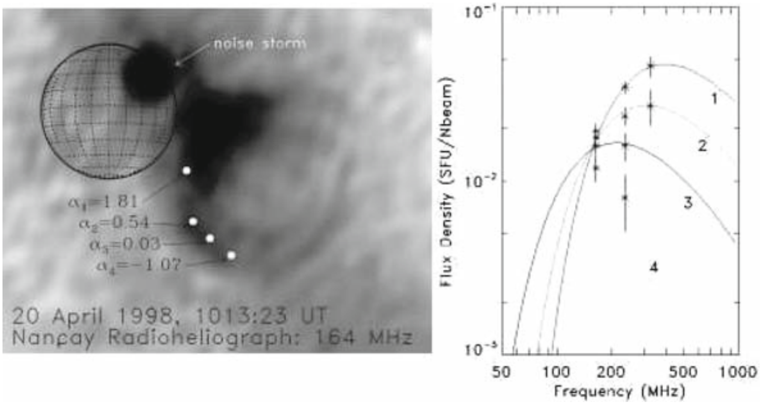


**Fig. 83** *Left panel* Snapshot map of the radio CME at a frequency of 164 MHz at the time of maximum flux. The background emission from the Sun has been subtracted. Time variable radio emission from a noise storm is present to the northwest. The brightness of the CME is saturated in the low corona because the map has been clipped at a level of 0.04 SFU beam$^{-1}$, corresponding to a brightness temperature TB $\approx 2.6 \times 10^5$ K. The radio CME is visible as a complex ensemble of loops extended out to the southwest. Also shown is the spectral index measured at four locations in the radio CME. *Right panel* Flux spectra measured at the four points shown in the left panel. All flux measurements have been normalized to SFU $N_{\rm beam}^{-1}$, where $N_{\rm beam}$ is the 164 MHz beam. Three model spectra are also shown in the same figure (from Bastian et al. 2001)

detection of radio emission from CME loops offers a number of important diagnostics on the early phase of CMEs, for instance, new constraints on the thermal plasma density, the number of relativistic electrons, or the magnetic field strength in the CME. The association between a radio CME and relativistic electrons detected in-situ near the Earth will also be discussed in Sect. 9.3.

We note that similarly to radio CMEs, many moving type IV bursts are explained as due to synchrotron emission from relativistic electrons; they are also closely associated with CMEs (see Munro et al. 1979; Kundu 1982). The detection of radio CMEs is in fact made possible when the strongest emitting radio sources are absent or occulted behind the solar limb.

## 6.7 Post eruptive phase

Hot post-eruptive arcades, or flare loops, result from reconnection processes in the aftermath of CMEs (e.g. Kahler and Hundhausen 1992). These arcades are often the seat of coronal electron acceleration, revealed by the presence of non-thermal radio continua (stationary type IV bursts) lasting for several hours, and of gradual soft X-ray emissions (LDE) (see, e.g. Lantos et al. 1981). When the CMEs are observed in white light, the source of these radio continua is found to be co-spatial with secondary white light loops (see, e.g. Gergely et al. 1979). These broad band continua may be produced either by plasma radiation (see Sect. 2 and Stewart 1985; Robinson 1985). or by synchrotron emission (Gergely et al. 1979; Dauphin et al. 2005) originating from energetic electrons injected in magnetic loops.

## 7 Coronal and interplanetary shocks, association with flares and CMEs

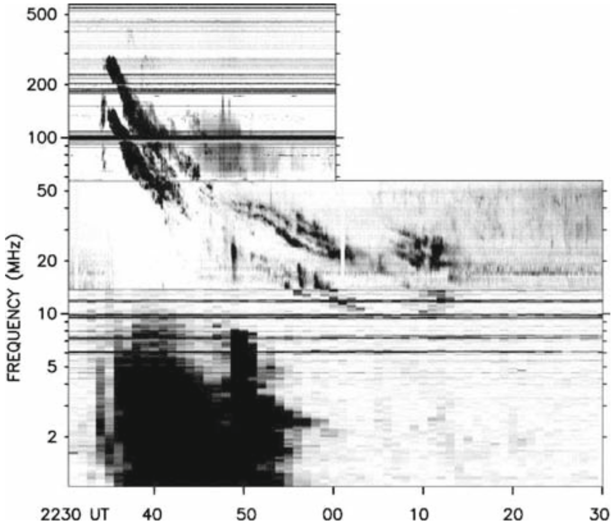


**Fig. 84** November 01, 2003 event. The continuous frequency coverage is obtained by combining the data from WAVES below 14 MHz, from BIRS between 14 and 57 MHz and from Culgoora data between 57 and 570 MHz (from Cane and Erickson 2005)

Shocks propagating in the corona and in the interplanetary medium generate slow frequency drifting radio emissions called type II bursts (see Sects. 2.1.2 and 2.2.2): metric to decametric type II bursts for coronal shocks and hectometric to kilometric type II bursts for interplanetary shocks. As the type II bursts in the interplanetary medium (IP type II bursts) were found to be closely associated with white light CMEs (Sheeley et al. 1985), it was concluded that they are produced by shocks driven by CMEs (Cane et al. 1987) and sometimes observed in-situ (Bale et al. 1999). One difficulty is the lack of continuous spectral coverage between the low-frequency part and the high-frequency part of the spectrum observed, respectively, by ground-based and space-based spectrographs. The BIRS (Bruny Island Radio Spectrometer) radio spectrometer covers the frequency range 62.5–5 MHz and is presently the only one to operate on ground at such a low frequency, when there is no strong ionospheric absorption (Erickson 1997). Figure 84 shows one example of a metric type II burst that extends from 300 to 10 MHz. The two bands (F–H) clearly vanish before reaching the IP medium.

The origin of the type II bursts in the solar corona is a more complex problem and there has been a long-lasting controversy on the relationship between type II bursts, flares and CMEs (e.g. Cliver et al. 1999; Gopalswamy et al. 1998) and on the origin of the coronal shock waves. These points are not yet clarified.

### 7.1 Origin of coronal shocks

Two origins have been proposed:

– The original one was that coronal shocks are blast waves produced at the time of the flare. They are not directly related to a CME and they quickly weaken with

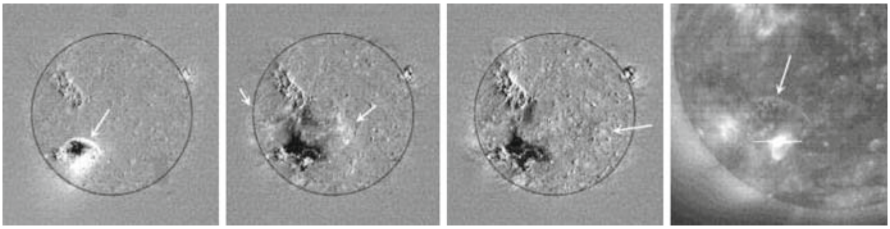

**Fig. 85** Example of an EIT wave from September 24, 1997. The *first three* panels show successive images at 02:49, 03:03 and 03:23 UT with a pre-event image digitally differenced from them. *Arrows* indicate the EIT-wave front(s). The *last panel* shows a subfield of the first panel (undifferenced), showing an example of a sharp brightening (from Biesecker et al. 2002)

distance (e.g. Wagner and MacQueen 1983). This blast wave is initiated by, e.g. a pressure pulse or a short localized energy release (e.g. Vršnak and Lulić 2000) and in that case no mass motion drives the shock wave.

– An alternative one is that it is the propagation of coronal material (piston driven scenario), e.g. a plasmoid ejection or a fast CME, at super Alfvenic speeds (see Cliver et al. 1999 for a detailed discussion) which creates the coronal shock wave.

The first scenario is supported by the observation that type II bursts in the low and middle corona (at metric wavelengths) are temporally associated with flares which initiate waves during their impulsive phase. These waves were first observed at H$\alpha$ wavelengths by Moreton and Ramsey (1960), and were detected as large scale disturbances propagating at speeds of the order of $10^3$ km s$^{-1}$. In the last decade, EUV observations from SOHO EIT as well as X-ray observations from Yohkoh (Hudson et al. 2003) and the GOES soft X-ray imager (Warmuth et al. 2005) have also shown global wave like features propagating in the corona (see also Sect. 6.4.2). Most EIT waves consist of diffuse brightenings propagating away from the active regions. Their speed, which is difficult to accurately determine due to the poor temporal cadence of the observations, appears to be a few hundreds of km s$^{-1}$. EIT waves have a strong association with CMEs and often with EUV dimmings, which are usually confined in the region traced by the transit of Moreton waves. It was thus suggested, as discussed in Sect. 6.4.2, that they are due to the compression of the plasma in the region surrounding the sudden magnetic field opening. Biesecker et al. (2002) established that EIT waves are poorly correlated with coronal type II bursts, except for a small subclass ($\approx$7%) that have sharp bright fronts as the event shown in Fig. 85. They suggested that these sharp wave fronts could be the coronal counterpart of H$\alpha$ Moreton waves. As shown in Sect. 6.4.2, this assumption was confirmed for a few events for which EIT and Moreton waves and coronal type II-like bursts appear in close spatial and temporal coincidence. Vršnak et al. (2005) also reported observations of a wave that is detected at metric wavelengths and propagate together with an H$\alpha$-Moreton/EIT wave. This wave is well associated with the coronal shock that causes a type II burst higher in the corona. Warmuth et al. (2004) analysed 8 events and found that all EIT waves with sharp wave fronts have a deceleration rate that decreases with increasing time and distance. They pointed out that the characteristics of these coronal waves, their rapid deceleration, the broadening of their intensity profile and the decrease of their amplitude with increasing distance and time, are characteristics of blast waves, rather than piston driven shocks. Additional evidence was provided by Khan and Aurass (2002), Narukage et al. (2002) and Hudson et al. (2003) who showed that the coronal waves detected by the Yohkoh/SXT telescope also have the expected relationship to Moreton waves and type II bursts.

As recalled above, a few combined observations of waves and type II bursts support the blast wave origin of the metric type II shock. From the comparison of different spatially resolved observations, Gopalswamy et al. (2000) (respectively, Khan and Aurass 2002) reported a close temporal and spatial association between an EIT wave (respectively, a soft X-ray wave) and the source location of the metric type II burst. Such observations support the blast wave scenario if neither mass motions, nor CMEs are detected during the event. However, the detection of CMEs close to the solar surface at heights where the metric type II burst is produced is rare and difficult for flares close to the disk centre while waves are easily observed.

Many observations of coronal type II bursts are not consistent with a blast wave interpretation. The alternative scenario postulates that the corresponding coronal shocks are driven by mass motions: ejecta, CMEs or their counterparts close to the solar disk. It needs to be carefully investigated by analysing combined images of ejecta and CMEs and type II radio sources at similar coronal heights.

At high altitude in the corona, some comparisons between radio and coronagraph images were performed with the Teepee Tee Array of the Clark Lake Radio Observatory below 80 MHz and with the Culgoora Radioheliograph at 80 and 43 MHz (Gergely et al. 1983; Robinson 1985, for a review see Pick 1999a). They indicate that 42% of the type II bursts sources are located near the leading edge of the associated CME event while 29% are well behind this leading edge. Thus both interpretation in terms of flare-related blast wave and of CME piston-driven shock could explain these observations. For type II burst sources located behind the leading edge, Steinolfson (1985) suggested alternatively that type II bursts are generated along the flanks of the CME-driven shocks. As shocks are rarely identified in white light, this assumption is difficult to check: an unambiguous distinction between a shock front and a coronal loop, or a wave, is difficult to establish. More recently, a clear identification of a shock propagating at CME flank was made by Vourlidas et al. (2003); the LASCO images of this event also showed streamers deflected when the shock impinges on them. This observation provides a firm support to the interpretation of the commonly seen streamer deflections as proxies of CME-induced coronal shocks (Sheeley et al. 2000).

At lower altitudes in the corona, the metric type II bursts are poorly correlated with the CMEs. The apparent lack of relationship between speed (e.g. Reiner et al. 2001), starting time or extrapolated positions pushes forwards the blast wave scenario. However, in the absence of images, the determination of the type II height depends on the coronal density model while the onset times of CMEs are usually derived from coronograph data, obtained at an altitude well above the height of the metric type II bursts. Combined observations of CMEs and of metric type II bursts imaged with the Nançay Radioheliograph (NRH) support the idea that metric type II bursts can also be related to piston or CME driven shocks:

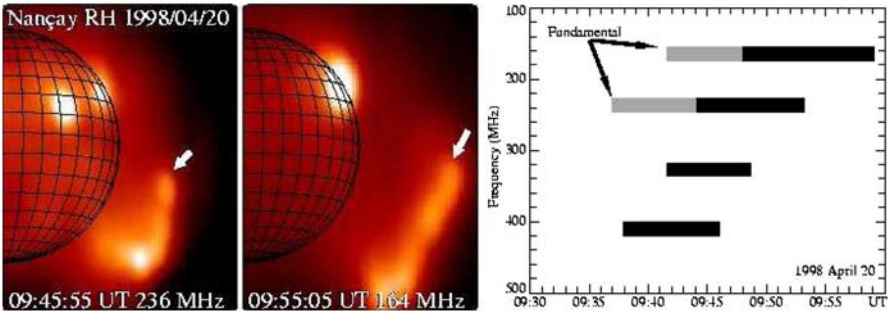


**Fig. 86** April 20, 1998 event: **a** NRH images showing the outward progression of a weak type II-like radio source (indicated by the *arrows*) in the southwest quadrant at two different frequencies (the source in the northwest quadrant is a stationary noise storm). **b** A radio spectrum constructed from consecutive images of the type II-like radio sources (adapted from Maia et al. 2000)

– The NRH observed a few events for which the radio type II-like signatures have the properties expected for a CME-driven shock and were associated in the low corona with the CME leading edge. These events are, however, weak and most often, cannot be detected by radio spectrographs (Maia et al. 2000). An example is displayed in Fig. 86 which shows the progression of a weak radio source at different frequencies. The spectrum built from the radioheliograph observations shows evidence for both the fundamental and the harmonic emissions. The elongated source closely matches the position and velocity of leading edge of the CME, whose speed is $1.4 \times 10^3\,\mathrm{km\,s^{-1}}$. For that event, the CME driven shock was probably formed at an altitude of the order of 0.7 $R_\odot$. The detection of such events is very rare, due to the frequent simultaneous presence of strong metric emitting sources; this detection is thus mostly limited to the cases where one deals with partly occulted events associated with eruptive regions located behind the solar limb.

– A support of the hypothesis of a driven shock wave event at low altitudes, has been given by Gopalswamy et al. (1997) who reported observations of a fast soft X-ray rising structure associated with the onset of a type II burst. Also, Klein et al. (1999) observed the onset of a metre type II source which appears at the same height as an X-ray ejecta seen by the SXT telescope aboard YOHKOH. These observations suggest, in both cases, the existence of a rising magnetic structure driving the type II associated shocks. Dauphin et al. (2006) analysed a type II burst starting at the unusual high frequency of 650 MHz and thus at low altitude. This allowed a direct comparison between the positions of the type II sources measured by the NRH and the soft X-ray images obtained by GOES. The analysis clearly shows that this type II burst is ignited by the shock wave created ahead of a $X$-ray rising loop when its velocity becomes larger than the local Alfven speed. It was furthermore shown that this rising loop is related to the signature of the CME at low altitude. The kinematic behaviour of the X-ray loop and of the white light CME shows that the two features can be related and is consistent with an impulsive acceleration of the CME at low altitude at the time of the HXR flare (see Fig. 87).

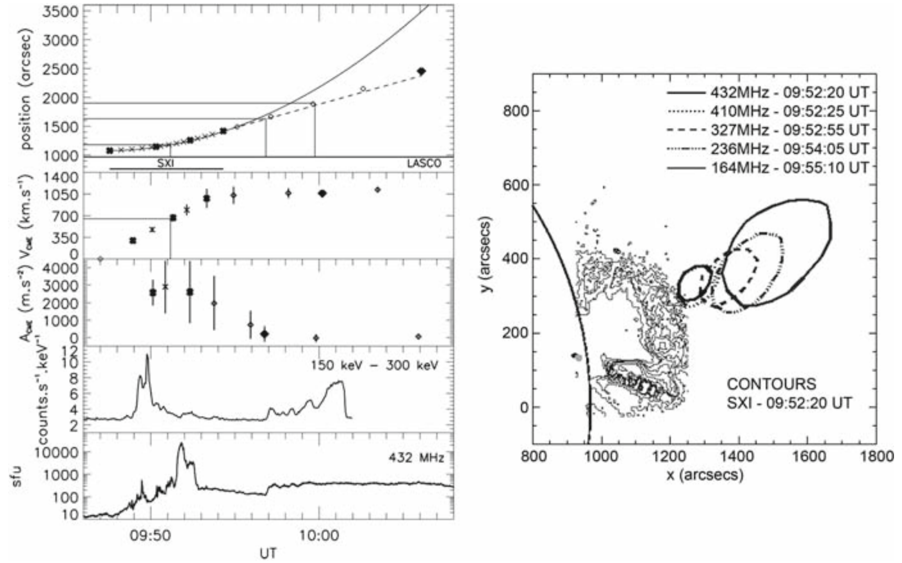


**Fig. 87** *Left panel* The *three first panels* show, respectively, the evolution with time of the projected height, velocity, and acceleration of the front of the X-ray rising loop seen with GOES/SXI (*thick cross marks*) and of the CME seen with LASCO C2 (*thick diamond marks*) during the November 03, 2003 event. The *thin marks* represent a quadratic interpolation of the data points. The *dashed line* represents the linear extrapolation of the two last GOES/SXI data points. The starting time, indicated by a *diamond* in the velocity panel is found by linear extrapolation to a null velocity from the two first GOES/SXI data points. The *two last panels* show, respectively, the time evolution of the RHESSI hard X-ray count rate in the 150–300 keV energy range and of the radio flux at 432 MHz. *Right panel* Contours of the type II sources (taken at 70% of the maximum) at different frequencies at the times indicated in the figure together with the contours of the GOES/SXI difference image. The X-ray sources from RHESSI are reported in the 20–25 keV (*grey*) and 60–150 keV (*black*) energy range (adapted from Dauphin et al. 2006)

– Klassen et al. (2003) found that the type II event shown in Fig. 88 is associated with a system of expanding SXR loops, with speeds of expansion ranging from 400 to 700 km s$^{-1}$. The type II precursor occurs above the expanding SXR loops that have average speeds around 300–400 km$^{-1}$. Conversely, the type II burst has strong spatial and temporal coincidence with a thin loop that emerges from the loop system at a speed of 700 km s$^{-1}$. These authors then suggested that the type II precursor was the signature of a moving reconnection process that occurs above the expanding soft X-ray loops and later generates the type II burst.

In summary, no consensus has yet been reached on the cause of coronal type II bursts. Most of them are associated with a Moreton wave and they do not penetrate the interplanetary medium as they are infrequently detected below 20 MHz (Gopalswamy et al. 1998). This is consistent with a blast wave origin. Alternatively small-scale ejecta and CMEs may generate a coronal shock. A compression wave or a piston-driven shock wave may be formed along the envelope of an expanding CME. The piston-driven shock sweeps the solar surface and then might become or not a blast wave.

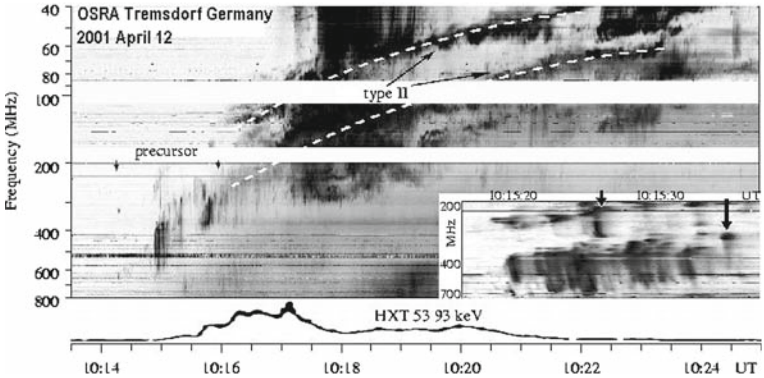


**Fig. 88** Dynamic radio spectrum and hard X–ray emission (53–93 keV) of the event on April 12, 2001. The event starts with a harmonic type II precursor, followed by a type II burst with multilane structure. The "backbone" of the fundamental and harmonic type II emissions is indicated by the *white dashed curves*. The precursor is cotemporal with the hard X-ray emission (*lower panel*) and consists mainly of sequences of fast reverse slope (RS) drift bursts, details of which are evident on the expanded time scale spectrum shown in the inset on the right (two of the RS bursts are indicated by the *arrows*) (adapted from Klassen et al. 2003)

### 7.2 Interplanetary type II bursts

The WAVE radio receivers on the WIND spacecraft provide since 1998 observations in the decametric-hectometric (D-H) domain (1–14 MHz). This corresponds to a 2–10 R s altitude range, and hence close the gap previously existing between metric and kilometric observations. It is thus now possible to investigate the relationship between the coronal type II bursts and their low frequency counterparts. When CMEs, flares and type II bursts are produced together, it is found that D-H type II burst often extends to the low frequency kilometric type II emission (Reiner and Kaiser 1999b; Reiner et al. 2003). No similar correlation is found between metric and kilometric type II bursts which are much more frequent than interplanetary type II bursts (Gopalswamy et al. 1998).

A causal relationship between metric and interplanetary type II bursts furthermore requires that the dynamics of the shock derived from the observed frequency drift rate corresponds to the projected origin time in these two frequency ranges. To relate the frequency drift rate to the radial shock speed, it is necessary to introduce a coronal density model. By requiring consistency between the type II frequency drift rate, and the height-time profile of the associated CME, Reiner et al. (2003) could fix the scale of the coronal density model (Saito et al. 1970). They could also show that, for a few events only, the frequency drift of the D-H emissions was a continuation of the frequency drift of the metric type II emission (see Fig. 89). A similar conclusion was reached by Dulk et al. (1999).

More recently, Cane and Erickson (2005) analysed simultaneously a large sample of type II bursts observed by WAVES and ground-based data from the Culgoora and BIRS radio spectrometers. They found that the slow-drift emissions observed by WAVES between 1 and 14 MHz could be divided into three groups: extensions of coronal metric type II bursts in the 1–14 MHz frequency range, blobs and bands, e.g. narrow band

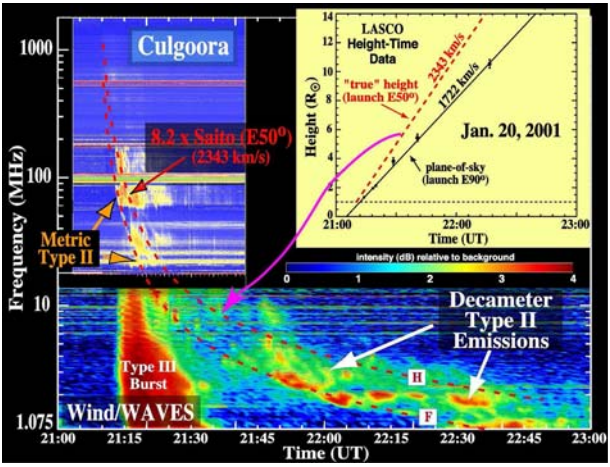


**Fig. 89** Dynamic spectra showing the decametric and metric frequency-drifting type II radio emissions associated with the January 20, 2001 CME event. The measured CME height-time data were used to obtain a frequency-time track, which was then simultaneously fit to the frequency drift of the metric and decametric type II radio emissions. It was found that to get a good fit it was necessary to assume a CME launch angle of E50$^{\mathrm{o}}$ with an enhanced Saito coronal density model, suggesting that the radio emissions originated in high density streamers (adapted from Reiner et al. 2003; see also Fig. 10 in Pick et al. 2006a)

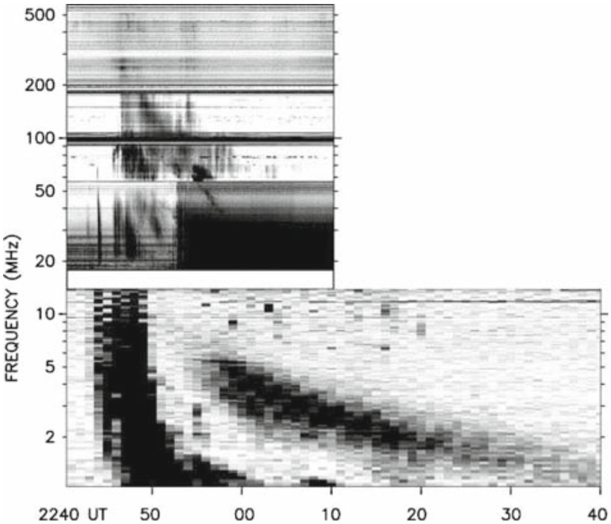


**Fig. 90** June 17, 2003 event: Example of an interplanetary type II burst observed by Culgoora radio spectrometer and by WAVES. This burst has a smooth and broad band of emission. It becomes prominent at ~6 MHz. (from Cane and Erickson 2005)

intermittent events (Reiner et al. 1997a) which represent ≈70% of the events (see for example Fig. 89), and strong IP type II events. IP type II bursts correspond to less than 25% of the events, but have a well defined single, smooth and broad band of emission over a rather long time period as shown in Fig. 90 (see also Cane et al. 1987).

Vourlidas et al. (2007) furthermore suggested that the conventional interpretation for the slow drift events observed by WIND and characterized by a very smooth intensity, as type II emission from a CME driven shock might not be true for all cases. They suggested that the emission mechanism would be the gyrosynchrotron emission of non-thermal electrons. A similar suggestion has been made recently by Bastian (2007) who showed that for an IP type II like burst, that occurred in association with a fast halo coronal mass ejection, the frequency drift with time was not consistent with what one expects for plasma radiation. He thus suggested that the emission was due to incoherent synchrotron radiation from nearly relativistic electrons entrained in the CME magnetic field or in the sheet region between the shock and the CME driver.

## 8 Interplanetary coronal mass ejections

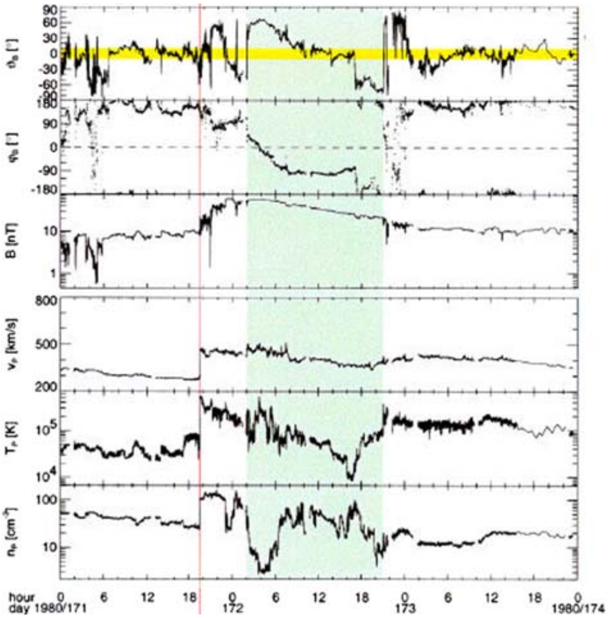


**Fig. 91** Magnetic cloud observed by the Helios 1 solar probe during 3 days in 1981, at a distance from the Sun of 0.53 AU. The *panels* show the solar wind parameters (from bottom to top): proton density, temperature, flow speed, magnetic field magnitude and its azimuthal and elevation angle. The jump in all parameters denotes the arrival of a fast shock wave. The time between 02:00 and 19:00 UT (*green area*) on day 172 denotes the passage of a magnetic cloud, with its characteristic change of the field direction (Schwenn et al. 2005)

Since 1995, CMEs have been routinely tracked through the corona out to 32 R⊙, by the SOHO coronagraphs. Nowadays, the SECCHI observations aboard STEREO provide a continuous coverage of the CMEs development from the low corona to the Earth's orbit. We shall focus here on the results which have been published before STEREO.

It is well known that the extension of the CMEs in the heliosphere goes beyond the field of view of the coronographs. Interplanetary CME (ICME) is the term used to describe the interplanetary disturbances which are believed to be associated with CMEs and which most often include an interplanetary shock preceding a turbulent plasma sheath and ejecta. The term magnetic cloud (MC) refers to a subset of ICMEs for which a smooth and continuous rotation of the magnetic field, in a plane vertical to the propagation direction, is observed following the interplanetary shock (Burlaga et al. 1981). This magnetic field is generally thought to follow a flux rope topology. MCs also correspond to a higher value of the magnetic field and a lower value of the temperature than the surrounding medium (i.e. a small value of the plasma parameter $\beta$). An example of magnetic cloud is shown in Fig. 91. Magnetic clouds are generally compatible with a flux rope configuration; an association with a CME having a typical three-part structure is often assumed. The bright front corresponds to the sheet of compressed solar wind and the dark cavity comprises the flux rope structure. Roughly

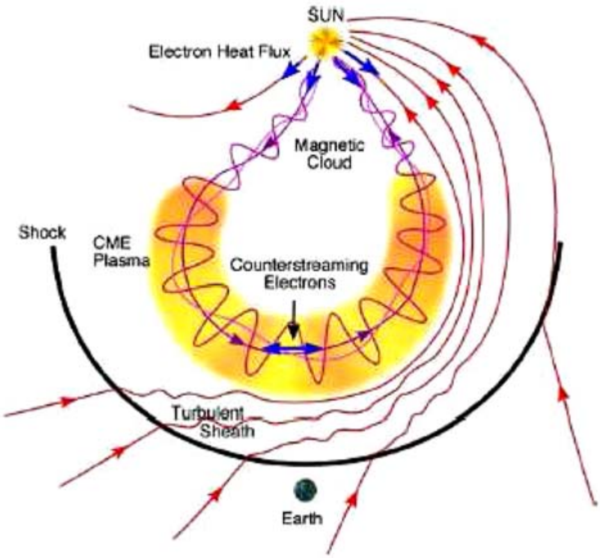


**Fig. 92** Schematic of the three-dimensional structure of an ICME and upstream shock, relating magnetic field, plasma and BDE signatures (Zurbuchen and Richardson 2006)

speaking 30% of the identified ICMEs show the large scale field rotation characteristic of flux ropes (Gosling et al. 1990).

The global magnetic structure of ICMEs has been a highly controversial debate for a long time: has it the shape of a bottle, of a bubble, or of a tongue? Is the structure still connected to the corona or not? Suprathermal electrons ($\geq$80 eV) constitute a continuous source of field-aligned particles from the Sun and provide a large amount of information about the ICME-connection. Counterstreaming beams are interpreted as a signature of closed field lines connected to the Sun at both ends and observation of bidirectional electrons (BDEs) provide a widely accepted identification of ICMEs (Gosling et al. 1987). Unidirectional beams which flow away from the Sun trace open field lines connected at only one end (Gosling et al. 1995). Studies of suprathermal electrons as well as of high-energy particles lead to conclude that ICMEs contain a mixture of closed, open and infrequently disconnected field lines (for references see Crooker and Horbury 2006; Wimmer-Schweingruber et al. 2006). A schematic representation, derived from magnetic field, plasma and BDE signatures, of the three dimensional structure of an ICME and of an upstream shock is shown in Fig. 92.

A complete discussion of ICMEs and of their link to CMEs is beyond the scope of this paper, we shall only recall here a few results for which radio observations have largely contributed.

## 8.1 Association between interplanetary disturbances and coronal mass ejections

As discussed in Sect. 6, radio images of the solar activity at decimetric/metric wavelengths provide characteristic signatures of the onset of CMEs above the solar disk.

This has been used by Vilmer et al. (2003) in their search of the CMEs which could be associated to a sample of 40 interplanetary disturbances. For many of them, the LASCO observations allowed to identify the corresponding CMEs. For some others, it was necessary to use the NRH observations of extended radio sources usually associated to the development of CMEs (see, e.g. Fig. 114) in the identification of the solar source of ICMEs. In fact, an association between interplanetary disturbances and LASCO/CMEs, or proxies on the disk, was found for 36 of the 40 events. Also, the solar sources for the CMEs were identified in most cases to be associated with a flare-like signature in an active region (not excluding of course the involvement of a filament).

## 8.2 The magnetic connection between the corona and the interplanetary medium. Existence of channels and topology of ICMEs

Several independent studies evidenced the existence in the interplanetary medium of spatial structures in which electron beams can propagate without nearly any scattering (McCracken and Ness 1966; Anderson et al. 1982; Anderson and Dougherty 1986). We show below, through a few examples, how the results of these studies provide a deeper understanding of the radio wave process and of the structure of the heliosphere.

Anderson and Dougherty (1986) observed occasional changes in the intensity of low energy interplanetary electrons and ions at 1 AU that are characterized by a square-wave appearance and a duration $<6$ h. They argued that these features represent spatial regions in which the particle intensities differ from the surrounding region. The local transverse dimension of these regions is of the order of $10^6$ km at 1 AU. In one such example, electrons associated with a solar flare and metric type III bursts flew away from the Sun in a well defined channel. They concluded that this "propagating channel" was connected to a region of the solar atmosphere which supplies these flare accelerated electrons.

Coronal and interplanetary type III bursts have been used to identify the trajectories followed by the electron beams associated with these bursts (e.g. Larson et al. 1997). These beams are often found to be highly collimated along the magnetic field lines of the interplanetary medium. This is due to the decrease of the field strength and also to the weak pitch angle scattering that the electrons encounter as they move from the Sun to the observer (mean-free path $\geq 1$ AU) (Beeck and Wibberenz 1986; Earl 1976, 1981). As recalled in Sect. 2.2.2, electrons and Langmuir waves measured in-situ by spacecrafts were associated with type III emissions (e.g. Lin et al. 1973; Gurnett and Anderson 1976). In 1992, Reiner et al. (1992) reported the first simultaneous detection of fundamental and harmonic local type III radio emission and in-situ Langmuir waves. They concluded that these emissions were generated in localized regions of the interplanetary medium (most probably the "propagating channels"), rather than uniformly along the extent of the electron exciter.

The Ulysses space probe provided an opportunity to investigate the existence of the "propagating channels" to larger distances from the Sun, when the spatial scale of the structures mapped out from the solar corona increases in proportion to the heliocentric distance. Buttighoffer et al. (1995) and Buttighoffer (1998) performed

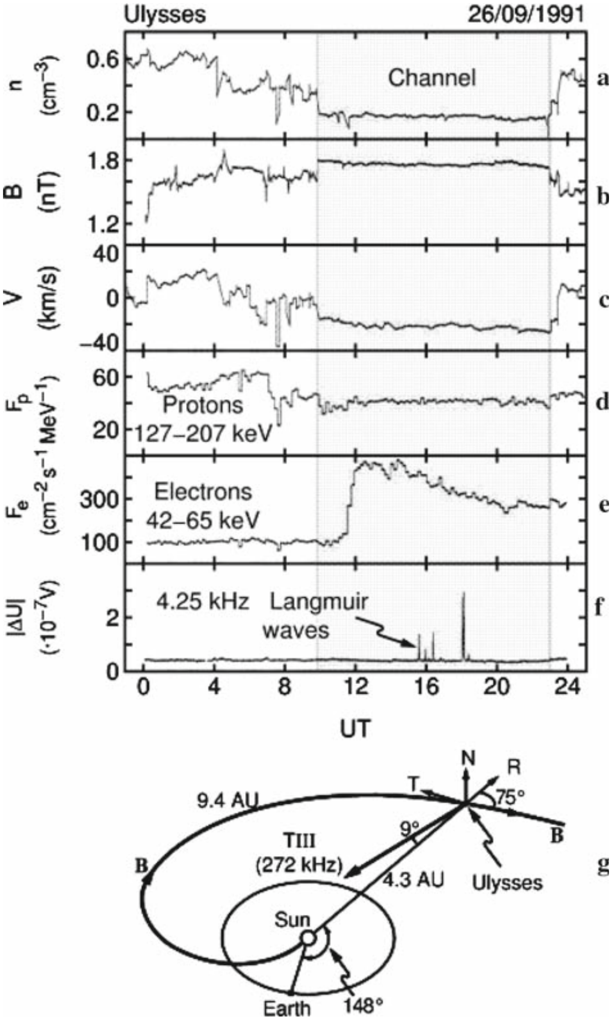


**Fig. 93** Summary of the September 26, 1991 observations. *Upper panel* from top to bottom, plasma density, magnetic field amplitude, transverse solar wind speed, ∼100 keV ion fluxes, 40–60 keV electron fluxes, radio noise at 4.25 kHz. The zone delimited in *grey* corresponds to the channel crossing clearly identified in the three upper panels. *Lower panel* Ulysses-sun connection configuration (Buttighoffer et al. 1995)

a joint analysis of the three aspects of interplanetary type III bursts, namely radio, particle and plasma waves. All the type III bursts selected for this study drifted to very low frequencies (close to the plasma frequency or its first harmonic) and were unambiguously associated with Langmuir waves and with solar electron events. One important result of this study was to establish that the interplanetary medium contains, well beyond 1 AU, propagating channels which are anchored in the solar corona. This is illustrated in Fig. 93. The main characteristic of these channels is their local low level of magnetic field fluctuations and the confinement of these fluctuations inside the plane perpendicular to the average magnetic field. This configuration may produce favourable conditions for scatter-free propagation along trajectory lengths beyond 10 AU (Buttighoffer et al. 1999). Some of these channels were also found inside ICMEs (see, e.g. Chaizy et al. 1995). The existence of channels in ICMEs is understandable, given that they are known to be regions of very quiet magnetic field.

A unidirectional (antisunward), nearly scatter-free, event of streaming 60 keV–5 MeV ions (energy spectrum peaked at 270 keV) and of 38–315 keV electrons was identified, for the first time on June 12–13, 1993, during the passage of an ICME over the Ulysses spacecraft at a radial distance of 4.6 AU and heliolatitude of 32° (Armstrong et al. 1994). This ICME had an internal structure similar to that expected for a large magnetic flux rope. The ion and electron pitch angle distributions (PADs) had a bidirectional component in the outer (large pitch) regions of the flux rope, while there were strongly (antisunward) beams in the inner (small-pitch) core of the structure, where the electron PADs also displayed a distinctive depletion of electrons moving sunward. No signature of particle acceleration by a local interplanetary shock was detected. The ion beam was associated with a large HXR and radio type IV burst detected on June 7, in a region magnetically connected to Ulysses for a solar wind speed of 700 km $s^{-1}$ (Pick et al. 1995). The abrupt increase and decrease of the particles and their pitch angle distribution (PAD) strongly suggest that the particles were streaming along the axis of the flux rope with IMF rooted in the coronal particle source. The absence of returning ions or electrons, during 13 h, suggests that the IMF allowed escape of these particles to distances at least 10–20 AU beyond Ulysses.

## 8.3 Origin and transport of accelerated particles detected at high heliolatitudes

Combined observations of radio emissions and particle pitch angle distributions in the interplanetary medium were also used to investigate the origin and transport of fast particles at various heliolatitudes. In the solar corona, there exists a great variety of loops connecting opposite magnetic field features at different scales. When a structure becomes unstable and loops start expanding, these loops interact with magnetic loops of higher altitude which may lead to a large-scale reorganization of the coronal structure. As shown in Sects. 5 and 6, these regions of magnetic field interaction can be the sources of electron acceleration. One of the highest heliolatitude electron events detected by Ulysses occurred at 73.8° S on October 25, 1994. This event was associated with a long-duration X-ray flare, observed close to the equator, that started with the expansion of twisted loops. Series of radio bursts, two remote X-ray brightening and new coronal loop connections also took place. They all are signatures of a large-scale reconnection process between the expanding twisted flare loops and overlying trans-equatorial loops connecting quiet Sun regions. Figure 94 shows a synthetic view of the magnetic field regions and of the main features observed during the development of this event. The external part of the overlying large-scale fields was pushed out in the solar wind by the expanding twisted loops. They lead to the formation of two coronal holes above weak magnetic field regions of opposite polarity. Strong radio continua were observed above the flare site which last several hours. Several type

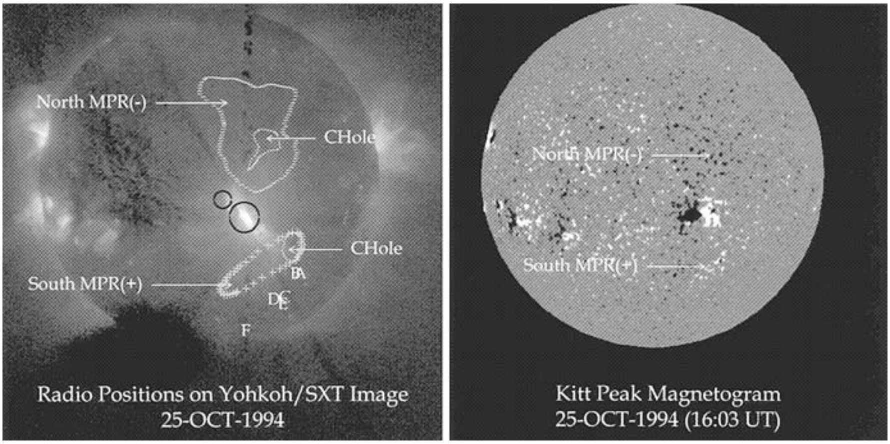


**Fig. 94** *Left panel* Projected positions of the radio bursts superposed on a Yohkoh image on October 25, 1994. The *symbols A–F* indicate the successive locations in time of type III radio bursts. Regions of continuum emission (and pulsating radio bursts north-east of the active centre) are shown as *circles*. The monopolar positive and negative magnetic field regions (from KPNO magnetogram) are outlined by the corresponding symbols (north, *minus* signs; south; *plus* signs). New coronal holes formed after the flare are indicated by *dotted lines* ("CHole"). Taking projection effects into account, the bursts A–F appear above the positive monopolar magnetic region. *Right panel* Magnetogram observed on the same day at KPNO (from Manoharan et al. 1996)

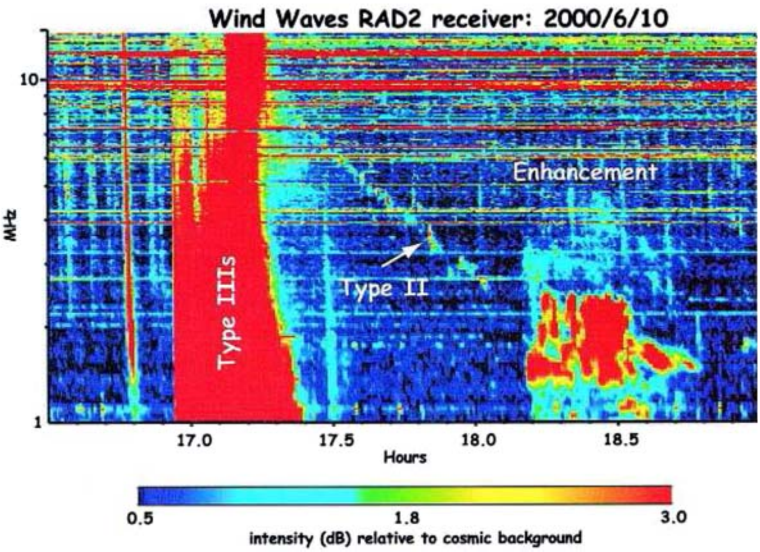


**Fig. 95** Wind/WAVES dynamic spectrum in the 1–14 MHz range. The vertical features are type III-like bursts. The *thin slanted feature* is a type II burst. The bright emission, seen between 18:12 and 18:48 UT, corresponds exactly to the time of interaction between two ICMEs (from Gopalswamy et al. 2001)

III bursts were also detected; their positions, marked by the symbols A–F in Fig. 94, move from the vicinity of the equatorial region to a south heliolatitude as high as

65°. These bursts follow the expansion of the X-ray loops both in time and in space. Interaction between the active region and the large-scale fields which persisted during several hours, may explain the opening of the magnetic field and the detection of the high energy electrons in the interplanetary medium.

## 8.4 ICME interactions

SOHO observations have shown that different CMEs can occur in close spatial and temporal proximity and that they can interact during their propagation in the IP medium. Some ICMEs can thus originate from more than one CME. The term "compound stream" describes high speed flows which are composed of multiple components, either streams or ICMEs (Burlaga 1975). Interactions between fast and slow CMEs have also been identified by long-wavelength radio and white light observations. During these interactions, intense localized radio emissions are detected as shown in Fig. 95 (Gopalswamy et al. 2001, 2002). These emissions occur at the low frequency end of the decametre/hectometre type II bursts. Gopalswamy et al. (2004) proposed that the efficiency of the CME-driven shocks is enhanced as they propagate through the preceding CMEs and that the Solar Energetic Particles (SEPs) are accelerated from the material of the preceding CMEs rather than from the quiet solar wind.

## 9 Radio diagnostics of energetic electron acceleration in the corona and in the interplanetary medium

Solar Energetic Particle events (SEP), which are detected in-situ from GeV down to keV energies, have been divided into two groups, referred to as "impulsive" and "gradual" events and this classification was commonly accepted until the launch of the Advanced Composition Explorer (ACE) in 1997. In the two-class paradigm for SEP events proposed by Reames (1995, 1999), the flare process accounts for the acceleration of the impulsive events which are not associated with CMEs. Conversely, for the gradual events the acceleration is dominated by CME driven coronal and interplanetary shocks (not flares). The narrow cones of emission (less than 30°) and high-Fe charge states (+20) of impulsive events are consistent with an acceleration from a localized, high temperature (3–5 MK), flare plasma. Energetic particles from impulsive events also show abundances of heavy elements (e.g. Fe) strongly enhanced with respect to coronal abundances. These events are also richer in electrons than in protons and are enriched in $^3$He. Conversely, acceleration by large-scale shocks is consistent with the large longitude cone of SEPs in long duration events and with their low Fe-charge states (+11 to 14) indicating an origin from 1 to 2 MK coronal/solar wind plasma. While the impulsive SEP events are all well connected with the flare region and are associated with metric type III bursts, the events associated with long-duration flares, can take place anywhere on the solar disk, extend to much higher proton energies and are well associated with coronal and interplanetary shocks (Cane et al. 1986).

The above two-class paradigm mainly originated from the classification of radio emissions and from the study of their link to interplanetary protons and geomagnetic effects, as introduced by Wild et al. (1963). As discussed in Sect. 2.1.3, these authors introduced the concept of two successive phases: an initial impulsive one and a subsequent gradual phase occurring only in large flares. During impulsive flares, the acceleration lasts typically a few minutes, while in the long duration flares, it lasts for tens of minutes, and the acceleration is supposed to take place at extended shocks revealed by type II bursts. In that case, the accelerated particles will be either partly trapped in coronal loops, or will escape into the interplanetary medium. Note that this model, which assumes a coronal trapping of the accelerated radiating electrons, should explain how the broadband emission of type IV bursts (flare continua) display similar intensity variations at all frequencies, despite the large distance in height of the emitting sources (see Sects. 2.1.2 and 2.1.3, Pick-Gutmann 1961; Kundu 1961).

During the past few years, however, several in-situ measurements of the composition and of the charge states of ions, more particularly from ACE, (e.g. Cohen et al. 1999), have indicated that this view is probably oversimplified. The new observations show indeed that gradual SEP events are accelerated not only from the solar wind plasma but also from an additional seed population (see for a review Mewaldt et al. 2006). Some gradual SEP events include a mixture of flare-accelerated and shock-accelerated types of particles. These new observations raised some questions on the validity of the previous classification.

Moreover, the ability of shocks to accelerate rapidly up to GeV energies coronal and solar wind particles has stimulated many controversial debates. Furthermore, it had already been noted for several years that HXR and radio signatures of energetic

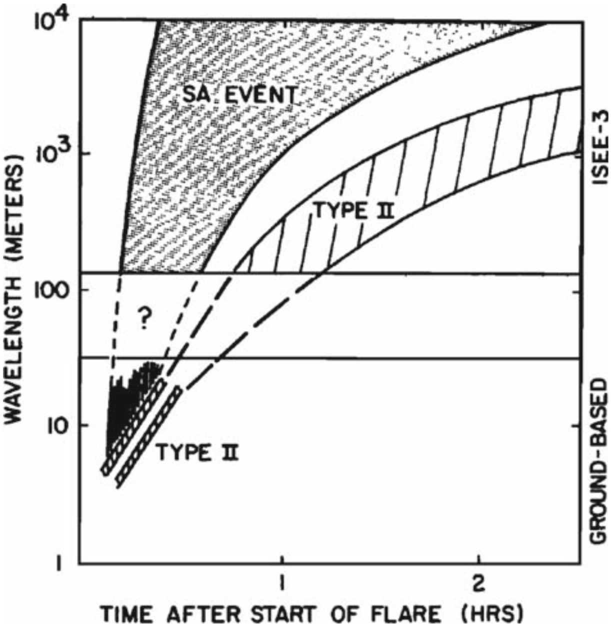


**Fig. 96** Schematic representation of the relationship between metre wavelength type II activity with herringbone structure (see text) and the activity observed at kilometric wavelengths. Only the long wavelength elements of the herringbone structure are shown (from Cane et al. 1981)

electrons at the Sun showed that these electrons could be accelerated quasi continuously for several tens of minutes or hours even in the absence of type II shocks (see Trottet 1986) and Sect. 4.2.1. Gamma ray observations also led to the conclusion that relativistic ions can be produced for hours at the Sun (e.g. Kanbach et al. 1993).

In conclusion, there is today a general agreement that the two class paradigm was too simplified. Gradual SEP events can in fact include particles which originate from flares and from CMEs in different ways: particles can be accelerated by CME driven shocks or in the reconnection sites of field lines pulled out by CMEs (see Sect. 6), or linked to CME interaction (see Sect. 8).

We review here how the radio observations significantly contributed to improve our knowledge on the origin and the propagation of these energetic particles. Let us nevertheless point out that, as radio emissions only give access to electron acceleration, any comparison between radio observations at the Sun and the energetic ions measured in-situ is an indirect one.

## 9.1 Role of the shock waves in the production of SEP events

Cane et al. (1981) introduced a new class of kilometric type III burst events originally called Shock Accelerated (SA) events since they were associated with metric type II bursts. These events are intense and of long duration (typically over 20 min at 1 MHz); they display signatures of multiple electron injections (see Fig. 96). Due to their association with type II bursts, it was proposed that the SA events are produced

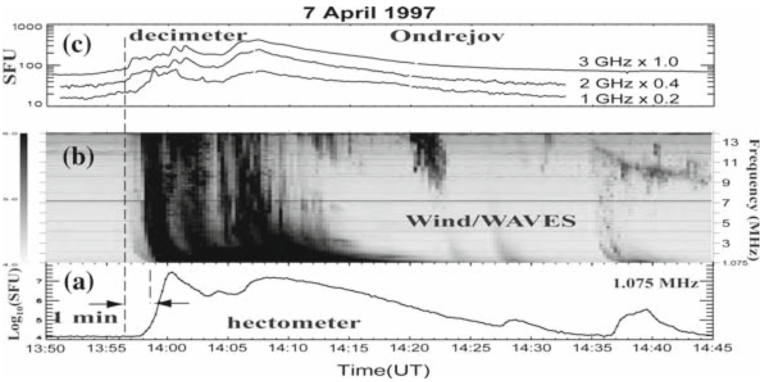


**Fig. 97** Comparison of the complex type III burst observed on April 7, 1997 by Wind/WAVES in the frequency range from 1 to 14 MHz with the radio emissions observed by Ondrejov observatory from 1 to 3 GHz. Note the similarity in the shape and duration of the intensity-time profiles in these widely separated frequency regimes (adapted from Reiner et al. 2001)

by electrons accelerated in the high corona by the same shock that produces the type II bursts. The authors concluded that this new class of bursts is the long wavelength continuation of the herringbone structure in type II bursts, first described by Roberts in 1959. An herringbone structure is composed of many fine bursts, resembling type III bursts, originating in the "backbone" of the type II burst and drifting to higher and/or lower frequencies. Herringbones are assumed to be produced by electrons which are accelerated by the shock front and escape up or down in the corona. This interpretation was commonly accepted (Cane and Stone 1984; MacDowall et al. 1987; Kahler et al. 1989). However, MacDowall et al. (1987) underlined that the lack of radio spectral observations in the frequency range 2–20 MHz made difficult the distinction between two components: the regular kilometric one attributable to metric type III activity and the component possibly due to shock accelerated electrons. Furthermore, Kundu and Stone (1984) also noted that the duration of this kind of kilometric type III events (SA events) was similar to the duration of associated microwave continua; they thus argued in favour of a low coronal acceleration process.

More recently, the new data from Wind in the 1–14 MHz window (Bougeret et al. 1995) provided a direct proof of the association between hectometric-kilometric emissions and the radio emissions at higher frequencies (Reiner and Kaiser 1999b). In the example shown in Fig. 97, the close similarity in the 3 GHz and 13.82 MHz profiles of the radio emission indicates that the complex type III-like emission detected by WAVES is produced by electrons accelerated in coronal regions, as formerly suggested by Kundu and Stone (1984). Reiner et al. (2001) also observed that complex type III-like emissions, including the original SA events identified by Cane et al. (1981), are usually associated with major flare/CME events of wide angular extent (see also Pick et al. 2005b).

More recently, Cane et al. (2002) showed, in agreement with previous results (Klein and Trottet 1994), that the long duration kilometric type III-events usually start at frequencies higher than the corresponding type II bursts, if present. They thus concluded that, contrary to the original interpretation, these observations argue against a shock-

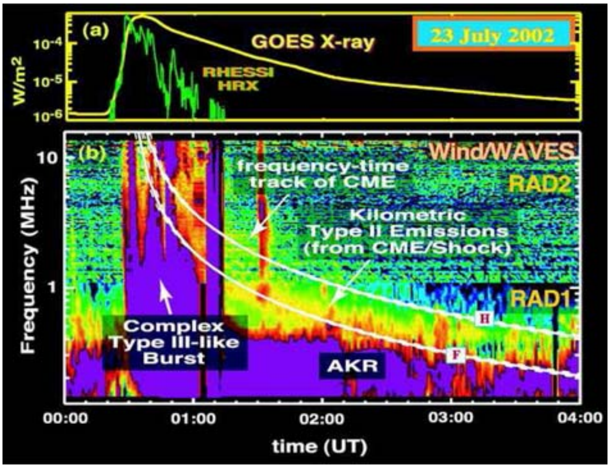


**Fig. 98** Overview of the X-ray and low-frequency radio emissions associated with the July 23, 2002 X4.8 LDE X-ray event. **a** GOES soft X-ray and RHESSI HXR emissions observed from 00:00 to 04:00 UT. **b** Radio dynamic spectrum in the frequency range from 125 kHz to 13.8 MHz, over the same time period, showing the intense, complex type III like emissions (overexposed) associated with the flare and the slowly frequency-drifting type II emissions generated by the propagation of the associated CME through the interplanetary medium. The *curves* on the dynamic spectrum correspond to the frequency-time track of the CME, generating radio emissions at the fundamental and harmonic of the plasma frequency (from Reiner et al. 2007a)

acceleration origin. Cane et al. (2002) also established that >20 MeV SEP events are associated with this class of complex type III like events, which also questions the production of SEPs by shock waves. This is consistent with results of Klein et al. (1999b) based on the comparison, for two large flares, of gamma-ray, X-ray and radio diagnostics of interacting particles and in-situ detection of ≥20 MeV protons at 1 AU. They indeed showed that (a) successive increases of protons fluxes can be traced back to episodes of coronal acceleration (see also Klein 2005); (b) the increasing richness of relativistic protons observed during the SEPs is associated with the injection of new coronal particles after the impulsive phase.

Finally, Reiner et al. (2007a) established, for the very energetic 2002 July 23 $\gamma$-ray event, that a good temporal relationship (similar duration and intensity variations) exists not only between the hectometre and decimetre/microwave fluxes but also with the HXR light curves measured by RHESSI. This suggests a single acceleration process for all the particles: while both HXR and microwave emissions are likely produced by a population of downward propagating high-energy electrons (∼100 keV), the low frequency-emissions are generated by a different but linked population of escaping electrons of lower-energy (<10 keV). Figures 98 and 99 show, respectively, an overview and an expanded view close to the onset of the event. For this event, as well as for others, the complex type III-like emissions exhibit diminished radiation intensities near 7 MHz, suggesting that the exciting electrons are accelerated low in the corona and lose their ability to generate radio emissions via the bump-on tail instability. Figure 99 shows that this diminution occurs when the electrons cross the turbulent region in the vicinity of the overlying CME and its associated shock.

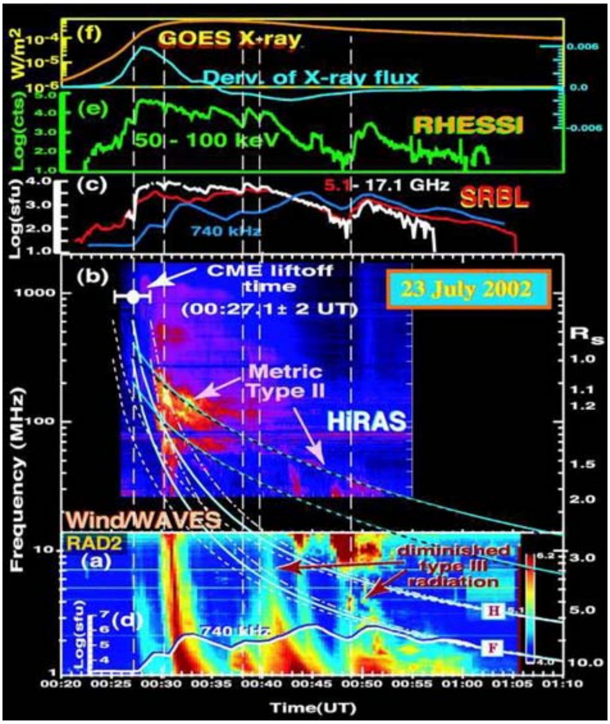


**Fig. 99** **a** High-frequency/time resolution Wind WAVES dynamic spectrum from 00:20 to 01:10 UT in the frequency range from 1 to 13.8 MHz showing, in more detail, the complexity of the type III radio emissions. **b** The Hiraiso radio (HiRAS) dynamic spectrum in the frequency range from 25 MHz to 2.5 GHz showing the metric type II, type III, and type IV radio emissions associated with this event. **c** The intensity profiles of the radio emissions measured by the Solar radio burst locator (SRBL) at 5.1 and 17.1 GHz and superposed flux density at 0.74 MHz. **d** The intensity-time profile of the radio emissions at 0.74 MHz. **e** The *light curves* of the various HXR sources observed by RHESSI. **f** The GOES soft X-ray flux (*orange curve*) and the derivative of this flux (*blue curve*). The curves overlying the dynamic spectra correspond to the frequency-time tracks of various possible coronal and CME-driven shocks associated with this event. Note that the projected lift-off time of the CME corresponds, to within the measurement uncertainties, to the onset of the impulsive RHESSI HXR event and sudden rise in the 2.5–17.1 GHz radio flux indicating a significant particle acceleration event (from Reiner et al. 2007a)

In summary, all these results are consistent with the interpretation that during flare/CME events, the accelerated electron streams originate in coronal regions possibly located in the aftermath of CMEs. They are presumably accelerated inside the changing magnetic configurations during the initial CME development in the low corona (see discussion in Sect. 6.4 and in the next subsection).

## 9.2 Impulsive electron events

### *9.2.1 Timing and location of energetic electron release at the Sun*

Krucker et al. (1999) and Haggerty and Roelof (2002) identified two different kinds of impulsive electron events at energies above 13 keV: (a) events released from the Sun

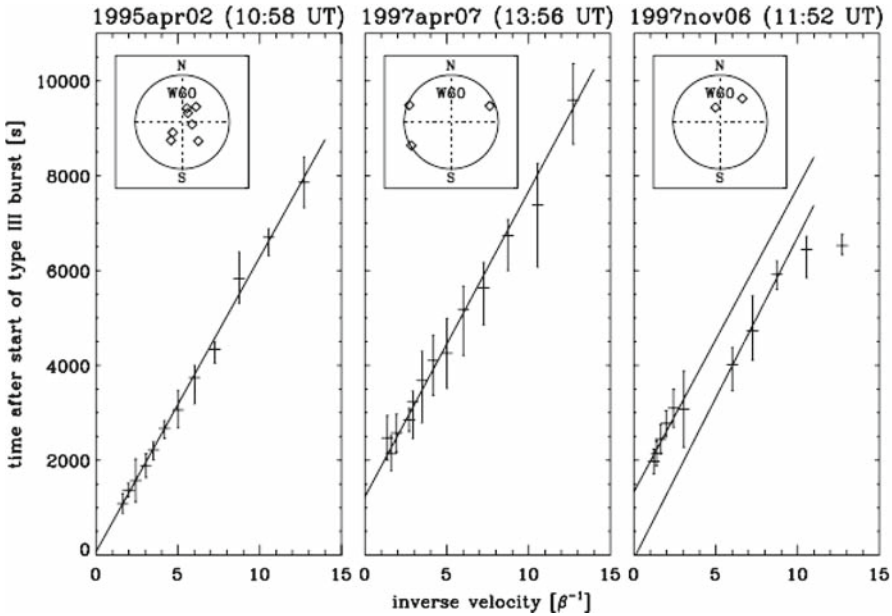


**Fig. 100** Examples of the three different classes of in-situ impulsive electron events that have very different velocity dispersion characteristics. In all cases, the light propagation time was added to permit direct comparison of the injection times with the times of the observed solar radio emission (adapted from Krucker et al. 1999)

at the onset of a radio type III burst, which suggests that these electrons are part of the population producing the type III radio emission and (b) events in which the electrons are released up to half an hour later than the onset of the type III burst. Estimates of the electron release time at the Sun strongly depend on the assumptions made on the particle propagation process. For those events that show highly collimated pitch angle distributions (which indicates field-aligned streaming), the release time can be calculated by determining the times it takes for particles of a particular energy to travel along a Parker spiral of length 1.2 AU (corresponding to a solar wind speed of 400 km $s^{-1}$). This is the method applied by Haggerty and Roelof (2002) to estimate the release time of impulsive, near-relativistic, electron events magnetically well connected to the injection site. Another possible analysis consists in plotting the arrival time of particles as a function of their inverse speed. Such a plot is expected to produce a straight line with a slope corresponding to the path length while the intercept on the time axis indicates the injection time. Using this method, Krucker et al. (1999) found that impulsive electron events could be classified into three categories depending on the characteristics of the observed velocity dispersion (see Fig. 100). In the first category, the onsets at all energies lie along the same straight line and the injection time coincides with the onset of type III emission; in the second category, the onset times still lie on a single straight line but the electron release time is delayed with respect to the type III burst onset. In the third category, the high (>25 keV) and low (<25 keV) onset times are now located on two different straight lines with the same slope, clearly

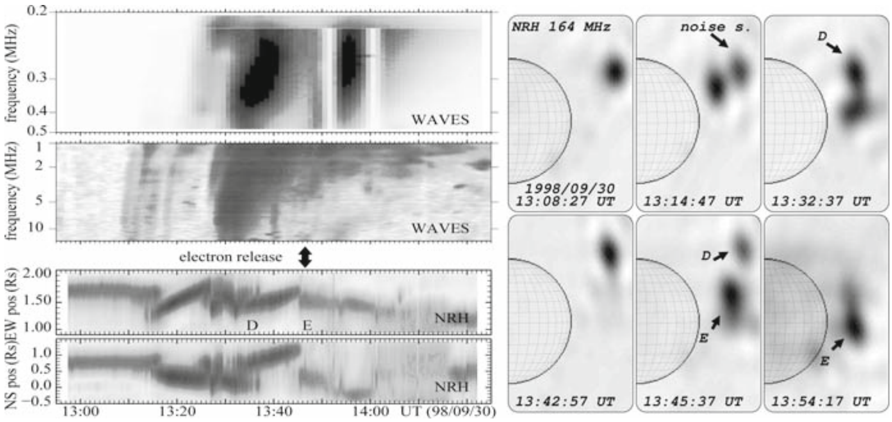


**Fig. 101** September 30, 1998: *Left panel* Comparison of the emission observed by the NRH (*bottom*) and WAVES (*top*). The *vertical white bands* seen in the WAVES spectrum are due to the saturation. The *one-dimensional plot* shows a series of radio-sources. D marks a moving continuum, followed by another one labelled E. The *arrow* indicates the inferred release time at the Sun for the electrons with energies above 100 keV. Note that this time coincides with the sudden disappearance of D, the onset of E, and with the low frequency type III burst detected by WAVES. *Right panel* Panel of images showing the positions of the sources seen by the NRH (from Maia and Pick 2004)

showing a delayed injection for high energy electrons (see also Wang et al. 2006). Several explanations have been proposed for these delayed events that involve a second acceleration process; the delayed acceleration may be due to the coronal counterpart of EIT waves detected by SOHO (Krucker et al. 1999) or to CME-driven shocks (Simnett et al. 2002) or to the change of magnetic field configuration in the corona (Pick et al. 2003). Cane and Erickson (2003) alternatively proposed that these delays result from the particle transport in the IP medium.

From the analysis of the time and places where the energetic particle are released in the corona, Maia and Pick (2004) and Klein et al. (2005b) showed that the delayed electron events are usually associated with complex and long lasting radio emissions observed in a broad frequency range; the NRH imaging observations show abrupt modifications in the emitting regions close to the estimated time of the electron release (see Fig. 101). These modifications, which are direct signatures of energetic electrons, are related with continua onsets or type II-like features and are also commonly associated with packets of complex type III-like emissions (Pick and Maia 2005c). This association is consistent, as in the previous cases, with an interpretation in which electron acceleration is triggered at different sites by magnetic reconnection in the wake of the CMEs. The electrons are then injected along discrete open magnetic flux structures (see Sect. 6.4) magnetically connected or not with the spacecraft. When the abrupt modifications of the radio emitting structures are associated with type II-like features, observations suggest that the coronal restructuring be also related to the interaction between magnetic structures, due to the passage of a coronal wave (Maia and Pick 2004; Lario and Pick 2007). As an example, the 2001 September 24 event was associated with an eastern flare (S16-E23), a fast CME, a type II burst at 7 and 4 MHz and a complex type III like event. As shown in Fig. 102, the west-

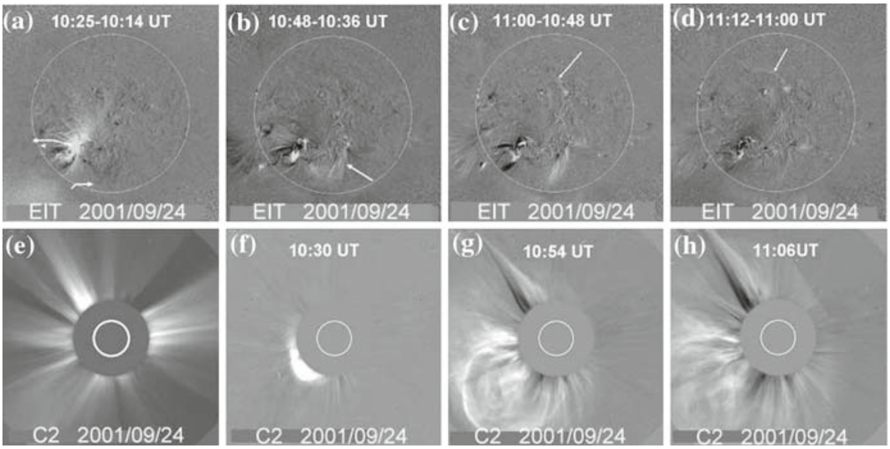


**Fig. 102** Difference images from EIT (*panels a–d*) and LASCO (*panels f–h*) showing the development of the September 24, 2001 event. *Panel e* shows the pre-event corona with a well marked streamer in the north-east quadrant. The *arrows in panel a* indicate the direction of displacement of the sources of type III burst as seen by the NRH. The *arrows in panels b–d* indicate the extension of the CME flanks toward the southwest (*panel b*) and north (*panel c–d*). *Panels g–h* show the extension of the CME and the direction of the north-east streamer (adapted from Lario and Pick 2007)

ern flank of the CME propagated from the flare region to about 20° W where it apparently stopped. Coronagraph and EUV images, combined with a magnetic field extrapolation, suggest that an area of open field lines is located beyond the boundary region where the propagation of the western CME flank stops. Beyond this region, all coronal structures also appear to be distorted consistently with the propagation of a coronal wave or a shock. The injection of energetic electrons in the interplanetary medium can be understood as follows: the CME creates a compression region at the interface between closed and open field line areas. As the CME flank reaches this specific region, approximately at the estimated time when the electrons measured by ACE are released, the high energy electrons are produced and injected in the IP medium from the vicinity of this boundary which is well connected to the Earth. In such an event, the electrons could be accelerated either in the current sheet created in this boundary region or alternatively by the coronal shock. Such a result is consistent with the detection of a Moreton wave found for similar events: this wave could create a secondary acceleration site far remote from the primary one (Krucker et al. 1999).

Krucker et al. (2007) compared electron spectral index deduced from hard-X-ray spectra observed by RHESSI with the electron spectral index of the associated solar particle events observed near 1 AU by the WIND 3DP instrument. They found that for the prompt electron events (no delay), the in-situ spectral index correlates well with the spectra deduced from HXRs for interacting electrons (see Fig. 103). Conversely, the events with "delays" show no meaningful spectral index correlation between in-situ electron spectra and the spectra deduced from HXRs. This confirms that an additional electron site is probable for delayed events.

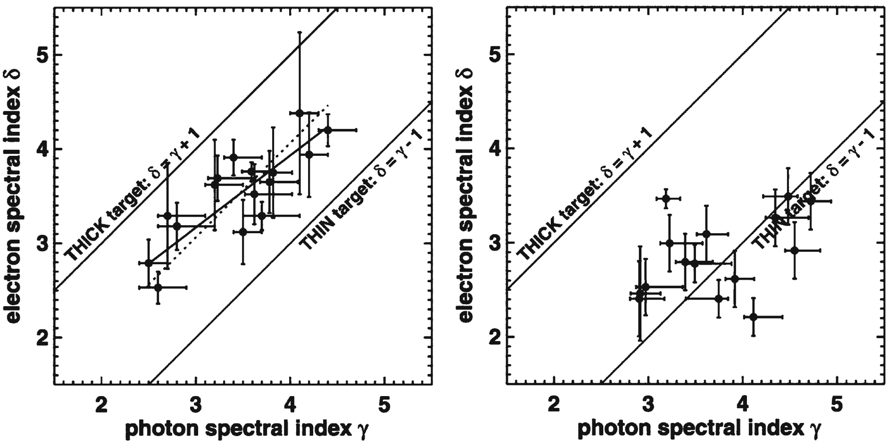


**Fig. 103** *Left panel* Correlation plot of the photon spectral index $\gamma$ and electron spectral index $\delta$ for prompt events; a positive correlation with a coefficient of 0.83 is observed. The *solid line* is a linear fit to the data; the *dotted line* is a fit to $\delta = \gamma$ giving $a = 0.1 \pm 0.1$. *Right panel* The same as the left panel but for delayed events; no correlation between the power low indices is observed, suggesting that two different acceleration mechanisms release the HXR-producing electrons and the escaping electron population for delayed events (adapted from Krucker et al. 2007)

### *9.2.2 Origin of solar $^3$He-rich impulsive energetic events*

As recalled in the introduction of this Section, impulsive SEP events are closely correlated with type III bursts (Reames 1999) and are very often characterized by $^3$He/$^4$He ratios greater than the coronal values by factors up to $10^3$–$10^4$, by enhancements in heavy ions as Ne and Fe, and by a dominance of electrons over protons (see for a review Mason 2007). The timing of the electron beams is correlated with observations of metric and kilometric type III bursts. These SEP events are focused into a relatively narrow ($\leq$30°) cone and are detectable only when a direct magnetic connection exists to the flare site which must be located in the western hemisphere. Kahler et al. (2001) discovered that a fast narrow ($\sim$20°) CME was associated with the $^3$He-rich SEP event of May 1, 2000. Pick et al. (2003) furthermore showed that this event was associated with a series of type III radio sources that moved outward with a velocity comparable to the projected CME velocity. In a study focused on the solar origin of 25 impulsive $^3$He-rich SEP events, Wang et al. (2006) found that, around the estimated particle injection time, EUV images often show a jet like ejection aligned with the open field lines which is interpreted as a signature of magnetic reconnection. These events are accompanied by fast (500–1,000 km s$^{-1}$) and narrow white-light ejections, which are, when observed, often directed out of the ecliptic plane (Fig. 104). Surveys of $^3$He emissions also show the existence of periods of nearly continuous emissions (Wiedenbeck et al. 2003), (see Fig. 104b). During these periods, recurrent white light jets or narrow CMEs are observed (Fig. 104d). As shown in Fig. 104c, for every jet that occurred during the viewing hours of the NRH, a type III burst was seen in the same area as the jet and impulsive electron events were also associated. Moreover Wang et al. (2006) showed, by applying a potential field source surface (PFSS) extrapolation

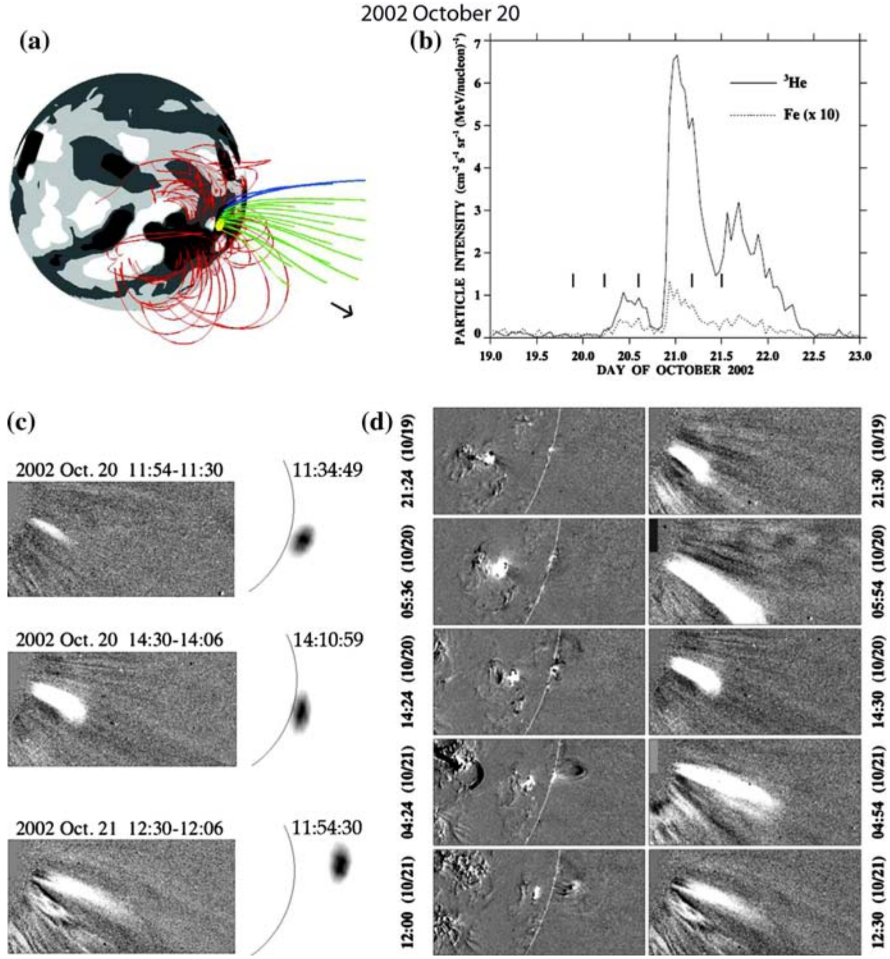


**Fig. 104** Sources of $^3$He events. *Panel a*: Solar disk showing magnetic field regions with intensity coded in *black, grey and white*, between $<-10$ and $+10$ G. Potential field source surface calculation (PFSS) shows closed field lines (*red*), open field lines (*green*) and *open field lines* to ecliptic (*blue*). The *yellow dot* near the source of open field lines is the identified source location (see text). *Panel b*: Extended $^3$He-rich period October 19–22, 2002 showing $^3$He abundance over several days. *Panel d*: Successive jets from associated flaring active region, with each flare indicated by *vertical line in panel b*. *Panel c*: Sources of type III bursts identified by the NRH during the same period (adapted from Wang et al. 2006; Pick et al. 2006b)

to magnetograph measurements of the photospheric field, that the Earth-directed open field lines are rooted next to the source of each impulsive event (Fig. 104a) which is identified from the location of the EUV or H$\alpha$ event (yellow dot); then, the injected energetic particles promptly reach the spacecraft following field lines that connect the source region to the ecliptic plane; they are not constrained to follow the same trajectory as the bulk of the CME (Pick et al. 2006b). These results are consistent with former studies which showed that the sources of type III bursts, when observed with a

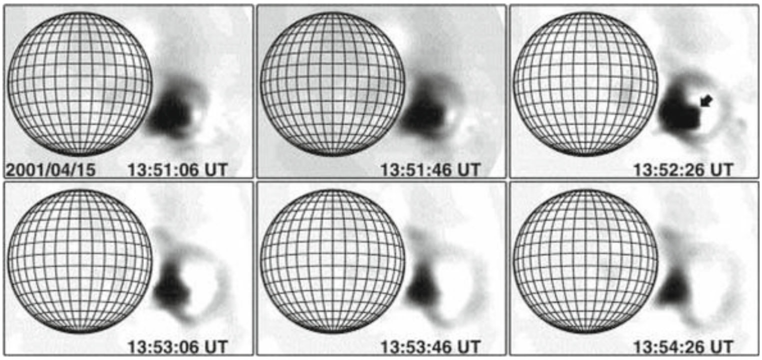


**Fig. 105** Series of NRH images showing the progression of a radio CME on April 15, 2001. The images are 10 s integrations at an observing frequency of 410 MHz (adapted from Maia et al. 2007)

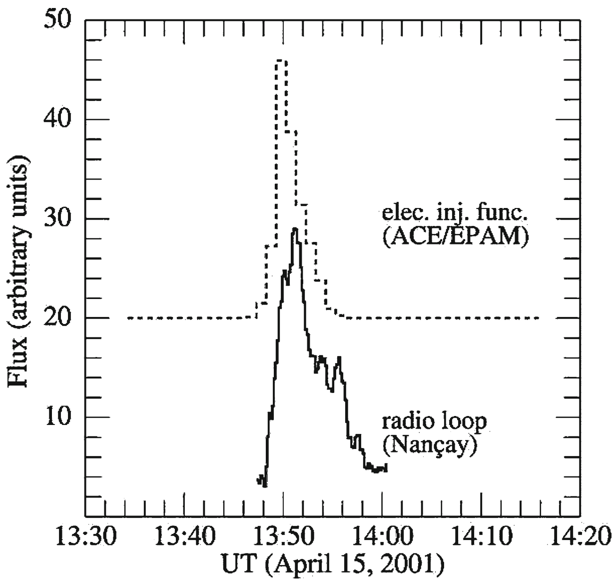


**Fig. 106** Comparison of the near-relativistic electron injection function and radio loop flux at 432 MHz. The *dashed line* shows the electron injection function that best fits the ACE EPAM electron observations; the *solid line* shows Nançay radioheliograph observations at 432 MHz of the radio loop. Both curves agree remarkably well in onset time and duration (from Maia et al. 2007)

high cadence $\leq 1$ s, are resolved in components located along diverging magnetic field lines (Raoult and Pick 1980).

### 9.3 Association between a radio CME and relativistic electrons measured in-situ

As discussed in Sect. 6.6, Bastian et al. (2001) identified expanding loops behind CME front illuminated by synchrotron radiation from 0.5 to 1 MeV electron (radio CMEs). The radio CME detected on April 15, 2001 was associated with an electron event measured in-situ by the ACE satellite (Maia et al. 2007). The progression of the radio loops was followed from a few tenths to more than one solar radius above the solar limb. The high energy cut-off of the gyrosynchrotron emitting electrons in the loop was estimated to be of the order of 1 to a few MeV which shows that particles both inside the loops and detected in-situ have comparable energies. A detailed transport model for the electrons detected in-situ showed that not only the inferred onset at the Sun but also the duration of the energetic electron release at similar energies were similar for the electrons injected in the radio loop and in the interplanetary medium (Figs. 105, 106); they are accelerated then released when the CME is very low in the corona, a few tenths of radius above the limb. Furthermore, the onset time of relativistic ions, deduced by Bieber et al. (2004) from ground-based measurements, as well as onset times of ions and electrons at different energies determined by Tylka et al. (2003) are in excellent agreement with the values determined by Maia et al. (2007). These results strongly suggest a similar origin of the electrons injected in the radio loops and of the particles measured in-situ. The detection of radio-loop CMEs is thus of primary importance since these loops are the only remote sensing signatures of electrons, in the high corona, with energies comparable with the highest energy electrons detected in-situ.

## 10 Input of radio observations on the forecasting of the arrival time of shocks on Earth

A major objective of solar–terrestrial relationship and of space weather is to forecast when CMEs and their associated shocks impact the magnetosphere. The Sun–Earth travel time of CMEs is difficult to estimate with a good accuracy. SOHO/LASCO was the first coronagraph to extend the field of view to 32 Rs and allowed to perform many statistical analyses. Large samples of LASCO CME events and of 1 AU in-situ observations led to the development of empirical models to predict the Earth arrival time of CMEs (e.g. Gopalswamy et al. 2000a, 2001a; Michałek et al. 2004; Schwenn et al. 2005).

Alternative techniques to predict the CME/shock arrival time have been developed that make use of spectral radio observations of type II bursts: they are either empirical models, or based on MHD and kinematic equations.

### 10.1 MHD and kinematic models of the propagation of CME/shocks

Three main classes of physical-based models have been used to predict the time of arrival at Earth of interplanetary shocks which follow solar metric type II bursts:

– In the STOA model (Shock Time of Arrival), the MHD calculations of Wu (1982) are used to study the propagation from the Sun to 1 AU of the front of solar-flare-initiated-shocks. The solar-flare-initiated-shock is initially a driven shock which transforms into a blast wave in the interplanetary medium. An empirical prediction scheme of the shock arrival has been developed in the work of Smart and Shea (1985) based on the model developed by Wu (1982) and on the following ideas: the shock is first driven during a time consistent with the duration of the SXR emission, at a constant velocity, given by the frequency drift rate of the type II burst. The shock then decelerates as a blast wave whose speed is the sum of the ambient solar wind velocity and of a term decreasing as $R^{-2}$.
– The ISPM (Interplanetary Shock Propagation Model) assumes that the transit time and the peak dynamic pressure at 1 AU can be computed from a MHD time dependant model in which the input parameters are the initial shock velocity, the duration of the driving pulse and its width in the vicinity of the Sun. The shock's travel time and the peak dynamic pressure can be computed at each point along the shock front and as a function of the net input energy (Smith and Dryer 1990).
– The HAF (Hakamada–Akasofu–Fry) kinematic model predicts the values of some solar wind parameters at the Earth (speed, density and interplanetary magnetic field) from observations made at the Sun, such as synoptic maps of the magnetic field; the latter provide the steady state boundary conditions that drive the model background solar wind (Fry et al. 2001). Previous studies have indeed shown that the ion bulk stream at Earth is inversely correlated with the magnetic field expansion near the Sun (see, Levine et al. 1977; Wang and Sheeley 1990). The HAF kinematic model takes also into account stream-stream interactions as the solar wind propagates outwards from the Sun. The disturbance associated with the

CME is represented by a velocity enhancement localized in time and space and the shock speed is derived from the metric type II frequency drift.

In a recent paper, Fry et al. (2003) compared the performance of these three models for 173 events. Each model predicts the shock arrival time at the Earth using real-time type II frequency drifts, coincident with X-ray and optical data for eruptions, and L1 satellite observations for verification. Statistical comparisons showed that these three models have the same overall predictability in forecasting the shock arrival time. The RMS error is about 12 h.

It should be noted that these three models use the same observational parameters to define the solar events (shock kinematics): the optical flares provide the location of the source event; the metric type II bursts provide the start time and the initial shock speed above the flare is measured from the frequency drift rate; the GOES X-ray duration provides the proxy to define the duration of the event. Yet as discussed in Sect. 7.2, three points are questionable in the interpretation of the input parameters:

– First, it is assumed that the origin of the shock wave is a blast wave while it is firmly established that the interplanetary shocks are ICME driven shocks.
– Second, the correspondence between metric type II bursts and coronal shocks as inferred from kilometric type II bursts is extremely poor (Gopalswamy et al. 2001).
– Third, metric type II bursts not associated with CMEs are generally not followed by an interplanetary type II burst.

## 10.2 Empirical models

Kilometric type II radio emissions are generally thought to be generated upstream of the CME-driven shocks (e.g. Lengyel-Frey et al. 1997; Bale et al. 1999). The distance between the driven shock and the CME, at the time when the event reaches the Earth, is typically 0.1–0.25 AU (see Reiner et al. 2007b).

– Cremades et al. (2007) performed a study of the drift rates of kilometric type II events that are temporally associated with shocks detected in-situ. Out of a total of 296 reported forward shocks, 92 shocks were unambiguously associated in time (within 3 days after the first appearance of radio emission) with kilometric type II bursts observed in the vicinity of the Earth. The slope of the drifting radio emission was calculated for all the radio events. Figure 107 shows the histogram of the difference between the shock arrival times and the values predicted from the drift rates, assuming a constant velocity propagation in the interplanetary medium. This histogram indicates that 66% of the shock arrival times were within $\pm 6$ h of their predicted values. Though this is a promising result, it must be, however, underlined that only 92 out of 296 shocks of shocks were found associated with a kilometric type II burst. This result is consistent with the results from Vilmer et al. (2003b) who showed that among 40 IP shocks, only 11 were associated with a kilometric type II burst.
– Several studies based on different techniques of observations, such as white-light observations (Yashiro et al. 2004), Doppler scintillation measurements of CME locations (Woo et al. 1985; Manoharan 2006), and interplanetary scintillations

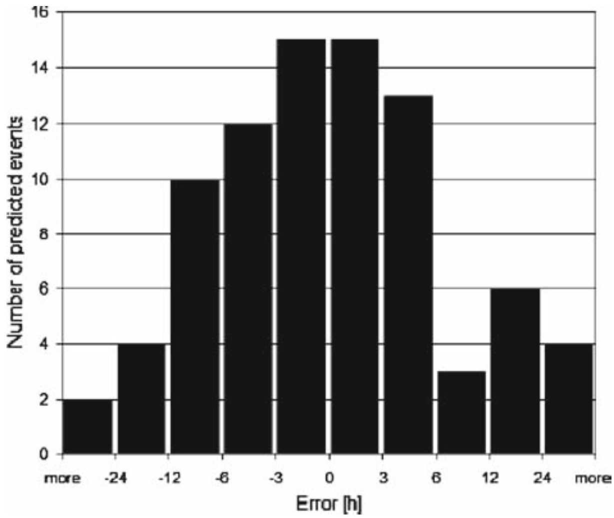


**Fig. 107** Histogram of the error in predicted shock arrival times, in consecutively duplicating bins. A negative value of the error indicates an underestimation of the real shock arrival time, while a positive one denotes an overestimation (from Cremades et al. 2007)

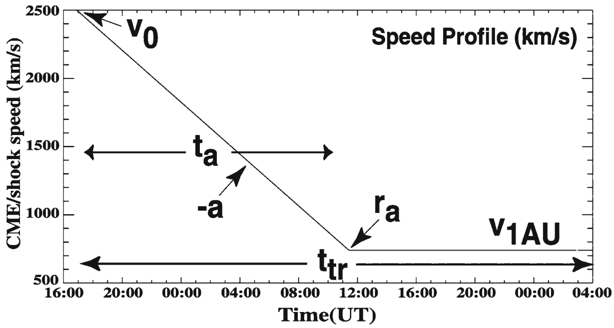


**Fig. 108** Generic speed profile identifying the various parameters that characterize the CME shock propagation in the model developed by Reiner et al. (2007b). The CME initially decelerates at a constant rate ($-$a) until a distance $r_a$ from the Sun and then propagates with a constant velocity v to 1 AU

measurements (Tokumaru et al. 2000; Manoharan et al. 2000) revealed a significant deceleration during the propagation of many ICMEs. Reiner et al. (2007b) developed a model in which it is assumed that the fast CMEs initially decelerate at a constant rate (consistent with LASCO observations, e.g. Yashiro et al. 2004), then, at some distance from the Sun, start to propagate with a constant velocity. Figure 108 shows the various parameters which characterize the CME shock propagation. The analysis is based on the measured parameters of the in-situ shock at 1 AU and on the frequency drift rate of the interplanetary type II burst which yield to a result consistent with the white light measurements. The method allows to deduce the radial speed and the distance profiles for individual

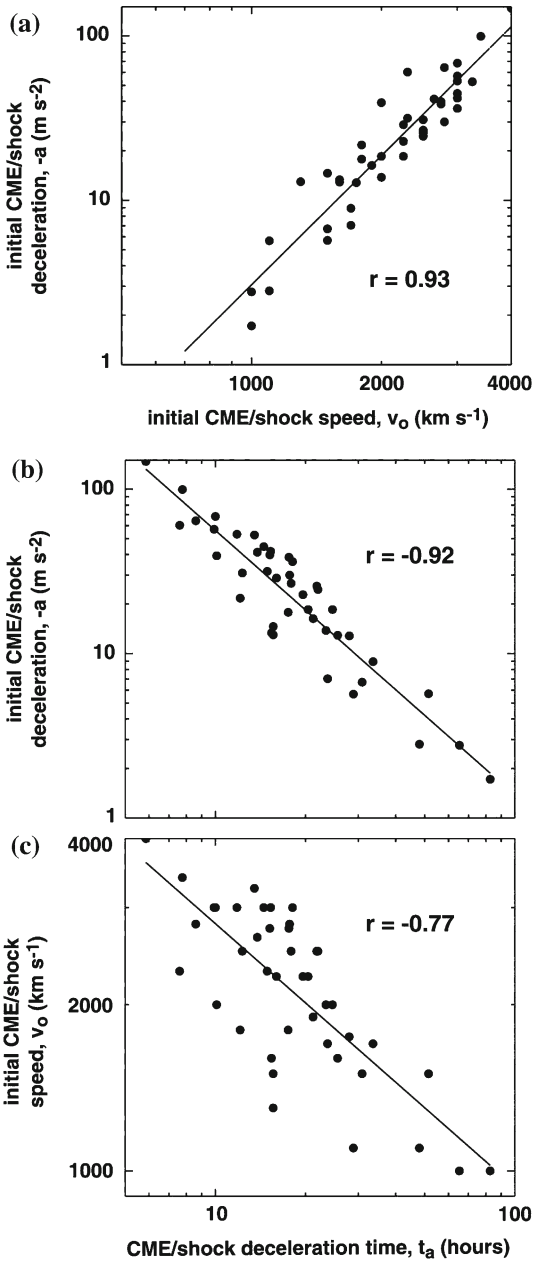


**Fig. 109** Correlation between the deceleration parameters of the speed profiles for the 42 CME/type II events in the study. **a** Initial deceleration versus the initial shock speed. **b** Initial deceleration versus the deceleration time. **c** Initial CME/shock versus the deceleration time (Reiner et al. 2007b)

CME/shock events as they propagate from the Sun to the Earth. The frequency drift yields the radial shock speed through the same method as described in Sect. 7.2: in the interplanetary medium, the plasma density varies approximatively as $R^{-2}$ (Bougeret et al. 1984); thus, plotting the inverse radio frequency versus time is essentially equivalent to plotting it as distance versus time. The measured shock at 1 AU and the transit time are used to derive possible radial speed and distance profiles. The observed frequency drift of the low frequency radio emissions is then used to select the speed/distance profile that provides the best simultaneous fit to these data. This study reveals that there are some significant correlations between the parameters that characterize the deceleration of these CMEs observed at 1 AU (see for example Fig. 109). At this present state, the results of this study have not been applied to predict the arrival time at the Earth of the CME compressed plasma front; the correlation between the CME initial speed and the transit time could be, however, used to predict the arrival time at the Earth of the CME shock by analysing when, where, and how fast CMEs decelerate during their propagation.

It must be also reported that a few ICMEs are found to accelerate near the Sun to a constant propagation speed later on in the IP medium (e.g. Hoang et al. 2007).

It is clear that the different methods predicting the CME/shock arrival times at the Earth will greatly benefit in the near coming future from the combination of radio and white-light observations from the Sun to 1 AU provided by the SECCHI experiment aboard STEREO. This combination will provide complementary view points on the propagation of the CME and on the type II associated shock at the same distance from the Sun.

## 11 Space weather and perspective of solar radio observations

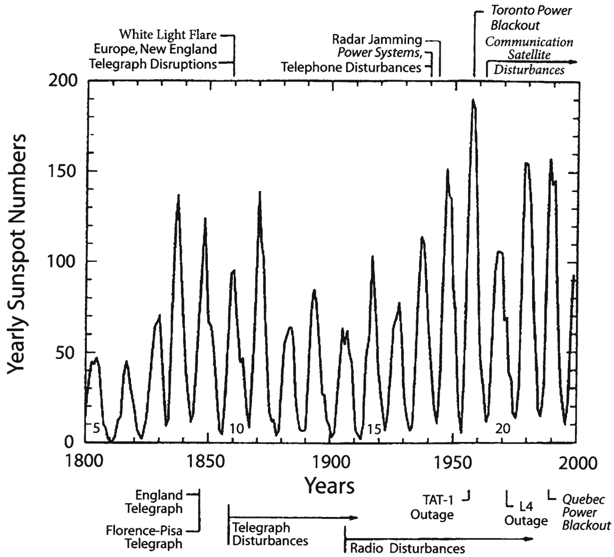


**Fig. 110** Yearly sunspot number with times indicated of selected major impacts of the solar–terrestrial environment on largely ground-based technical systems. The *numbers* above the horizontal axis are the conventional numbers of the sunspot cycles (from Lanzerotti 2007)

The term "space weather" refers to conditions on the Sun and in the solar wind, magnetosphere, ionosphere and thermosphere that can influence the performance and reliability of space-borne and ground-based technological systems and that can affect human life and health (Schwenn 2006). The fact that new technologies can be affected by the Sun and by the space environment of Earth has been discussed for more than a century (see for a review Lanzerotti 2007). This is illustrated in Fig. 110 which shows the yearly sunspot number from 1800 to 2000; the dates of technological impacts caused by disturbances of solar origin such as telegraph disruptions in the late nineteenth century to power outrages in the late twentieth century are reported in this figure. Figure 111 illustrates the time scale of solar effects at 1 AU.

The modern hi-tech society has become more and more vulnerable to disturbances from outside the Earth system, in particular to those initiated by explosive events on the Sun. Different phenomena related to solar activity can disturb our space environment: amount of solar flux, in particular ionizing solar flux impinging on the Earth, level of geomagnetic activity or production of energetic particles reaching the Earth's orbit. Flares release flashes of ionizing radiation that can result in such a large heating of the terrestrial atmosphere that satellites are slowed down and drop into lower orbits. Solar energetic particles accelerated to near-relativistic energies may endanger astronauts travelling through interplanetary space and may also induce some degradation on spacecraft solar panels and perturb on-board computers. Gigantic CMEs may hit the

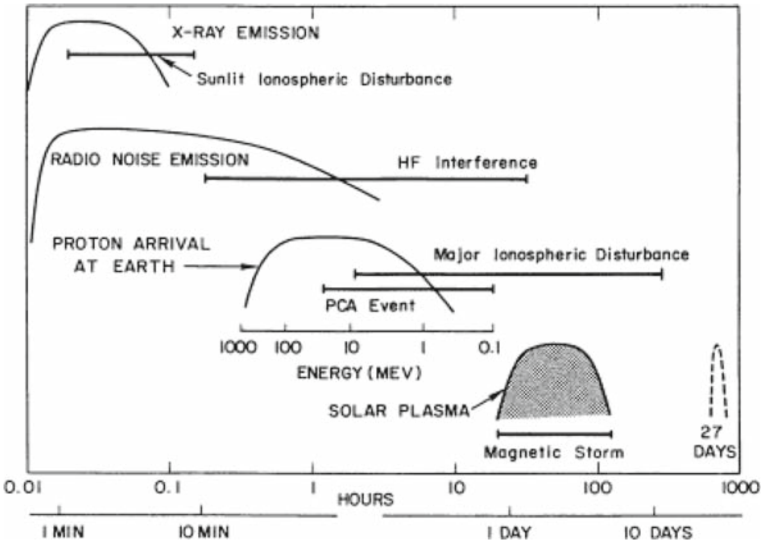


**Fig. 111** Time scale of solar effects at 1 AU (from Shea and Smart 1996)

Earth after a few days and cause geomagnetic storms. The production of solar wind streams with different velocities is at the origin of corotating interaction regions and shocks which can also produce geomagnetic activity. As recalled in Sect. 2, solar radio bursts were discovered during the second world war through the severe interferences that they caused in radars, when these systems were oriented towards the Sun. This brief section will describe how radio observations can help understanding and forecasting some space weather effects.

## 11.1 Radio flux variations and impacts on the Earth's atmosphere and on wireless communication systems

The radio flux measured at 10.7 cm (f10.7), which is directly associated with the sunspots, is considered as a useful proxy for many problems linked with the ionizing effects of solar activity (Kundu and Denisse 1958); for example, f10.7 is one of the indices used for reproducing irradiance in the 10–200 nm (e.g. Schmahl and Kundu 1994), which is a key parameter for aeronomy and for orbitography. Spacecrafts on Low Earth Orbits (LEO) indeed undergo increased drag in case of an increased ionizing radio flux which causes them to slow down, lose altitude and finally re-enter the atmosphere.

Radio burst effects on wireless communications were also recently analysed. As the solar radio noise amplitude is highly variable and can reach many dB above the quiet Sun background in case of activity and flares, it can produce interference in radar systems. The possibility that solar radio noise might affect the wireless communication, by causing disturbances to cell sites, was also recently evaluated (e.g. Gary and Keller 2004). Figure 112 from Nita et al. (2002) shows the cumulative distribution in events per day above 2 GHz ($\nu = 2.8$ GHz is one of the wireless frequency bands), as

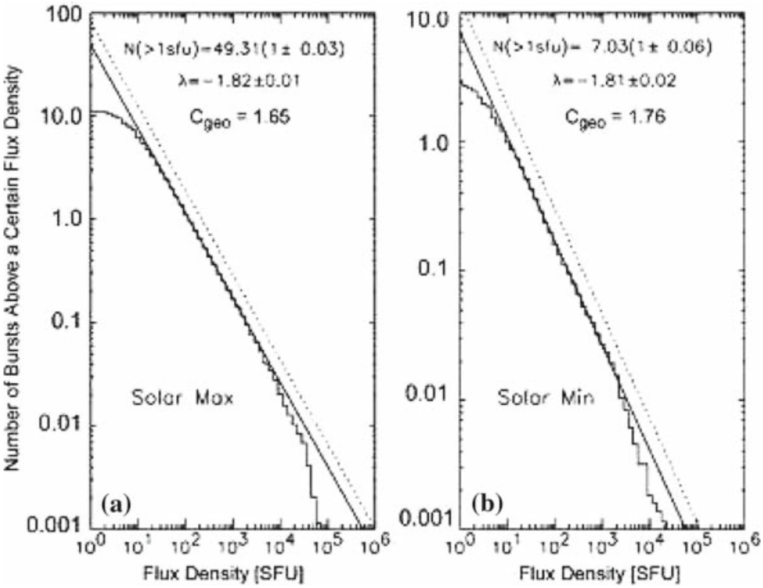


**Fig. 112** Comparison of cumulative probability histogram of the number of solar radio bursts observed above 2 GHz, above given flux densities at solar maximum and solar minimum (from Nita et al. 2002)

observed (histogram), as fitted (solid line) and after application of geographical corrections, Cgeo (dotted line) for both solar maximum and minimum periods. Cgeo is a factor which takes account of missed elements due to an uneven coverage at different longitudes on the Earth. Assuming that the roll-over at low flux densities is due to the instrumental sensitivities limit, the distributions are well fitted with a power law. Using these power law distributions, the probability of a burst affecting a specific receiver can be estimated: bursts, with amplitudes $>10^3$ solar flux unit (sfu) at $\nu \sim 1$ to 2 GHz, will cause interference in a wireless cell site on average once every 3–4 days during solar maximum and may be a few times a year during solar minimum (see also Bala et al. 2002).

## 11.2 Main sources of geomagnetic activity: solar wind stream interaction regions; interplanetary coronal mass ejections and shocks

The primary causes of geomagnetic storms at Earth are the strong electric fields generated by the passage and the impact on the magnetosphere of a disturbance having a southward directed interplanetary magnetic field, Bs, during sufficiently long time; the solar wind energy transfer mechanism is the magnetic reconnection between the interplanetary magnetic field (IMF) and the Earth's magnetic field (e.g. Gonzalez et al. 1994; Kamide 2007). The greatest effects are obtained when these disturbances correspond to large plasma velocities and large Bs values. Geomagnetic storms are produced by two types of solar wind disturbances: Corotating regions formed by the interaction between two solar wind stream (CIR) which produce recurrent storms and

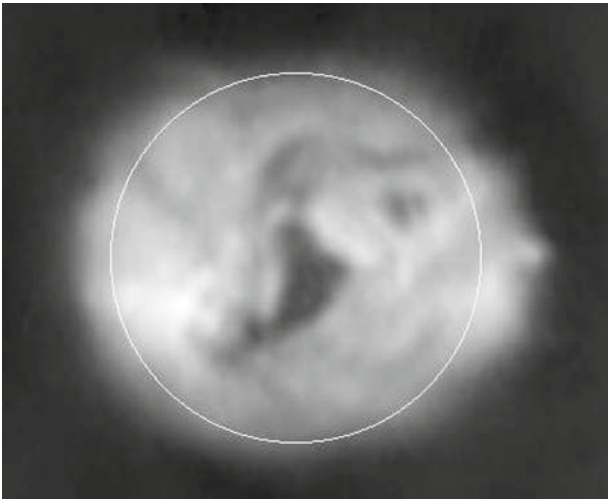

**Fig. 113** Coronal hole observed at 432 MHz on June 27, 2004 (courtesy from G. Chambe and C. Mercier)

the interplanetary coronal mass ejections (ICMEs). The latter are believed to be the main source of the interplanetary transient events and shocks that produce strong geomagnetic storms. Of special importance for space weather is the prediction of the geo-efficiency of these two types of events. In a recent study, Zhang et al. (2007) showed that for a sample of 88 major geomagnetic storms, $\sim$87% were driven by ICMEs and hence originated from eruptive solar events, the remainder being associated with CIRs (see also Gosling et al. 1991; Richardson et al. 2001).

In the case of recurrent storms, CIRs are due to the shocked and compressed fields and plasma produced by the collision of a high-speed solar wind stream with the slower solar wind preceding it; a CIR is formed on the leading edge of the high speed stream (e.g. Pizzo 1991). The high-speed streams originate from solar coronal holes which are easily identified in coronal EUV or radio maps at decimetric wavelengths (see Fig. 113).

In the case of disturbances due to transient events, the geo-efficiency of ICMEs depends on their intrinsic magnetic fields and velocities. The compressed plasma sheath behind shocks and the ejecta itself may both contain strong southward components of the magnetic field. The sheath region can drive a storm even if the ICME itself does not hit the magnetosphere. In this region, the IMF component may be also amplified by draping of the ambient magnetic field over the ejected material; this can lead to a southward IMF component even in case where the pre-existing IMF is slightly north (Gosling et al. 1987). The strongest southward magnetic fields of long duration are found in magnetic clouds (see the definition of MC in Sect. 8) which have a well-formed flux rope structure.

### 11.3 Space weather effects due to energetic particles

Solar flares together with CMEs are the main sources of Solar Energetic Particles (SEPs). During quiet periods, the Earth's geomagnetic field is an effective shield against charged particles; this field creates vertical cut-off rigidity which is less than about 0.2 GV at the magnetic poles and increases to about 15 GV at the magnetic equator; only fluxes of particles more energetic than ∼0.5 GeV can be detected on Earth by the network of neutron monitors. These Ground Level Events (GLEs) are rare, about 70 events since 1942 (Lopate 2006); their arrival time on Earth can be within a few minutes of the X-ray and radio emission. At lower energies, SEPs enter the Earth's close environment only in the polar caps where they produce Polar Cap Absorptions (PCA) with major ionospheric disturbances. Their space weather effects are then usually restricted to high latitude regions. The PCAs, which are generated by 10–100 MeV particles, have onset times about 1 h after their acceleration at the Sun; they last from several tens of minutes to several hours after the flares, well before the onset of geomagnetic storms. As recalled in Sect. 2.2.3, the relationship between PCA events and intense type IV bursts was already found in the 1960s: type IV bursts remain today one of the best indicators of the proton events which reach the Earth. These type IV bursts are characterized by: (a) a flux density measured in the microwave domain, typically 2.8 GHz, greater than $10^{-17}$ $\mathrm{Jm}^{-2}$ Hz and a duration greater than 10 min, (b) a second long duration phase in the metric domain. The heliolongitudinal distribution of solar flares associated with solar proton events observed at the Earth is a function of the particle energy (Smart and Shea 1996). For >100 MeV proton events, the distribution is wider than the distribution for proton events containing energies exceeding 1 GeV. Several transport models of solar energetic particles in the interplanetary medium have been developed (e.g. Ruffolo 1995; Dröge 2006). They assume that the magnetic field can be considered as an average field, represented by a smooth archimedian spiral, with superimposed irregularities.

It is admitted that most major proton energetic events usually result from particle acceleration occurring in the outer corona and in the interplanetary space at shocks driven by fast CMEs (see, e.g. Reames 1999). The intensity-time profiles at the observer's site are determined by the spatial and temporal variable acceleration at the shock and the subsequent interplanetary propagation (e.g. Kallenrode 1997; Lario et al. 1998). Kahler et al. (2001) found that the SEP intensity correlates with the CME speed, but for a given speed the intensity variation can be several orders of magnitude from event to event. The correlation is improved by taking into account the ambient SEP intensities preceding CMEs. These large proton events are generally associated with type II and type IV bursts at metric/decametric wavelengths; the latter are still used, together with the measurements of large and long duration soft X-ray flares, as predictors of large SEPs(see Sect. 9). However, as discussed in the previous section, the shock speed in the corona deduced from metric type II bursts is not necessarily a good indicator of the shock speed in the interplanetary medium.

Finally, the occurrence of a geomagnetic storm will allow the energetic interplanetary particles to reach Earth regions at lower latitude than normally. During geomagnetic storms, the size of the polar cap region increases due to a restructuring of the magnetosphere, the cut-off rigidity for particles entering the magnetosphere is reduced and particles of lower energy i.e. more (including also Galactic Cosmic rays, GCR) can penetrate into regions of low latitude. This increased flux of particles can generate serious problems to technological systems, modify the conditions in

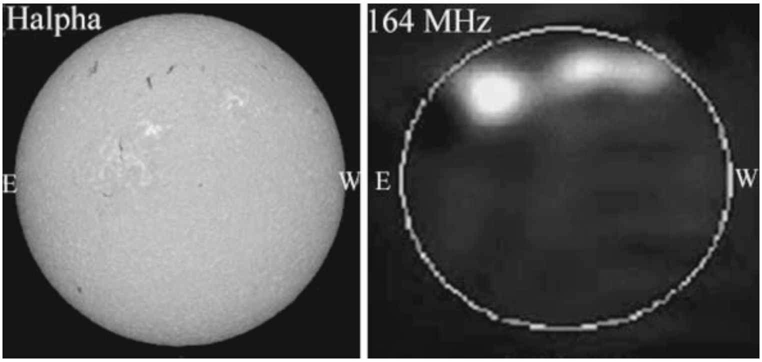


**Fig. 114** *Left panel* H$\alpha$ observations (BASS 2000 Meudon) on June 15, 1997 showing a chain of filaments in the north hemisphere close to the central meridian. *Right panel* NRH observation at 164 MHz showing the brightening of an extended radio source. This source is related to the development on the disk of the CME (from Vilmer et al. 2003b)

the ionosphere and thermosphere and cause ground level enhancements of secondary cosmic rays.

## 11.4 Input of radio observations to predict geomagnetic storms

The above brief summary, related to different space weather effects of geo-magnetic storms, shows the importance of being able to predict these events. As geomagnetic storms are the consequence of a chain of events originating from the Sun, propagating in the interplanetary medium and finally evolving into a geo-effective solar wind flow near the Earth, their prediction is a complex and difficult problem. We shall summarize here how solar radio observations can contribute to this problem.

### *11.4.1 How can we infer the source region of CMEs?*

Appearance of a large-scale, closed, magnetic structure on the Sun can be considered as the basic requirement for a pre-CME evolution. This simple closed field structure will have to be distorted by various processes (shearing motions, flux emergence and cancellation, etc.) during its pre-eruption evolution to gain enough energy to be ejected as a CME. Yet, we are far from predicting whether and when a solar region will erupt by looking at its evolution (see for a review Gopalswamy et al. 2006).

### *11.4.2 How can we identify the source regions and predict the geo-efficiency of ICMEs?*

Of special importance for space weather are Earth directed halo CMEs (see, e.g. Webb et al. 2000) and CMEs having a width greater than 120 degrees (Vilmer et al. 2003), as most of them reach the Earth environment. H$\alpha$, EUV, X-ray and radio observations are needed to investigate the source region of a CME. A large proportion of cases is found to be associated with an active region and a flare signature, which does not exclude the involvement of a filament. Other events are found to be associated with a

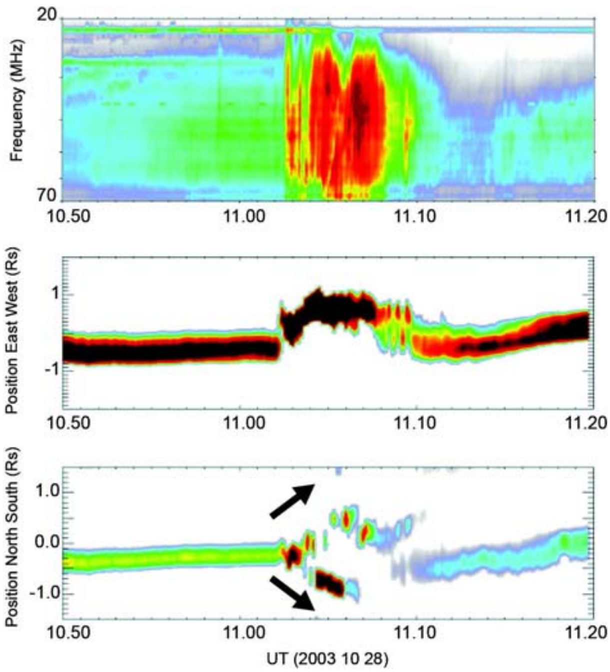


**Fig. 115** Halo CME on October 28, 2003. *Top panel* DAM spectrum during the initial phase of development. *Middle and low panels*: One dimensional dynamic plots obtained, at 164 MHz, by integrating the NRH images in the south-north and east-west directions, respectively

quiescent filament (Vilmer et al. 2003b; Zhang et al. 2007). Furthermore, these disk observations allow us to discriminate between frontside and backside CMEs.

In EUV, the best signature of an on-disk CME is the extended dimming region roughly surrounding the region of eruption. This dimming is interpreted as the opening of the initially closed field lines during the initial phase of CMEs. For large flare/CME events, this dimming is associated with a coronal wave well detected in radio (see Sect. 6.4, e.g. Fig. 75).

Location and angular opening of on-disk and limb flare/CME events can be also obtained by imaging the space and time evolution of the radio metric emission(see also Sect. 6), as illustrated in Fig. 115 for the halo CME event which occurred on October 28, 2003. The top panel displays the decametric (DAM) spectrum during the initial phase of development. The middle and bottom panels show two dynamical plots obtained, at 164 MHz, by integrating the NRH images in the north-south and east-west directions, respectively. The onset of this event, seen in projection on the disk is located at $\approx$0.2 W and 0.3 S in $R_\odot$. The arrows show the projected directions of the angular progression of the CME which covered the entire west hemisphere in a few minutes. The corresponding projected expansion speed is estimated to be of the order of $2.4 \times 10^3\ \mathrm{km\,s^{-1}}$. Moreover, as complex type III-like events at hectometric wavelengths and CMEs are closely associated (see Sect. 9.1), joint spectral and imaging observations may represent an appropriate and easy method to identify the CMEs that will reach the Earth environment with a high probability. However, as a statistical study has not yet been performed, this method needs to be validated.

At present time, most of the studies predicting the geoeffectiveness of ICMEs focus on magnetic clouds (MCs), which are present only in a subset of ICMEs (properties of MCs are recalled in Sect. 8). The southward interplanetary magnetic field component is a dominant parameter governing the intensity of geomagnetic intensity. Bothmer and Schwenn (1994, 1998) showed that the orientation and helicity of filaments before an eruption are often related to those in the MC (see also Schwenn 2006 for a detailed discussion). However, some MCs show a significant rotation of their axis, sometimes greater than 40°, compared to their associated filament (Marubashi 1997). A detailed discussion on this question is beyond the scope of this review (see Forsyth et al. 2006; Démoulin 2007 and see Fig. 2 in Bothmer and Schwenn 1994). Radio observations have not today the capability to contribute significantly to the forecasting of the sign of the magnetic field in the interplanetary medium. Improvement of this is expected in a near future and it is expected that radio maps at cm-dm wavelengths will provide strong constraints on extrapoled magnetic field models(see Gary and Keller 2004).

### *11.4.3 How can we forecast the arrival of ICMEs near the Earth?*

At present time, most methods predicting the CME/shock arrival times at the Earth use spectral radio observations of type II bursts. These methods were reviewed in Sect. 10. As was concluded in this section, all kinematic and MHD models lead to a RMS error of about 12 h on the shock arrival time. Empirical models based on the observations of kilometric type II bursts associated with CME driven shocks lead to a slightly smaller uncertainty of ±6 h; however, the weakest point is that only about 30% of the CMEs are associated with an interplanetary type II burst.

Schwenn et al. (2005) and Gopalswamy et al. (2001a) developed empirical models which consist of algorithms which make use of coronagraphic observations of halo CMEs for predicting the arrival time of an ICME itself (not of its shock). These algorithms are obtained by fitting scattered plots of ICME arrival times versus an estimate of the initial CME velocity. These models predict arrival times of ICME disturbances with uncertainties of about ±1 day at the 90% level (14 h RMS error). However, false alarms statistics are more favourable for predictions based on halo CMEs signatures than for predictions based on physical models and shock arrival times. 85% of front-side halo CMEs were followed by an ICME disturbance at Earth (for a detailed discussion, see Siscoe and Schwenn 2006).

Another empirical model was developed by Caroubalos in 1962 (see Sect. 2.2.4). It was based on: (a) the high probability of type IV bursts (observed at microwave and metre wavelengths) to be associated to an IP disturbance responsible for sudden commencements of geomagnetic storms, SSC; (b) the statistical relationship existing between the Sun–Earth transit time ($\Delta$t) of the disturbances responsible for SSCs and the radiated energy (E) measured at microwavelengths ($\Delta$t is inversely proportional to logE). The RMS error is comparable to the errors found by the other methods. Today, these disturbances responsible for SSCs are identified as flare/CMEs and related ICMEs. LogE is rather easy to measure so that the relationship $\Delta$t versus $(\mathrm{LogE})^{-1}$ may lead to a rather simple method for forecasting the transit time of ICMEs to the Earth.

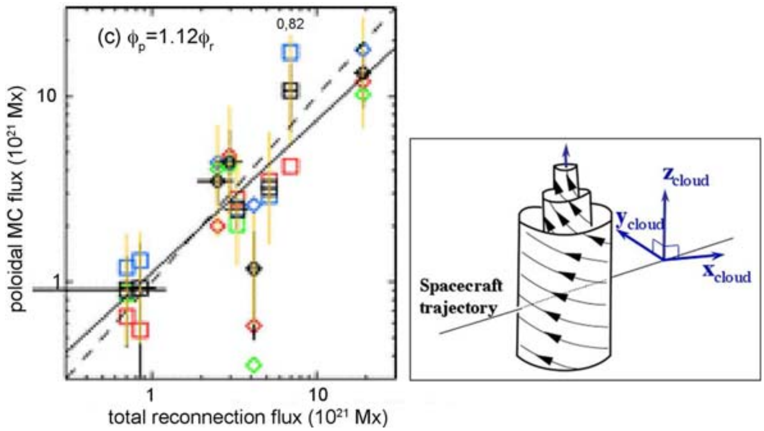


**Fig. 116** *Right panel* Flux rope schema (see Démoulin 2007). *Left panel* Poloidal MC flux versus total reconnection flux in nine events. *Squares* indicate events associated with filament eruption, and *diamond* indicate events without filament region. *Red, blue and green* symbols indicate MC flux measurements by three different methods (adapted from Qiu et al. 2007)

Moreover, this relationship also shows that the release of magnetic energy in the flare region contributes not only to the number of accelerated electrons generating the synchrotron emission at 10 cm but also to the initial acceleration of material related to the ICME transit. Moreover, this energy is likely released by magnetic reconnection. This is supported by the presence of a long lasting metric emission (stationary type IV burst) which is associated with post-eruptive loops formed above the flaring region (see Sects. 2 and 6). This is also supported by the few observations showing a close link between the acceleration phase of the CME in the low corona and the flare particle acceleration phase evidenced by X-ray emissions (see Sect. 6). In the context of this discussion, it is interesting to briefly report on a recent study (Qiu et al. 2007) which also showed the importance of the magnetic reconnection in the flare region for the determination of some characteristics of magnetic clouds. One of the Qiu's conclusions is that the magnetic flux, resulting from the magnetic reconnection Φr and measured from flare ribbons, contributes significantly to the interplanetary poloidal magnetic flux Φp of the magnetic cloud (see Fig. 116, right panel). Figure 116, left panel shows the poloidal MC Φp versus the total reconnection flux measured in 9 events.

Whatever the method used, the main difficulty in predicting more accurately the arrival time of a perturbation to the Earth is the lack of information on the interplanetary evolution of CMEs. This is due to their coupling with variable ambient flows in the interplanetary medium which modifies their evolution in a presently unknown way. The relation Δt, logE shed some light on two important aspects of the problem: first, a disturbance which follows, within a few days, a previous disturbance, travels in the interplanetary medium at a speed faster than the initial disturbance. Second, the conditions encountered by the second disturbance are much more regular than those encountered by the first one (see Sect. 2).

We suggest to reconsider the Caroubalos's method, taking into account the present knowledge on CMEs and taking benefit of the existing data.

## 12 Conclusions and the future of radioastronomy

This review has attempted to present key areas in which 65 years of radio observations have helped transforming our knowledge of solar activity linked to flares and CMEs, of their links with the interplanetary medium and of their effects in the Earth environment. We summarize here the main conclusions of this paper. The discovery of solar radio bursts in the 1940s, opened a new era in our vision of solar activity. Solar radio physics has grown rapidly; it stimulated research on the generation and propagation of radio waves and revealed the nature of many physical processes which occur in ionized plasmas. In this long history, one can very schematically distinguish three successive periods:

- During the first period, which started a few years after the second war, radio emission from the Sun has been thoroughly studied. The necessity of recording radio emissions with adequate time and space resolution led to the development of specialized equipments like radiometers observing the Sun at discrete frequencies, radio spectrographs and multi-element interferometers. Near the end of the 1950s, all the components of solar radio emission (the quiet Sun, the slowly varying component and various types of bursts) had been identified.
- The second period, after 1960, could be characterized on the one hand by the introduction of satellite observations, allowing the bursts to be observed at very low frequencies. Radio observations were extended to the interplanetary medium and to distances close to the Earth's orbit. On the other hand, in 1967, the first images of the solar corona were obtained at 80 MHz by the Australian Culgoora Radioheliograph which operated, after 1967, at three frequencies, i.e. at three distinct altitude ranges of the high corona.
- The third period started with the launch in 1973 of the Skylab mission which carried a coronagraph with an unprecedented sensitivity; this coronagraph detected, during 100 days, many CMEs. Since this time, important results have emerged from coordinated studies of radio observations coupled with data obtained in other spectral domains and with in-situ measurements of particles at various energies. SMM mission then YOHKOH opened a new horizon by making available observations covering a large spectral range (Gamma, X-ray, and EUV together with coronagraph observations). Multifrequency radio imaging with a high temporal resolution, 1 s or less, became available. Coordinated studies of flare observations with in-situ measurements became possible with, e.g. the ISEE3 mission.

Today many observations are obtained from powerful spacecrafts, such as SOHO, TRACE, and RHESSI and recently from STEREO. Measurements in the interplanetary medium are provided in particular by WIND, ACE and Ulysses.

Solar radio astronomy is coupled with other disciplines like plasma physics, solar–terrestrial physics, geophysics and space-weather applications; it makes it difficult to cover, in a single review all the interesting topics.

IMPORTANT DISCOVERIES BEFORE 1970

Many pioneer results laid the first stones for important discoveries. Many of them could not be interpreted at that time and it took several years to understand their full significance. Here are a few examples among the selected pre-1970 results.

– The theoretical foundations of the role played by the coronal magnetic field in determining the coronal structure above an active centre and in providing the energy for flares.
– The interpretation of strong microwave emissions above active regions in terms of gyroresonance opacity.
– The discovery of the accelerated electron beams and of the coronal shocks, identified by their radio signatures.
– The fast time scale ($\sim 1$ s) of the electron acceleration process, nowadays systematically studied with X-ray observations, were already known by radio astronomers.
– The importance, for the understanding of the development of flares and eruptive events (and CMEs after their discovery), of the coupling and interplay between magnetic structures at different spatial scales was already pointed out by combined radio and optical observations. It was also known from the radio observations that the energy release sites are not limited to the active regions in which the H$\alpha$ flare is produced but may imply structures far away from the active region and from different layers of the solar atmosphere. These early findings have now been confirmed by the most recent observations of flares and CMEs.
– The production of radio emitting electrons resulting from the interaction of shock waves with pre-existing coronal structures revealed a possible way through which a shock wave can trigger prominence eruptions at distances far from the active region, as well as other flares, by causing instabilities in neutral sheets. Nowadays, the observations on the solar disk of Moreton, EIT, radio waves and of shock-like features observed in radio spectra have brought new observational proofs for the triggering of eruptive phenomena at large distances from the flare region and for the development of CMEs.
– The importance of the type IV radio emission which is characterized by the magnitude of the peak flux in the microwave domain and by a prolonged emission at lower frequencies was very early highlighted as one of the main parameters for the forecasting of solar energetic particle events. It must be emphasized that type IV bursts remain today one of the best indicators of the proton events which reach the Earth.
– Radio signatures of coronal magnetic field interactions resulting in ejecta and in the build-up of post-erupting loops were found through the observations of moving and stationary type IV bursts. The combination of high temporal cadence and spatially resolved observations of radio emissions at metric/decimetric wavelengths with X-rays, EUV or white light observations have now strongly confirmed these early findings.
– The first combined studies of flares in H$\alpha$ and of type IV radio emissions showed the importance of the magnetic gradient (shear) and twist, and of the presence of parasitic polarities (i.e. the magnetic topology) for the production of flares leading to an efficient particle acceleration. This is still one of the criteria for the prediction of solar flares.
– The radio bursts in the interplanetary medium and then the spiral configuration of the interplanetary magnetic field were discovered. The first in-situ measurements of energetic electrons in the interplanetary medium and the first detection of radio emissions at frequencies below 10 MHz made clear that radio observations of elec-

tron beams at all frequencies provide useful information about the link between the coronal electron acceleration sites and the structures in the interplanetary medium where electrons are detected. Radio emissions are tracers of the magnetic field in the corona and in the interplanetary medium; they are then fundamental for the understanding of the acceleration and transport of energetic particles in the interplanetary medium.

SUMMARY OUTLOOK ON THE PRESENT SITUATION

Following these early findings, radio observations provided over the three last decades new insights in the understanding of solar activity and of its link with the interplanetary medium. Many results have emerged from coordinated ground-based and space radio observations with observations in other parts of the electromagnetic spectrum. These studies have benefited (a) of spatially resolved observations at radio and X-ray wavelengths obtained at high temporal cadence, (b) of the nearly continuous solar coverage provided by the EUV and coronagraph instruments of the SOHO mission, (c) of in-situ measurements in the interplanetary medium (solar wind parameters and solar energetic particles). We have shown in all these studies that radio emissions can remotely detect structures or sites of particle acceleration where magnetic energy release occurs that would not be visible otherwise.

*Sources of radio bursts: tracers of coronal structures*

The location of the burst radio sources, measured at several frequencies, provides information on the large scale coronal magnetic field patterns. It was, for example, well established during the 70's and early 80's period that the regions of electron acceleration cover a wide range of open diverging magnetic field lines and that the transport of electrons in the corona occurs in a large angular cone.

*Radio diagnostics of coronal magnetic fields*

Many observations confirmed the early findings that the gyroresonance emission is usually the dominant mechanism above sunspots. Maps of the magnetic field were obtained for several active regions together with plasma temperature and emission measure maps when multifrequency radio observations or additional X/UV observations were available. Measurements of the longitudinal component of weak magnetic fields in both active and quiet regions of the Sun were also obtained from radio observations. Major advances on the measurement of coronal magnetic fields are expected in the future from broadband imaging spectroscopy in the microwave domain.

*Electron and proton acceleration during flares*

Spatially resolved observations in the metric/decimetric domain, in combination with X-ray and gamma-ray observations provide useful information on the time scales of electron acceleration, the location of the electron acceleration sites and the link between the characteristics of the energetic particles (e.g. spectra, electron to proton ratio) and the production sites of energetic electrons.

– It is confirmed from the observations of radio-spikes and of radio and X-ray bursts that the flare acceleration sites are located near the top of $10^4$ km magnetic loops, possibly in the cusp region (X type reconnection point) or close to interaction

regions between loops, or loop systems of different size. However, these spatially resolved radio observations have been limited so far to the 450–150 MHz range. Further probing of the electron acceleration sites by radio images in a complete frequency range, and in particular in the 500 MHz–1 GHz range, never imaged so far, are clearly needed.
– During a flare, variations of HXR emitting electron spectra coincide with step-wise changes of metric/decimetric spectra and with the appearance of new radio sources, i.e. of distinct magnetic structures illuminated by energetic electrons. A similar result is found for X-ray/gamma ray events: for these events, different electron to proton ratio may be observed from one peak to the other in good coincidence with changes of the magnetic structures illuminated by radio emitting electrons
– Observations of plasma radio emission in the metric/decimetric domain only give qualitative information on energetic electrons in the corona. Spatially resolved observations in the microwave domain, combined with X-ray observations provide quantitative measurements on the electron number, spectra and even in some cases on the angular distributions of energetic electrons produced in solar flares together with information on the location of electron acceleration sites in the low corona. The most recent submillimetre observations of solar flares have revealed the existence of a new radio component, whose origin is not yet well understood and which could result from the most energetic electrons and/or ions produced in solar flares. To improve our knowledge of this new component, new observing windows must be open in the submm/far IR range, i. e. in the THz domain, to bring additional information on the spectrum of this component. It is expected that future projects, such as the French/Chinese SMESE project, will bring new observations on the extremes of particle acceleration in solar flares.

*Evidence for magnetic reconnection in the solar corona*

At present many radio observations, in flares and in CMEs are consistent with the general concept of magnetic reconnection and support reconnection models for magnetic energy release.

– Type III radio bursts reveal the presence of beams of non-thermal electrons. Above 1 GHz, type III bursts generally have a downward motion in the corona. At lower frequencies, typically 0.5–1 GHz, pairs of type III bursts show that the corresponding electron beams propagate in opposite direction (upward and downward).
– Signatures of coronal loop interactions, leading to repetitive electron acceleration, are found during radio continua of long duration.
– Post eruptive arcades, or flare loops, which result from reconnection processes are the site of coronal electron acceleration revealed by the presence of non-thermal continua lasting for several hours and well associated with soft X-ray emissions. The accelerated electrons responsible for these emissions are continuously produced in the corona, even in the late phase of flares. These emissions do not support long duration coronal electron trapping (as envisioned in the 60 s).
– In the decimetric frequency range, radio emissions, associated with soft-X-ray ejecta, show occasionally long series of quasi-periodic pulsations deeply modulat-

ing a continuum that slowly drifts towards lower frequencies. These observations provide evidence for the formation of large scale current sheets in which the pulsations of the radio flux are caused by quasi-periodic particle acceleration episodes that result from a dynamic magnetic reconnection.

- Spectral and multifrequency radio imaging observations coordinated with HXR emissions are also consistent with an erupting flux rope accompanied by the formation of a current sheet behind.
- Radio observations provide evidence that, during the CME development, radio signatures of magnetic reconnection are found far away from the flare region (see below). They are identified, at various altitudes in the dm-dam spectrum.

*Flares, CMEs and ICMEs; association with shocks*

Distinguishing between the various models of CME initiation is extremely difficult. Though the radio observations have only been analysed for very specific cases, their contributions appear today as already extremely important for the understanding of CME's initiation and development.

- Combined EUV, X-ray and coronagraph observations with radio observations obtained at high cadence with both the Nobeyama and the Nançay Radioheliographs in two different frequency domains, show a strong coupling between the CME acceleration phase, i.e. the force acting on the plasma, and the flare particle acceleration. It reveals a strong link (probably related to magnetic reconnection at the origin of both phenomena) between flares and CMEs. It is interesting to point out that the associated ICMEs transit time to the Earth, which is related to the speed reached at the end of the acceleration phase, shows also a close relationship with the flare particle acceleration process measured by the radio importance of the flare, i.e. the radiated energy measured typically at 10 cm.
- Radio images of fast flare/CME events show that many CMEs originate from a rather small coronal region in the vicinity of the flare site; they reach their full coronal angular extension in a few minutes (much faster than the cadence of the coronagraphs), through successive magnetic field interactions that produce energetic electrons. The opening of the loops leaves a region dimmed in EUV. The successive radio signatures of magnetic loop interactions are associated with Moreton waves; yet, the association with EUV/EIT waves remains an open question.
- The results on flare/CME events, based on radio observations, are consistent with the so called "breakout" model.
- The discovery of "radio CMEs" is quite promising for providing important diagnostics in the early phase of CMEs, such as plasma thermal density, number of relativistic electrons, magnetic field strength. All this information is derived from the synchrotron radiation of energetic electrons in the CME loops. The detection of radio CMEs is, however, infrequent; this is partly due to the presence of other strong radio sources and to the limited dynamic range of the existing radioheliographs.
- Radio observations of type II bursts in the corona and in the interplanetary medium provide one of the only evidences of the propagation of large scale shock waves in these media. There is a general agreement that interplanetary type II bursts are shocks driven by CMEs/ICMEs. The origin of coronal shocks remains partly an open question: are they blast waves produced at the time of the flare? Alternatively,

are they shocks driven by a plasmoid ejection or by a fast CME as revealed by several radio imaging observations combined with SXR and white light observations? Compression or shock waves are detected in radio and white light on the flanks of CMEs, during their angular expansion.

– Radio type II bursts allow tracking the propagation of shocks in the heliosphere and are one of the unique tools existing so far to forecast the arrival times of shocks at the Earth. They also reveal together with white-light observations interactions regions in the interplanetary medium between fast and slow CMEs and the related electron acceleration.
– It is however worthwhile to mention that some of the low frequency drift emissions in the interplanetary medium which could be identified as an interplanetary type II burst may in fact not be related to the propagation of the shock wave. They could be due to incoherent synchrotron radiation from relativistic electrons carried out in the CME magnetic field or in the sheet region between the shock and the CME driver.
– Joint analysis of radio, plasma waves and particles, all data obtained during the Ulysses mission, show that the interplanetary medium contains, well beyond 1 AU, propagating channels which are anchored at the Sun. Such channels (open magnetic flux tubes) which are also detected inside ICMEs, allow scatter-free propagation of electron and proton beams from coronal origin. The main characteristic of these channels is their local low level of magnetic field fluctuations.

*Radio diagnostics of energetic in-situ electrons*

A wealth of new observations shows that the classification of SEP events ("the two class paradigm"), commonly accepted until the launch of ACE in 1997, was too simplified. This classification defined two groups: the "impulsive" one in which the flare process accounts for the particle acceleration and the "gradual" one for which the acceleration is dominated by CME driven shocks revealed by type II bursts. The two class paradigm is also inconsistent with several radio observations:

– SEP electron events are associated with long duration kilometric type III-like events which usually start at frequencies higher than the corresponding type II (shock) bursts. These complex type III bursts occur in conjunction with wide CMEs. All these observations argue in favour of a single acceleration process for the electrons. The results are consistent with the interpretation, that during flare/CME events, accelerated electron streams are generated in coronal regions of magnetic interactions located in the aftermath of CMEs.
– A similar conclusion holds for impulsive electron events for which the inferred solar release times of electrons are significantly delayed from the onset time of the flare and of the associated type III burst. These delayed electron events are produced and injected in the interplanetary medium from a second acceleration site remote from the flare site and linked to magnetic reconfiguration following the passage of a shock wave or of a CME.
– The high energy protons and relativistic electrons measured in-situ and detected in association with radio CMEs also originate in the low corona, may be from the

same acceleration process as the relativistic electrons injected in the radio CME loops.

*Space weather effects*

- Radio observations have been since their first detection and are still now crucial tools to understand and forecast some of the space weather effects. The radio flux measured at 10.7 cm (f10.7) is still used nowadays as a proxy for the UV ionizing flux in the Earth's atmosphere and is a key parameter for aeronomy and orbitography.
- Type II and type IV bursts at metric/decimetric wavelengths together with measurements of large and long duration soft X-ray flares are still used as predictors of large energetic particle events.
- Imaging radio observations of coronal waves propagating on the solar disk or of bright extended radio sources both observed at metric wavelengths can be used to detect the first signatures of halo CMEs which can then propagate towards the Earth.
- Models based on the propagation of radio type II bursts in the interplanetary medium are used to forecast the arrival of the shock and of the ICME at the Earth. However, the prediction of the geo-efficiency of the ICME and then of the importance of the geomagnetic effects would need the ability to predict the southward component of the magnetic field of the magnetic cloud and therefore of the CME at the Sun. Radio observations have not today the capability to significantly contribute to this problem.

FUTURE OF SOLAR RADIO ASTRONOMY

In the preceding sections we have shown how solar radio observations have contributed to transform our knowledge of active phenomena at the Sun (in particular flares and CMEs) and of solar–terrestrial relationship. The summary of the results presented in this paper underlines the main directions along which the future of solar radio astronomy should be aimed: First, solar radio observations represent now a tool which cannot be ignored for most of the coordinated studies. Second, even in the case of phenomena already known at other wavelengths, radio observations point to new and essential parameters (like the radio importance of a flare measured at 10 cm) not attainable by other observations. Third, a lot of discoveries made on flares or CMEs from radio observations (like, e.g. radio CMEs) could not have been done without solar dedicated instruments, since the events, sources of the discovery are usually rare and not predictable. This strongly supports the idea that to achieve significant progress in the field of solar and interplanetary physics from radio observations, solar ground-based or space dedicated instruments are the only way. Furthermore, statistical observations are necessary to progress in the field of solar–terrestrial physics and of its space weather applications. This requires systematic observations from solar-dedicated instruments. Nevertheless, non-dedicated instruments should be used in specific cases e. g. when very high spatial resolution is necessary.

Major progresses are expected from ground-based solar dedicated radioheliographs designed to produce images at high spatial resolution and with high-dynamic range over a broad frequency range, such as the FASR (Frequency Agile Solar Radiotelescope) project designed to operate in the $\sim$24 GHz–50 MHz range in USA and the CSRH (Chinese Solar Radio Heliograph) project in the 1.6 GHz–500 MHz frequency range. A high dynamic range is furthermore required to be able to detect weak radio sources (e.g. radio signatures of magnetic reconnection, radio CMEs), which are often not detectable because of the presence of very bright sources due to the flare. Such performances require a large number of interferometer base lines. FASR will be the first instrument with all the needed characteristics, and will be available 7–14 h per day above 2 GHz. The problem of man made radio interferences, is as for other radio instruments, a very important one, especially for images with a high dynamic range and it must be taken into account in the design of the instrument. FASR will provide a wide variety of radio-diagnostic tools in order to study the Sun from the mid chromosphere to the high corona; one of its capability will be the measurements of the coronal magnetic field, through a variety of techniques, using in particular gyroresonance absorption in active centres and free–free absorption in regions of weak magnetic field.

Multifrequency radio imaging instruments must be complemented by radio spectral data which contribute to the complete specification of the radio bursts; although many ground-based sophisticated radio spectrographs exist at different sites, there is, however, no adequate spectral coverage. Indeed, the different existing radio spectrographs have been defined independently at different sites, usually with no coordination. Covering the entire radio spectrum with ground-based and space-borne radio spectrographs, obtaining continuous full day spectra patrols of good data quality and making data products(spectra and images) readily available to the whole community, represent a major and crucial step for: first, an active and efficient participation to solar–terrestrial research with space weather application and also a support to all future solar or interplanetary space-missions such as Solar Orbiter or the sentinels. For the same reasons, a network of simplified radioheliographs allowing 24 h per day solar survey is highly desirable.

In a more distant future, space or lunar-based imaging instruments will allow very low frequency imaging and will provide the definitive protection against man made interferences.

**Acknowledgments** The authors are very indebted to Martin Huber who gave them the opportunity to write this long review on some aspects of solar radioastronomy, who invited them to undertake this project and provided patience during the long production period. They would like to thank their colleagues Pascal Démoulin and Alain Kerdraon for discussions and comments and wish to acknowledge the efficient and very helpful support provided by Sylvain Knudde for revising a lot of the graphics that are published in this review. One of the authors (M.P.) would like to express her special thanks to Antoinette Raoult for her careful reading of the manuscript and Robert Pick for his help in rewriting some parts of it. The authors would like to express their special thanks to the three referees (Mukul Kundu, Marian Karlicky and Gordon Hurford) for reading carefully our manuscript and for their wise comments. We are especially grateful to Gordon Hurford for his wise suggestions to include the discussion on magnetic field measurements and imaging spectroscopy.

**Appendix: The general context of radio wave propagation and emission**

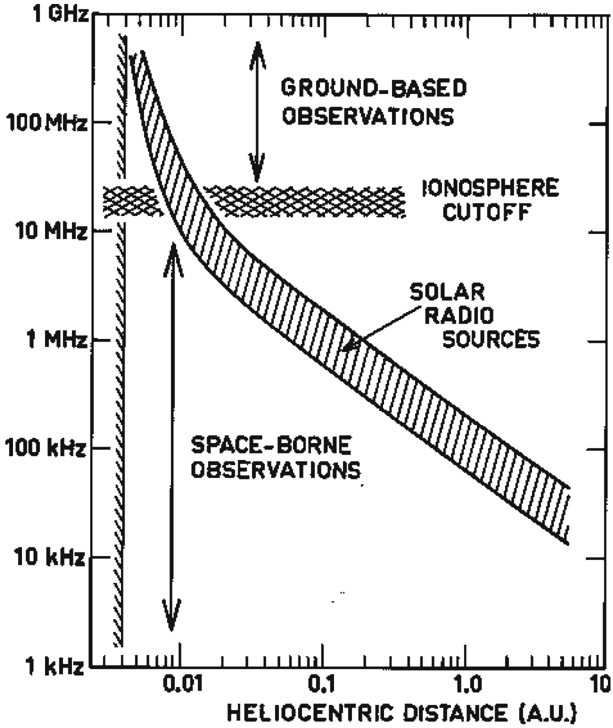


**Fig. 117** Distribution of the observed frequency of solar radio sources versus altitude in the corona and the interplanetary medium (Bougeret and Pick 2007, Chap. 6)

Radio waves can only propagate in a medium where the refractive index is real The refractive index $n$ for a plasma, neglecting the magnetic field, is $n^2 = 1 - f_p^2/f^2$ where $f_p$ and $f$ are, respectively, the plasma and observing frequencies. The electronic density N$_e$, thus the plasma frequency $f_p \sim N_e^2$ of the solar atmosphere decreases monotonically with increasing altitude; therefore, for each frequency, there is an altitude below which propagation does not take place and the range of heights above the photosphere which is observable by a radio telescope is determined by its frequency window. This is illustrated in Fig. 117. At 1 AU, the plasma frequency is 30 kHz.

In an isotropic medium, the radiation path is determined by the Snell–Descartes law:

$$n \sin \alpha = \text{constant} \tag{1}$$

where $\alpha$ is the angle of propagation relative to the gradient of the refractive index. For increasing index of refraction, as is the case for radiation propagating from the Sun to

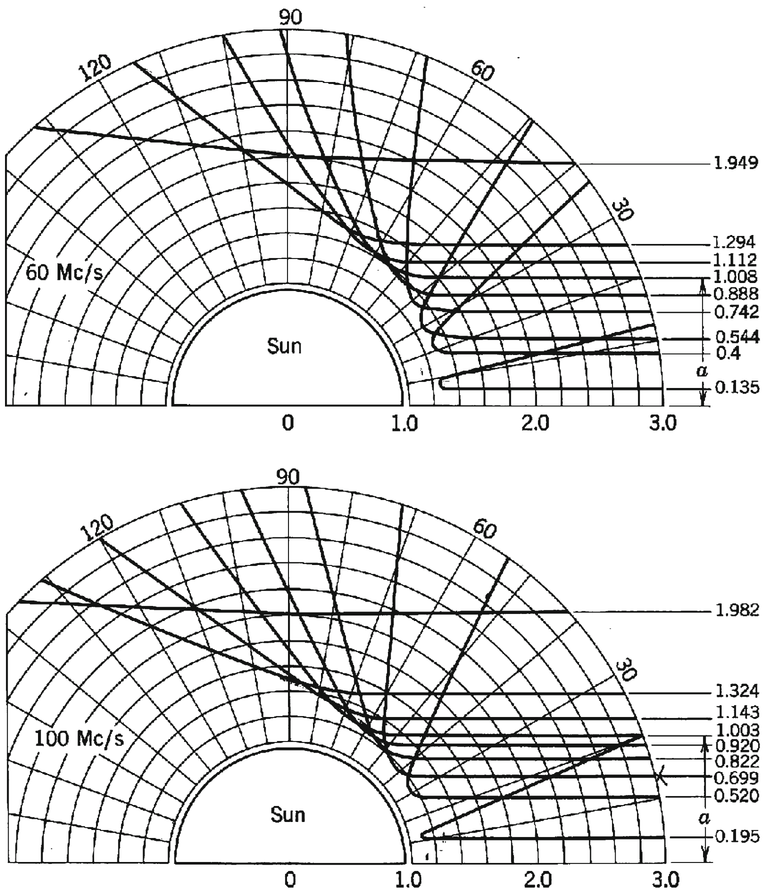


**Fig. 118** Ray trajectories in the solar atmosphere for 60 and 100 MHz. The radial scale is in units of 705,000 km (= photospheric radius + 7, 650 km). The *numbers* on the curves give the dimension $\alpha$ in the same unit (Kundu 1965, p 109)

the Earth, the radiation is refracted toward the direction of the gradient as illustrated in Fig. 118.

Moreover, fluctuations in the refractive index, due to coronal inhomogeneities, cause multipath propagation between the source and the observer. This effect modifies the observed properties of the radio sources, introduces an angular broadening and therefore prevents very high angular observations of radio emissions. Finally, the limits of the shortest and longest wavelengths which can be observed from ground are fixed, respectively, by the transparency of the Earth's atmosphere and by the frequency cut-off of the ionosphere; indeed, below approximately 10 MHz, which is the plasma frequency of the ionosphere, the radio waves cannot propagate down to the ground. Satellite observations extend the observable radio spectrum.

Radio emissions result from thermal and non-thermal mechanisms. For thermal emissions, the "source" function, $B_f$ is given by the Planck function (Rayleigh–Jeans

**Table 1** Principal identified radio bursts; $f_p$= plasma frequency; $f_b$= gyro frequency

| Incoherent radio emission mechanisms | Emission mechanism | Source |
|---|---|---|
| Microwave and millimetre bursts | Free–free emission | Thermal plasma |
| Type IV bursts continua | Gyrosynchrotron emission | |
| Millimetre | | *Ultrarelativistic elect.* |
| Microwave and dm-dam | | *Relativistic elect.* |
| Coherent radio emission mechanisms | | |
| Dm-dam type IV bursts | Plasma emission | Trapped energetic electrons |
| Type II bursts | $f_p; 2f_p$ | Shocks |
| Type III and V bursts | $f_p; 2f_p$ | Upward propagating electron beams |
| Reverse slope burstss | $f_p; 2f_p$ | Downward propagating electron beams |
| Type J and U bursts | $f_p; 2f_p$ | Beams along close loops |
| Dm-m pulsation | $f = sf_b$ | Loss- cone instability *trapped electrons* |
| Dm spikes | | Loss-cone instability |
| Dm-m type I storms | Plasma emission | Trapped and escaping |
| Dam-Km type III storms | | accelerated electrons |

limit):

$$B_f = k_b T f^2/c^2 \tag{2}$$

where $k_b$ is the Boltzman constant,$T$ is the temperature, $f$ the frequency and $c$ the speed of light.

For non-thermal emissions, an effective temperature $T_{\text{eff}}$ can be similarly defined:

$$B_f = kbT_{\text{eff}} f^2/c^2 \tag{3}$$

Spatially resolved observations are limited in angular resolution to a solid angle $\Omega$. The intensity $I$ is defined as the received power emitted per unit area, unit frequency and unit solid angle:

$$I_f = k_b T_b f^2/c^2 \tag{4}$$

where $T_b$ is called the brightness temperature and is defined by the above formula.

$T_b$ and $T_{\text{eff}}$ (or $T$) are related by the radiative transfer equation:

$$\mathrm{d}T_b/\mathrm{d}\tau = -T_b + T_{\text{eff}} \tag{5}$$

where, $d\tau = kdr$ is the optical depth, $k$ is the absorption coefficient of electromagnetic waves, and r the distance along the line of sight.

If $T$ (or $T_{\text{eff}}$) is constant (for example for the quiet corona):

$$\mathrm{T}_b = \mathrm{T}(1 - \mathrm{e}^{-\tau}) \tag{6}$$

For an optically thick source, $T_b$= T; for an optically thin source $\tau \ll 1$, $T_b \sim \tau T$ (for example emission of some coronal structures).

The flux of a radio source is the power received per unit surface and unit frequency. It is expressed in solar flux unit (sfu $= 10^{-22}\,\mathrm{Wm}^{-2}\,\mathrm{Hz}^{-1} = 10^4$ Jansky).

In the presence of a magnetic field and in the case of the "cold plasma approximation", two modes of propagation exist, the extraordinary, x, and the ordinary, o, modes. The polarization characteristics of the observed radio waves are determined by the emission mechanism and/or by the propagation conditions. In general, the two electromagnetic modes propagate independently (weak mode coupling) and, if the radiation travels through a region in which the longitudinal component of the magnetic field changes sign, so does the orientation of the circular polarization. Note that this is not the case under strong mode coupling conditions.

Radio emission produced by non-thermal electrons is attributed principally to gyrosynchrotron (at higher harmonics of the gyrofrequency or producing a synchrotron continuum emission, depending on the energy of the electrons) and coherent plasma emission. Table 1 summarizes the principal identified solar radio bursts.

## References


Akhmedov SB, Gelfreikh GB, Bogod VM, Korzhavin AN (1982) Sol Phys 79:41
Alexander JK, Malitson HH, Stone RG (1969) Sol Phys 8:388
Alissandrakis CE, Kundu MR (1984) A&A 139:271
Alissandrakis CA, Chiuderi Drago F (1995) Sol Phys 160:171
Alissandrakis CE, Borgioli F, Chiuderi Drago F, Hagyard M, Shibasaki K (1996) Sol Phys 167:167
Allen CW (1944) MNRAS 104:13
Allen CW (1947) MNRAS 107:386
Alvarez H, Haddock FT (1973) Sol Phys 29:197
Anderson KA (1958) Phys Rev Lett 1:335
Anderson KA, Lin RP, Potter DW (1982) Space Sci Rev 32:169
Anderson KA, Dougherty WM (1986) Sol Phys 103:165
Anderson KA, Sommers J, Lin RP, Pick M, Chaizy P, Murphy N, Smith EJ, Phillips JL (1995) J Geophys Res 100:3
Antiochos SK, DeVore CR, Klimchuk JA (1999) ApJ 510:485
Appleton EV, Hey JS (1946a) Phil Mag Ser 7(37):73
Appleton EV, Hey JS (1946b) Nature 158:339
Armstrong TP et al (1994) Geophys Res Lett 21:1747
Aschwanden MJ, Guedel M (1992) ApJ 401:736
Aschwanden MJ, Benz AO, Dennis BR, Schwartz RA (1995) ApJ 455:347
Aschwanden MJ, Benz AO (1997) ApJ 480:825
Aschwanden MJ, Schwartz RA, Dennis BR (1998) ApJ 502:468
Aulanier G, DeLuca EE, Antiochos SK, McMullen RA, Golub L (2000) ApJ 540:1126
Avignon A, Pick M (1959) Compt Rend Acad Sci 249:2276
Avignon Y, Martres MJ, Pick M (1964) Ann Astrophys 27:23
Avignon Y, Caroubalos C, Martres MJ, Pick M (1965) Stellar Solar Magn Fields 22:373
Avignon Y, Martres MJ, Pick M (1966) Ann Astrophys 29:33
Axisa F (1974) Sol Phys 35:207
Bala B, Lanzerotti LJ, Gary DE, Thomson DJ (2002) Radio Sci 37:2
Bale SD, Reiner MJ, Bougeret J-L, Kaiser ML, Krucker S, Larson DE, Lin RP (1999) Geophys Res Lett 26:1573
Barat C, Trottet G, Vilmer N, Dezalay J-P, Talon R, Sunyaev R, Terekhov O, Kuznetsov A (1994) ApJ 425:L109
Bárta M, Karlický M (2001) A&A 379:1045

Bastian TS, Gary DE (1997) J Geophys Res 102:14031
Bastian TS, Benz AO, Gary DE (1998) ARA&A 36:131
Bastian TS, Pick M, Kerdraon A, Maia D, Vourlidas A (2001) ApJ 558:L65
Bastian TS (2007) ApJ 665:805
Baumback MM, Kurth WS, Gurnett DA (1975) NASA STI/Recon Technical Report N 76:21111
Beeck J, Wibberenz G (1986) ApJ 311:437
Belkora L (1997) ApJ 481:532
Bentley RD, Klein K-L, van Driel-Gesztelyi L, Démoulin P, Trottet G, Tassetto P, Marty G (2000) Sol Phys 193:227
Benz AO, Barrow CH, Dennis BR, Pick M, Raoult A, Simnett G (1983) Sol Phys 83:267
Benz AO (1985) Sol Phys 96:357
Benz AO (1986) Sol Phys 104:99
Benz AO, Kane SR (1986) Sol Phys 104:179
Benz AO (1993) Astrophys Space Sci Library, 184
Benz AO, Saint-Hilaire P, Vilmer N (2002) A&A 383:678
Benz AO, Grigis PC, Csillaghy A, Saint-Hilaire P (2005) Sol Phys 226:121
Bieber JW, Evenson P, Dröge W, Pyle R, Ruffolo D, Rujiwarodom M, Tooprakai P, Khumlumlert T (2004) ApJ 601:L103
Biesecker DA, Myers DC, Thompson BJ, Hammer DM, Vourlidas A (2002) ApJ 569:1009
Blum EJ, Boischot A, Ginat M (1957) Ann Astrophys 20:155
Bogod VM, Grebinskij AS, Opeikina LV, Gelfreikh GB (1998) Three-Dimensional Struct Solar Active Regions 155:279
Boischot A (1957) CRAS 244:1326
Boischot A, Denisse JF (1957) C R A S 245:2199
Boischot A (1958) Ann Astrophys 21:273
Boischot A, Warwick JW (1959) J Geophys Res 64:683
Bonmartin J et al (1983) Sol Phys 88:383
Bothmer V, Schwenn R (1994) Space Sci Rev 70:215
Bothmer V, Schwenn R (1998) Ann Geophys 16:1
Bougeret J-L, King JH, Schwenn R (1984) Sol Phys 90:401
Bougeret J-L et al (1995) Space Sci Rev 71:231
Bougeret JL, Pick M (2007) In: Kamide Y, Chian A (eds) Handbook of the solar-terrestrial environment. Springer, Berlin, p 134
Brosius JW, Landi E, Cook JW, Newmark JS, Gopalswamy N, Lara A (2002) ApJ 574:453
Brown JC (1971) Sol Phys 18:489
Bruggmann G, Vilmer N, Klein K-L, Kane SR (1994) Sol Phys 149:171
Burlaga LF (1975) Space Sci Rev 17:327
Burlaga L, Sittler E, Mariani F, Schwenn R (1981) J Geophys Res 86:6673
Buttighoffer A, Pick M, Roelof EC, Hoang S, Mangeney A, Lanzerotti LJ, Forsyth RJ, Phillips JL (1995) J Geophys Res 100:3369
Buttighoffer A (1998) A&A 335:295
Buttighoffer A, Lanzerotti LJ, Thomson DJ, Maclennan CG, Forsyth RJ (1999) A&A 351:385
Cane HV, Stone RG, Fainberg J, Steinberg JL, Hoang S, Stewart RT (1981) Geophys Res Lett 8:1285
Cane HV, Stone RG (1984) ApJ 282:339
Cane HV, McGuire RE, von Rosenvinge TT (1986) ApJ 301:448
Cane HV, Sheeley NR Jr, Howard RA (1987) J Geophys Res 92:9869
Cane HV, Erickson WC, Prestage NP (2002) J Geophys Res (Space Phys) 107:1315
Cane HV, Erickson WC (2003) J Geophys Res (Space Phys) 108:1203
Cane HV, Erickson WC (2005) ApJ 623:1180
Caroubalos C (1964) Ann Astrophys 27:333
Chaizy P, Pick M, Reiner M, Anderson KA, Phillips J, Forsyth R (1995) A&A 303:583
Chen PF, Wu ST, Shibata K, Fang C (2002) ApJ 572:L99
Christiansen WN, Warburton JA (1953) Aust J Phys 6:262
Christiansen WN, Mathewson DS (1959) URSI Symp. 1 Paris Symp Radio Astronomy 9:108
Chupp EL, Trottet G, Marschhauser H, Pick M, Soru-Escaut L, Rieger E, Dunphy PP (1993) A&A 275:602
Claßen HT, Mann G, Klassen A, Aurass H (2003) A&A 409:309
Cliver EW, Webb DF, Howard RA (1999) Sol Phys 187:89

Cohen CMS et al (1999) Geophys Res Lett 26:149
Correia E, Kaufmann P, Magun A (1994) Infrared Solar Phys 154:125
Covinton AE (1948) Proc IRE 36:454
Covington AE, Harvey GA (1958) JRASC 52:161
Cremades H, St. Cyr OC, Kaiser ML (2007) Space Weather 5:8001
Crooker NU, Horbury TS (2006) Space Sci Rev 123:93
Croom DL (1970) Sol Phys 15:414
Crosby N, Vilmer N, Lund N, Klein K-L, Sunyaev R (1996) Sol Phys 167:333
Daigne G, Lantos-Jarry MF, Pick M (1971) IAU Symp. 43: Solar Magn Fields 43:609
Dauphin C, Vilmer N, Lüthi T, Trottet G, Krucker S, Magun A (2005) Adv Space Res 35:1805
Dauphin C, Vilmer N, Krucker S (2006) A&A 455:339
Delannée C, Aulanier G (1999) Sol Phys 190:107
Delannée C, Hochedez J-F, Aulanier G (2007) A&A 465:603
Démoulin P (2007) Ann Geophys (in press)
Dennis BR (1988) Sol Phys 118:49
Denisse JF (1948) Doctoral thesis, University of Paris
Denisse JF, Boischot A, Pick M (1960) In: Kallman Bijl H (ed) Space Science Proceeding of the first International Space Science Symposium, Nice. North Holland, Amsterdam, p 638
Dodson HW, Hedeman ER, Owren L (1953) ApJ 118:169
Dodson HW, Hedeman ER, Covington AE (1954) ApJ 119:541
Droege F (1977) A&A 57:285
Dröge W (2006) In: Gopalswamy N, Mewaldt R, Torsti J (eds) Solar eruptions and energetic particles. Washington DC American Geophysical Union, Geophysical Monograph Series, 165(9):297
Dulk GA, Marsh KA (1982) ApJ 259:350
Dulk GA (1985) ARA&A 23:169
Dulk GA, Leblanc Y, Bougeret J-L (1999) Geophys Res Lett 26:2331
Duncan RA (1981) Sol Phys 73:191
Earl JA (1976) ApJ 205:900
Earl JA (1981) ApJ 251:739
Ellison MA, McKenna SMP, Reid JH (1961) MNRAS 122:491
Ellison MA, McKenna SMP, Reid JH (1962) MNRAS 124:263
Erickson WC, Fisher JR (1974) Radio Sci 9:387
Erickson WC (1997) Publ Astron Soc Aust 14:278
Fainberg J, Evans LG, Stone RG (1972) Science 178:743
Fainberg J, Stone RG (1974) Space Sci Rev 16:145
Felli M, Pampaloni P, Tofani G (1974) Sol Phys 37:395
Firor J (1959) IAU Symp. 9: URSI Symp. 1: Paris Symp Radio Astronomy 9:136
Fitzenreiter RJ, Fainberg J, Weber RR, Alvarez H, Haddock FT, Potter WH (1977) Sol Phys 52:477
Forbes TG, Priest ER (1995) ApJ 446:377
Forbes TG (1996) Am Inst Phys Conf Ser 374:275
Forbes TG (2000) J Geophys Res 105:23153
Forsyth RJ et al (2006) Space Sci Rev 123:383
Frank LA, Gurnett DA (1972) Sol Phys 27:446
Frost KJ, Dennis BR (1971) ApJ 165:655
Fry CD, Sun W, Deehr CS, Dryer M, Smith Z, Akasofu S-I, Tokumaru M, Kojima M (2001) Geophys Res 106:20985
Fry CD, Dryer M, Smith Z, Sun W, Deehr CS, Akasofu S-I (2003) J Geophys Res (Space Phys) 108:1070
Gallagher PT, Lawrence GR, Dennis BR (2003) ApJ 588:L53
Gary DE (1985) ApJ 297:799
Gary DE, Hurford GJ (1990) ApJ 361:290
Gary DE, Hurford GJ (1994) ApJ 420:903
Gary DE, Bastian TS, Vourlidas A (1998) BAAS, SPD meeting30, SH-32A-11
Gary DE, Keller CU (2004) In: Gary DE (ed) Solar and space weather radiophysics—current status and future developments. Center for solar-terrestrial research, New Jersey Institute of Technology, Newark, NJ. Christoph U. Keller, National Solar Observatory, Tucson. Astrophysics and Space Science Library, vol 314. Kluwer, Dordrecht
Gergely TE, Kundu MR, Munro RH, Poland AI (1979) ApJ 230:575

Gergely TE, Kundu MR, Hildner E (1983) ApJ 268:403
Gilbert HR, Holzer TE (2004) ApJ 610:572
Gonzalez WD, Joselyn JA, Kamide Y, Kroehl HW, Rostoker G, Tsurutani BT, Vasyliunas VM (1994) J Geophys Res 99:5771
Gopalswamy N, Kundu MR (1992) ApJ 390:L37
Gopalswamy N, Kundu MR, Manoharan PK, Raoult A, Nitta N, Zarka P (1997) ApJ 486:1036
Gopalswamy N et al (1998) J Geophys Res 103:307
Gopalswamy N, Kaiser ML, Sato J, Pick M (2000) NASA STI/Recon Technical Report N, 32759
Gopalswamy N, Lara A, Lepping RP, Kaiser ML, Berdichevsky D, St. Cyr OC (2000a) Geophys Res Lett 27:145
Gopalswamy N, Yashiro S, Kaiser ML, Howard RA, Bougeret J-L (2001) ApJ 548:L91
Gopalswamy N, Lara A, Yashiro S, Kaiser ML, Howard RA (2001a) J Geophys Res 106:29207
Gopalswamy N, Yashiro S, Michałek G, Kaiser ML, Howard RA, Reames DV, Leske R, von Rosenvinge T (2002) ApJ 572:L103
Gopalswamy N, Yashiro S, Krucker S, Stenborg G, Howard RA (2004) J Geophys Res (Space Phys) 109:12105
Gopalswamy N, Mikić Z, Maia D, Alexander D, Cremades H, Kaufmann P, Tripathi D, Wang Y-M (2006) Space Sci Rev 123:303
Gosling JT, Baker DN, Bame SJ, Feldman WC, Zwickl RD, Smith EJ (1987) J Geophys Res 92:8519
Gosling JT, Bame SJ, McComas DJ, Phillips JL (1990) Geophys Res Lett 17:901
Gosling JT, McComas DJ, Phillips JL, Bame SJ (1991) J Geophys Res 96:7831
Gosling JT, Birn J, Hesse M (1995) Geophys Res Lett 22:869
Guedel M, Benz AO, Aschwanden MJ (1991) A&A 251:285
Gurnett DA, Anderson RR (1976) Science 194:1159
Habbal SR, Mossman A, Gonzalez R, Esser R (1996) J Geophys Res 101:19943
Hachenberg O, Volland Z (1961) Astrophys 47:69
Hachenberg O, Wallis G (1961b) Z Astrophys 52:42
Haddock FT, Graedel TE (1970) ApJ 160:293
Haggerty DK, Roelof EC (2002) ApJ 579:841
Hakura Y (1958) J Rad Res Lab Jpn 5:283
Hakura Y, Goh T (1959) J Rad Res Lab Jpn 6:635
Hanaoka Y (1997) Sol Phys 173:319
Hanaoka Y (1999a) PASJ 51:483
Hanaoka Y (1999b) In: Bastian TS, Gopalswamy N, Shibasaki K (eds) Proceedings of the Nobeyama Symposium, held in Kiyosato, Japan, Oct. 27–30, 1998, NRO Report No. 479, pp 229–234, 229
Hartz TR (1964) Ann Astrophys 27:831
Hartz TR (1969) Planet Space Sci 17:267
Hey JS (1942) Observatory 64:263
Hey JS (1946) Nature 157:47
Hernandez AM, Machado ME, Vilmer N, Trottet G (1986) A&A 167:77
Hoang S, Lacombe C, MacDowall RJ, Thejappa G (2007) J Geophys Res (Space Phys) 112:9102
Howard RA, Michels DJ, Sheeley NR Jr, Koomen MJ (1982) ApJ 263:L101
Holman GD, Sui L, Schwartz RA, Emslie AG (2003) ApJ 595:L97
Hori K (1999) In: Bastian TS, Gopalswamy N, Shibasaki K (eds) Proceedings of the Nobeyama Symposium, held in Kiyosato, Japan, Oct. 27–30, 1998. NRO Report No. 479, pp 267–272
Hudson HS (1978) ApJ 224:235
Hudson HS (2000) ApJ 531:L75
Hudson HS, Khan JI, Lemen JR, Nitta NV, Uchida Y (2003) Sol Phys 212:121
Kai K (1970) Sol Phys 11:310
Kai K (1986) Sol Phys 104:235
Kahler SW, Cliver EW, Cane HV (1989) Sol Phys 120:393
Kahler SW, Hundhausen AJ (1992) J Geophys Res 97:1619
Kahler SW, Reames DV, Sheeley NR Jr (2001) ApJ 562:558
Kakinuma T, Tanaka H (1961) Proc Res Inst Atmosph Nagoya Univ, Japan 8:39
Kakinuma T, Swarup G (1962) ApJ 136:975
Kallenrode M-B (1997) J Geophys Res 102:22347

Kamide Y, Maltsev YP (2007) In: Kamide Y, Chian A (eds) Handbook of the solar-terrestrial environment. Berlin, Springer, p 356
Kanbach G et al (1993) A&As 97:349
Kane SR (1972) Sol Phys 27:174
Kane SR, Pick M, Raoult A (1980) ApJ 241:L113
Kane SR (1981) ApJ 247:1113
Kane SR, Raoult A (1981) ApJ 248:L77
Kane SR, McTiernan J, Loran J, Fenimore EE, Klebesadel RW, Laros JG (1992) ApJ 390:687
Kane SR, McTiernan JM, Hurley K (2005) A&A 433:1133
Karlický M, Odstrcil D (1994) Sol Phys 155:171
Karlický M, Sobotka M, Jiřička K (1996) Sol Phys 168:375
Karlický M, Fárník F, Mészárosová H (2002) A&A 395:677
Karlický M (2004) A&A 417:325
Karlický M, Bárta M (2005) Space Sci Rev 121:153
Kathiravan C, Ramesh R (2005) ApJ 627:L77
Kaufmann P et al (2004) ApJ 603:L121
Kaufmann P, Raulin J-P (2006) Phys Plasmas 13:701
Kaufmann P et al (2007) Am Astron Soc Meet Abstr 210:#93.30
Kerdraon A, Pick M, Trottet G, Sawyer C, Illing R, Wagner W, House L (1983) ApJ 265:L19
Kerdraon A, Delouis J-M (1997) Coronal Phys Radio Space Observ Lect Phys 483:192
Khan JI, Hudson HS (2000) Geophys Res Lett 27:1083
Khan JI, Aurass H (2002) A&A 383:1018
Khan JI, Vilmer N, Saint-Hilaire P, Benz AO (2002) A&A 388:363
Khan JI, Aurass H (2006) A&A 457:319
Klassen A, Pohjolainen S, Klein K-L (2003) Sol Phys 218:197
Klein L, Pick M, Trottet G, Vilmer N, Anderson K, Kane S (1983) Sol Phys 84:295
Klein K-L, Trottet G, Magun A (1986) Sol Phys 104:243
Klein K-L (1987) A&A 183:341
Klein K-L, Trottet G (1994) High-energy Solar Phenomena New Era Spacecraft Measure 294:187
Klein K-L, Chupp G, Trottet EL, Magun A, Dunphy PP, Rieger E, Urpo S (1999b) A&A 348:271
Klein K-L, Khan JI, Vilmer N, Delouis J-M, Aurass H (1999) A&A 346:L53
Klein K-L (2005) Adv Space Res 35:1759
Klein K-L, Krucker S, Trottet G, Hoang S (2005b) A&A 431:1047
Kliem B, Karlický M, Benz AO (2000) A&A 360:715
Krucker S, Benz AO, Aschwanden MJ (1997) A&A 317:569
Krucker S, Larson DE, Lin RP, Thompson BJ (1999) ApJ 519:864
Krucker S, Kontar EP, Christe S, Lin RP (2007) ApJ 663:L109
Krueger A (1979) Geophysics and Astrophysics Monographs. Reidel, Dordrecht
Kundu MR, Denisse JF (1958) J Atmosph Terr Phys 13:176
Kundu MR (1959a) URSI Symp.: Paris Symp Radio Astronomy 9:222
Kundu MR (1959b) Ann Astrophys 22:1
Kundu MR, Haddock FT (1960) Nature 186:610
Kundu MR (1961) J Geophys Res 66:4308
Kundu MR (1962) J Phys Soc Jpn Suppl 17:215
Kundu MR (1965) Solar Radio Astronomy. Interscience Publication, New York
Kundu MR, Bobrowsky M, Velusamy T (1981) ApJ 251:342
Kundu MR (1982) Sol Phys 113:87
Kundu MR, Stone RG (1984) Adv Space Res 4:261
Kundu MR, White SM, Gopalswamy N, Lim J (1994) ApJ 90:599
Kundu MR, Raulin JP, Nitta N, Hudson HS, Shimojo M, Shibata K, Raoult A (1995) ApJ 447:L135
Kundu MR, Nindos A, Vilmer N, Klein K-L, Shibata K, Ohyama M (2001) ApJ 559:443
Kundu MR, White SM, Garaimov VI, Manoharan PK, Subramanian P, Ananthakrishnan S, Janardhan P (2004) ApJ 607:530
Kunow H, Crooker NU, Linker JA, Schwenn R, von Steiger R (2006) Space Sci Rev 123:1
Lacombe C, Mangeney A (1969) A&A 1:325
Lang KR, Willson RF, Felli M (1981) ApJ 247:338
Lantos PA (1968) Ann Astrophys 31:105

Lantos P, Kerdraon A, Rapley GG, Bentley RD (1981) A&A 101:33
Lantos P, Pick M, Kundu MR (1984) ApJ 283:L71
Lanzerotti JL (2007) In: Handbook of the solar-terrestrial environment. Berlin, Springer, p 424
Lario D, Sanahuja B, Heras AM (1998) ApJ 509:415
Lee JW, Gary DE (1994) Sol Phys 153:347
Heyvaerts J, Priest ER, Rust DM (1977) ApJ 216:123
Lario D, Pick M (2007) In: Balogh A, Lanzerotti LJ, Suess ST (eds) The heliosphere through the solar activity cycle, p 151
Larson DE et al (1997) Geophys Res Lett 24:1911
Lee J, White SM, Gopalswamy N, Kundu MR (1997) Sol Phys 174:175
Lee J, White SM, Kundu MR, Mikić Z, McClymont AN (1999) ApJ 510:413
Lee J, Gary DE (2000) ApJ 543:457
Lee J, Gary DE, Shibasaki K (2000b) ApJ 531:1109
Lengyel-Frey D, Thejappa G, MacDowall RJ, Stone RG, Phillips JL (1997) J Geophys Res 102:2611
Levine RH, Altschuler MD, Harvey JW (1977) J Geophys Res 82:1061
Lin J, Forbes TG (2000) J Geophys Res 105:2375
Lin RP, Anderson KA (1973) BAAS 5:275
Lin RP, Evans LG, Fainberg J (1973) Astrophys Lett 14:191
Lin RP et al (2003) ApJ 595:L69
Lingenfelter RE, Ramaty R (1967) Planet Space Sci 15:1303
Linker JA, Mikic Z (1995) ApJ 438:L45
Lopate C (2006) In: Gopalswamy N, Mewaldt R, Torsti J (eds) Solar Eruptions and energetic particles. Washington DC American Geophysical Union, Geophysical Monograph Series, 165, 9, 283
Loughead RE, Roberts JA, Cabe MK (1957) Aust J Phys 10:483
Lu ET, Petrosian V (1989) ApJ 338:1122
Lüthi T, Magun A, Miller M (2004) A&A 415:1123
Lüthi T, Lüdi A, Magun A (2004) A&A 420:361
Lynch BJ, Antiochos SK, MacNeice PJ, Zurbuchen TH, Fisk LA (2004) ApJ 617:589
MacDowall RJ, Kundu MR, Stone RG (1987) Sol Phys 111:397
Machado ME, Somov BV, Rovira MG, de Jager C (1983) Sol Phys 85:157
MacNeice P, Antiochos SK, Phillips A, Spicer DS, DeVore CR, Olson K (2004) ApJ 614:1028
Maia D, Vourlidas A, Pick M, Howard R, Schwenn R, Magalhães A (1999) J Geophys Res 104:12507
Maia D, Pick M, Vourlidas A, Howard R (2000) ApJ 528:L49
Maia D, Pick M, Hawkins SE III, Fomichev VV, Jiřička K (2001) Sol Phys 204:197
Maia D, Aulanier G, Wang SJ, Pick M, Malherbe J-M, Delaboudinière J-P (2003) A&A 405:313
Maia DJF, Pick M (2004) ApJ 609:1082
Maia DJF, Gama R, Mercier C, Pick M, Kerdraon A, Karlický M (2007) ApJ 660:874
Malitson HH, Fainberg J, Stone RG (1973) Astrophys Lett 14:111
Mandrini CH, Nakwacki MS, Attrill G, van Driel-Gesztelyi L, Démoulin P, Dasso S, Elliott H (2007) Sol Phys 244:25
Manoharan PK, van Driel-Gesztelyi L, Pick M, Demoulin P (1996) ApJ 468:L73
Manoharan PK, Kojima M, Gopalswamy N, Kondo T, Smith Z (2000) ApJ 530:1061
Manoharan PK (2006) Sol Phys 235:345
Marsh KA, Hurford GJ, Zirin H, Hjellming RM (1980) ApJ 242:352
Marsh KA, Hurford GJ (1980) ApJ 240:L111
Marsh KA, Hurford GJ, Zirin H, Dulk GA, Dennis BR, Frost KJ, Orwig LE (1981) ApJ 251:797
Marsh KA, Hurford GJ (1982) ARA&A 20:497
Marschhäuser H, Rieger E, Kanbach G (1994) High-energy Solar Phenomena New Era Spacecraft Measure 294:171
Marubashi K (1997) In: Crooker N, Joselyn JA, Feynman J (eds) Coronal mass ejection, American Geophysical Union. Geophys Monogr 99:147
Marqué C, Lantos P, Klein K-L, Delouis JM (2001) A&A 374:316
Marqué C, Lantos P, Delaboudinière JP (2002) A&A 387:317
Martres M-J, Pick M (1962) Ann Astrophys 25:293
Mason GM (2007) Space Sci Rev, 93
Masuda S, Kosugi T, Hara H, Tsuneta S, Ogawara Y (1994) Nature 371:495
Masuda S, Kosugi T, Hara H, Sakao T, Shibata K, Tsuneta S (1995) PASJ 47:677

McCracken KG, Ness NF (1966) J Geophys Res 71:3315
McLean DJ, Labrum NR (1985) Solar radiophysics: studies of emission from the sun at metre wavelengths
Mewaldt RA, Cohen CMS, Mason GM (2006) In: Gopalswamy N et al (eds) Solar eruptions and energetic particles. AGU Monograph, 165, 115126
Melnikov VF, Silva AVR (1999) Magn Fields Solar Process 448:1053
Melnikov VF, Shibasaki K, Reznikova VE (2002) ApJ 580:L185
Melo AM, Kaufmann P, Kudaka AS, Raulin J-P, Marcon R, Marun A, Pereyra P, Levato H (2006) PASP 118:1558
Melrose DB (1986) In: Melrose DB (ed) Instabilities in space and laboratory plasmas, ISBN 0521305411. Cambridge University Press, Cambridge, p 288
Meyer P, Parker EN, Simpson JA (1956) Phys Rev 104:768
Michałek G, Gopalswamy N, Lara A, Manoharan PK (2004) A&A 423:729
Molodij G, Trottet G (2005) EAS Publ Ser 14:199
Moreton GE, Ramsey HE (1960) PASP 72:357
Moses D et al (1997) Sol Phys 175:571
Munro RH, Gosling JT, Hildner E, MacQueen RM, Poland AI, Ross CL (1979) Sol Phys 61:201
Myagkova IN, Kuznetsov SN, Yushkov BY, Kudela K (2004) 35th COSPAR Sci Assembly 35:1511
Nakajima H et al (1991) Nobeyama Radio Observatory Report, p 1
Narukage N, Hudson HS, Morimoto T, Akiyama S, Kitai R, Kurokawa H, Shibata K (2002) ApJ 572:L109
Neupert WM (1968) ApJ 153:L59
Neupert WM, Thompson BJ, Gurman JB, Plunkett SP (2001) J Geophys Res 106:25215
Newkirk GJ (1967) ARA&A 5:213
Newton HW (1943) MNRAS 103:244
Nitta N, Kosugi T (1986) Sol Phys 105:73
Nindos A, White SM, Kundu MR, Gary DE (2000) ApJ 533:1053
Nishio M, Yaji K, Kosugi T, Nakajima H, Sakurai T (1997) ApJ 489:976
Nita GM, Gary DE, Lanzerotti LJ, Thomson DJ (2002) ApJ 570:423
Nita GM, Gary DE, Lee J (2004) ApJ 605:528
The Radioheliograph Group (1989) Sol Phys 120:193
Ohki K, Hudson HS (1975) Sol Phys 43:405
Ohyama M, Shibata K (1998) ApJ 499:934
Paesold G, Benz AO, Klein K-L, Vilmer N (2001) A&A 371:333
Pawsey JL, Yabsley DE (1949) Aust J Sci Res Phys Sci 2:198
Payne-Scott DE, Yabsley R, Bolton JG (1947) Nature 160:256
Payne-Scott R (1949) R Aust J Sci Res A 2:214
Peterson L, Winckler JR (1958) Phys Rev Lett 1:205
Peterson LE, Winckler JR (1959) J Geophys Res 64:697
Pick-Gutmann M, Steinberg JL (1959) C R A S 2452
Pick-Gutmann M (1961) Ann Astrophys 24:183
Pick M (1977) Sol Phys 53:241
Pick M et al (1995) Space Sci Rev 72:315
Pick M et al (1998) Sol Phys 181:455
Pick M (1999a) In: Bastian TS, Gopalswamy N, Shibasaki K (eds) Proceedings of the Nobeyama Symposium, held in Kiyosato, Japan, Oct. 27–30, 1998. NRO Report No. 479, pp 187–198
Pick M, Maia D, Vourlidas A, Benz AO, Howard RA, Thompson BJ (1999b) Am Inst Phys Conf Ser 471:649
Pick M, Maia D, Wang SJ, Lecacheux A, Hawkins SE (2003) Adv Space Res 32:2527
Pick M, Démoulin P, Krucker S, Malandraki O, Maia D (2005a) ApJ 625:1019
Pick M, Malherbe J-M, Kerdraon A, Maia DJF (2005b) ApJ 631:L97
Pick M, Maia D (2005c) Adv Space Res 35:1876
Pick M et al (2006a) Space Sci Rev 123:341
Pick M, Mason GM, Wang Y-M, Tan C, Wang L (2006b) ApJ 648:1247
Pizzo VJ (1991) J Geophys Res 96:5405
Pohjolainen S et al (2001) ApJ 556:421
Pohjolainen S, Vilmer N, Khan JI, Hillaris AE (2005) A&A 434:329
Preka-Papadema P, Alissandrakis CE (1992) A&A 257:307
Qiu J, Hu Q, Howard TA, Yurchyshyn VB (2007) ApJ 659:758

Ramaty R (1969) ApJ 158:753
Ramaty R, Schwartz RA, Enome S, Nakajima H (1994) ApJ 436:941
Ramesh R, Subramanian KR, Sundararajan MS, Sastry CV (1998) Sol Phys 181:439
Raoult A, Pick M (1980) A&A 87:63
Raoult A, Pick M, Dennis BR, Kane SR (1985) ApJ 299:1027
Raulin JP, Kerdraon A, Klein K-L, Trottet G, Willson RF, Lang KR (1991) A&A 251:298
Raulin JP, Klein K-L (1994) A&A 281:536
Raulin J-P, Vilmer N, Trottet G, Nitta N, Silva AVR, Kaufmann P, Correia E, Magun A (2000) A&A 355:355
Raulin JP, Makhmutov VS, Kaufmann P, Pacini AA, Lüthi T, Hudson HS, Gary DE (2004) Sol Phys 223:181
Reames DV (1995) Rev Geophys 33:585
Reames DV (1999) Space Sci Rev 90:413
Reber G (1944) ApJ 100:279
Reiner MJ, Stone RG, Fainberg J (1992) ApJ 394:340
Reiner MJ, Kaiser ML, Fainberg J, Bougeret J-L, Stone RG (1997) Correlated Phenomena at the Sun, in the Heliosphere and in Geospace 415:183
Reiner MJ, Kaiser ML (1999) J Geophys Res 104:16979
Reiner MJ, Kaiser ML (1999b) Geophys Res Lett 26:397
Reiner MJ, Kaiser ML, Gopalswamy N, Aurass H, Mann G, Vourlidas A, Maksimovic M (2001) J Geophys Res 106:25279
Reiner MJ, Vourlidas A, Cyr OCS, Burkepile JT, Howard RA, Kaiser ML, Prestage NP, Bougeret J-L (2003) ApJ 590:533
Reiner MJ, Krucker S, Gary DE, Dougherty BL, Kaiser ML, Bougeret J-L (2007a) ApJ 657:1107
Reiner MJ, Kaiser ML, Bougeret J-L (2007b) ApJ 663:1369
Ryabov BI, Pilyeva NA, Alissandrakis CE, Shibasaki K, Bogod VM, Garaimov VI, Gelfreikh GB (1999) Sol Phys 185:157
Richardson IG, Cliver EW, Cane HV (2001) Geophys Res Lett 28:2569
Riddle AC (1970) Sol Phys 13:448
Roberts (1952) Doctoral thesis, University of Cambridge
Robinson RD, Smerd SF (1975) Proc Astron Soc Aust 2:374
Robinson RD (1985) Solar radiophysics: studies of emission from the sun at metre wavelengths, p 385
Ruffolo D (1995) ApJ 442:861
Saito K, Makita M, Nishi K, Hata S (1970) Ann Tokyo Astron Observatory 12:51
Sakai JI, Nagasugi Y, Saito S, Kaufmann P (2006) A&A 457:313
Sakurai K, Maeda H (1961) J Geophys Res 66:1966
Saint-Hilaire P, Benz AO (2003) Sol Phys 216:205
Salomonovich AE (1962) Sov Astronomy 6:55
Schmahl EJ, Kundu MR (1994) Sol Phys 152:167
Shea MA, Smart DF (1996) Solar Drivers Interplanetary Terrestrial Disturbances 95:266
Share GH et al (2003) ApJ 595:L85
Schwenn R, dal Lago A, Huttunen E, Gonzalez WD (2005) Ann Geophys 23:1033
Schwenn R (2006) "Space Weather", Living Rev. Solar Phys, 3:2. http://www.livingreviews.org
Schwenn R et al (2006a) Space Sci Rev 123:127
Sheeley NR Jr et al (1975) Sol Phys 45:377
Sheeley NR Jr, Howard DJ, Michels RA, Koomen MJ, Schwenn R, Muehlhaeuser KH, Rosenbauer H (1985) J Geophys Res 90:163
Sheeley NR, Walters JH, Wang Y-M, Howard RA (1999) J Geophys Res 104:24739
Sheeley NR, Hakala WN, Wang Y-M (2000) J Geophys Res 105:5081
Sheridan KV (1970) Proc Astron Soc Aust 1:376
Sheridan KV, Jackson BV, McLear DJ, Dulk GA (1978) Proc Astron Soc Aust 3:249
Silva AVR, Wang H, Gary DE (1999) In: Bastian TS, Gopalswamy N, Shibasaki K (eds) Proceedings of the Nobeyama Symposium, held in Kiyosato, Japan, Oct. 27–30, 1998. NRO Report No. 479, pp 255–260
Silva AVR, Share GH, Murphy RJ, Costa JE, Gimenez de Castro CG, Raulin JP, Kaufmann P (2007) American Astronomical Society Meeting Abstracts, 210:37.05
Simnett GM, Benz AO (1986) A&A 165:227
Simnett GM, Roelof EC, Haggerty DK (2002) ApJ 579:854

Simon P (1960) Ann Astrophys 23:102
Simon P (1962) Ann Astrophys 25:12
Sinno K (1959) J Rad. Res. Lab. Japan 6:17
Siscoe G, Schwenn R (2006) Space Sci Rev 123:453
Slottje C (1978) Nature 275:520
Southworth GC (1945) J Franklin Inst 239:285
Smart DF, Shea MA (1985) J Geophys Res 90:183
Smart DF, Shea MA (1996) Adv Space Res 17:113
Smith Z, Dryer M (1990) Sol Phys 129:387
Smith DM, Share GH, Murphy RJ, Schwartz RA, Shih AY, Lin RP (2003) ApJ 595:L81
Srivastava N, Schwenn R, Inhester B, Stenborg G, Podlipnik B (1999a) Space Sci Rev 87:303
Srivastava N, Schwenn R, Inhester B, Martin SF, Hanaoka Y (2000) ApJ 534:468
Steinolfson RS (1985) Washington DC Am Geophys Union Geophys Monogr Ser 35:1
Sterling AC, Hudson HS (1997) ApJ 491:L55
Stewart RT, Duncan RA, Suzuki S, Nelson GJ (1978) Proc Astron Soc Aust 3:247
Stewart RT (1985) Solar radiophysics: studies of emission from the sun at metre wavelengths, p 361
Sui L, Holman GD (2003) ApJ 596:L251
Sui L, Holman GD, Dennis BR (2004) ApJ 612:546
Sui L, Holman GD, White SM, Zhang J (2005) ApJ 633:1175
Svestka Z, Dennis BR, Woodgate BE, Pick M, Raoult A, Rapley CG, Stewart RT (1982) Sol Phys 80:143
Swarup G, Kakinuma T, Covington AE, Harvey GA, Mullaly RF, Rome J (1963) ApJ 137:1251
Takakura T (1959) URSI Symp 1: Paris Symp Radio Astronomy 9:562
Takakura T, Inda M, Makishima K, Kosugi T, Sakao T, Masuda S, Sakurai T, Ogawara Y (1993) PASJ 45:737
Takano T et al (1997) Coronal Phys Radio Space Obs 483:183
Tanaka H, Kakinuma T (1955) Proc Res Inst Atmosph Nagoya Univ, Japan 3:102
Thompson AR, Maxwell A (1960) Planet Space Sci 2:104
Thompson BJ, Plunkett SP, Gurman JB, Newmark JS, St Cyr OC, Michels DJ, Dolaboudinière JP (1998) Geophys Res Lett 25:2461
Thompson BJ, Cliver EW, Nitta N, Delannée C, Delaboudinière J-P (2000) Geophys Res Lett 27:1431
Tokumaru M, Kojima M, Fujiki K, Yokobe A (2000) J Geophys Res 105:10435
Tousey R (1973) Space Res 713
Trottet G, Kerdraon A (1980) IAU Symp 86: Radio Phys Sun 86:329
Trottet G (1986) Sol Phys 104:145
Trottet G (1994) Space Sci Rev 68:149
Trottet G, Chupp, EL, Marschhaeuser H, Pick M, Soru-Escaut I, Rieger E, Dunphy PP (1994) A&A 288:647
Trottet G, Vilmer N, Barat C, Benz A, Magun A, Kuznetsov A, Sunyaev R, Terekhov O (1998) A&A 334:1099
Trottet G, Rolli E, Magun A, Barat C, Kuznetsov A, Sunyaev R, Terekhov O (2000) A&A 356:1067
Trottet G, Raulin J-P, Kaufmann P, Siarkowski M, Klein K-L, Gary DE (2002) A&A 381:694
Trottet G, Schwartz RA, Hurley K, McTiernan JM, Kane SR, Vilmer N (2003) A&A 403:1157
Trottet G, Correia E, Karlický M, Aulanier G, Yan Y, Kaufmann P (2006) Sol Phys 236:75
Tylka AJ et al (2003) Int Cosmic Ray Conf 6:3305
Uchida Y (1960) PASJ 12:376
Veronig AM, Karlický M, Vršnak B, Temmer M, Magdalenić J, Dennis BR, Otruba W, Potzi W (2006) A&A 446:675
Vilmer N, Trottet G (1997) Coronal Phys Radio Space Obs Lect Notes Phys 483:28
Vilmer N, Trottet G, Barat C, Schwartz RA, Enome S, Kuznetsov A, Sunyaev R, Terekhov O (1999) A&A 342:575
Vilmer N, Krucker S, Lin RP, The Rhessi Team (2002) Sol Phys 210:261
Vilmer N, Krucker S, Trottet G, Lin RP (2003) Adv Space Res 32:2509
Vilmer N, Pick M, Schwenn R, Ballatore P, Villain JP (2003b) Ann Geophys 21:847
Vourlidas A, Wu ST, Wang AH, Subramanian P, Howard RA (2003) ApJ 598:1392
Vourlidas A, Pick M, Hoang S, Démoulin P (2007) ApJ 656:L105
Vršnak B, Lulić S (2000) Sol Phys 196:181
Vršnak B, Warmuth A, Brajša R, Hanslmeier A (2002) A&A 394:299

Vršnak B, Magdalenić J, Temmer M, Veronig A, Warmuth A, Mann G, Aurass H, Otruba W (2005) ApJ 625:L67
Wagner WJ, MacQueen RM (1983) A&A 120:136
Wang H, Gary DE, Lim J, Schwartz RA (1994) ApJ 433:379
Wang H, Gary DE, Zirin H, Schwartz RA, Sakao T, Kosugi T, Shibata K (1995) ApJ 453:505
Wang H, Gary DE, Zirin H, Nitta N, Schwartz RA, Kosugi T (1996) ApJ 456:403
Wang Y-M, Sheeley NR Jr (1990) ApJ 365:372
Wang Y-M, Pick M, Mason GM (2006) ApJ 639:495
Wang L, Lin RP, Krucker S, Gosling JT (2006) Geophys Res Lett 33:3106
Warmuth A, Vršnak B, Magdalenić J, Hanslmeier A, Otruba W (2004) A&A 418:1101
Warmuth A, Mann G, Aurass H (2005) ApJ 626:L121
Warmuth A (2007) CESRA (in press)
Webb DF, Cliver EW, Crooker NU, Cry OCS, Thompson BJ (2000) J Geophys Res 105:7491
White SM, Kundu MR (1992) Sol Phys 141:347
White SM (1999) In: Bastian TS, Gopalswamy N, Shibasaki K (eds) Proceedings of the Nobeyama Symposium, held in Kiyosato Japan Oct 27–30, 1998. NRO Report No 479, pp 223–228
White SM, Krucker S, Shibasaki K, Yokoyama T, Shimojo M, Kundu MR (2003) ApJ 595:L111
White SM, Thompson BJ (2005) ApJ 620:L63
Wiedenbeck ME et al (2003) Solar Wind Ten 679:652
Wild JP, McCready LL (1950) Aust J Phys 3:387
Wild JP, Murray JD, Rowe WC (1954) Aust J Phys 7:439
Wild JP, Sheridan KV, Trent GH (1959a) IAU Symp 9: URSI Symp 1: Paris Symp Radio Astronomy 9:176
Wild JP, Sheridan KV, Neylan AA (1959b) Aust J Phys 12:369
Wild JP, Smerd SF, Weiss AA (1963) ARA&A 1:291
Wild JP (1967) Proc Astron Soc Aust 1:38
Wild JP (1968) Proc Astron Soc Aust 1:137
Wild JP (1969) Proc Astron Soc Aust 1:181
Wild JP, Smerd SF (1972) ARA&A 10:159
Willson RF (2005) Sol Phys 227:311
Wimmer-Schweingruber RF et al (2006) Space Sci Rev 123:177
Woo R, Armstrong JW, Sheeley NR Jr, Howard RA, Michels DJ, Koomen MJ, Schwenn R (1985) J Geophys Res 90:154
Wu ST (1982) Space Sci Rev 32:115
Yan Y, Pick M, Wang M, Krucker S, Vourlidas A (2006) Sol Phys 239:277
Yashiro S, Gopalswamy N, Michalek G, St Cyr OC, Plunkett SP, Rich NB, Howard RA (2004) J Geophys Res (Space Phys) 109:7105
Yoshimori M (1989) Space Sci Rev 51:85
Zandanov VG, Altyntsev AT, Lesovoi SV (1999) In: Bastian TS, Gopalswamy N, Shibasaki K (eds) Proceedings of the Nobeyama Symposium, held in Kiyosato, Japan, Oct 27–30, 1998. NRO Report No. 479, pp 425–428
Zarro DM, Sterling AC, Thompson BJ, Hudson HS, Nitta N (1999) ApJ 520:L139
Zhang J, Dere KP, Howard RA, Kundu MR, White SM (2001) ApJ 559:452
Zhang J, Dere KP, Howard RA, Vourlidas A (2004) ApJ 604:420
Zhang J et al (2007) J Geophys Res (Space Phys) 112:10102
Zheleznyakov VV (1962) Sov Astronomy 6:3
Zurbuchen TH, Richardson IG (2006) Space Sci Rev 123:31